UNIVERSIDAD NACIONAL AUTONOMA DE MÉXICO

PROGRAMA DE MAESTRÍA Y DOCTORADO EN CIENCIAS (ASTRONOMÍA)

INSTITUTO DE ASTRONOMÍA

ESTUDIO ESTRUCTURAL DE LA REGIÓN DE LÍNEAS ANCHAS EN CUASARES

TESIS

QUE PARA OPTAR POR EL GRADO DE:

DOCTOR EN CIENCIAS (ASTRONOMÍA)

P R E S E N T A:

Castalia Alenka Negrete Peñaloza

DIRECTORAS DE TESIS:

Deborah Dultzin Kessler
Paola Marziani

Ciudad Universitaria, México D.F. 2011

Universidad Nacional Autónoma de México
UNAM
Biblioteca Central
Dirección General de Bibliotecas de la UNAM

UNAM – Dirección General de Bibliotecas
Tesis Digitales
Restricciones de uso

DERECHOS RESERVADOS ©
PROHIBIDA SU REPRODUCCIÓN TOTAL O PARCIAL

Todo el material contenido en esta tesis esta protegido por la Ley Federal del Derecho de Autor (LFDA) de los Estados Unidos Mexicanos (México).

El uso de imágenes, fragmentos de videos, y demás material que sea objeto de protección de los derechos de autor, será exclusivamente para fines educativos e informativos y deberá citar la fuente donde la obtuvo mencionando el autor o autores. Cualquier uso distinto como el lucro, reproducción, edición o modificación, será perseguido y sancionado por el respectivo titular de los Derechos de Autor.

En tus ojos y en tu risa,
mi querido Elián,
habita el universo de mi alma.

Agradecimientos

Quiero agradecer a mis tutoras Deborah y Paola por haberme propuesto el tema de esta tesis y por haberla hecho más interesante en el camino, enriqueciédola con nuevos planteamientos y nuevas ideas. En particular, quiero agradecer a Deborah por sus enseñanzas en el tema y el apoyo que tuve durante mi estancia en el Instituto. Por los seminarios en la maestría, su ayuda en los generales, por guiarme en las temporadas de observación, pero sobre todo, por su amistad y su cariño. A mi tutora Paola, por las miles de explicaciones, en vivo y por videoconferencia, y por su infinita paciencia. Por insistir en que el trabajo de esta tesis quedara ”sparkling”. Por su apoyo, su amistad y hospitalidad en mis viajes a Padua.

A mis sinodales Jack, Vahram y Gloria. Agradezco sus correcciones y su apoyo para mi titulación. También aprovecho para agradecer a mis maestros de la maestría. Ellos me dieron las bases y las herramientas para mi trabajo astronómico.

Asímismo, quiero agradecer a Bertha por los incontables trámites y al departamento de cómputo, por el apoyo otorgado.

A la banda pava, Liliana, Ary, Tomás, Lucía, Vero, Mario, Juan, Lirio. Por los viajes, los cumpleaños, las bodas, las invariables e infaltables comidas de los viernes y las largas sobremesas. Por las noches de pizza y chela y porque en el estado inconsciente de la anestesia general, invoqué sinceramente esos momentos. A Giovanny, Primoz, Bernardo, Manolo, Oscar, Yari y con cuantos compartí mi estancia en el Instituto. Son lo mejor que me llevo.

No hay palabras que expresen mi inmensa gratitud al compañero de mi vida, Andrés, por el apoyo incondicional a mi carrera y a mis sueños y por aguantarme en mis estados de estrés, te mereces una medalla a la paciencia mi amor. Me emociona compartir contigo y con nuestro retoño, mi preciosísimo Elián, este trabajo que en gran parte también es tuyo. Querido hijo, mi corazón late intensamente cuando pienso en cuánto te quiero.

A mi papá y mi mamá por haberme mostrado el camino de la ciencia y por enseñarme a ser perseverante para alcanzar mis metas. Ustedes son mi inspiración. A mis queridísimos Mirsa y Pável, agradezco a la vida por tenerlos como hermanos. Manito, siempre estás a mi lado para apoyarme; Mirsita, tu sola presencia alegra mi vida.

A mi segunda familia, Sra. Francisca, Sr. Leopoldo (¡cuánto lo extraño!), Sandra y Carlos, por hacerme parte de la suya y apoyarme siempre que lo necesito.

A las maestras Lilia, Nidia, Irma, Elsa. Ustedes ya forman parte de mi familia.

Resumen

El trabajo de esta tesis está basado en el estudio de espectros en el óptico y UV de las líneas anchas de cuasares de tipo 1. Este tipo de cuasares poseen líneas tanto anchas (ancho total a altura media FWHM>2000 km s^{-1}) como delgadas (FWHM<2000 km s^{-1}), mientras que los de tipo 2 sólo tienen líneas angostas. En esta tesis nombraremos cuasares a todos los tipos de galaxias con núcleo activo de tipo 1 (*Active Galaxy Nuclei*, AGN), es decir, que tienen espectro de líneas anchas en emisión. Dentro esta categoría incluimos a las galaxias Seyfert tipo 1, los cuasares y las radio galaxias de líneas anchas (del inglés *Broad Line Radio Galaxy* BLRG). Nuestro estudio se enfoca en las líneas anchas porque son las que se están emitiendo en la región más cercana al hoyo negro central, la Región de Líneas Anchas (*Broad Line Region*, BLR). Esta es una región que a pesar de ser compacta, con tamaños menores a 1 parsec, es muy compleja, pues se ha visto que no sólo está estratificada, sino que posee otras características como nubes de alta densidad y vientos salientes de alta ionización. Se piensa que es en esta región donde se genera la intensa actividad que percibimos.

Los cuasares son objetos lejanos y dado que la BLR es muy pequeña, hasta ahora no ha sido posible obtener imágenes directas de esta región, por lo que la forma de estudiarlos es a través de la espectroscopía. Es así como se han realizado numerosos estudios de las líneas en emisión, que tienen como propósito descifrar su estructura interna, sus condiciones físicas, el tamaño de la BLR (r_{BLR}), la masa del hoyo negro central ($M_{\rm BH}$), entre otros parámetros. A lo largo de los estudios en amplias muestras de cuasares, se han visto una gran diversidad de perfiles para una misma línea en emisión, lo que da la idea de que existe algún tipo conexión entre todos los cuasares, quizá evolutiva, o de orientación de la línea de visión o una convolución de ambos.

Es importante destacar que en las últimas dos décadas ha habido un gran avance en el mejoramiento de la señal a ruido (S/N) de los espectros al contar con telescopios que tienen la suficiente resolución que nos permite ver a detalle los perfiles de las líneas. Es así como nos podemos dar cuenta que una línea en emisión puede tener varias componentes, cada una de ellas generada en distintas regiones de la BLR con diferencias cinemáticas e in-

cluso con diferentes condiciones físicas. Así, cada línea nos provee de información acerca de las condiciones físicas que la produjeron, como por ejemplo, la densidad o el grado de ionización. Todas estas componentes son piezas del rompecabezas que estamos construyendo para conocer la estructura de la BLR y en esta tesis contribuimos con una pieza más al aislar cada componente para trabajar con ellas por separado.

Uno de los parámetros más importantes de los cuasares es el tamaño de la BLR y el método directo para conocerlo es mediante el mapeo de reverberación (Peterson et al. 2004). Sin embargo, éste método no es conveniente en términos prácticos porque se necesita mucho tiempo de monitoreo, por lo que el más ampliamente usado es una correlación obtenida empíricamente que relaciona la r_{BLR} con la luminosidad del cuasar (Bentz et al. 2009). Éste es un método muy práctico puesto que es muy fácil medir la luminosidad. Sin embargo, todavía no existe un fundamento físico sólido que explique esta correlación. Otra de las contribuciones de esta tesis es que proveemos de un método para calcular la r_{BLR} basado en cocientes de líneas sensibles a las condiciones físicas (densidad electrónica y parámetro de ionización) existentes en la BLR.

A lo largo de la tesis trabajamos con tres muestras espectrales. La primera de ellas está en el UV y consiste de 130 espectros a bajo corrimiento al rojo ($z < 0.93$) que fueron obtenidos de la base de datos del Telescopio Espacial Hubble (HST) perteneciente a la NASA. Un segundo conjunto de espectros en el UV consiste de 8 espectros de alto z (~ 3), resultado de la observación con el Very Large Telescope (VLT) operado por el Observatorio Europeo Austral (ESO), en modo de servicio. Asímismo, también trabajamos con 18 espectros en el óptico provienentes de un trabajo previo de Marziani et al. (2003). Una característica importante de estos espectros, es que poseen una alta señal a ruido, indispensable para el análsis de las componentes espectrales de cada línea involucrada en nuestro estudio. Las líneas que estudiamos en estos espectros son: Lyα, SiIVλ1397, CIVλ1549, SiIIλ1814, AlIIIλ1860, SiIII]λ1892, CIII]λ1909, MgIIλ2800 y Hβ. La componente principal de estas líneas es la ancha central (*broad component* BC). Así como los pseudocontinuos que forman con las emisiones de FeIII en el UV y FeII en el óptico y el UV.

Una de las líneas en emisión más intensas en el UV, después de Lyα, es CIVλ1549. Esta última es una línea muy importante porque puede ser usada para estimar la r_{BLR} y

la $M_{\rm BH}$. En espectros de alta resolución se puede apreciar que CIVλ1549 no siempre es una línea simétrica o tiene un perfil suave. Del análisis de las componentes espectrales en cuasares a bajo z encontramos que CIVλ1549 presenta, además de la BC, una componente corrida al azul, la cual llega a ser muy intensa en los objetos con FWHM(H$\beta_{\rm BC}$)$\leqslant$4000 km s^{-1} (a los que llamamos Población A, definido para Hβ pero aplicable a todas las líneas anchas incluyendo CIVλ1549, como se explica en el capítulo 3). Para objetos con FWHM(H$\beta_{\rm BC}$)>4000 km s^{-1} (Población B) esta componente es casi nula. La interpretación de este resultado es la existencia de un viento que emerge desde el disco de acreción y está siendo eyectado radialmente hacia afuera de la BLR. Posteriormente, estimamos la r_{BLR} usando una relación empírica que la relaciona con la luminosidad en el UV (a 1350Å) desarrollada por Vestergaard & Peterson (2006) a partir de observaciones de cuasares de bajo z mediante mapeo de reverberación. Conociendo la r_{BLR} y por medio del teorema del virial, podemos estimar la $M_{\rm BH}$ usando al FWHM(CIVλ1549) como indicador de la velocidad. Es necesario hacer notar que con la técnica usada en este trabajo para ajustar el perfil de la línea, no separamos la componente central de la corrida al azul, dando como resultado masas sistemáticamente mayores a las calculadas con H$\beta_{\rm BC}$.

Tomando como base las líneas más intensas de los espectros UV y óptico: Lyα, CIVλ1549, SiIIλ1814, AlIIIλ1860, SiIII]λ1892, CIII]λ1909, MgIIλ2800 y Hβ, realizamos un estudio para 6 objetos representativos de la diversidad de cuasares de las poblaciones A y B que se resume en el Eigenvector 1 (E1), el cual evidencia correlaciones entre algunos de los parámetros observados y es explicado en el capítulo 1. En este análisis mostramos que todas las componentes anchas centrales de un mismo objeto, son similares tanto en sus perfiles como en el FWHM. Más aún, la similitud se basa en la línea Hβ, la cual solo es escalada en intensidad para ajustarse a las otras líneas.

Usando los resultados de los puntos anteriores, ajustamos componentes gaussianas y/o lorentzianas en el espectro UV: SiIVλ1397, CIVλ1549, SiIIλ1814, AlIIIλ1860, SiIII]λ1892, CIII]λ1909, para los 8 cuasares a $z \sim 3$. Posteriormente usamos mapas de diagnóstico para calcular la densidad electrónica $N_{\rm e}$ y el parámetro de ionización U obtenidos de simulaciones de CLOUDY y aplicados a los cocientes de líneas: AlIIIλ1860/SiIII]λ1892, CIVλ1549/AlIIIλ1860 y SiIIλ1814/ SiIII]λ1892, obteniendo como resultado un acotamiento

más preciso de $N_{\rm e}$ y U que los propuestos en trabajos previos en donde sólo se daba un valor estimado, es decir, sólo se estima que la zona donde se emite la BC es de alta densidad y de bajo parámetro de ionización. Conociendo $N_{\rm e}$ y U, podemos calcular la r_{BLR} y la masa del hoyo negro $M_{\rm BH}$, mediante el cálculo de los parámetros físicos $N_{\rm e}$ y U, al interior de los cuasares, al contrario de métodos indirectos como la correlación r_{BLR} - luminosidad. Finalmente, calibramos la correlación r_{BLR} - luminosidad, con los resultados obtenidos del análisis de las condiciones físicas y con los cálculos usando el mapeo de reverberación.

Índice general

1. Introducción **1**

1.1. Descubrimiento de los cuasares. 1

1.2. Núcleos Activos de Galaxias. 2

1.2.1. Procesos Físicos en los AGNs. 4

1.2.2. Medios de estudio de la BLR 13

1.2.3. El Eigenvector 1 17

1.2.4. Condiciones físicas de la BLR y obtención de parámetros fundamentales. 20

1.3. Esquema de la tesis. 27

2. CIVλ1549 como un parámetro del Eigenvector 1 para Cuasares. **29**

2.1. Introducción 31

2.2. Mediciones de la línea CIVλ1549 y correlaciones. 32

2.3. Evidencia de dos poblaciones de AGNs con líneas anchas. 37

2.4. Emisión de la línea angosta de CIVλ1549. 43

2.5. Cálculo de la $M_{\rm BH}$ usando el ancho de CIVλ1549. 48

2.6. Conclusiones 49

2.7. Apéndice 50

3. Condiciones físicas de la Región de Líneas Anchas para Cuasares a $z < 1$ a lo largo del Eigenvector 1. 53

3.1. Introducción 55

3.2. Selección de los objetos y observaciones. 58

3.3. Análisis de datos. 58

3.4. Resultados 59

3.5. Discusión 64

3.6. Conclusiones 68

3.7. Apéndice 70

4. Condiciones físicas en la Región de Líneas Anchas para Cuasares a $z \sim 3$. 71

4.1. Introducción 73

4.2. Observaciones 75

4.3. Reducción de los datos 75

4.4. Análisis de datos 77

4.5. Resultados del análisis de las líneas para objetos individuales 81

4.6. Simulaciones con CLOUDY 89

4.7. Resultados para dos casos extremos 92

4.8. Resultados para los cuasares a z $\sim$ 3 96

4.9. Un método de fotoionización para calcular la r_{BLR} y la $M_{\rm BH}$ 104

4.10. Discusión 105

4.11. Conclusiones 107

4.12. Apéndice. Desarrollo de los cálculos para r_{BLR} y $M_{\rm BH}$. 109

5. Calibrando la relación empírica $r \propto L^{\alpha}$ **115**

5.1. Introducción 116

5.2. Definición de la muestra y reducción de los datos 117

5.3. Método y comparación 117

5.4. Discusión y conclusiones 118

5.5. Apéndice. La muestra completa de cuasares. 120

6. Conclusiones generales. **127**

7. Trabajo a futuro. **129**

Capítulo 1

Introducción

1.1. Descubrimiento de los cuasares.

Las primeras observaciones se iniciaron en los años 50's. Se hicieron con el interferómetro Jordell Bank de 1 segarc de resolución y de de 250 pies, que dio como origen varios catálogos que se publicaron en Cambridge, y que evidenciaron la existencia de objetos puntuales como fuentes de energía muy intensas. En el trabajo de Seyfert (1943) se mostraban galaxias espirales con un núcleo muy brillante y espectros en emisión de líneas de alta ionización muy intensas. Los objetos que se descubrieron primero con emisión intensa fueron las radio galaxias, como Cygnus A, en donde simplemente se describía que la emisión en radio se originaba cerca del núcleo y que podría ser debida a partículas relativistas expulsadas desde la galaxia en direcciones opuestas a lo largo del eje de rotación. Para explicar la enorme cantidad de energía emitida se invocaba a el mecanismo de sincrotrón, capaz de proveer al menos $10^{60} ergs$ en forma de partículas relativistas y campos magnéticos débiles. Fue hace casi 50 años, en 1962, cuando se identificó a la radio fuente 3C273 y con ella se reconoció a una nueva clase de objeto astronómico, los objetos puntuales cuasi estelares emisores en radio (*quasi stellar radio source QSRs*). Se nombró a 3C273 un objeto cuasi estelar debido a que tiene una magnitud 13 y es una fuente pun-

tual, similar a la de una estrella. Las líneas espectrales que se identificaron fueron las de Balmer y MgIIλ2800 y con ellas se determinó un corrimiento al rojo de $z = 0.158$. A esta distancia, la energía emitida por el cuasar debía ser de $\sim 10^{47} ergss^{-1}$. Dada la resolución de la época y a que además las líneas están entremezcladas entre sí, la descripción de los perfiles de las líneas anchas en emisión, en particular las de Balmer, se limitaba a decir que por lo general era simétrico aunque en ocasiones se encontraba una ligera asimetría hacia el rojo. Así mismo, se observaban en los espectros de las galaxias Seyfert y las radio galaxias, un número considerable de estructuras en las líneas como si estuvieran involucradas numerosas nubes a diferentes velocidades. Aunado a esto, en esa estructura se observaban cambios.

Al ser los primeros en ser detectados, se pensaba que las radio fuentes eran las que predominaban. Sin embargo, se empezaron a detectar fuentes puntuales radio calladas. Se les llamó objetos cuasi estelares (QSOs) a los que se les describía como objetos no resueltos con líneas intensas en emisión a altos corrimientos al rojo (z). Nosotros nos referiremos a ambas clases de objetos como ”cuasares”. Ya en los 80’s, Weedman (1983) reporta muchas similitudes en las propiedades observadas de las galaxias Seyfert 1 y los cuasares.

Para explicar las grandes cantidades de energía emitida por los cuasares, Zel’Dovich & Novikov (1964) por un lado y Salpeter (1964) por otro, propusieron que en el centro de los QSRs habita alguna especie de cuerpo masivo compacto u hoyo negro que acreta material del medio circundante.

1.2. Núcleos Activos de Galaxias.

Actualmente, se agrupan a los cuasares, galaxias Seyfert y otros objetos similares bajo el término Núcleos Activos de Galaxias ó AGNs por sus siglas en inglés. Todos son objetos cuya característica principal son líneas intensas en emisión derivadas de su actividad interna y de la emisión de gas de alta ionización no relacionada con actividad estelar. Fueron nombrados de esta manera debido a que los cuasares son fuentes puntuales (y se

creyó que eran ”estrellas azules”) y las glaxias Seyfert tienen un núcleo prominente similar a los cuasares. También se han detectado nebulosidades alrededor de los cuasares que seguramente son sus galaxias anfitrionas. Con interferometría en radio se confirmó que los jets de las radiogalaxias emanan del núcleo. Algunas veces se usa el término ”Galaxia Activa”, éste se refiere a galaxias que albergan núcleos activos. Las galaxias activas se diferencian unas de otras por la intensidad y el ancho de sus líneas, entre otras características.

Los AGNs son los objetos que emiten más energía de forma continua (los estallidos de rayos-γ, los GRBs, son muy intensos pero su duración varía desde unos nanosegundos hasta cerca de una hora, aunque por lo general, un brote típico suele durar unos pocos segundos). Emiten en todas las longitudes de onda: radio, milimétrico, infrarojo (IR), óptico, ultravioleta (UV), rayos-X y rayos-γ. Involucran todos los procesos físicos como por ejemplo, emisión de sincrotrón en el continuo, reemisión de polvo que se observa en el IR, Compton, Compton inverso (en el continuo), emisión de cuerpo negro que se cree se emite en el disco de acreción y da lugar al *big blue bump*, una emisión extensa en el UV. Un excelente artículo de revisión acerca de la emisión de continuo de los AGNs está en Ulrich et al. (1997).

Existen diversas maneras de clasificar a los AGNs, como la realizada con base en su emisión en radio y en el óptico, más específicamente por medio del cociente de Kellerman r_K (Kellermann et al. 1989) definido por la razón de los flujos de intensidad en el radio (a 6 cm) y el óptico (a 4400Å). Otra manera de clasificarlos es basándose en los anchos de sus líneas, dando lugar a los llamados de tipo 1 que tienen anchos de sus líneas permitidas que pueden ir desde FWHM $\geq$ $1000 km\ s^{-1}$ hasta ∼20,000km s^{-1} y los de tipo 2 con líneas permitidas con anchos desde unos cientos hasta menos de 1000km s^{-1}, igual que las prohibidas (Khachikian & Weedman 1974). Los AGNs de tipo 1 son objeto de estudio de esta tesis dado que nos proveen de información de la dinámica en su interior. Sin embargo, éste tipo de clasificación no explica las causas físicas subyacentes a ésta dicotomía.

1.2.1. Procesos Físicos en los AGNs.

Emisión de continuo.

La emisión del continuo de los cuasares proviene de diversas fuentes, como por ejemplo, de procesos térmicos como la emisión de cuerpo negro y la emisión libre–libre. Un **cuerpo negro** es un absorbedor y emisor perfecto a todas las longitudes de onda. Está en equilibrio térmico con sus alrededores, tiene una única temperatura que lo define y su pico está directamente relacionado con la temperatura absoluta del cuerpo descrito por la ecuación de radiación de Planck

$$B_\nu(T) = \frac{2h\nu^3}{c^2\,(e^{h\nu/kT} - 1)} \tag{1.1}$$

cuyas unidades son watts por metro cuadrado por unidad de ángulo sólido por unidad de frecuencia ($Wm^{-2}sr^{-1}Hz^{-1}$). B_ν es la intensidad de radiación emitida por intervalo de frecuencia, a una frecuencia dada, h es la constante de Planck, c es la velocidad de la luz, k es la constante de Boltzmann y T la temperatura. La ecuación de Planck puede simplificarse en dos regiones: la Rayleigh–Jeans, para frecuencias menores que el pico de emisión; y la región de Wien, para frecuencias mayores.

$$B_\nu(T) = \frac{2kT}{c^2}\nu^2 \qquad \text{región Rayleigh–Jeans} \tag{1.2}$$

$$= \frac{2h\nu^3}{c^2 e^{h\nu/kT}} \qquad \text{región Wien.} \tag{1.3}$$

La luminosidad radiada por un cuerpo negro esférico está dada por

$$L = 4\pi r^2 \sigma T^4, \tag{1.4}$$

donde r es el radio del cuerpo, σ es la constante de Stefan–Boltzmann y T es la temperatura absoluta. Esta ecuación puede verse en dos partes, por un lado tenemos σT^4 que es la tasa a la cual el cuerpo negro radía por unidad de área, también conocida como la ley de Stefan–Boltzmann. Y por otro lado tenemos a $4\pi r^2$, que es la superficie total del cuerpo negro.

La **emisión libre–libre** es indicativa de gas caliente ionizado y es producida donde existe una densidad adecuada de electrones libres. Otra manera de llamar a esta emisión

es bremsstrahlung (en alemán, radiación de frenado), que describe la desaceleración de un electrón en el campo de una partícula cargada, como por ejemplo un electrón en el campo de un protón, radiando en el proceso. Ejemplos donde existe ésta emisión incluyen atmósferas estelares, plasmas densos y calientes (que pueden ocurrir en el núcleo de una galaxia activa) y en las regiones HII. Una región HII que rodea una estrella muy caliente es formada por la fotoionización del hidrógeno por los fotones UV de la estrella. La emisión del continuo de esta región proviene de la emisión libre–libre producida por los electrones del gas y puede extenderse desde la región en el óptico hasta el radio. En una región HII, si tomamos el caso ópticamente grueso en donde la opacidad τ_ν es mucho mayor a 1, la región se vuelve opaca y su espectro se aproxima al de un cuerpo negro a temperatura T. Así, la intensidad I_ν emitida como función de la frecuencia ν es

$$I_\nu = \frac{2kT}{c^2}\nu^2. \tag{1.5}$$

Es decir, el índice espectral de la ley de potencias, α ($I_\nu \propto \nu^\alpha$), es igual a 2. El caso ópticamente delgado se da a altas frecuencias, cuando la opacidad τ_ν es muy baja y la región se vuelve casi transparente. La intensidad depende muy poco de la frecuencia, con un índice espectral de -0.1, es decir, el espectro producido es casi plano. El quiebre en el espectro corresponde a una frecuencia para la cual $\tau_\nu \approx 1$.

Los procesos de altas energías como la radiación sincrotrón, Compton y Compton inverso no son de origen térmico e involucran tanto a partículas como a fotones. La **radiación sincrotrón** es una señal común de procesos de altas energías en la astrofísica y denota la presencia de electrones relativistas y un campo magnético. A diferencia del mundo clásico de bajas energías, donde un electrón radía como un dipolo, la emisión sincrotrón de un electrón es enconada en dirección de su movimiento, dando lugar a un cono de radiación con un ángulo de apertura inversamente proporcional al factor relativista

$$\gamma = \left(1 - \frac{v^2}{c^2}\right)^{-1/2} \tag{1.6}$$

de los electrones. Los electrones de una energía E dada radían a una frecuencia ν específica en un campo magnético B particular dado por la ecuación $\nu \propto BE^2$, con $E = \gamma mc^2$. La emisión sincrotrón de electrones relativistas es importante cuando se está viendo en la

dirección de su movimiento, y en ocasiones se llegan a ver movimientos superlumínicos, como es el caso de los blazares, que son cuasares con el jet orientado directamente a nosotros. Un ejemplo de blazares son los objetos BL Lacertae (o BL Lac) que se caracterizan por mostrar una gran variabilidad en el flujo.

Una distribución de energía de ley de potencias produce un espectro de ley de potencias de la radiación sincrotrónica con el índice de la distribución del electrón s, y está ligada con el índice espectral (α) del espectro de radiación ópticamente delgada, por la ecuación

$$\alpha = \frac{1-s}{2}. \tag{1.7}$$

El espectro de emisión de sincrotrón se espera que sea de ley de potencias y la observación de α permite determinar s. Para muchas fuentes, se encuentra que $\alpha \sim -0.7$ y por tanto $s \sim 2.4$. A bajas frecuencias, los fotones emitidos se auto absorben por el ensamble de electrones, lo que produce un quiebre en el espectro de emisión. La pendiente espectral en el régimen ópticamente grueso es $\alpha = 2.5$

El **efecto Compton** es observado cuando un fotón de alta energía interactúa con un electrón de baja energía. El electrón es impulsado y el fotón pierde energía. La emisión de Compton es importante en regiones donde los electrones están inmersos en un campo de fotones de alta energía, como ocurre cerca del disco de acreción de un hoyo negro. La subsecuente aceleración de partículas actúa como un proceso que enfría a los fotones. El efecto Compton es fuente de la emisión del continuo que se observa desde el infra rojo hasta los rayos–γ, dependiendo de los fotones que están interactuando con los electrones.

El caso contrario también es posible debido a la presencia de electrones con altas energías. En este caso, un electrón de alta energía interactúa con un fotón cediéndole su energía. Haciendo analogía de la radiación sincrotrón donde electrones relativistas interactúan con un campo magnético, el efecto **Compton inverso** involucra también electrones relativistas pero interactuando con fotones. La ecuación que describe la tasa de pérdida de energía de un electrón relativista interactuando con un campo magnético con densidad de energía U_{mag} (ó de fotones U_{rad}) es

$$\frac{dE}{dt} = \frac{4}{3}\sigma_T c \gamma^2 U. \tag{1.8}$$

Donde σ_T es la sección recta de interacción de Thompson, c es la velocidad de la luz, γ es el factor relativista definido por la ecuación 1.6 y U puede ser de origen magnético o de fotones. Cabe mencionar que en esta interacción la densidad de fotones se conserva y los fotones son impulsados a energías más altas por un factor

$$\nu \approx \gamma^2 \nu_0, \tag{1.9}$$

donde ν_0 es la frecuencia inicial de los fotones. Así, fotones de longitudes de onda en radio pueden ser impulsados hasta rayos–X, o fotones en el rango óptico pueden llegar hasta los rayos–γ.

Las emisiones sincrotrón y Compton inverso tienen roles complementarios y dan lugar al proceso "*synchrotron self–Compton*" (SSC). En este proceso, los fotones de sincrotrón dispersan a los electrones a energías más altas los cuales producen más fotones sincrotrón por la interacción con el campo magnético y así el ciclo se repite. Este proceso es detenido por la emisión Compton inverso que provee un mecanismo de enfriamiento de los electrones, lo cual ocurre cuando las densidades de energía de los fotones y los electrones son lo suficientemente grandes para que los electrones de altas energías producidos por la emisión de sincrotrón ahora dispersen sus propios fotones de sincrotrón a altas frecuencias. Debido a esto, los fotones de alta energía del Compton inverso tienen una profundidad óptica muy baja en el medio y escapan fácilmente, proveyendo de un mecanismo de enfriamiento. El espectro de Compton inverso debe mostrar la misma dependencia en la energía como el espectro del sincrotrón del cual se deriva, pero desplazado hacia frecuencias mayores, tal y como lo describe la ecuación 1.9 y se muestra esquemáticamente en la figura 1.1.

Estos procesos son importantes donde existe un campo de fotones grande como los alrededores de la fuente central de los AGNs.

Líneas de emisión como diagnóstico.

Las líneas de emisión son muy importantes para hacer deducciones de la física del gas que las emite, en especial del que existe en la BLR, cuya geometría la podemos considerar

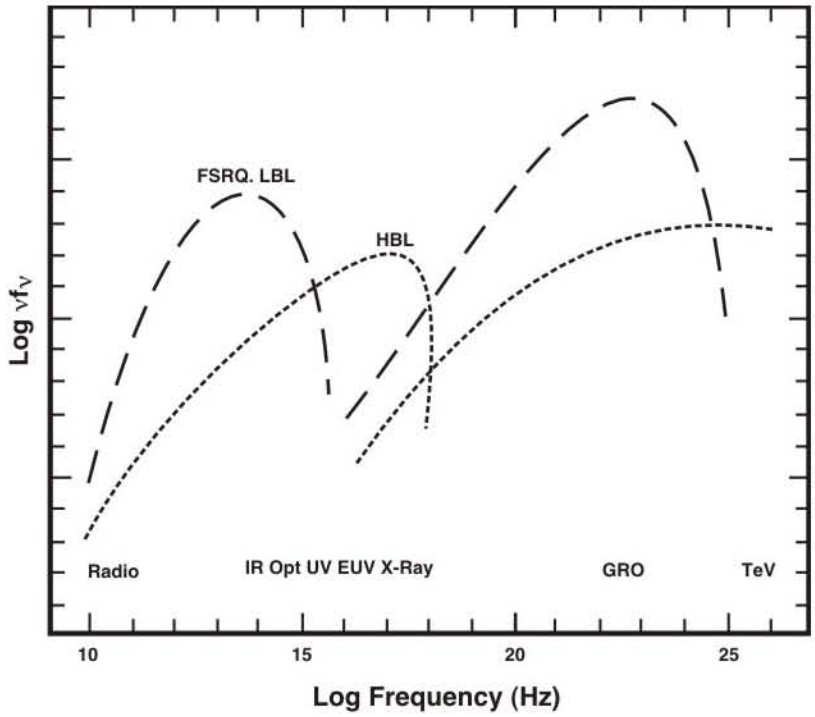

Figura 1.1: Espectro esquemático de banda ancha de blazares de radio hasta rayos–γ en TeV. La componente de baja energía es probablemente debida a la radiación sincrotrónica y la componente de alta energía a la dispersión de Compton de los fotones de baja energía que la alimentan, y que posiblemente sean fotones del sincrotrón o fotones UV/rayos–X provenientes del disco. Dos curvas distintas representan las formas espectrales promedio (Sambruna et al. 1996) de los HBL (objetos BL Lac de altas energías "peaked"; línea punteada) y los LBL (objetos BL Lac de baja energía "peaked"; línea rayada) definido por los cocientes de flujo de rayos–X y radio (de 5Ghz a 1keV) α_{rx}<0.75 ó >0.75, respectivamente. Los blazares de líneas intensas en emisión (es decir, los radio cuasares de espectro plano o FSRQ), tienen un continuo parecido a los LBL. Tomado de Ulrich et al. (1997).

de un disco formado por nubes. Por simplicidad haremos primero un análisis de la emisión de líneas considerando a una región HII, es decir, una nube esférica fotoionizada y homogénea de hidrógeno que rodea a una estrella caliente y produce una región ionizada acotada por un borde bien definido llamado esfera de Strömgren. Más adelante veremos que esta simplificación no es completamente válida para la BLR, sin embargo tomaremos el desarrollo que a continuación se describe como una primera aproximación para la obtención de la densidad electrónica N_e y el parámetro de ionización U.

Suponiendo equilibrio termodinámico, el coeficiente de emisión de una línea está dado por

$$j_{mn} = A_{mn} E_{mn} N_m \tag{1.10}$$

donde mn se refiere a la transición del estado atómico m al n, A_{mn} es la probabilidad de transición espontánea, E_{mn} es la energía del fotón emitido en esa transición y N_m es el número de átomos por unidad de volumen en el estado atómico m (ó número de población). Las unidades del coeficiente de emisión son watts por metro cúbico $[Wm^{-3}]$, es decir, es una medida de la potencia radiada por la línea por unidad de volumen del gas. De este modo, la luminosidad total es j_{mn} multiplicado por el volumen del gas.

En equilibrio termodinámico podemos suponer que los átomos tienen una distribución Maxwelliana de velocidades,

$$N(v)dv \propto v^2 e^{-m_p v^2/2kT} dv \tag{1.11}$$

donde $N(v)$ es el número de átomos de masa m_p con una velocidad en el rango v y $v + dv$, k es la constante de Boltzman y T la temperatura. Nótese que la energía de una partícula es $\frac{1}{2} m_p v^2$.

Asímismo, en equilibrio termodinámico, las poblaciones relativas entre dos niveles atómicos está dada por la ecuación de Boltzmann

$$\frac{N_m}{N_n} = \frac{g_m}{g_n} e^{-E_{mn}/kT}, \tag{1.12}$$

donde g_m y g_n son los pesos estadísticos de los niveles m y n, y E_{mn} es la diferencia de enregía entre los niveles m y n. Es así como podemos conocer las densidades relativas entre dos niveles energéticos.

Para el caso de los AGNs, una manera de simplificar el cálculo de la emisión de líneas es a través de la aproximación del **caso B**. Ésta es aplicable en profundidades ópticas grandes para Lyα y consiste en suponer que los fotones de las líneas Lymann son dispersados varias veces en el gas y finalmente son convertidas en fotones Lα más fotones de las líneas de Balmer y otros fotones. Estos últimos pueden escapar fácilmente mientras que los fotones Lα son atrapados por dispersiones sucesivas y por tanto tienen una mayor probabilidad de ser destruidos por el polvo presente en el medio. En este caso, no es posible determinar los valores individuales de N_m y N_n, sin embargo se puede usar el cociente de dos líneas espectrales, por ejemplo Hα/Hβ, el cual se predice que tenga un valor de entre 2.75 y 3.0. Este cociente se le conoce como el **decremento de Balmer**. En el caso de los AGNs, se esperaría que la situación fuera la misma, sin embargo se observa que no es así. Por lo general los valores encontrados son mucho mayores a 3. Para explicar este desacuerdo se pueden invocar dos posibilidades. La primera tiene que ver con la existencia de polvo, el cual se piensa que se encuentra entre la región de líneas anchas (BLR) y la de líneas angostas (NLR), absorbiendo preferentemente a los fotones más energéticos, es decir, absorbe más fotones de Hβ que de Hα, llevando así el decremento de Balmer a valores mayores. Una segunda aproximación es la existencia en los AGNs de fotones de altas energías (energías mayores que las de las regiones HII), producidos por el espectro del continuo de la fuente central ionizante. Aunque esto bajaría el valor del decremento de Balmer hacia el valor esperado, no es congruente con el espectro observado del continuo de muchos AGNs. Sin embargo cabe mencionar que la emisión entre UV y los rayos–X suaves (EUV) proveniente del continuo de alta energía, no está bien determinado debido a que no existen observaciones en este rango.

El uso de líneas prohibidas es ampliamente empleado para la determinación de la densidad y la temperatura en regiones ionizadas tipo HII. La diferencia entre las líneas permitidas y las prohibidas es que las primeras se producen de recombinaciones de niveles mayores que caen en cascada a niveles menores, mientras que las segundas son el resultado de excitaciones colisionales provenientes de los niveles menores. Además, tienen un valor pequeño de la probabilidad de transición A_{nm} (del nivel n al m, $A_{nm} = 1/\tau$), lo que significa que el átomo se mantendrá un largo tiempo τ en el estado excitado n antes de decaer radiativamente al nivel m. Es por esto que las líneas prohibidas son producidas en

regiones de baja densidad y tienen una densidad crítica para la cual la línea se desexcita colisionalmente.

El promedio de la densidad electrónica en una región ionizada puede ser medido observando los efectos de la desexcitación colisional. Esto se hace comparando la intensidad de dos líneas del mismo ión, emitidas por diferentes niveles con energía de excitación similares, de modo que la tasa de excitación relativa en los dos niveles depende únicamente del cociente de las intensidades colisionales. Si los dos niveles tienen distintas probabilidades de transición radiativa o diferentes tasas de desexcitación colisional, las poblaciones relativas de los dos niveles dependerán de la densidad y de este modo, el cociente de intensidades de las líneas que ellas emitan también dependerá de la densidad.

La ecuación de equilibrio para el balance entre las tasas de excitación y desexcitación de un nivel excitado es, en general

$$N_e N_m \sigma_{mn} = N_e N_n \sigma_{nm} + N_n A_{nm} \tag{1.13}$$

donde σ_{nm} es la sección recta colisional para excitación del nivel m al nivel n, integrada sobre todas las velocidades (Osterbrock & Ferland 2006). Tomando en cuenta las ecuaciones para dos niveles n y m, la solución es

$$\frac{N_n}{N_m} = \frac{N_e \sigma_{mn}}{A_{nm}} \left[1 + \frac{N_e \sigma_{nm}}{A_{nm}} \right]^{-1}. \tag{1.14}$$

Para las líneas prohibidas, $N_n/N_m \ll 1$ mientras que para las permitidas es $\gg 1$. Así, el coeficiente de emisión es

$$j_{nm} = N_m A_{nm} E_{nm} \frac{\sigma_{mn}}{\sigma_{nm}} \left[\frac{N_{e-crit}}{N_e + 1} \right]^{-1} \tag{1.15}$$

(Robson 1996), donde se ha definido una ”densidad crítica”

$$N_{e-crit} = \frac{A_{nm}}{\sigma_{nm}}. \tag{1.16}$$

Si consideramos un sistema de dos niveles donde m es el estado base, entonces $N_m = XN_e$ es la densidad del estado base que está relacionada con la densidad en toda la región y es

proporcional a la densidad electrónica N_e, donde X es una constante de proporcionalidad. Para el caso de alta densidad, $N_e \gg N_{e-crit}$ y la ecuación 1.15 se convierte en

$$j_{21} = XN_eA_{nm}E_{nm}\left(\frac{\sigma_{mn}}{\sigma_{nm}}\right). \tag{1.17}$$

Así, en el caso de alta densidad donde la densidad electrónica es mucho mayor que la crítica, la emisión de las líneas de recombinación dominan a las líneas prohibidas. Para el caso de baja densidad, $N_e \ll N_{e-crit}$ y la ecuación 1.15 se convierte en

$$j_{nm} = XN_e^2E_{nm}\sigma_{mn}. \tag{1.18}$$

Como ejemplos, mencionaré las densidades críticas para las líneas prohibidas del doblete [OIII]$\lambda\lambda$4959,5007 que es cerca de $10^{12}m^{-3}$, para la línea semiprohibida CIII]λ1909 es $10^{16}m^{-3}$ y para CIVλ1549, una línea permitida, es $10^{22}m^{-3}$.

Para el caso de la región de líneas anchas (BLR), encontramos dificultades en la aplicación de los modelos de fotoionización descritos previamente, puesto que como su nombre lo dice, sólo existen líneas anchas, las cuales son en su gran mayoría permitidas. Una de las líneas semiprohibidas anchas mas referidas es la de CIII]λ1909, la cual establece una cota superior para la densidad en la zona en la que se emite. Sin embargo, como veremos en el capítulo 4 las densidades en la BLR pueden llegar a ser algunos órdenes de magnitud mayor. En general, el uso de las líneas anchas de los cuasares en mapas de diagnóstico ha sido difícil de interpretar. Una excepción la podemos encontrar en el trabajo de Matsuoka et al. (2008) quienes analizaron la región parcialmente ionizada que emite la mayor parte de las líneas de baja ionización (*Low Ionization Lines* LILs) en los espectros de los cuasares. Ellos sugieren que las líneas de [OIII]$\lambda\lambda$4959,5007 y el triplete de CaII están siendo emitidas en un gas denso de baja ionización, probablemente localizado en la periferia de la BLR. Por otro lado, como lo mencionan Baldwin et al. (1996), si la densidad electrónica y las condiciones de ionización son conocidas, es posible derivar, con algunas otras suposiciones adicionales, la distancia a la BLR.

Las condiciones físicas del gas fotoionizado pueden ser descritas por la densidad electrónica $N_{\rm e}$ o equivalentemente el número total de la densidad de hidrógeno $N_{\rm H}$ (para

un medio totalmente ionizado $N_e \approx 1.2\ N_H$), la densidad columnar del hidrógeno N_c, la metalicidad y el parámetro de ionización U. éste último se define como el cociente adimensional del número de fotones ionizantes y la densidad electrónica

$$U = \frac{\int_{\nu_0}^{+\infty} \frac{L_\nu}{h\nu} d\nu}{4\pi N_H c r^2} \tag{1.19}$$

donde L_ν es la luminosidad específica por unidad de frecuencia, h es la constante de Planck, ν_0 es la frecuencia de Rydberg, c es la velocidad de la luz y r puede ser interpretada como la distancia entre la fuente central de la radiación ionizante y la región emisora de líneas. De este modo, si conocemos el producto $N_H \cdot U$, podemos estimar el radio r de la BLR.

1.2.2. Medios de estudio de la BLR

Actualmente es ampliamente aceptada la idea de que la fuente de energía de los cuasares es debida a procesos relacionados con la acreción de gas al hoyo negro supermasivo que esta en su interior. De hecho, la mayoría de las galaxias con bulbo probablemente tengan uno en su centro. Una de las primeras evidencias observacionales más directa viene de la observación de máseres de agua (Miyoshi et al. 1995) y la contundente, del estudio de las órbitas de estrellas cercanas al hoyo negro en el centro de nuestra galaxia (e.g. Ghez et al.,2003, 2005, 2008).

Observacionalmente, el espectro de un cuasar se compone de un intenso continuo al que se sobreponen líneas anchas en emisión. El continuo se produce muy cerca del centro, pues se debe a la acreción del gas hacia el hoyo negro, mientras que las líneas emergen del gas que se encuentra más lejos y está siendo ionizado por la radiación del continuo. Sin embargo está lo suficientemente cerca del hoyo negro para producir el efecto Doppler que hace que se ensanchen las líneas. Ésta es justamente la Región de Líneas Anchas, cuyo gas es el más próximo al hoyo negro y produce las líneas en emisión, por lo que el estudio detallado de sus condiciones físicas y su dinámica nos da información de la actividad nuclear.

Otros métodos con los que se estudian los cuasares varía de acuerdo al tipo de fenómeno y la longitud de onda que nos interese. Así, en el óptico e IR, se usa fotometría para estudiar su variabilidad, y la imagen directa (en cuasares cercanos) para el análisis de la galaxia anfitriona y su ambiente. Por otro lado, en casi todas las bandas espectrales se usa la espectroscopía para el análisis de las líneas tanto de emisión como de absorción.

Para obtener perfiles de líneas anchas con buena S/N se pueden usar telescopios relativamente chicos (e.g. 2m del Observatorio Astronómico Nacional, San Pedro Mártir OAN–SPM, Marziani et al. 1996) con largos tiempos de exposición (1 a 2 horas para magnitudes de hasta 17). Para objetos más débiles, se requieren telescopios mucho más grandes. En esta tesis usamos observaciones del OAN-SPM, el Telescopio Espacial Hubble (HST), el SDSS (*The Sloan Digital Sky Survey*) y del VLT.

Con la construcción de telescopios cada vez más grandes, la resolución de la espectroscopía ha mejorado enormemente y se ha convertido en una poderosa herramienta que permite obtener información más detallada de los cuasares. Durante muchos años sólo se usó para determinar z, pues con la baja resolución de los espectros se creía que todos eran similares, incluso hubo trabajos (Francis et al. 1991) en los que se promediaban cientos de espectros para aumentar la S/N. En esta tesis trabajamos con espectros de alta S/N que nos permite ver a detalle los perfiles de las líneas en emisión. Veremos que los espectros son muy distintos y por lo tanto para tener algún sentido al sumarlos, habría que hacerlo por ”tipos”, como los espectros estelares. En la tesis se toca el tema de los distintos tipos de espectros en el capítulo 3.

Dinámica de la BLR.

La BLR está lo suficientemente cerca de la fuente que la ioniza como para que cualquier cambio en el continuo ionizante se refleje, tiempo después, en la variación de las líneas anchas. La escala de tiempo de respuesta de estas variaciones es de horas hasta semanas. Calculando el tiempo de respuesta (τ) de las líneas al continuo y conociendo la velocidad a la que viaja la radiación ionizante (c, la velocidad de la luz), podemos conocer

la distancia a la BLR

$$r_{BLR} = c \cdot \tau. \tag{1.20}$$

A esta técnica se le conoce como **mapeo de reverberación**. Los estudios que monitorean las variaciones de las líneas, involucran la participación de varios telescopios y mucho tiempo de observación. Por ejemplo, Kaspi et al. (2000) tardó cerca de 8 años en monitorear las líneas Hα y Hβ, entre otras, para 28 cuasares a $z \sim 0.4$. Hasta ahora este tipo de campañas se han realizado para menos de 50 cuasares cercanos ($z < 1$, Kaspi et al.2000, 2005, Peterson et al.2004, Bentz et al.2010).

Una suposición esencial para la geometría de la BLR, apoyada por varias observaciones, es que el gas que emite las líneas reverberadas está virializado, es decir, que el movimiento de este gas es kepleriano y está dominado por la gravedad del hoyo negro central. Además de la distancia a la BLR, otro resultado importante del mapeo de reverberación, es que las líneas responden con distintos tiempos de retraso, lo que nos habla de una estratificación en la BLR.

Para objetos en los que no se puede aplicar el mapeo de reverberación, se usan diversas correlaciones empíricas entre el valor de la luminosidad del continuo en el óptico (5100Å) y en el UV (1350Å; Kaspi et al. 2005, Vestergaard & Peterson 2006, también ver Bentz et al. 2009)

$$r_{BLR} \propto L^{\alpha}, \tag{1.21}$$

con $\alpha = 0.52$ y L(5100Å) para el óptico (Bentz et al. 2009) y $\alpha = 0.53$ y L(1350Å) para el UV (Vestergaard & Peterson 2006).

Una manera alternativa de determinar la distancia a la BLR, es deduciéndola de la fórmula del parámetro de ionización (ec. 1.19), lo cual se describe en el capítulo 4.

En vista de que la masa del hoyo negro domina la dinámica y cinemática de las líneas anchas, es importante poder calcularla. La masa del hoyo negro puede ser calculada por medio de la dinámica estelar o del gas en el centro galáctico por medio de la ecuación

$$M_{BH} = f\frac{\Delta v^2 r_{BLR}}{G} \tag{1.22}$$

donde Δv es la dispersión de velocidades (σ) que sale cuando se observan las líneas de absorción provenientes de las estrellas de la galaxia subyacente. Cuando éstas no se observan en el espectro, se toma el ancho Doppler de las líneas en emisión del gas virializado. Este ancho lo obtenemos del FWHM, que es la anchura total a media altura que presenta una determinada línea de emisión.

El estudio de la dinámica estelar se puede hacer en AGNs cercanos (e.g galaxias Seyfert), pues su núcleo no es tan luminoso. Sin embargo el núcleo de los cuasares es tan brillante que no permite ver la luz proveniente de las estrellas de la galaxia huésped (no se observa el espectro de absorción de las estrellas). A esto se suma el hecho de que son objetos lejanos y gran parte de su actividad se encuentra en una región confinada de apenas unas décimas de parsec, que es en donde se emite casi toda su luz.

Cabe mencionar que los espectros muestran variaciones en el tiempo y en esta tesis trabajamos sobre espectros de una época. En algunos casos la variabilidad es grande (e.g. Shapovalova et al.2008) y puede llegar a ser una fuente de incertidumbre en el cálclulo de la masa. Otras fuentes de incertidumbre provienen de tomar el FWHM mezclando componentes de distintas regiones de emisión, en algunos casos incluso de la región de líneas angostas (NLR), y del desconocimiento del ángulo de inclinación del eje principal del cuasar (Collin et al. 2006).

En esta tesis, hemos determinado las masas del hoyo negro a partir de las distancias obtenidas con nuestro método (descrito en el capítulo 4, con base en las condiciones físicas), y al compararlas con las masas determinadas con distancias de reverberación, obtenemos un buen resultado.

En trabajos previos (e.g. Sulentic et al. 2006), se ha demostrado que existe una cota superior a la masa del hoyo negro de $10^{10} M_{\odot}$ para objetos de z hasta ~ 7, determinada por la virialización. Esto es congruente con el límite para la velocidad de dispersión esperada en el bulbo de una galaxia (con un máximo de aproximadamente 700 km s^{-1}). La masa está relacionada con la velocidad de dispersión de las estrellas en el bulbo por la ecuación

$$M \propto \sigma^{\alpha}. \tag{1.23}$$

Como ejemplo, Gültekin et al. (2009) encontraron, basándose en una amplia muestra de masas de hoyos negros en galaxias cercanas, que

$$\log\left(\frac{M}{M_\odot}\right) \approx 8.12 \; + \; 4.24 \log\left(\frac{\sigma}{200 \text{ km } s^{-1}}\right) \tag{1.24}$$

es decir, $\alpha \approx 4.2$.

A su vez, la masa del bulbo esta asociada a la masa del hoyo negro (ver e.g. Magorrian et al. 1998, Tremaine et al. 2002, Marconi & Hunt 2003) por medio de la ecuación:

$$\log\left(\frac{M_{BH}}{M_\odot}\right) \; \approx \; -1.79 \; + \; 0.96 \; \log\left(\frac{M_{bulbo}}{M_\odot}\right) \tag{1.25}$$

1.2.3. El Eigenvector 1

Hasta ahora hemos visto que los cuasares presentan, por un lado, una gran diversidad de propiedades tales como la luminosidad, intensidades y perfiles de líneas, anchos equivalentes (EW) y flujos en distintas bandas del espectro. Por otro lado, tenemos a los procesos físicos que las determinan, derivados principalmente de la acreción de gas hacia el hoyo negro. En un esfuerzo por correlacionar causa y efecto, Boroson & Green (1992) (BG92) usaron un método estadístico llamado análisis de las componentes principales (PCA por sus siglas en inglés). El PCA es un método estadístico que permite determinar el número mínimo de variables independientes o que no tienen una correlación evidente, de un gran número de variables observadas. El número de ”factores significativos” nos habla de la dimensionalidad del espacio de variables generado por las variables observadas. Este tipo de análisis dimensional es una herramienta muy útil en estudios que requieren clasificación de variables y resulta muy importante para entender las correlaciones entre variables independientes. Una explicación a detalle con un ejemplo de la aplicación de éste método, se encuentra en Dultzin-Hacyan & Ruano (1996).

Usando el PCA, BG92 estudiaron la correlación entre 18 parámetros, que incluyen las intensidades de líneas, flujos en el continuo, anchos equivalentes y FWHM, incluyendo a las líneas Fe II$_{\text{opt}}$, [O III]λ5007, Hβ_{BC}, logr_K (el cociente de Kellermann), y el indice

espectral del óptico a rayos-X, α_{ox}. Su muestra contiene 87 cuasares del catálogo Palomar-Green (PG, cuyos objetos se caracterizan por tener exceso en el UV) con $z \leqslant 0.5$, de los cuales 17 son radio fuertes. Con los parámetros antes mencionados, formaron una matriz de correlación y aplicando el PCA vieron que el primer eigenvector (es decir, la diagonal de la matriz de correlaciones estadistícas) destaca una fuerte correlación entre W(FeII)/W(H$\beta_{\rm BC}$) y la luminosidad de [OIII]λ5007.

Más tarde, Sulentic et al. (2000) trabajaron sobre tres muestras con un total de 132 cuasares (108 RQ y 55 RL). Realizaron una búsqueda para un nuevo diagrama de correlación en el que sólo tomaron en cuenta propiedades de la BLR y el continuo, por lo que la línea de [OIII]λ5007 inicalmente incluida por BG92, fué excluida. También, se tomó el índice espectral en rayos x suaves a partir de los datos de ROSAT (Wang et al. 1996). Encontraron un espacio de correlaciones en donde les fue posible discriminar entre AGNs de tipo 1 "normales", las llamadas NLSy1 (Narrow Line Seyfert 1, ver Komossa 2008), cuasares RL y RQ. A este espacio lo llamaron Eigenvector 1 en tres dimensiones (3DE1), que refleja parcialmente sus raíces en el estudio realizado por BG92. Las principales tres correlaciones ortogonales involucran a (1) la intensidad de FeII, definida como el cociente entre los anchos de FeIIλ4570 y Hβ, $R_{\rm FeII}$= W(FeIIλ4570)/W(H$\beta_{\rm BC}$), (2) el FWHM(H$\beta_{\rm BC}$), y como complemento a (3) el indice espectral de los rayos X suaves Γ_{soft} (medido entre 0.8 y 2.4 Kev de los espectros del catálogo de ROSAT).

Los resultados de este estudio se muestran en la figura 1.2, en donde se destaca la correlación del FWHM(H$\beta_{\rm BC}$) con el $R_{\rm FeII}$. Sulentic et al. (2000) definen dos poblaciones, la A con FWHM(H$\beta_{\rm BC}$) $\leqslant$ 4000km s^{-1} y la B con FWHM(H$\beta_{\rm BC}$)>4000km s^{-1}. Más adelante, veremos que esta clasificación en dos poblaciones mostró tener distintas propiedades físicas subyacentes. En la figura 1.3 (izq.) se presenta nuevamente esta relación para una conjunto más amplio de cuasares en donde además se han subdividido las poblaciones A y B en subconjuntos con el propósito de mostrar una secuencia en los tipos espectrales que corresponde a una secuencia de propiedades físicas. En la figura 1.3 (der.) se muestra una media de los espectros de cada subconjunto. Se aprecian las diferencias en intensidad de FeII y el cambio en el perfil de la línea.

Con la convolución de estos tres parámetros físicos, la separación de las poblaciones

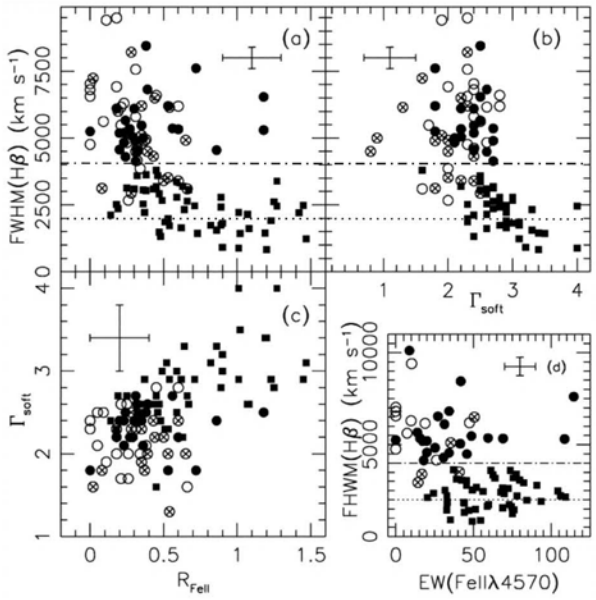

Figura 1.2: Proyecciones bidimensionales del E1. Los objetos RQ son los círculos llenos, los RL, de espectro plano, son los círculos vacíos y los RL, de espectro inclinado, son los cuadros vacíos. En el panel inferior derecho, se identifica a las poblaciones A y B de los RQ. Los restantes tres paneles son los tres planos del E1. En los dos paneles superiores, la línea punteada-rayada indica el límite de las poblaciones A y B (FWHM(H$\beta_{\rm BC}$)=4000 km s^{-1}), mientras que la línea punteada marca el máximo FWHM(H$\beta_{\rm BC}$) = 2000 km s^{-1} para las NLSy1. Tomado de Sulentic et al. (2000).

A y B tienen una base física mas sólida que la definida por RL y RQ. Más recientemente, como parte de la contribución de esta tesis, se ha definido un espacio de parámetros de cuatro dimensiones llamado 4DE1, agregando medidas de la asimetría al azul de la línea de CIVλ1549. En la figura 1.4, se muestra una proyección del espacio tridimensional en el que una cuarta dimensión está dada por círculos llenos (RQ) o vacíos (RL). En esta figura, se agregan propiedades físicas que probablemente corresponden a una secuencia evolutiva.

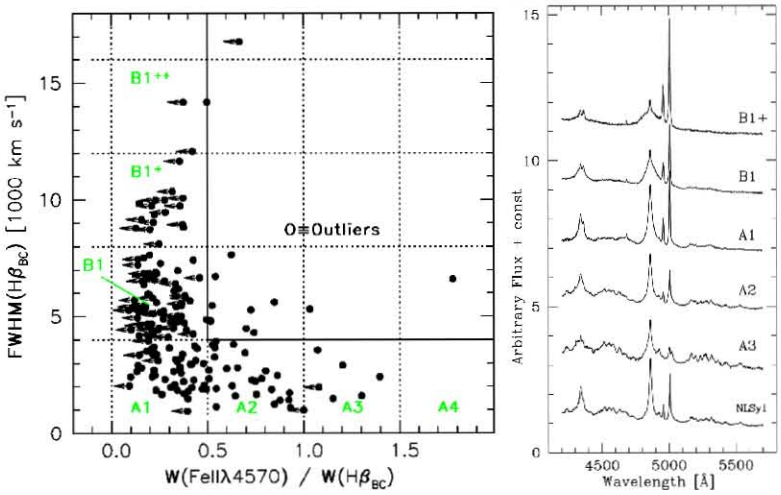

Figura 1.3: *Izquierda*: Plano óptico del E1. La diferencia con la figura 1.2(a), es que en ésta se amplió la muestra. Las líneas punteadas muestran las subclases de las poblaciones A y B, mientras que las líneas sólidas separan la región de mayor ocupación del E1 de los valores atípicos (outliers). Las flechas denotan el límite superior de Fe II λ4570. *Derecha*: Espectros promedio de las subclases del E1. Tomado de Sulentic et al. (2002).

1.2.4. Condiciones físicas de la BLR y obtención de parámetros fundamentales.

Las correlaciones entre las propiedades observadas no sólo llevan a las bases físicas para los esquemas de clasificación, sino que, en un campo en donde incluso la fuente de energía y el mecanismo de transporte son todavía discutidos, pueden discriminarse de entre modelos antagónicos. Algunas de las propiedades físicas que, a través de modelos, hacen predicciones acerca de las correlaciones entre las propiedades son la tasa de acreción, la geometría del disco de acreción, el tamaño de (o la distancia a) la BLR, la relación entre la geometría y la cinemática de la BLR, la orientación del eje principal respecto a la línea de visión y el mecanismo por el cual la energía es transportada a la BLR.

Marziani et al. (2001), buscaron los parámetros físicos que gobiernan esas correlaciones y la distribución en el E1, enfocándose en la correlación en el óptico del FWHM(Hβ) y

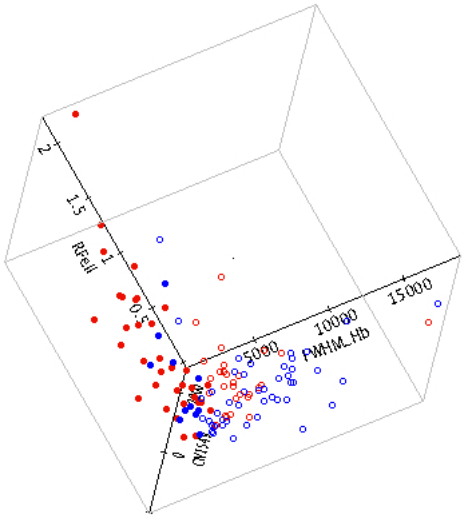

Figura 1.4: Proyección tridimensional del 4DE1. Los ejes son: FWHM(H$\beta_{\rm BC}$), $R_{\rm FeII}$ y el corrimiento al azul de CIVλ1549. Los círculos llenos son objetos de Población A, mientras que los vacíos son los de Población B (Anguiano et al. en preparación).

el $R_{\rm FeII}$. Encontraron que los objetos de Población A muestran una clara correlación dentro de los parámetros del E1, mientras que los objetos de Población B RQ y RL, muestran una gran dispersión sin una correlación obvia. Los objetos RL se encuentran preferentemente en el mismo dominio que los RQ de Población B y raramente se encuentran en el dominio de la Población A.

De la figura 1.2 se puede inferir una especie de ”secuencia principal” que se extiende desde las fuentes con perfiles más anchos hasta los que presentan Fe II$_{\rm opt}$ más intenso y son los de perfiles más angostos. En el trabajo de Marziani et al. (2001), hicieron un análisis con los resultados de las mediciones de los anchos W(H$\beta_{\rm BC}$), W(FeIIλ4570) (línea de emisión de baja ionización), W(CIVλ1549) (de emisión de alta ionización), de $R_{\rm FeII}$ y del cociente de líneas I(SiIII]λ1892)/I(CIII]λ1909), sensible a $N_{\rm e}$. Encontraron que el W(CIVλ1549) es más grande en la Población B y que el W(FeIIλ4570) es mayor en la Población A, lo cual sugiere un decremento en el nivel de ionización que va de la Población B a la Población A. El comportamiento de I(SiIII]λ1892)/ I(CIII]λ1909), normalizado respecto a W(H$\beta_{\rm BC}$) y a W(CIVλ1549), como función de la densidad electrónica $N_{\rm e}$ y el

parámetro de ionización U, sugiere un decremento en U y un incremento en $N_{\rm e}$, tendencia que va de la Población B hacia la Población A, y que va de log$U$∼-1 a-1.5 para log$N_{\rm e}$ ∼9.5 a log$U$ ∼-2 a -2.5 para log$N_{\rm e}$∼11.5. De modelos de fotoionización realizados con CLOUDY (Ferland 2000) se sugiere que

$$\frac{I(SiIII]\lambda1892)}{I(CIII]\lambda1909)} \approx -3.91 + 0.41 \log N_e. \tag{1.26}$$

Un análisis mucho más a fondo de la obtención de $N_{\rm e}$ y U se presenta en el capítulo 4.

Uno de los aspectos de gran relevancia en el estudio de los cuasares es la orientación del plano de la BLR respecto a la línea de visión. En algunos objetos como I Zw 1, se observa que el perfil de CIVλ1549 tiene una gran componente al azul (un ejemplo similar lo encontramos en J12014+0116, Fig. 10(a) del capítulo 4), mientras que el perfil de Hβ es muy angosto. Este resultado observacional se explica en un escenario de disco más viento, argumentando que el disco que emite Hβ es ópticamente grueso y está obscureciendo el lado opuesto del viento de alta ionización que emite a CIVλ1549. De este modo, los corrimientos al azul de CIVλ1549 serían dependientes de la orientación.

La región donde el cociente entre los anchos de FeIIλ4570 y Hβ, $R_{\rm FeII}\leqslant$0.5 de la figura 1.3(izq.) sugiere que la orientación es parcialmente responsable de la división entre las Poblaciones A y B. Desafortunadamente es casi imposible determinar la orientación salvo en algunos pocos casos (e.g. Rokaki et al. (2003)). Hacia la mitad de la figura 1.3(izq.) se puede argumentar que el ángulo de visión i decrece con el aumento de L/M. El decremento de i implica por un lado, que el FWHM(H$\beta_{\rm BC}$) también decrece, pues el efecto Doppler que ensancha las líneas se ve disminuido, y por el otro, dado que las masas son menores para la Población A, aunado a que la luminosidad es mayor en estos objetos, se observa un incremento de L/M. Las correlaciones entre la naturaleza del corrimiento al azul sistemático de CIVλ1549 sugiere un modelo para cuasares radio callados donde: (i) las nubes que emiten CIVλ1549 muestran una predominancia de movimiento radial (flujo de salida porque asumimos que el otro extremo está oscurecido) en una estructura bicónica con un amplio ángulo de apertura. (ii) La emisión óptica de FeII emerge de una distribución aplanada (probablemente del disco de acreción), y (iii) Hβ emerge en una distribución distinta a la de FeII, menos aplanada (Fig. 1.5).

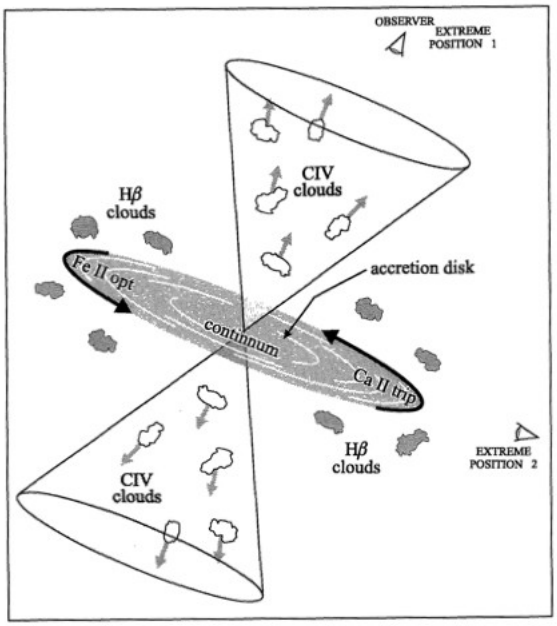

Figura 1.5: Estructura esquemática de la configuración propuesta para la BLR y la cinemática en cuasares radio callados. Fe II$_{opt}$ y CaII son emitidos en la parte externa del disco de acreción. El continuo desde el óptico hasta el UV también está siendo emitido por el disco que se asume es ópticamente grueso y geométricamente delgado. Las líneas de Balmer son emitidas por nubes en una configuración un tanto aplanada, pero no gravitacionalmente acotadas. Tomado de Dultzin-Hacyan et al. (1999).

Otro parámetro que afecta las condiciones físicas en la BLR es el cociente de Eddington. Este cociente está definido por la razón entre la luminosidad bolométrica del objeto y la luminosidad de Eddington (L_{bol}/L_{Edd}). Ésta última es derivada del equilibrio de la presión de radiación y la fuerza gravitacional y es igual a

$$L_{\rm Edd} \cong 3.3 \times 10^4 \left(\frac{M}{M_\odot} \right) L_\odot. \tag{1.27}$$

Dado que $L_{\rm Edd}$ depende sólo de la masa, podemos considerar que el cociente de Eddington es equivalente al cociente de la luminosidad entre la masa

$$\frac{L_{\rm bol}}{L_{\rm Edd}} \propto \frac{L_{\rm bol}}{M} \tag{1.28}$$

Una de las preguntas fundamentales acerca de los cuasares es cómo la energía, que se detecta como radiación, es generada. Este paradigma se puede explicar con el modelo de un disco de acreción que rodea a un hoyo negro supermasivo. La energía es generada por la caída de material calentado a altas temperaturas (20,000 a 30,000 K), mediante mecanismos de fricción y viscosidad debidos a la rotación diferencial del plasma en el disco de acreción (Shakura & Sunyaev 1973). El proceso fundamental que opera en los cuasares es la liberación de la energía de origen gravitacional, la cual se realiza con una eficiencia η. Para la métrica de Swarzchild η es 0.1 y para un hoyo negro de Kerr es 0.4 (e.g. Misner et al. 1973). Como referencia, la fusión nuclear tiene una eficiencia de apenas el 0.007. Para el caso de los cuasares se requiere una eficiencia en la conversión de energía mucho mayor, para explicar las luminosidades observadas.

La tasa a la cual la energía es emitida por el núcleo, $L = dE/dt$, nos da la tasa a la cual la energía debería ser suministrada al hoyo negro mediante la accreción. Para la luminosidad bolométrica

$$L_{\rm bol} = \eta c^2 \dot{m}_{\rm bol}, \tag{1.29}$$

donde $\dot{m}_{\rm bol} = dm/dt$ es la tasa de accreción. Para la luminosidad de Eddington, considerando la ecuación 1.27

$$L_{\rm Edd} = \eta c^2 \dot{m}_{\rm Edd} \propto M. \tag{1.30}$$

De esta manera, podemos considerar una tasa de acreción adimensional ($\dot{m}$) como

$$\dot{m} \equiv \frac{\dot{m}_{\rm bol}}{\dot{m}_{\rm Edd}} = \frac{L_{\rm bol}}{L_{\rm Edd}} = \frac{L_{\rm bol}}{cte \cdot M}. \tag{1.31}$$

es decir, podemos ver a $\dot{m}$ como un equivalente de L/M. Para ilustrar la tendencia de L/M en el E1, se encuentra un valor de $\log(L/M)_\odot = 4.6$ para los objetos extremos de Población A y de $\log(L/M)_\odot = 3.1$ para el otro extremo de la Población B.

La presencia del exceso en rayos–x a través del Γ_{soft} sugiere que el cociente de Eddington (ó equivalentemente L/M) puede ser un parámetro muy importante del E1. En la figura 1.6 se muestra la correlación entre el logaritmo de la tasa de accreción adimensional $\log(\dot{m})$ y el FWHM($H\beta_{\rm BC}$).

La relación entre estos dos parámetros es predicha por modelos de disco más viento derivado de la presión de radiación. De la figura 1.6 (Marziani et al. 2001), con $\dot{m}$ como la

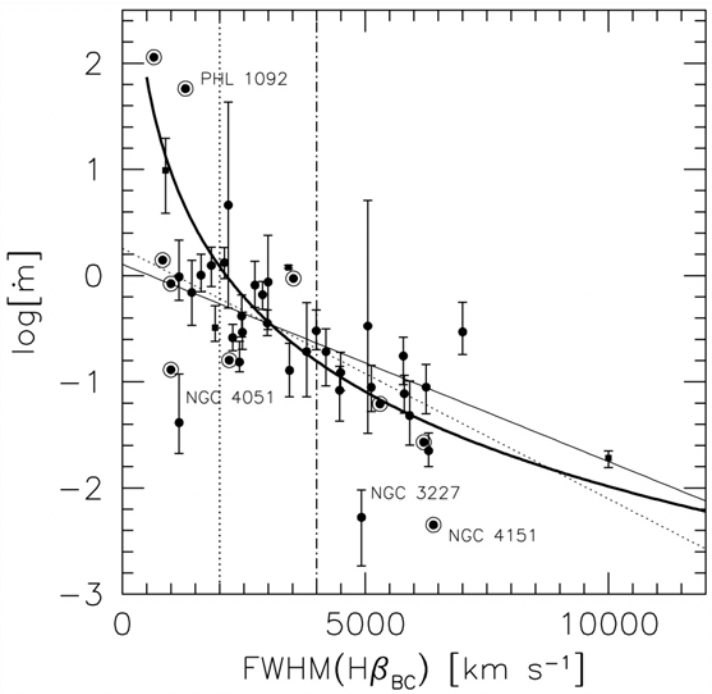

Figura 1.6: Relación entre la tasa de acreción adimensional y el FWHM(H$\beta_{\rm BC}$). Los círculos y cuadrados llenos son AGNs RQ y RL respectivamente, cuya masa fue determinada del mapeo de reverberación. Los círculos con anillo son AGNs con masas determinadas de la variabilidad en rayos–X. La línea gruesa marca la predicción de un modelo de disco+viento. La línea delgada es el mejor ajuste, mientras que la punteada es el mismo ajuste sin considerar a los RL. La línea rayada–punteada vertical es la división entre las Poblaciones A y B. La línea punteada vertical marca el límite de las NLSy1s. Tomado de Marziani et al. (2001)

tasa de accreción adimensional, y de las relaciones de la ecuación 1.31, se obtiene que

$$(\lambda L_\lambda/M)_\odot \approx 6.2\times10^3 FWHM_{1000}(H\beta_{BC})^{-2} \tag{1.32}$$

donde L_λ es la luminosidad específica a $\approx$ 5000Å y el FWHM(H$\beta_{\rm BC}$) está expresado en unidades de 1000km s^{-1}. Sin embargo, la tasa de acreción está relacionada con la luminosidad total ó bolométrica, no con la luminosidad a una λ específica, por ello se ha supuesto una corrección bolométrica con un valor de ∼-2.5. Para las NLSy1s (la gran mayoría de la Población A), se encuentra que $0.3 \leqslant \dot{m} \leqslant 0.7$. Asumiendo que el cociente I(Si III]λ1892)/I(C III]λ1909) está directamente correlacionado con el FWHM(H$\beta_{\rm BC}$) (Wills

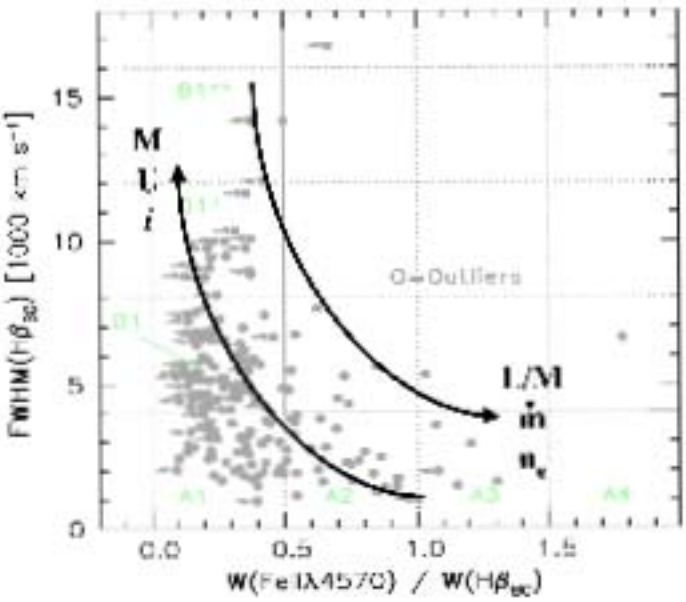

Figura 1.7: Tendencias de los parámetros físicos dominantes de los AGNs. La masa M, el parámetro de ionización U y el ángulo de inclinación i muestran una tendencia creciente de la Población A a la Población B. Mientras que el cociente entre la luminosidad y la masa (L/M), la tasa de accreción $\dot{m}$ y la densidad electrónica N_e, decrecen de la Población B a la Población A.

et al. 1999), se puede encontrar a partir de las ecuaciones 1.26 y 1.32,

$$\begin{aligned} \log N_e &\approx 11.1 - 1.33 \log FWHM_{1000}(H\beta) \\ &\approx 7.72 + 0.67 \log(L_{bol}/M)_{\odot} \end{aligned} \tag{1.33}$$

O bien, usando 1.19,

$$U = 0.26(L_{bol}/M)_{\odot,4}^{-1.67} M_{\odot,7}^{-1} \tag{1.34}$$

con la masa en unidades de $10^7 M_{\odot}$ y el cociente (L/M) en unidades de 10^4 veces el valor solar $[(L/M)_{\odot} \approx 1.9 ergs s^{-1} g^{-1}]$.

Un resumen de todas estas tendencias se muestra en la figura 1.7.

1.3. Esquema de la tesis.

La tesis está estructurada como sigue. Los capítulos 2 y 3 están dedicados al análisis de las líneas de emisión. En el capítulo 2 nos enfocamos en CIVλ1549, una línea emitida en el UV, y su correlación con el E1, definido hasta ese momento para el óptico y los rayos-X. En el capítulo 3 realizamos un análisis de las líneas de emisión más prominentes desde el UV hasta el óptico, para una breve muestra de la secuencia del E1. Este análisis nos ayudó a definir el tipo de perfil (gaussiano o lorentziano) así como el número de componentes para cada línea.

El capítulo 4 es el más extenso de la tesis. Está enfocado al desarrollo y uso de un nuevo método para la obtención del tamaño de la r_{BLR}, basado en la cálculo de la densidad electrónica $N_{\rm e}$ y el parámetro de ionización U, mediante la comparación de datos observacionales con resultados de simulaciones de las condiciones físicas en la BLR. En este análisis usamos observaciones hechas en el IR con espectros de alta S/N, provenientes del VLT. A lo largo del capítulo explicamos los criterios usados para el ajuste de las líneas de donde separamos la componente central ancha, mostramos los cocientes de líneas usados para la obtención de $N_{\rm e}$ y U, y describimos la simulación realizada con CLOUDY. Exploramos una condición diferente para la emisión de las líneas con una metalicidad distinta a la solar. Comparamos éste método con uno ampliamente usado que relaciona la r_{BLR} con la luminosidad del cuasar. La calibración del cálculo de la r_{BLR} usando nuestro método con mediciones directas mediante el mapeo de reverberación, la presentamos en el capítulo 5.

En el capítulo 6 presentamos las conclusiones generales de la tesis y en el 7 los proyectos de trabajo a futuro.

Capítulo 2

CIVλ1549 como un parámetro del Eigenvector 1 para Cuasares.

Éste capítulo, junto con el siguiente, se refieren al análisis de las líneas de emisión. La propuesta realizada por Sulentic et al. (2000) de introducir un espacio de parámetros gobernados por el Eigenvector 1 (E1) ha sido de gran ayuda para el entendimiento de la relación entre las propiedades espectroscópicas observadas en los cuasares. En este trabajo se manejaron las variables en el óptico y los rayos–X descritas en la introducción, sin embargo, las observaciones en el UV realizadas por el telescopio espacial Hubble (HST) dieron pie al trabajo realizado en este capítulo. En esta primera parte de la tesis abordaré el estudio de la línea CIVλ1549 emitida en el UV de todos los espectros del archivo del HST que cubrieran dos requisitos, el primero es que fueran cuasares tipo 1 o de líneas anchas y lo segundo es que tuvieran una señal a ruido S/N lo suficientemente buena, de modo que la línea no sea confundida con el ruido subyacente. El trabajo que presento en este capítulo es el ajuste de la línea ancha de CIVλ1549 de todos los espectros seleccionados del HST (130 en total) descartando la angosta en los casos que exista, bajo la premisa de que tiene un FWHM < 2000 km s^{-1}. De estos ajustes se desprenden numerosas mediciones, entre ellas el FWHM de la componente ancha, los centroides de la línea a 1/4, 1/2 y 0.9 de altura y el índice de asimetría de la línea. Posteriormente, se hicieron correlaciones de

éstos parámetros entre sí y con los del E1, en especial con el FWHM(H$\beta_{\rm BC}$) y el cociente entre la intensidad de Fe IIλ4570 y H$\beta_{\rm BC}$, $R_{\rm FeII}$. Encontramos correlaciones que involucran al FWHM(C IVλ1549$_{\rm BC}$), $c(1/2)$ y el ancho equivalente sólo para objetos de Población A. Los de Población B muestran una mayor dispersión sin una tendencia significativa.

Posteriormente, usamos la suposición (que finalmente vimos que es errónea) de un sistema virializado para calcular la masa del hoyo negro usando C IVλ1549. El cálculo de la masa para un sistema virializado está basado en movimientos Keplerianos del gas al rededor del hoyo negro, sin embargo la línea C IVλ1549 al mostrar una componente asimétrica al azul nos refiere a que parte de esta línea está siendo emitida en un viento saliente. Es así como las masas obtenidas son sistemáticamente mayores a las calculadas con H$\beta_{\rm BC}$.

Trabajo publicado en *The Astrophysical Journal*, Sulentic et al. 2007, 666, 757.

The Astrophysical Journal, 666:757–777, 2007 September 10
© 2007. The American Astronomical Society. All rights reserved. Printed in U.S.A.

C IV λ1549 AS AN EIGENVECTOR 1 PARAMETER FOR ACTIVE GALACTIC NUCLEI

Jack W. Sulentic,[1] Rumen Bachev,[2] Paola Marziani,[3] C. Alenka Negrete,[4] and Deborah Dultzin[4]

Received 2006 November 9; accepted 2007 May 11

ABSTRACT

We are exploring a spectroscopic unification for all types of broad-line emitting AGNs. The four-dimensional Eigenvector 1 (4DE1) parameter space organizes quasar diversity in a sequence primarily governed by Eddington ratio. This paper considers the role of C IV λ1549 measures as 4DE1 diagnostics. We use *HST* archival spectra for 130 sources with S/N high enough to permit reliable C IV λ1549 broad-component measures. We find a C IV $\lambda 1549_{\rm BC}$ profile blueshift that is strongly concentrated among (largely radio-quiet [RQ]) sources with FWHM($H\beta_{\rm BC}$) $\lesssim 4000$ km s^{-1} (which we call Population A). Narrow-line Seyfert 1 (NLSy1; with FWHM $H\beta \leq 2000$ km s^{-1}) sources belong to this population but do not emerge as a distinct class. The systematic blueshift, widely interpreted as arising in a disk wind/outflow, is not observed in broader line AGNs (including most radio-loud [RL] sources), which we call Population B. We find new correlations involving FWHM(C IV $\lambda 1549_{\rm BC}$), C IV λ1549 line shift, and equivalent width only among Population A sources. Sulentic et al. suggested C IV λ1549 measures enhance an apparent dichotomy between sources with FWHM($H\beta_{\rm BC}$) *less and greater than* 4000 km s^{-1}, suggesting that it has more significance in the context of broad-line region structure than the more commonly discussed RL versus RQ dichotomy. Black hole masses computed from FWHM C IV $\lambda 1549_{\rm BC}$ for about 80 AGNs indicate that the C IV λ1549 width is a poor virial estimator. Comparison of mass estimates derived from $H\beta_{\rm BC}$ and C IV λ1549 reveals that the latter show different and nonlinear offsets for Population A and B sources. A significant number of sources also show narrow-line C IV λ1549 emission that must be removed before C IV $\lambda 1549_{\rm BC}$ measures can be made and interpreted effectively. We present a recipe for C IV λ1549 narrow-component extraction.

Subject headings: line: profiles — quasars: emission lines — quasars: general

Online material: Machine-readable tables

1. INTRODUCTION

The search for a parameter space that might provide spectroscopic unification for all classes of broad line emitting active galactic nuclei (AGNs) motivated the "four-dimensional Eigenvector 1" (4DE1) concept (Sulentic et al. 2000b, 2000c). Such a correlation space might serve as an equivalent to the stellar Hertzsprung-Russell diagram. Domain space occupation differences and parameter correlations might then provide the empirical clues from which underlying physics could be inferred. At the very least it can be used to highlight important differences between sources that can also drive our physical understanding of the geometry, kinematics, and physics of the broad line emitting region (BLR). From the outset it was expected that a parameter space for AGNs would require more than two dimensions, because source orientation and "physics" (e.g., black hole mass $M_{\rm BH}$ and Eddington ratio) drive AGN parameter values and correlations. A suitably chosen *n*-dimensional space should help to remove the degeneracy between these two drivers.

4DE1 has roots in the *Rossi X-Ray Timing Explorer* (*RXTE*) PCA analysis of the Bright Quasar Sample (87 sources; Boroson & Green 1992, hereafter BG92) as well as in correlations that emerged from *Röntgentsatellit* (*ROSAT*; e.g., Wang et al. 1996). 4DE1 as we define it involves BG92 measures: (1) full-width at half maximum of broad Hβ (FWHM Hβ) and (2) equivalent-width ratio of optical Fe II and broad Hβ: $R_{\rm Fe\,II} = W({\rm Fe\ II}\ \lambda 4570)/W(H\beta_{\rm BC})$. We added a measure defined in Wang et al. (1996) involving (3) the soft X-ray photon index ($\Gamma_{\rm soft}$) and a measure of (4) C IV λ1549 broad line profile velocity displacement at half-maximum [$c(\frac{1}{2})$] to arrive at our 4DE1 space. Other points of departure from BG92 involve our comparison of radio-quiet (RQ) and radio-loud (RL) sources as well as subordination of BG92 [O III] λ5007 measures (although, see Zamanov et al. 2002; Marziani et al. 2003a). Finally, we divide sources into two AGN populations using a simple division at FWHM $H\beta_{\rm BC} = 4000$ km s^{-1} with sources narrower and broader than this value designated Populations A and B, respectively. It was motivated by the observation that almost all RL sources show FWHM $H\beta_{\rm BC} \gtrsim 4000$ km s^{-1} (Sulentic et al. 2000b). This division appears to be more effective than the more traditional divisions into: (1) RQ-RL sources as well as (2) narrow-line Seyfert 1 (NLSy1) sources defined with FWHM($H\beta_{\rm BC}$) $\lesssim 2000$ km s^{-1} and broader line sources above this value. Results presented in this paper strongly support the Population A-B distinction. Exploration of possible physical drivers of source occupation/correlation in 4DE1 (Marziani et al. 2001, 2003b; Boroson 2002) suggest that it is primarily driven by the luminosity to black hole mass ($M_{\rm BH}$) ratio which is proportional to the Eddington ratio ($L_{\rm bol}/L_{\rm Edd}$) with Population A sources being high accreting/low $M_{\rm BH}$ AGNs and Population B being low accreting/large $M_{\rm BH}$ AGNs.

Past 4DE1 studies focused on the optical 4DE1 plane (FWHM Hβ vs. $R_{\rm Fe\,II}$) at low redshift because more high signal-to-noise ratio (S/N) optical spectra exist than UV or X-ray measures. Complementary high-*z* measures of the Hβ region at infrared (IR) wavelengths are ongoing (Sulentic et al. 2004, 2006a). This paper focuses on an expanded sample of C IV λ1549 measures and explores their utility as 4DE1 parameters. The work is supplemental to a recent paper (Bachev et al. 2004) that discusses data processing and analysis of 123 C IV λ1549 spectra from the

[1] Department of Physics and Astronomy, University of Alabama, Tuscaloosa, AL 35487, USA; giacomo@merlot.astr.ua.edu.
[2] Institute of Astronomy, Sofia 1784, Bulgaria.
[3] INAF, Osservatorio Astronomico di Padova, Vicolo dell'Osservatorio 5, I-35122 Padova, Italy; paola.marziani@oapd.inaf.it.
[4] Instituto de Astronomía, Universidad Nacional Autonoma de México (UNAM), Apdo. Postal 70-264, 04510 Mexico D.F., Mexico; deborah@astroscu.unam.mx.

Hubble Space Telescope (*HST*) archive. The new C IV λ1549 sample is almost twice the size of that discussed in the defining 4DE1 paper (Sulentic et al. 2000c). We present (§ 2) new 4DE1 correlation diagrams involving measures of the C IV λ1549 line shift and then look (§ 2.3) at the implications of C IV λ1549–defined source occupation for BLR structure and for the hypothesized AGN populations (A and B; § 3). Section 4 discusses the reality of a significant narrow-line C IV λ1549 component in many sources and compares our C IV λ1549 measures with other recent studies utilizing the same spectra. Section 5 considers the implications of our C IV λ1549 results on the use of FWHM C IV λ1549 to estimate black hole masses.

2. C IV λ1549 LINE MEASURES AND CORRELATIONS

2.1. *Sample Definition and Data Analysis*

We searched the *HST* archive[5] and found usable C IV λ1549 spectra for 130 of 141 low-redshift sources. Excluded sources are mostly C IV λ1549 BAL quasars where reliable measures of the C IV λ1549 emission profile are difficult. OI 363 was not included because of low S/N. IRAS 13218+0552 (J132419.9+053705) was excluded, because it shows no broad lines that would warrant a type 1 AGN designation. We assume that our sample is large enough to reasonably represent the broad emission line properties of low-z AGNs. It is likely to be the only UV data set of reasonable-quality quasar spectra in the foreseeable future. The sample should be particularly valuable for RQ versus RL comparisons because the two populations are almost equally represented while in a complete sample only $\approx$10% are found to be RL (Jiang et al. 2007; Cirasuolo et al. 2003; Sulentic et al. 2003). A PG quasar subsample was identified and includes 43 sources with 26% RL reflecting the overrepresentation of RL sources in the *HST* archive.

The uncertainty due to instrumental errors in wavelength calibration are estimated to be $\approx$200 km s^{-1} (Marziani et al. 1996). In order to reduce wavelength calibration errors *HST* spectra were "re-aligned" using expected rest-wavelengths of strong low-ionization, Galactic absorption lines including Mg II 2796.35, 2803.53 Å, Fe II 2600.17, 2586.65, 2382.77, 2374.46, 2344.21 Å, Al II 1670.79 Å, Si II 1526.71 Å, C II 1334.53 Å, and Si II 1260.42 Å (Savage et al. 2000). In case only one or two Galactic lines were available in the spectra, any shift between expected Galactic line wavelength and the wavelength measured on the spectra was double checked to avoid spurious results due to low S/N. Suitable Galactic lines were found for 110 sources in our sample with three or more lines available for 71 sources. The average rms of the residuals between measured line wavelengths after realignment and tabulated wavelengths is $\langle \mathrm{rms} \rangle \approx 40$ km s^{-1}. This provides an estimate of the wavelength calibration uncertainty (at 1 σ confidence level) for the realigned spectra.

The broad component of C IV λ1549 (C IV $\lambda1549_{\mathrm{BC}}$) was extracted after correction for contaminating lines (N IV] λ1486, and especially He II λ1640 and O III] λ1663) and subtraction of Fe II$_{\mathrm{UV}}$ emission (details of data reduction are given in Bachev et al. [2004] and Marziani et al. [1996]). The continuum underlying C IV λ1549 was estimated from nearby regions that are free of strong emission lines (between the λ1400 blend and N IV] λ1486 on the blue side as well as 1700–1800 Å on the red side). A narrow component (C IV $\lambda1549_{\mathrm{NC}}$) was subtracted from the profile when warranted. There is still disagreement about the existence, frequency of occurrence, and strength of any C IV $\lambda1549_{\mathrm{NC}}$. We discuss the evidence for narrow-line region (NLR) C IV λ1549 and describe our C IV $\lambda1549_{\mathrm{NC}}$ subtraction procedure in §4.

2.2. *Immediate Results*

Figure 1 shows individual cleaned C IV $\lambda1549_{\mathrm{BC}}$ profiles fit with high-order spline functions to minimize effects of noise and to preserve the complexity of the shape (following Marziani et al. 1996, 2003a). The spline fit is shown as a thick line in Figure 1 while identified narrow components (that were subtracted in this analysis) are seen above the spline.

Table 1 gives an identification list of all sources shown in Figure 1 along with 4DE1 optical and X-ray parameters. Table 1 includes column (1): IAU code identification; column (2): a common name for the source; column (3): available source redshift with number of significant figures indicating accuracy of the determination; column (4): redshift reference. Column (5): an asterisk (*) indicates that the sources belong to the BG92 PG sample; a "B" indicates that the source is a "blue outlier" (Zamanov et al. 2002). Column (6): Galactic absorption (A_B, in magnitudes); column (7): available measures of FWHM for Hβ broad component [FWHM(Hβ_{BC}), units km s^{-1}] taken from Marziani et al. (2003b) measures of Sloan Digital Sky Survey (SDSS)[6] spectra or, as a last resort, literature spectra; column (8): measures of the ratio $R_{\mathrm{Fe\,II}}$ from same sources as column (7); column (9): decimal logarithm of the specific flux at 4400 Å over the flux at 6 cm (a source is assumed RL if $\log R_K \geq 1.8$); column (10): a measure of the soft X-ray excess (photon index Γ_{soft}), from Sulentic et al. (2000b, 2000c) and from various literature sources.

The reported optical redshifts come from measures of low-ionization optical emission lines (LILs), typically Hβ_{NC}, Hγ_{NC}, and Hα_{NC} supplemented by values derived from [O III] $\lambda\lambda$4959, 5007 if the source is not a blue outlier (see Marziani et al. 2003a; Zamanov et al. 2002). In these cases, the agreement between LILs and high-ionization lines (HILs) is reasonable within the accuracy limits of the present study. We remind the reader that "blue outliers," i.e., sources with large [O III] $\lambda\lambda$4959, 5007 blueshift relative to optical LILs, tend to be extreme Population A sources with very weak [O III] $\lambda\lambda$4959, 5007 and are relatively rare. The recipe described in Marziani et al. (2003a) is applied for all sources with references indicated as ESO (unpublished European Southern Observatory spectra), SPM (unpublished spectra obtained with the 2.2 m telescope at San Pedro Martir), M03 (Marziani et al. 2003a), M96 (Marziani et al. 1996), SDSS (spectra retrieved from SDSS Web site), and G99 (Grupe et al. 1999). All other sources have redshift measured on the basis of the optical lines. None of the remaining sources are likely to be blue outliers on the basis of published spectra so redshift computed using optical lines should be a reliable estimate even if [O III] $\lambda\lambda$4959, 5007 lines were used.

Table 2 presents our C IV λ1549 parameter measures with format as follows: column (1): IAU code; column (2): specific continuum flux at 1550 Å (units $\times 10^{14}$ ergs s^{-1}Å^{-1} cm^{-2}); column (3): flux in the C IV $\lambda1549_{\mathrm{NC}}$ (units $\times 10^{13}$ ergs s^{-1} cm^{-2}); column (4): peak C IV $\lambda1549_{\mathrm{NC}}$ radial velocity, in km s^{-1}; column (5): flux in the C IV $\lambda1549_{\mathrm{BC}}$ (same units as col. [3]); columns (6), (7), (8): centroid profile shift at $\frac{1}{4}$ maximum [$c(\frac{1}{4})$] followed by the estimated uncertainties on the blue and red wings of the

[5] Data sets covering the C IV λ1549 sources listed in Table 1 can be all identified and retrieved from the Web site at http://archive.stsci.edu/hst and are not reported here. A list with the actual data sets employed is available from the authors at http://web.oapd.inaf.it/marziani.

[6] The SDSS Web site is http://www.sdss.org/.

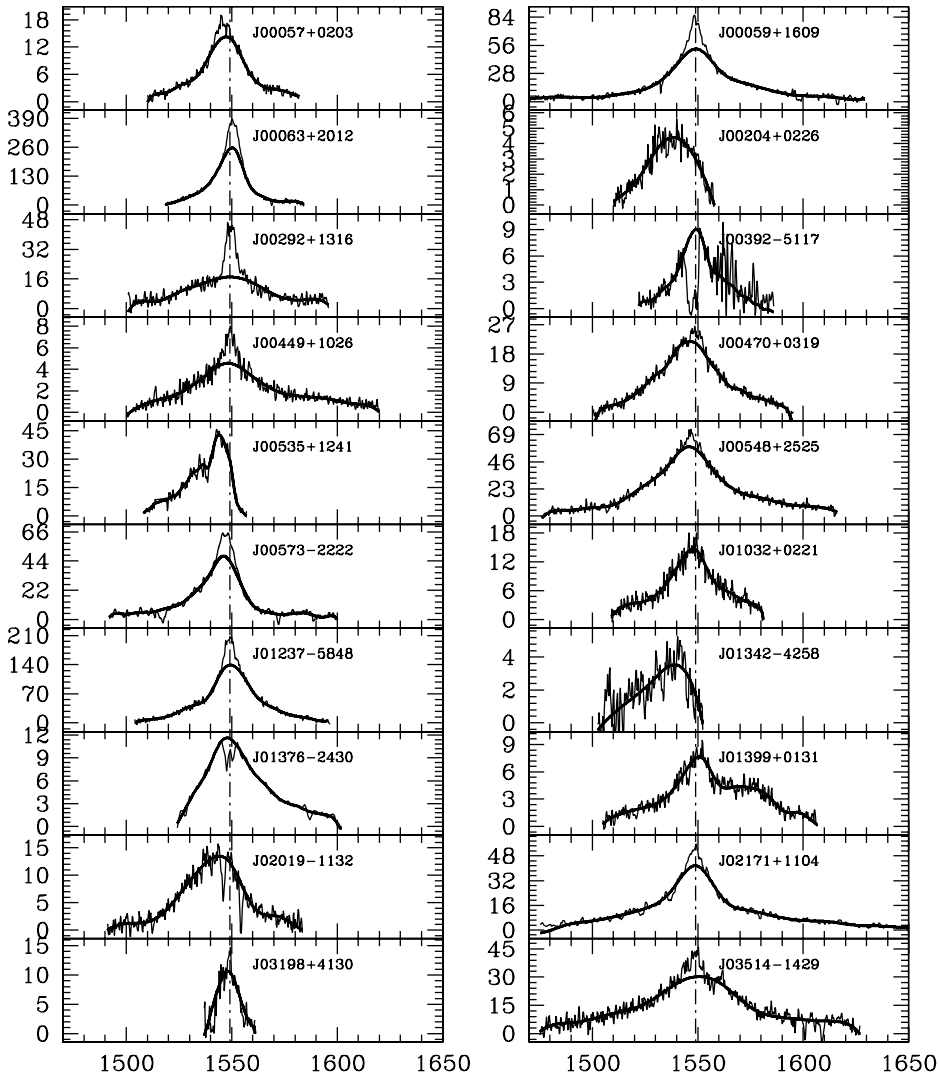

FIG. 1.—C IV λ1549 profiles for the 130 AGNs used in the present study. They are presented in right ascension order. Abscissa is rest-frame wavelength (in angstroms); ordinate is rest-frame specific flux (10^{-15} ergs s^{-1} cm^{-2} Å^{-1}). Thick curves are high-order spline fits to C IV λ1549$_{BC}$ and anything above them is considered to be narrow-line emission. The major thick spacing (50 Å) corresponds to a radial velocity range of $\Delta v_r \approx 9700$ km s^{-1}.

profile (units km s^{-1}); columns (9), (10), (11): same at half-maximum [$c(\frac{1}{2})$, which is an adopted 4DE1 parameter]; columns (12), (13): centroid at $\frac{3}{4}$ maximum [$c(\frac{3}{4})$] with symmetric uncertainty; columns (14), (15): centroid at the 90% intensity level of the C IV λ1549 broad line [$c(0.9)$], with symmetric uncertainty; columns (16), (17): FWHM(C IV λ1549$_{BC}$) and estimated uncertainty (units km s^{-1}); columns (18), (19), (20): C IV λ1549$_{BC}$ asymmetry index with estimated uncertainties on the blue and red profile wings; columns (21), (22): C IV λ1549$_{BC}$ kurtosis measure and estimated uncertainty.

No C IV λ1549$_{NC}$ measures are given in Table 2 if the profile is affected by partial (a) or strong (A) absorption. In sources labeled "a" in Table 2 residual C IV λ1549$_{NC}$ is sometimes visible but the NC width and flux cannot be recovered. NC shifts and fluxes are accurate (within ±40% at a 2 σ confidence level) only if C IV λ1549$_{NC}$ emission shows an intensity at least 0.05 C IV λ1549$_{BC}$. Note that our adopted C IV λ1549$_{NC}$ component is often not "[O III] λλ4959, 5007–like." It is often significantly broader and stronger than would be subtracted if we used [O III] λ5007 as a template for the C IV λ1549 doublet. See § 4 for both empirical and theoretical justifications for our procedure.

Measured centroids at different fractional intensities were defined as

$$c\left(\tfrac{i}{4}\right) = \frac{\lambda_B + \lambda_R - 2\lambda_0}{2\lambda_0}\, c, \qquad \forall i = 0, \ldots, 4, \qquad (1)$$

where c is the speed of light. Values $c(\frac{i}{4})$ for $i = 0$ are not listed in Table 2 due to the difficulty of assessing λ_B and λ_R at zero intensity. We give $c(9/10)$ instead of peak radial velocity. This has been shown to be a good surrogate and less dependent on C IV λ1549$_{NC}$

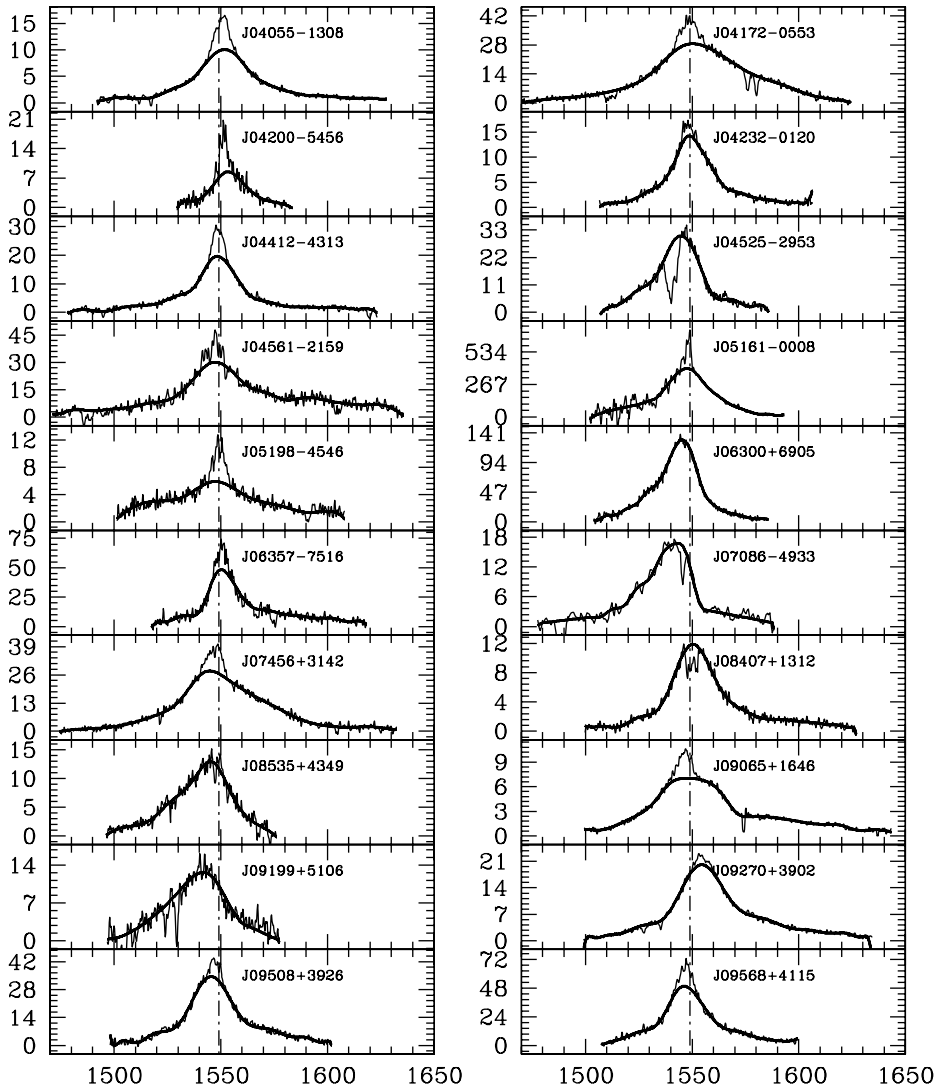

FIG. 1—*Continued*

subtraction as well as line profile irregularities (Marziani et al. 2003a). The asymmetry index is defined as

$$\mathrm{AI} = \frac{\lambda_B(1/4) - \lambda_R(1/4) - 2\lambda_P}{\lambda_P}, \quad (2)$$

where for λ_P we use $c(9/10)/c$. The kurtosis index is defined as (cf. Marziani et al. 1996)

$$\mathrm{kurt} = \frac{\lambda_R(3/4) - \lambda_B(3/4)}{\lambda_R(1/4) - \lambda_B(1/4)}. \quad (3)$$

Uncertainties reported in Table 2 were estimated by measuring the wavelengths λ_R and λ_B at $\pm 5\%$ fractional intensity and then quadratically propagating the errors in the relationships reported above. All uncertainties reported in Table 2 represent a 2 σ confidence level. Uncertainties in estimating the rest-frame velocity, relative to which the centroids are computed, can be as large as 300 km s^{-1} or as small as $\sim$30 km s^{-1} (at 1 σ confidence level) depending on the availability of moderate-resolution spectra (SDSS is, or will be, improving the situation for about 50% of the sample). The error in estimating the local rest frame $\Delta z \approx 0.00014 \pm 0.0006$ was derived from the distribution of differences between z values used in this work and those given in the NASA/IPAC Extragalactic Database (NED). Combining the typical uncertainty on systemic velocity, on UV wavelength calibration, and the average of the measurement uncertainty reported in Table 2, the typical uncertainties (at a 2 σ confidence level) are $\approx$230 and $\approx$170 km s^{-1} for $c(\frac{1}{2})$ and $c(\frac{3}{4})$, respectively.

2.3. C IV λ1549 Line Parameters in the RQ-RL Context

Figure 2 shows source occupation in 4DE1 planes involving the $c(\frac{1}{2})$ parameter (as defined in Sulentic et al. 2000b; $c(\frac{1}{2})$ was chosen from among possible C IV λ1549 profile measures

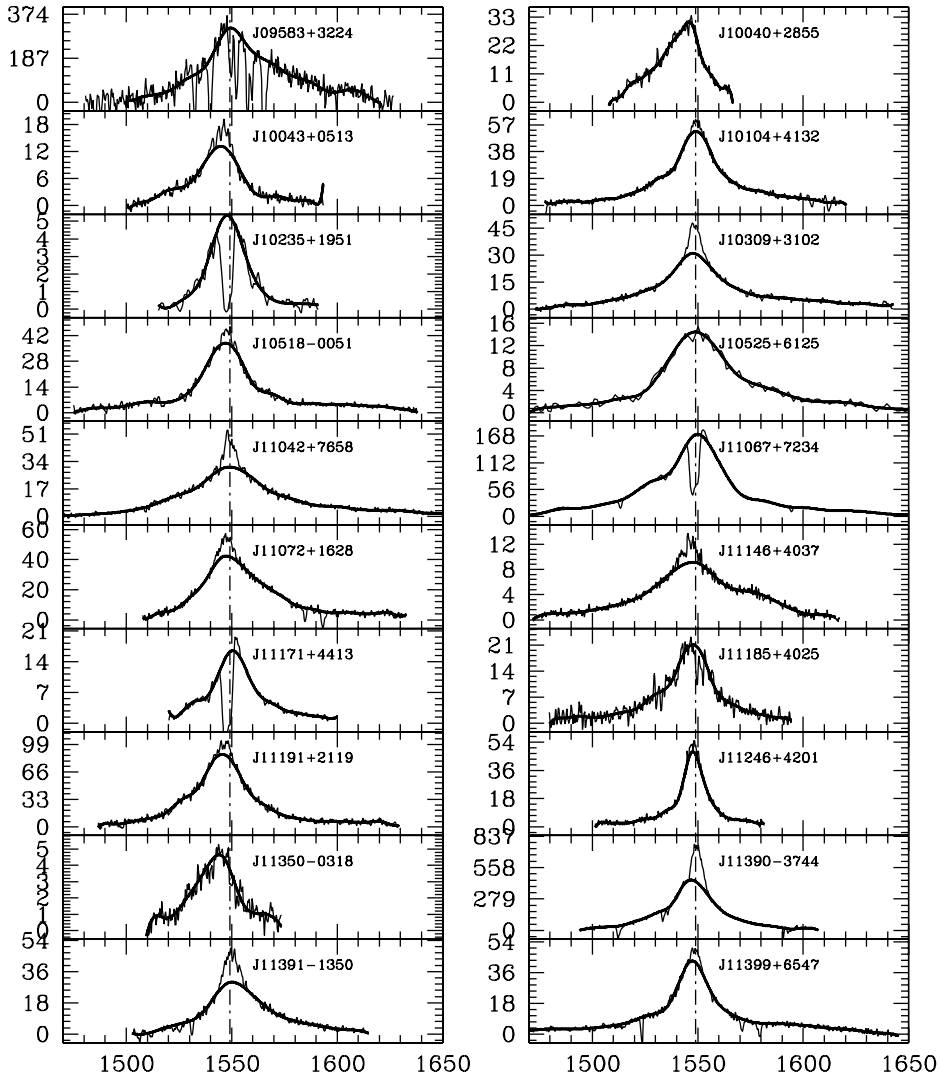

FIG. 1—*Continued*

[FWHM, $c(\frac{1}{2})$ and equivalent width] because (1) it is not obviously luminosity dependent, (2) it showed the largest intrinsic dispersion, and (3) it showed possible correlations with the other principal 4DE1 parameters. As a luminosity-normalized measure W(C IV $\lambda 1549_{\rm BC}$) is ruled out even if the well-known "Baldwin effect" now appears to be driven by dependence on the Eddington ratio (Bachev et al. 2004; Baskin & Laor 2004). This does not mean that we regard it as an unimportant measure but only that we reject it as one of the principal 4DE1 parameters. A surrogate measure might involve a direct measure of C IV $\lambda 1549_{\rm BC}$ line flux, but the parameter dispersion of that measure is less than for $c(\frac{1}{2})$. The same is true for FWHM(C IV $\lambda 1549_{\rm BC}$), which also shows less dispersion than FWHM($H\beta_{\rm BC}$). Line broadening may be due to both rotational and nonrotational velocity components, especially if a disk + wind model is applicable to our sources. On the contrary, $c(\frac{1}{2})$ is most likely related to the amplitude of any nonvirial motions in the BLR. It is this parameter that adds a new element that can be argued to be *physically orthogonal* to previously defined E1 parameters: FWHM($H\beta_{\rm BC}$) estimates the virial broadening in the LIL-emitting part of the BLR; $R_{\rm Fe\,II}$ measures the ionization conditions, while $\Gamma_{\rm soft}$ provides a measurement of the continuum shape.

RQ and RL sources are indicated by circles and squares respectively in Figure 2 (sources with radio/optical flux ratio $\log R_K \gtrsim 1.8$ are considered RL; Sulentic et al. 2003). The large number of squares reflects the overrepresentation of RL sources in our sample. Figure 2*a* shows that sources with C IV $\lambda 1549$ profile blueshifts strongly favor RQ AGN with FWHM $H\beta_{\rm BC} \lesssim 4000$ km s^{-1}. RL sources show a large scatter of both red and blue C IV $\lambda 1549$ shifts. Figures 2*b* and 2*c* show that sources with C IV $\lambda 1549$ blueshift especially favor RQ sources with large $R_{\rm Fe\,II}$ (strong optical Fe II emission) and $\Gamma_{\rm soft}$ (a soft X-ray excess) measures, respectively. RL sources are much more strongly concentrated in the latter two 4DE1 planes.

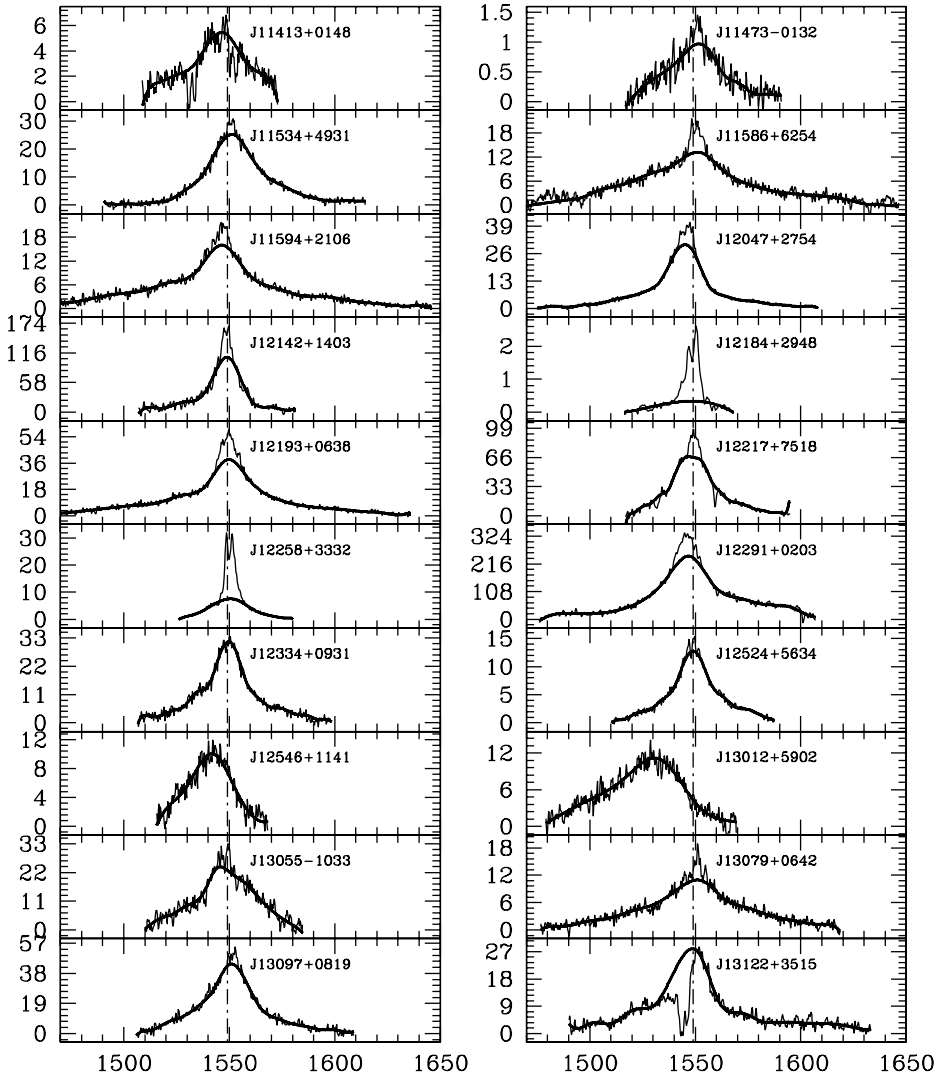

FIG. 1—*Continued*

Table 3 gives mean parameter values (sample standard deviations in parenthesis) for total sample, RQ, RL, and our previously defined Population A-B subsamples that will be considered in § 3. Values are given for column (2): number of sources; column (3): equivalent width measure of the C IV $\lambda 1549_{BC}$ line; column (4): $c(\frac{1}{2})$ of C IV $\lambda 1549_{BC}$; column (5): FWHM(C IV $\lambda 1549_{BC}$); column (6): FWHM(Hβ_{BC}); column (7): $R_{Fe\,II}$; column (8): Γ_{soft}. Columns (4), (6), (7), and (8) represent the principal parameters in 4DE1. We find that RL sources show broader Hβ_{BC} and C IV $\lambda 1549_{BC}$ profiles than RQ AGNs, while RQ sources show stronger $R_{Fe\,II}$, Γ_{soft}, and $c(\frac{1}{2})$ (blueshift) than the RL sample. FWHM C IV $\lambda 1549_{BC}$ is on average (17%) broader than FWHM Hβ_{BC} for RQ sources while FWHM Hβ_{BC} is (16%) narrower than FWHM C IV $\lambda 1549_{BC}$ for RL sources. These differences relate to one of the most significant results of our earlier work where a restricted optical domain space occupation was found for RL sources. Figure 2 also shows this restricted occupation as a strong concentration of RL sources in a small region of the $c(\frac{1}{2})$ versus $R_{Fe\,II}$ and Γ_{soft} planes. RL sources are rarely found with 4DE1 parameter values: FWHM(Hβ_{BC}) $\lesssim$ 4000 km s^{-1}, $R_{Fe\,II} \gtrsim 0.3$, $\Gamma_{soft} \gtrsim 2.5$, and $c(\frac{1}{2}) \lesssim 0$ km s^{-1}. The expanded C IV $\lambda 1549$ sample confirms and strengthens this result which likely indicates a fundamental difference in BLR structure, kinematics, and/or physics between RL and RQ populations (see Sulentic et al. [2003] for discussion in the context of a RQ-RL dichotomy).

Spearman rank correlation coefficients and associated probabilities are given in Table 4 for C IV $\lambda 1549$ equivalent width, FWHM, and centroid measures versus the three other principal 4DE1 parameters. The total-sample correlation coefficients for this sample are larger than corresponding values given for the smaller sample of sources in Sulentic et al. (2000b) as one might hope to see if the correlations are in some sense real. Table 4 emphasizes the spectroscopic differences between RQ versus RL sources by showing no evidence for correlations among 4DE1

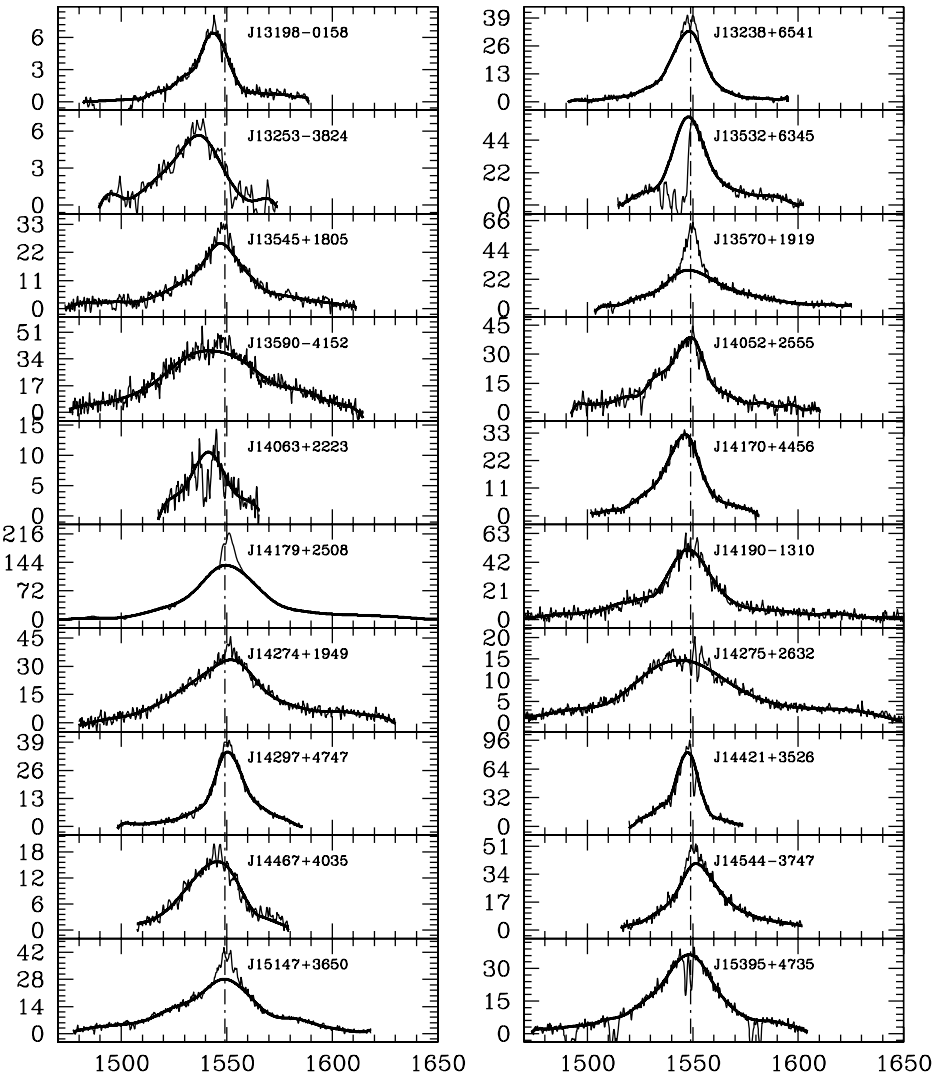

FIG. 1—*Continued*

parameters for RL sources. Real or marginal correlations are only found among RQ sources with the strongest correlations involving $c(\frac{1}{2})$, $R_{\rm Fe\,II}$, and $\Gamma_{\rm soft}$. Restriction to a BG92 overlap subsample shows no significant difference in correlation coefficients.

3. EVIDENCE FOR TWO POPULATIONS OF BROAD-LINE AGNs

So far we have compared sources on the conventional basis of a RQ versus RL dichotomy; however, it is important to point out that about 25% of RQ sources in our sample occupy the same 4DE1 parameter domain as the RL AGNs. If 4DE1 parameters reflect broad-line physics/kinematics, then this overlap may be important. The restricted 4DE1 parameter space occupation for RL sources motivated us (Sulentic et al. 2000b) to hypothesize the existence of two AGN "populations" (A and B) defined in an optical spectroscopic context (4DE1) rather than on the basis of radio loudness. Following our scheme, Population A sources show FWHM($H\beta_{\rm BC}$) $\lesssim$ 4000 km s^{-1}, strong $R_{\rm Fe\,II}$, strong $\Gamma_{\rm soft}$ (a soft X-ray excess), and a $c(\frac{1}{2})$ blueshift with estimated probability of radio loudness $P \lesssim 0.01$. Population B sources show FWHM($H\beta_{\rm BC}$) $\gtrsim$ 4000 km s^{-1}, weak $R_{\rm Fe\,II}$, no soft X-ray excess, or C IV λ1549 blueshift with estimated probability of radio loudness $P \approx 0.30$. Revisiting Figure 2*a* in the Population A-B context shows that C IV λ1549 blueshifts are strongly concentrated among Population A sources with FWHM($H\beta_{\rm BC}$) $\lesssim$ 4000 km s^{-1}. Filled and open symbols in Figure 2 identify Population A and B sources, respectively. It is important to point out that FWHM($H\beta_{\rm BC}$) = 4000 km s^{-1} was chosen as a Population A-B boundary before $c(\frac{1}{2})$ was selected as an 4DE1 parameter. Population A-B is more effective than the RQ-RL distinction for highlighting spectroscopic differences.

Population B sources show a scatter of line shifts within $c(\frac{1}{2}) = \pm 2000$ km s^{-1} (Table 2) with mean value in Table 3 consistent with zero shift. A large part of the Population B scatter

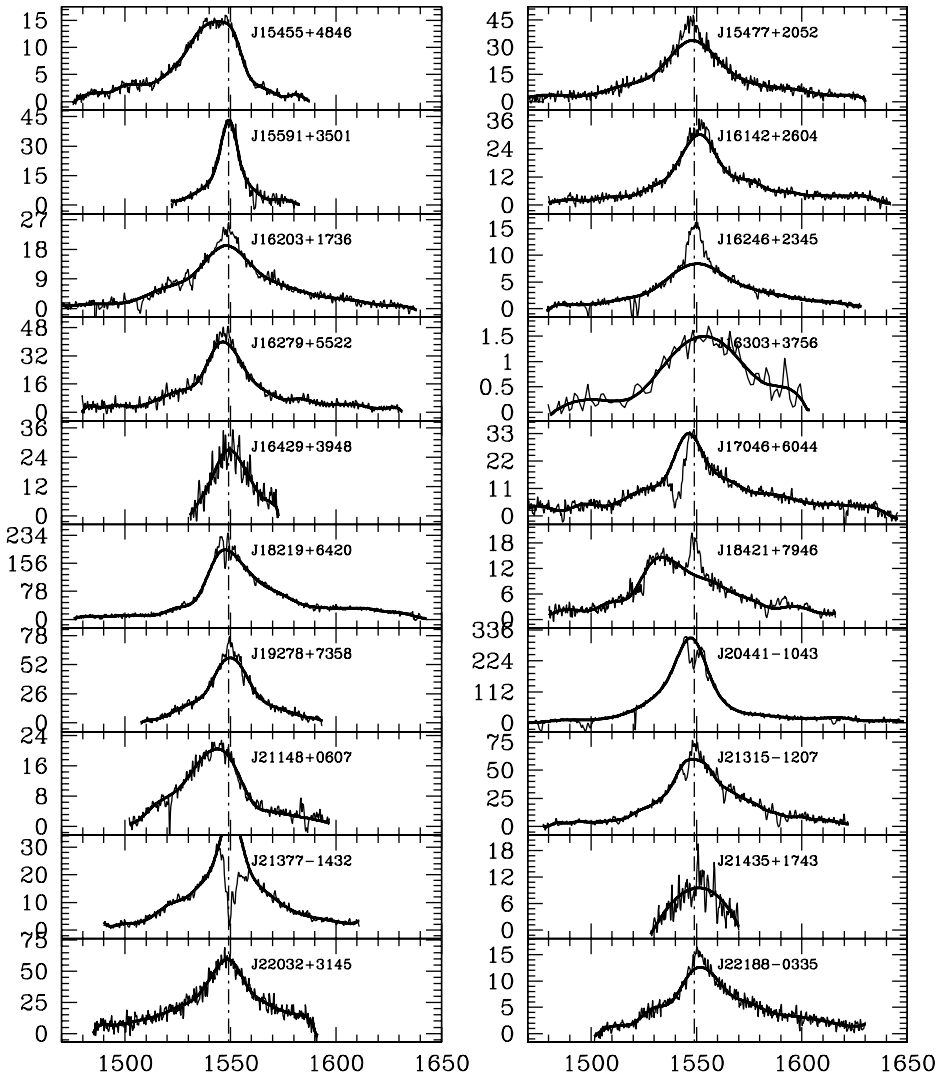

FIG. 1—*Continued*

may be associated with C IV λ1549 measurement uncertainties (the 3 σ shift uncertainty is $\approx$400 km s^{-1}). Figure 2 shows that Population A sources have a wider parameter dispersion than Population B sources. The majority of Population B sources are so concentrated that one can assign unique (within measurement errors) values of $R_{\rm Fe\,II} \sim 0.15 \pm 0.15$ and $\Gamma_{\rm soft} \approx 2.1 \pm 0.5$ to the entire population. These two values along with $c(\frac{1}{2}) = -70 \pm 1000$ km s^{-1} (consistent with 0) represent the 4DE1 coordinates with highest probability of radio-loudness.

The strong parameter concentration of Population B sources relative to the Population A RQ majority reenforces the interpretation (Sulentic et al. 2003) that RL quasars represent a distinct AGN population and perhaps the endpoint of quasar activity in sources with largest $M_{\rm BH}$ and lowest $L_{\rm bol}/L_{\rm Edd}$. The obvious question then involves the relationship between Population B RQ sources and Population B RL AGNs. RL and RQ Population B sources show strong similarity in most properties, but $c(\frac{1}{2})$ suggests a possible small separation with mean C IV $\lambda 1549_{\rm BC}$ shift values of about -200 and $+70$ km s^{-1}, respectively, for Population B RQ and RL sources. However, both values are consistent with zero shift given measurement uncertainties. A $K-S$ test for the two $c(\frac{1}{2})$ distributions confirms no significant difference. If C IV $\lambda 1549_{\rm BC}$ blueshift and negative asymmetry index are the signature of a disk wind that is driven by high $L_{\rm bol}/L_{\rm Edd}$, then 60%–80% of RQ and very few RL sources show evidence for it. RQ sources in our sample have an average negative asymmetry index (-0.1), and a $K-S$ test confirms a significant difference with the distribution for RL sources (whose average is +0.08). The simplest answer to the above question then would be that for a given $M_{\rm BH}$, RL sources lie at the extreme low end of an $L_{\rm bol}/L_{\rm Edd}$ sequence; perhaps they are expiring quasars. Perhaps Population B RQ sources with lowest values of C IV $\lambda 1549_{\rm BC}$ shift are the RQ expiring quasars. In that case our Population B designation has a physical significance, although

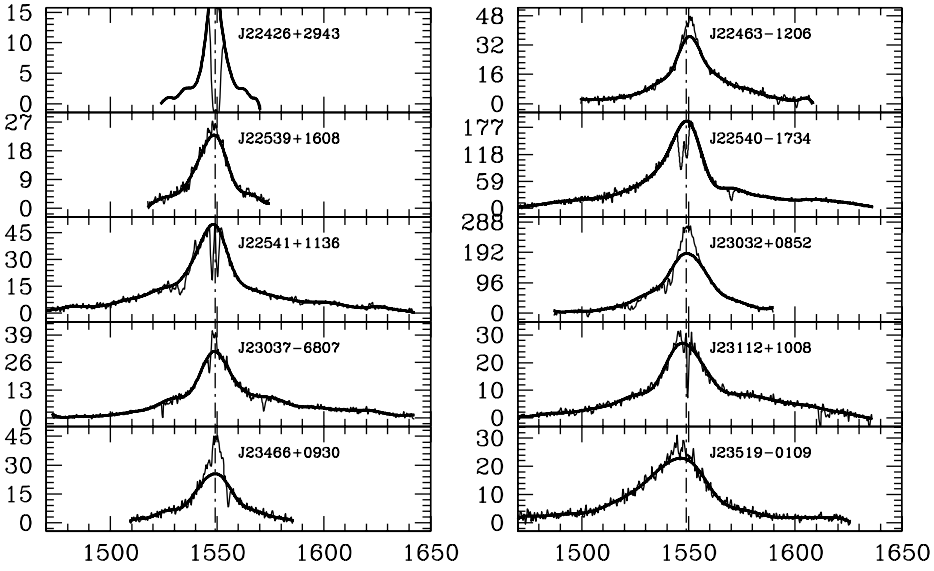

FIG. 1—*Continued*

we do not yet know what physical property allows/inhibits RL activity.

3.1. *Population A and NLSy1s*

The distinction between Populations A and B may be more fundamental than RQ-RL or NLSy1-BLSy1. Figure 2 shows that C IV λ1549 blueshifts are equally divided between sources with FWHM($H\beta_{BC}$) $\lesssim$ 2000 km s^{-1} (traditional NLSy1) and sources with FWHM($H\beta_{BC}$) in the range 2000–4000 km s^{-1} (BLSy1). A $K-S$ test reveals no significant distribution difference between the two groups of sources suggesting that the 2000 km s^{-1} cutoff for NLSy1 is artificial. The same is true for comparisons involving W(C IV $\lambda1549_{BC}$), FWHM(C IV λ1549), and Γ_{soft} parameter distributions. Only $R_{Fe\,II}$ seems to show possible evidence for a difference ($D_{KS} \approx 1.65$ with probability $P \approx 0.01$ that the two $R_{Fe\,II}$ data sets are not drawn from the same parent population). Caution is needed because the precision of the $R_{Fe\,II}$ measure depends on both S/N and the line width (Marziani et al. 2003a). Considering the similarity in Γ_{soft} and C IV λ1549 centroid shifts (which are likely related accretion rate and disk wind properties) the Population A-B distinction can be viewed as a physically motivated redefinition of the NLSy1-BLSy1 boundary originally introduced by Osterbrock & Pogge (1985) and subsequently adopted by 4DE1 for different (RL) reasons.

TABLE 1
SOURCE IDENTIFICATION AND 4DE1 PARAMETERS

IAU Code (1)	Common Name[a] (2)	z[b] (3)	z Ref. (4)	PG/BO[c] (5)	A_B[d] (mag) (6)	FWHM($H\beta_{BC}$) (km s^{-1}) (7)	$R_{Fe\,II}$ (8)	log(R_K) (9)	Γ_{soft} (10)
J00057+0203.....	LBQS 0003+0146	0.234	C97		0.10	3315	0.26	−1.00	3.08
J00059+1609.....	PG 0003+158	0.4504	M03	*	0.22	5519	0.14	2.53	2.34
J00063+2012.....	Mrk 0335	0.0252	M03	*	0.15	1950	0.28	−0.54	2.90
J00204+0226.....	LBQS 0017+0209	0.401	F89		0.10	2535	1.07	−1.00	...
J00292+1316.....	PG 0026+129	0.1451	M03	*	0.31	2405	0.28	−0.10	2.07
J00392−5117.....	[WPV85] 007	0.0290	G99		0.05	1203	0.68	...	9.00:
J00449+1026.....	[HB89] 0042+101	0.5857	SPM		0.29	8978	0.40	0.00	2.48
J00470+0319.....	PG 0044+030	0.6231	M03		0.09	5759	0.19	1.83	1.72
J00535+1241.....	UGC 00545	0.0605	M03	*	0.28	1151	1.30	−0.47	3.10
J00548+2525.....	PG 0052+251	0.1543	M03	B*	0.21	5772	0.15	−0.39	2.49

NOTES.—A colon indicates a very unusual published measure. Table 1 is published in its entirety in the electronic edition of the *Astrophysical Journal*. A portion is shown here for guidance regarding its form and content.

[a] In a format recognized by NED.

[b] Accuracy of z-values can be in general assumed to be ±0.0001 at a 1 σ confidence level in case four decimal digits are provided; ±0.001 otherwise.

[c] An asterisk (*) indicates that the sources belongs to the BG92 PG sample; a "B" indicates that the source is a "blue outlier" (Zamanov et al. 2002).

[d] From Schlegel et al. (1998).

REFERENCES.—(M03) Marziani et al. 2003a; (G99) Grupe et al. 1999; (SDSS) Spectra retrieved from http://www.sdss.org; z-values were measured as described in the text of the paper and may differ from those reported in NED; (L67) Lynds 1967; (SPM) unpublished spectra obtained with the 2.2 m telescope at San Pedro Martir; (B96) Brotherton 1996; (ESO) unpublished ESO spectra; (KPNO) unpublished KPNO spectra; (T93) Tadhunter et al. 1993; (JB91) Jackson & Browne 1991; (C97) Corbin 1997; (M96) Marziani et al. 1996; (W00) Wisotzki et al. 2000; (K96) Keel 1996; (EH04) Eracleous & Halpern 2004; (A91) Allen et al. 1991; (HB89) Hewitt & Burbidge 1989; (HB80) Hewitt & Burbidge 1980; (F89) Foltz et al. 1989

TABLE 2
C IV λ1549 Emission Line Parameters

IAU Code (1)	f_λ[a] (2)	F_{NC}[b] (3)	Δv_{rNC} (km s^{-1}) (4)	F_{BC}[c] (5)	$c(\frac{1}{4})$ (km s^{-1}) (6)	Δ^- (km s^{-1}) (7)	Δ^+ (km s^{-1}) (8)	$c(\frac{1}{2})$ (km s^{-1}) (9)	Δ^- (km s^{-1}) (10)	Δ^+ (km s^{-1}) (11)	$c(\frac{3}{4})$ (12)	Δ (km s^{-1}) (13)	$c(0.9)$ (km s^{-1}) (14)	Δ (km s^{-1}) (15)	FWHM (km s^{-1}) (16)	Δ (km s^{-1}) (17)	A.I. (18)	Δ^- (19)	Δ^+ (20)	Kurt. (21)	Δ (22)
J00057+0203.....	0.55	0.23	−726	4.0	−824	331	560	−455	121	120	−404	110	−365	78	4168	252	−0.12	0.10	0.16	0.16	0.35	0.06
J00059+1609.....	2.53	1.94	−66	22.5	866	591	522	35	200	228	−8	143	−1	92	5347	455	0.16	0.12	0.10	0.12	0.29	0.04
J00063+2012.....	7.97	7.33	314	50.7	−221	259	229	19	98	94	147	81	195	53	2927	195	−0.17	0.11	0.10	0.11	0.37	0.05
J00204+0226.....	0.44	0.00	...	1.2	−2426	174	155	−2144	122	117	−2063	140	−2064	106	5378	244	−0.10	0.07	0.07	0.07	0.50	0.05
J00292+1316.....	2.82	1.64	95	8.5	1035	1077	244	−501	199	215	−201	261	−19	160	8595	429	0.14	0.17	0.06	0.17	0.36	0.06
J00392−5117.....	0.20	A	...	2.0	338	262	265	−78	108	186	−54	81	−6	55	3056	371	0.11	0.09	0.09	0.09	0.28	0.03
J00449+1026.....	0.12	0.18	56	2.3	1433	846	705	−37	268	281	−124	203	−144	125	7385	563	0.20	0.10	0.09	0.10	0.26	0.04
J00470+0319.....	1.09	0.22	126	8.2	−418	322	490	−750	203	229	−568	143	−591	91	6274	458	0.03	0.07	0.10	0.10	0.33	0.04
J00535+1241.....	3.25	A	...	8.7	−2264	338	212	−1669	110	211	−875	68	−954	47	3804	422	−0.47	0.07	0.06	0.07	0.27	0.04
J00548+2525.....	2.11	0.74	−378	27.7	−104	767	649	−800	292	289	−624	177	−604	107	6659	585	0.08	0.12	0.10	0.12	0.28	0.04

Note.—Table 2 is published in its entirety in the electronic edition of the *Astrophysical Journal*. A portion is shown here for guidance regarding its form and content.

[a] Specific continuum flux at 1550 Å in units of 10^{14} ergs s^{-1} Å^{-1} cm^{-2}.

[b] Flux of C IV $\lambda1549_{NC}$ in units of 10^{13} ergs s^{-1} cm^{-2}. The letter "A" indicates major absorptions (typically of mini-BALs) affecting the profile of C IV $\lambda1549_{BC}$. The "a" indicates narrow absorptions that "eat away" C IV $\lambda1549_{NC}$ but that do not hamper C IV $\lambda1549_{BC}$ measurements.

[c] Flux of C IV $\lambda1549_{BC}$ in units of 10^{13} ergs s^{-1} cm^{-2}.

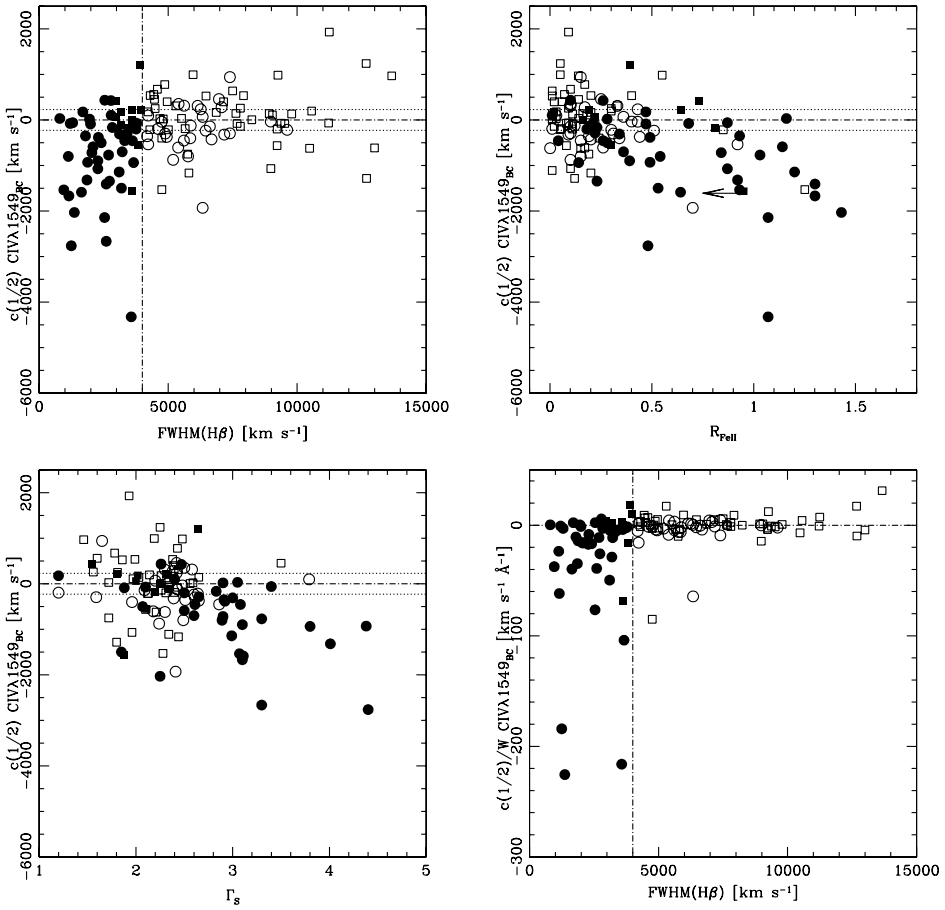

FIG. 2.—4DE1 parameter planes involving C IV $\lambda1549_{BC}$ profile shift at half-maximum [$c(\frac{1}{2})$, see text] vs. FWHM($H\beta_{BC}$) in km s^{-1} (*top left*), $R_{Fe\,II}$ (*top right*), and Γ_{soft} (*bottom left*). *Bottom right*: $c(\frac{1}{2})$ normalized by EW C IV $\lambda1549_{BC}$ in order to emphasize the difference between Population A and B sources which are denoted with filled and open symbols, respectively; RL sources are represented by squares and RQ by circles. The vertical line in the *top left* and *bottom right* panels marks the nominal Population A-B boundary. Dotted lines indicate ±2 σ confidence intervals for $c(\frac{1}{2})$ (see §2.2) meaning that sources within that range do not show significant C IV $\lambda1549$ line shift.

3.2. *Population Subdivision and Quasar Structure*

Tables 3 and 4 show that the Population A-B discrimination is more effective than the RQ-RL distinction for emphasizing source differences. Table 3 shows that almost all sample mean differences between Populations A and B are *larger* than equivalent differences between RQ and RL. Since the entire RQ source population shows a larger parameter spread than Population A RQ sources alone, it should be *more* sensitive to correlation than Population A RQ alone. Table 4 confirms that in no case does the entire RQ sample show a higher correlation coefficient than Population A sources alone. In all cases the correlation coefficient improves (or remains the same) when we restrict the RQ sample to Population A RQ alone. We interpret these results as support for our hypothesis that the Population A-B distinction is *more fundamental* than that of RQ-RL. So far we have distinguished between

TABLE 3
AVERAGE VALUES

AGN Pop (1)	$N_{sources}$ (2)	EW(C IV $\lambda1549_{BC}$) (Å) (3)	$c(\frac{1}{2})$ C IV $\lambda1549_{BC}$ (km s^{-1}) (4)	FWHM(C IV $\lambda1549_{BC}$) (km s^{-1}) (5)	FWHM($H\beta_{BC}$) (km s^{-1}) (6)	$R_{Fe\,II}$ (7)	Γ_{soft} (8)
All QSO	130	93 ± 66	−294 ± 837	5284 ± 1787	5387 ± 3268	0.36 ± 0.38	2.41 ± 0.58
RQ only	71	84 ± 69	−582 ± 860	4733 ± 1482	4100 ± 2681	0.48 ± 0.43	2.64 ± 0.63
RL only	59	104 ± 60	+52 ± 667	5946 ± 1905	6936 ± 3259	0.22 ± 0.25	2.15 ± 0.38
Population A	52	57 ± 34	−677 ± 966	4451 ± 1269	2604 ± 891	0.60 ± 0.45	2.67 ± 0.68
Population B	78	117 ± 71	−39 ± 627	5839 ± 1871	7242 ± 2943	0.20 ± 0.22	2.24 ± 0.43

TABLE 4
CORRELATION ANALYSIS FOR C IV λ1549$_{BC}$ PARAMETERS

C IV λ1549$_{BC}$ (1)	W		FWHM		$c(\frac{1}{2})/W$		FWHM(Hβ_{BC})		$R_{Fe\,II}$		Γ_{soft}	
	r_S (2)	P_{r_S} (3)	r_S (4)	P_{r_S} (5)	r_S (6)	P_{r_S} (7)	r_S (8)	P_{r_S} (9)	r_S (10)	P_{r_S} (11)	r_S (12)	P_{r_S} (13)
All Sources[a]												
$c(\frac{1}{2})$	0.411	5.951E−07	0.008	4.6E−01	0.970	8.7E−81	0.331	6.0E−05	−0.431	1.5E−07	−0.327	1.5E−04
W	...	...	0.141	5.5E−02	0.485	2.5E−09	0.469	9.1E−09	−0.530	4.5E−11	−0.284	9.1E−04
FWHM	...	...	...	...	0.040	3.3E−01	0.512	2.4E−10	−0.175	2.3E−02	−0.354	4.2E−05
$c(\frac{1}{2})/W$	...	...	...	...	...	...	0.381	3.9E−06	−0.471	7.8E−09	−0.336	9.9E−05
RQ[b]												
$c(\frac{1}{2})$	0.634	1.467E−09	−0.206	4.2E−02	0.959	8.2E−40	0.365	8.7E−04	−0.498	5.0E−06	−0.396	7.2E−04
W	...	...	−0.008	4.7E−01	0.783	3.6E−16	0.488	7.9E−06	−0.529	1.1E−06	−0.424	3.0E−04
FWHM	...	...	...	...	−0.206	4.2E−02	0.392	3.6E−04	0.056	3.2E−01	−0.296	9.7E−03
$c(\frac{1}{2})/W$	...	...	...	...	...	...	0.393	3.5E−04	−0.538	6.5E−07	−0.401	6.2E−04
RL[c]												
$c(\frac{1}{2})$	−0.024	4.3E−01	−0.108	2.1E−01	0.965	4.0E−35	−0.068	3.0E−01	−0.107	2.1E−01	−0.048	3.6E−01
W	...	...	0.145	1.4E−01	−0.095	2.4E−01	0.219	4.8E−02	−0.371	1.9E−03	−0.004	4.9E−01
FWHM	...	...	...	...	−0.092	2.4E−01	0.482	5.5E−05	−0.225	4.3E−02	−0.137	1.5E−01
$c(\frac{1}{2})/W$	...	...	...	...	...	...	−0.049	3.6E−01	−0.083	2.7E−01	0.001	5.0E−01
Population A[d]												
$c(\frac{1}{2})$	0.668	3.1E−08	−0.384	2.5E−03	0.978	5.3E−36	0.257	3.3E−02	−0.549	1.3E−05	−0.504	1.8E−04
W	...	...	−0.299	1.6E−02	0.746	1.1E−10	0.127	1.8E−01	−0.555	9.8E−06	−0.364	6.4E−03
FWHM	...	...	...	...	−0.279	2.3E−02	0.327	9.0E−03	0.113	2.1E−01	−0.281	2.9E−02
$c(\frac{1}{2})/W$	...	...	...	...	...	...	0.250	3.7E−02	−0.542	1.7E−05	−0.484	3.3E−04
Population B[e]												
$c(\frac{1}{2})$	0.032	3.905E−01	−0.067	2.8E−01	0.967	3.5E−47	−0.015	4.5E−01	−0.167	7.2E−02	−0.118	1.6E−01
W	...	...	0.089	2.2E−01	0.080	2.4E−01	0.092	2.1E−01	−0.134	1.2E−01	−0.006	4.8E−01
FWHM	...	...	...	...	−0.060	3.0E−01	0.481	4.1E−06	−0.068	2.8E−01	−0.260	1.4E−02
$c(\frac{1}{2})$/FWHM	...	...	...	...	...	...	−0.005	4.8E−01	−0.184	5.3E−02	−0.080	2.5E−01

NOTES.—The number P yields the probability that the coupled variables are not correlated. A significant correlation can be assumed if $P \lesssim 0.01$.
[a] 130 sources of which 118 with available Γ_{soft}.
[b] 71 sources of which 62 with available Γ_{soft}.
[c] 59 sources of which 56 with available Γ_{soft}.
[d] 52 sources of which 46 with available Γ_{soft}.
[e] 78 sources of which 72 with available Γ_{soft}.

Population A and B sources using FWHM Hβ_{BC} alone. The mean values given in Table 3 allow us to give best estimates for the Population A-B boundary using the other three principal 4DE1 parameters: $R_{Fe\,II} \approx 0.4$, $\Gamma_{soft} \approx 2.60$, and $c(\frac{1}{2}) \approx 0$ km s^{-1}.

One-dimensional projections of the 4DE1 space like Figures 2*a*–2*c* show a main sequence of source occupation/correlation. The Population A-B concept reflects either a continuous variation in physical/geometric/kinematic properties along this sequence or a true source dichotomy possibly driven by a critical value of L_{bol}/L_{Edd} (with Population B RQ-RL dichotomy due perhaps to BH spin, host galaxy properties, and a role for secular evolution in BH growth). In the former case Population A-B remain useful as a vehicle for emphasizing source extrema providing a valuable challenge to models of BLR structure/kinematics as well as changes in them due to physics and/or source evolution (Marziani et al. 2001, 2003b; Boroson 2002). In the past few years we have favored the possibility of two disjoint AGN populations on the basis of multifold evidence:

1. A possible gap or paucity of sources with FWHM(Hβ_{BC}) $\approx$ 4000 km s^{-1}, which is also appreciable in, e.g., Figure 6 of Wang et al. (1996), Figure 2 of Boller (2004), Figure 1 of Sulentic et al. (2000b), Figure 3 of Baskin & Laor (2005), and most impressively in Figure 7 (*right*) of Corbin & Boroson (1996); see also Collin et al. (2006).

2. Most RL sources lie above FWHM H$\beta_{BC} \approx 4000$ km s^{-1} while most RQ sources lie below this value. The few RL sources with FWHM H$\beta_{BC} \lesssim 4000$ km s^{-1} are likely viewed at an orientation that minimizes any rotational component associated with BLR motions (Sulentic et al. 2003; they fall there because of orientation rather than physics).

3. Sources with FWHM(Hβ_{BC}) $\lesssim 4000$ km s^{-1} show average profiles well fit by a Lorentzian function, while broader line sources show profiles that are frequently redward asymmetric and that require two Gaussians for a reasonable fit (Sulentic et al. 2002).

4. Sources with FWHM(Hβ_{BC}) $\lesssim 4000$ km s^{-1} often show a soft X-ray excess ($\Gamma_{soft} \gtrsim 2.8$) while those above this limit almost never show one (Boller 2004; Sulentic et al. 2000c).

5. Sources with weak (usually less than 10 Å equivalent with) and blueshifted [O III] λ5007 (the so-called blue outliers) are found only in sources with FWHM(Hβ_{BC}) $\lesssim 4000$ km s^{-1} (Zamanov et al. 2002; Marziani et al. 2003b).

6. All sources with C IV λ1549 $c(\frac{1}{2}) \lesssim -3000$ km s^{-1} show FWHM H$\beta_{BC} \lesssim 4000$ km s^{-1} (Fig. 2*a*). Most sources with C IV λ1549 $c(\frac{1}{2}) \lesssim -1000$ km s^{-1} also lie below the same FWHM limit. Sources with broader Hβ_{BC} show a scatter of values between C IV λ1549 $c(\frac{1}{2}) \pm 2000$ km s^{-1}. The *W*(C IV λ1549) measures also show a strong difference (not correlation) in mean values for source greater and less than FWHM H$\beta_{BC} = 4000$ km s^{-1}.

7. Comparison of C IV λ1549 and Hβ_{BC} profiles suggests a discontinuity at FWHM(Hβ_{BC}) ≈ 4000 km s^{-1}. FWHM(Hβ_{BC}) and FWHM(C IV λ1549$_{BC}$) are correlated above this value but not below (Marziani et al. 1996; Baskin & Laor 2005; see also our Table 4).

8. Figure 3 shows a possible new correlation between C IV λ1549 FWHM and $c(\frac{1}{2})$ measures. Comparison of Figures 3*a* and 3*b* for Population B and A sources, respectively, indicates that the correlation exists only for sources with FWHM(Hβ_{BC}) $\lesssim$ 4000 km s^{-1} (Population B sources show a scatter diagram). This C IV λ1549 intercorrelation for Population A sources shows a reasonably strong correlation (correlation coeff. 0.5). The best-fit relation is $c(\frac{1}{2})$(C IV λ1549$_{BC}$) $= 963 - 0.426$FWHM $\times$ (C IV λ1549$_{BC}$) in km s^{-1}.

The correlation in Figure 3 might be expected from (and constraining of) models that view Population A sources as the highest accreting AGNs that generate a disk wind (Murray et al. 1995; Bottorff et al. 1997; Proga & Kallman 2004). Previous results may also indicate a change in BLR structure, perhaps at a critical value of L_{bol}/L_{Edd} [corresponding to FWHM(Hβ_{BC}) $\approx$ 4000 km s^{-1}] with an accretion disk + outflowing high-ionization wind required to explain Population A source measures (Marziani et al. 1996, 2001, 2003a). Population B sources do not allow us to rule out the possibility of a single stratified emission region producing both LILs and HILs. Population A and B sources differ in almost every mean property that can be defined. Table 5 summarizes both phenomenological differences (mean values given where available) as well as some physical differences that can be inferred from the empiricism. Note that not all of the cited works make a distinction between Population A and B.

Table 3 shows that *W*(C IV λ1549$_{BC}$) differs by a factor of $\approx$2 between Population A and B sources, with Population A sources showing lower values. Since Populations A and B do not show a significant difference in mean source luminosity (Bachev et al. 2004), we ascribe the EW difference to a difference in L_{bol}/L_{Edd} which is known to be stronger than the luminosity dependence (Bachev et al. 2004; Baskin & Laor 2004). Populations A and B differ systematically in L_{bol}/L_{Edd}, as shown by Marziani et al. (2003b, 2006). While not a principal 4DE1 parameter, it is clear that *W*(C IV λ1549$_{BC}$) is an important measure.

4. C IV λ1549 NARROW-LINE EMISSION

All tabulated parameter means and correlation coefficients discussed above depend on proper processing of the C IV λ1549 spectra. Confusion exists about the reality and strength of a narrow-line C IV λ1549 component (C IV λ1549$_{NC}$) presumably arising from the same NLR as, e.g., [O III] λλ4959, 5007 and narrow Hβ. There is now no doubt that C IV λ1549$_{NC}$ emission is common in AGNs (see also Sulentic & Marziani 1999). High- and low-redshift type 2 AGNs with obvious C IV λ1549$_{NC}$ emission have recently been found in significant numbers (Barger et al. 2002; Jarvis et al. 2005*; Norman et al. 2002*; Stern et al. 2002*; Szokoly et al. 2004; Mainieri et al. 2005*; Severgnini et al. 2006). According to Meiksin (2006) only four confirmed high-redshift ($z > 1.6$) type 2 AGNs are known (references marked with an asterisk above). All four show prominent C IV λ1549$_{NC}$ (see also Dawson et al. 2001).

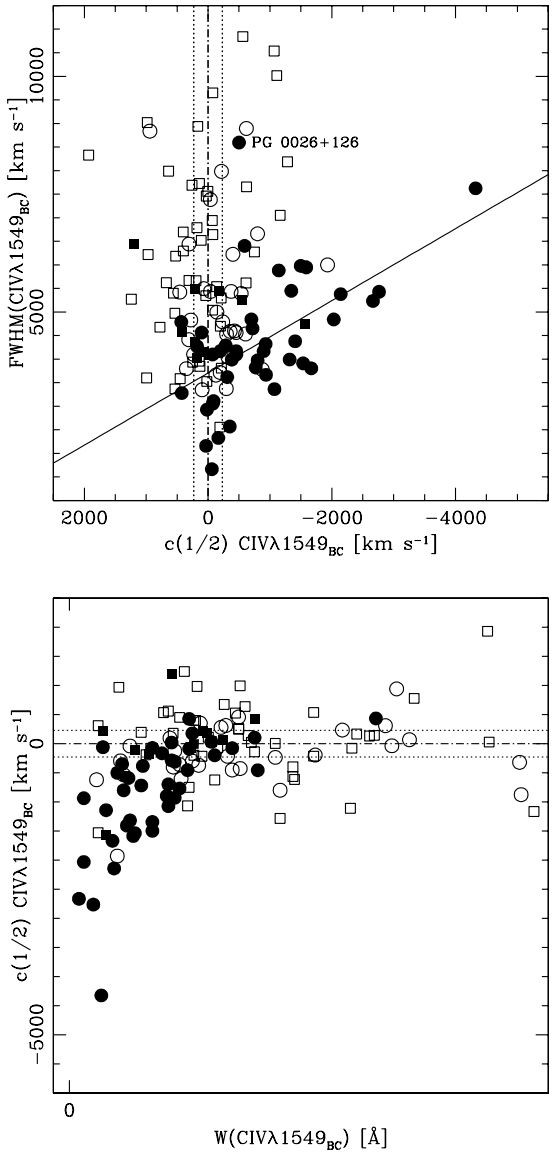

FIG. 3.— *Top*: Correlation diagram for measures of FWHM C IV λ1549$_{BC}$ vs. $c(\frac{1}{2})$ for Population B and Population A sources. Symbols and $c(\frac{1}{2})$ confidence intervals are the same as in Fig. 2. The best-fit regression line (least-squares, unweighted) for the Population A correlation (RQ only) is shown. Both $c(\frac{1}{2})$ and FWHM(C IV λ1549$_{BC}$) are in units of km s^{-1}. See Appendix for a discussion of the outlier PG 0026+126. *Bottom*: $c(\frac{1}{2})$ vs. rest-frame *W*(C IV λ1549$_{BC}$).

In contrast to Hβ a clear, unique NLR/BLR inflection is less often seen in the C IV λ1549 profiles making NLR correction less certain. This is not surprising when one considers that the intrinsic velocity resolution at C IV λ1549 is 3 times lower than at Hβ. NLR C IV λ1549 can also be broader than other narrow lines because (1) it is a doublet with $\Delta v \approx 500$ km s^{-1} and (2) it can arise in denser-than-average parts of the NLR (as for O III λ4363; e.g., Marziani et al. 1996; Sulentic & Marziani, 1999). We argue

TABLE 5
MAIN TRENDS ALONG THE 4DE1 SEQUENCE

Parameter	Population A	Population B	References
FWHM(Hβ_{BC})	800–4000 km s^{-1}	4000–10,000 km s^{-1}	1, 2, 3, 4, 5
log M_{BH}[a]	6.5–8.5	8.0–10.0	6, 7, 8, 9
L_{bol}/L_{Edd}[a]	0.1–1.0	0.01–0.5	6, 7, 8, 9
W(Hβ_{BC})	~80 Å	~100 Å	1, 2, 3, 4
Hβ_{BC} profile shape	Lorentzian	Double Gaussian	2, 3, 5, 10, 11
$c(\frac{1}{2})$ Hβ_{BC}	~0	+500 km s^{-1}	1, 2, 3
$R_{Fe\,II}$	0.7	0.3	1, 2
Si III]/C III]	0.4	0.2	12, 13
log n_e[a]	11	9.5–10	12
log U[a]	−2/−1.5	−1.0/−0.5	12
FWHM C IV λ1549$_{BC}$	(2–6) × 10^3 km s^{-1}	(2–10) × 10^3 km s^{-1}	This paper
W(C IV λ1549$_{BC}$)	58 Å	105 Å	This paper
AI(C IV λ1549$_{BC}$)	−0.1	0.05	This paper
$c(\frac{1}{2})$C IV λ1549	−800 km s^{-1}	0	2, 3, This paper, 14, 15
Γ_{soft}	Often large	Rarely large	2, 3, 16
X-ray variability	Extreme/rapid common	Less common	17, 18
Optical variability	Possible	More frequent/higher amplitude	19
Probability RL	≈3%–4%	≈15%–18%	2, 20, 21
BALs	Extreme BALs	Less extreme BALs	22, 23

[a] Physical difference.

REFERENCES.—(1) Marziani et al. 1996; (2) Sulentic et al. 2000c; (3) Sulentic et al. 2000b; (4) Marziani et al. 2003a; (5) Véron-Cetty et al. 2001; (6) Kaspi et al. 2000; (7) Marziani et al. 2003b; (8) Peterson et al. 2004; (9) Sulentic et al. 2006a; (10) Sulentic et al. 2002; (11) Sulentic et al. 2000a; (12) Marziani et al. 2001; (13) Wills et al. 1999; (14) Yuan & Wills 2003; (15) Baskin & Laor 2005; (16) Wang et al. 1996; (17) Turner et al. 1999; (18) Grupe et al. 2001; (19) Giveon et al. 1999; (20) Sulentic et al. 2003; (21) J. W. Sulentic et al. 2007, in preparation; (22) Reichard et al. 2003; (23) Sulentic et al. 2006b.

that cautious subtraction of a suitable narrow component is essential for exploiting the information content in the C IV λ1549 line (see Bachev et al. 2004). We subtracted a significant ($W > 1$ Å) NLR component from 76 of 130 sources in this sample. Figure 1 shows the individual C IV λ1549 profiles with narrow components indicated in order to assist visual assessment of the component on a source-by-source basis.

Baskin & Laor (2005) recently pointed out that our earlier C IV λ1549$_{BC}$ and C IV λ1549$_{NC}$ measurements (Marziani et al. 1996) were "nonunique." Every experimental measure is nonunique, and the lack of uniqueness is customarily indicated by error bars. Rather than uniqueness, the question we are addressing is whether or not there is a significant narrow component in the C IV λ1549 line. The second question, assuming that such a component is present, involves how accurately we can measure it. The third question, assuming we can accurately measure it, is whether correction for C IV λ1549$_{NC}$ matters. The goals of this section are to provide a recipe for consistent C IV λ1549$_{NC}$ correction and to show that very different results emerge from corrected C IV λ1549 measures.

The strong and relatively narrow core (FWHM $\lesssim$ 2000 km s^{-1}) observed in many C IV λ1549 profiles was previously noted and an *ad hoc* intermediate line region (ILR) was introduced in order to account for it (Brotherton et al. 1994; Brotherton & Francis 1999). The ILR was defined as having some properties typical of the canonical BLR necessitating the postulation of an additional VBLR component in order to explain the broad wings often seen in C IV λ1549 spectra (e.g., Fig. 1). Unfortunately, the ILR approach is not fully consistent because narrow C IV λ1549 cores are significantly narrower than corresponding Hβ_{BC} profiles (Sulentic & Marziani 1999) which are a canonical BLR feature. They are sometimes as narrow as the [O III] λ5007 lines. Intermediate ionization lines of C III] λ1909 and Si III] λ1892 measured in average spectra (Bachev et al. 2004) show widths that are more consistent with Hβ_{BC} and much broader than the narrow cores of C IV λ1549 that we ascribe to the NLR. In addition density-sensitive ratios measured near the C III] λ1909 blend are consistent with BLR density ($n_e \sim 10^{10}$ cm^{-3}; see Brotherton et al. 1994; Bachev et al. 2004). This reinforces our interpretation that the hypothesized ILR+VBLR components as simply the more canonical NLR + BLR. The larger width of C IV λ1549$_{NC}$ compared to Hβ_{NC} or [O III] λ5007 can be easily explained within the framework of a density/ionization gradient within the NLR, as further described below.

Almost all other studies of C IV λ1549 line properties (Wills et al. 1995, 1999; Corbin & Boroson 1996; Vestergaard 2002; Warner et al. 2004) do not subtract C IV λ1549$_{NC}$ emission. Baskin & Laor 2005 assume that the width and strength of C IV λ1549$_{NC}$ and [O III] λ5007 are correlated. In most cases this implies that the ratio C IV λ1549/[O III] λ5007 $\lesssim$ 1. The physical relationship between forbidden [O III] $\lambda\lambda$4959, 5007 and permitted C IV λ1549$_{NC}$ is however unclear leaving little basis for assuming a fixed relation. The [O III] $\lambda\lambda$4959, 5007 lines often show a strong blue wing that might be described as a semibroad component. So-called blue outlier sources show this component and it is expected to be a *strong* C IV λ1549 emitter (Zamanov et al. 2002). Our analysis suggests that C IV λ1549$_{NC}$ is likely absorbed by dust or is intrinsically weak in ≈50% of sources. Among the remainder, about 1/3 of the sources show C IV λ1549$_{NC}$ significantly broader than narrow Balmer and [O III] $\lambda\lambda$4959, 5007 emission. It is probably emitted by a reddening-free high-density (or high-ionization) innermost region of the NLR. Whatever its origin and relationship to other narrow lines, it is present in the spectra of many sources and will affect our efforts to parameterize C IV λ1549$_{BC}$.

The motivation for relatively high density emission in the NLR stems from the clear evidence of relatively large C IV λ1549$_{NC}$/[O III] λ5007 intensity ratios in several sources: NGC 5548, NGC 7674, and I Zw 92 (Kraemer et al. 1994, 1998), with C IV λ1549$_{NC}$/[O III] λ5007 ≈ 2. In addition, even if Baskin &

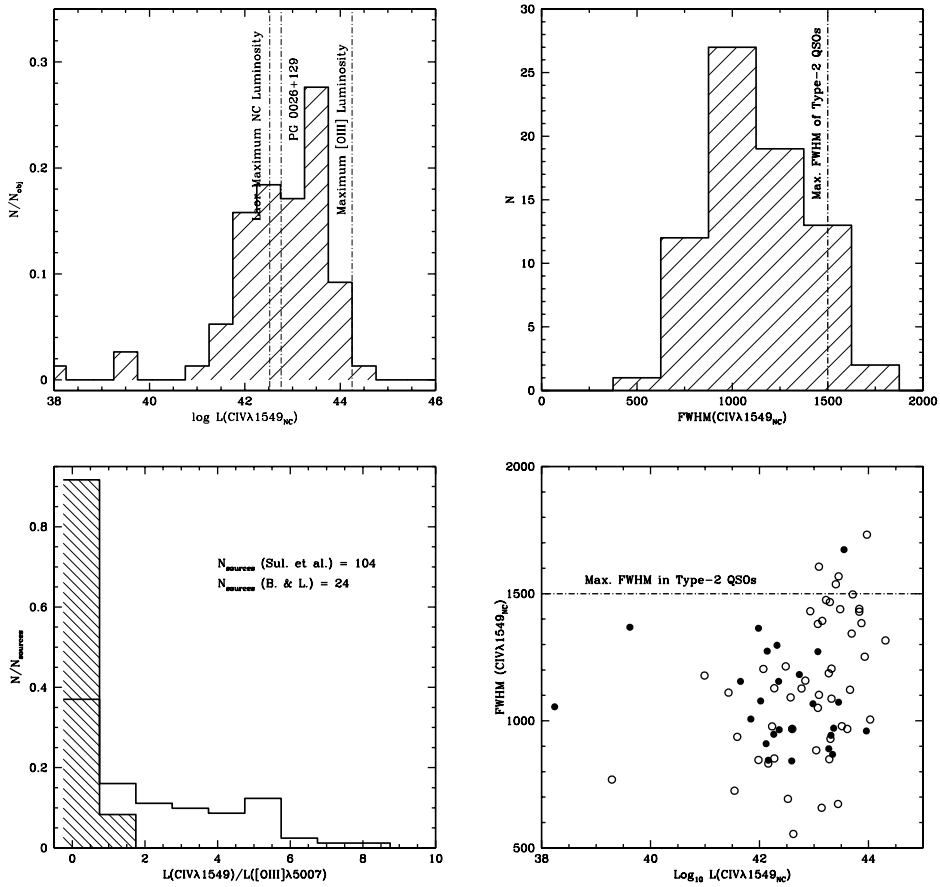

FIG. 4.—C IV $\lambda1549_{NC}$ analysis. *Top left*: Luminosity distribution of C IV $\lambda1549_{NC}$ components identified in our *HST* sample [$\log L$(C IV $\lambda1549_{NC}$) in units of ergs s^{-1}; *shaded histogram*]; *top right*: FWHM distribution for C IV $\lambda1549_{NC}$ components; *bottom left*: distribution of the ratio L(C IV $\lambda1549_{NC}$)/L([O III] $\lambda5007$) for our *HST* sample (corrected for Galactic extinction) and for the sample of Baskin & Laor (2005). *Bottom right*: FWHM(C IV $\lambda1549_{NC}$) vs. $\log L$(C IV $\lambda1549_{NC}$) for our *HST* sample. Filled circles indicate Population A sources; open circles indicate Population B sources.

Laor (2005) subtracted little C IV $\lambda1549_{NC}$, the average nonzero subtraction for the 16 sources in common with the present study implies C IV $\lambda1549_{NC}$/[O III] $\lambda5007 \approx 0.3$. This value already indicates bulk emission from $\log n_e \gtrsim 5.5$, much above the "standard" NLR density $n_e \sim 10^4$ cm^{-3}. The C IV $\lambda1549$/[O III] $\lambda5007$ intensity ratio increases with density around the [O III] $\lambda\lambda4959$, 5007 critical density because of the drastic collisional quenching that suppresses [O III] $\lambda\lambda4959$, 5007 but not C IV $\lambda1549$. The observed FWHM differences between [O III] $\lambda\lambda4959$, 5007, Hβ_{NC}, and C IV $\lambda1549_{NC}$ are recovered under standard assumptions if a density gradient is assumed for the NLR, with $3 \lesssim \log n_e \lesssim 7$–8 (Sulentic & Marziani 1999).

We suggest the following C IV $\lambda1549_{NC}$ subtraction procedure as the most reliable way to obtain reasonable and reproducible C IV $\lambda1549_{NC}$ measures.

Step 1: Inflection.—Sources showing a C IV $\lambda1549$ NLR/BLR inflection can be treated the same as Hβ as long as the width/shift/intensity constraints given below are not violated. See the profiles in Figure 1 and Appendix discussion of PG 0026+126, which shows a strong profile inflection. There was no simultaneous fitting. The underlying C IV $\lambda1549_{BC}$ was fit with an high-order spline function. The overlying narrow component was set by bordering the fitting range at inflection points which defined a core that met the FWHM and flux ratio criteria described below. The FWHM was measured using a Gaussian fit or by measuring the half-maximum wavelengths if the profile was absorbed or very different from Gaussian.

Step 1a: No inflection or multiple inflections.—Most sources do not show an inflection or sometimes show multiple inflections between reasonable limits of width and strength. This motivates us to set a conservative limit on FWHM C IV $\lambda1549_{NC}$. Simple models suggest that lines like C IV $\lambda1549$ can be significantly broader than [O III] $\lambda5007$ (Sulentic & Marziani 1999). C IV $\lambda1549$ lines with FWHM $\lesssim$1500 km s^{-1} are now observed in higher redshift type 2 AGNs (see above references). We therefore suggest again subtracting a C IV $\lambda1549_{NC}$ component with FWHM $\leq$ 1500 km s^{-1} subject to shift and intensity constraints that follow (see Fig. 4). In just two cases (3C 110 and 3C 273) our data suggested a somewhat broader component but inclusion/exclusion of these few sources as processed, or reduction of the NLR component to this limit will not affect the main conclusions of this study. The choice was usually to maximize the C IV $\lambda1549_{NC}$ FWHM within the flux ratio condition as described below. Any narrow feature with FWHM $\lesssim$ 900 km s^{-1} has no physical meaning. The feature we identify as C IV $\lambda1549_{NC}$ shows

FWHM $\approx 1200 \pm 300$ km s^{-1} in 95% of sources with significant narrow emission (Fig. 4).

Step 2: Nebular Physics and Observations.—There is no strong upper limit for the expected C IV λ1549/[O III] λ5007 intensity ratio in the absence of internal dust extinction. Both high ionization and high density can produce an arbitrarily large ratio (Contini & Viegas 2001; Kraemer et al. 1998; Baldwin et al. 1995). We adopt C IV λ1549/[O III] λ5007 $\approx$ 10, derived for the high-ionization region of NGC 5548 (Kraemer et al. 1998), as a *strict* upper limit. Using again observational results as a guideline, we consider Seyfert 1 sources in our sample that show prominent, unambiguous C IV $\lambda1549_{\rm NC}$ (NGC sources, PKS 0518-45, and 3C 390.3). We find a large dispersion in the reddening-corrected C IV $\lambda1549_{\rm NC}$/[O III] λ5007 ratio with a mean value $\approx$2 and a maximum $\approx$5 (NGC 3783). Therefore, we can safely regard an C IV $\lambda1549_{\rm NC}$/[O III] λ5007 intensity ratio $\approx$5 as an observationally defined boundary. If this condition is appropriate the (A_B-corrected) distribution of C IV λ1549/[O III] λ5007 intensity ratios (shown in Fig. 4) does not pose any special challenge, including the few sources for which $5 \lesssim$ C IV $\lambda1549_{\rm NC}$/[O III] $\lambda5007 \lesssim 10$ (with an uncertainty of $\pm$50% these sources are not significantly above our adopted limit of 5).

Step 3: NLR shift.—In most sources the [O III] λ5007 and/or H$\beta_{\rm NC}$ profile centroid is used to define the rest frame of a source. Limited available H I and CO measures of host galaxy emission support this definition except for a few extreme Population A (some but not all formally NLSy1s) blue outlier sources. We use the peak of Hβ to define the source rest frame of blue outliers. The C IV $\lambda1549_{\rm NC}$ profile centroid (Table 2) agrees with the optically defined rest frame in most sources. Of our sources, 90% show a C IV $\lambda1549_{\rm NC}$ centroid within $\pm$400 km s^{-1}. This is reasonable considering that the average FWHM(C IV $\lambda1549_{\rm NC}$) = 1120 km s^{-1} and that C IV $\lambda1549_{\rm NC}$ is strongly sensitive to S/N. Shifts of several hundred km s^{-1} are occasionally observed and may be due to (1) an intrinsic C IV $\lambda1549_{\rm NC}$ blueshift, (2) narrow-line absorption that creates a spurious shift to the red (and, indeed, inspection of Fig. 1 reveals that this is the case for most sources where C IV $\lambda1549_{\rm NC}$ appears to be significantly redshifted), and (3) poor rest-frame determination. However only five sources out of 29 with $|\Delta v_r|$(C IV $\lambda1549_{\rm NC}) \gtrsim 300$ km s^{-1} show a $\Delta z \approx \pm 0.001$.

Figure 4 summarizes our C IV $\lambda1549_{\rm NC}$ measures: line luminosity distribution of C IV $\lambda1549_{\rm NC}$ (Fig. 4, *top right*), distribution of C IV $\lambda1549_{\rm NC}$/[O III] λ5007 luminosity ratios (Fig. 4, *bottom left*), distribution of C IV $\lambda1549_{\rm NC}$ FWHM measures (Fig. 4, *top right*), and distribution of C IV $\lambda1549_{\rm NC}$ measures in the line luminosity–FWHM plane (Fig. 4, *bottom right*). Application of the above procedures resulted in a subtracted NLR component usually less than W(C IV $\lambda1549_{\rm NC}) \approx 10$ Å but with a few extreme cases, usually low-luminosity Seyfert 1s. RL sources show the largest fraction of detectable C IV $\lambda1549_{\rm NC}$ components (0.71) compared to 0.48 for RQ AGNs. Our Population B sources show a slightly larger fraction of C IV $\lambda1549_{\rm NC}$ components (0.63) than Population A (0.51). Some sources do not allow an unambiguous C IV $\lambda1549_{\rm NC}$ subtraction with a significant range of acceptable solutions. This ambiguity and its effect on C IV $\lambda1549_{\rm BC}$ are usually within the adopted errors (even if the effect on C IV $\lambda1549_{\rm NC}$ is much larger), that have been estimated changing the fractional intensity levels by $\pm$5%. As described earlier, the random scatter in Galactic line radial velocity after realignment is just $\approx$40 km s^{-1}. Therefore, it is possible that several C IV $\lambda1549_{\rm NC}$ shifts are significant, because they show values larger than the expected calibration and measurement uncertainties. Examining spectra in Figure 1 one will occasionally see a C IV λ1549 profile with a peak as narrow as some subtracted C IV $\lambda1549_{\rm NC}$ (e.g., J13253−3824 and J15591+3501). In these cases subtraction of the sufficiently narrow peak would violate other selection rules (e.g., in the above two cases C IV $\lambda1549_{\rm NC}$/[O III] $\lambda5007 \gg 10$). Note that we also verified a posteriori that the C IV $\lambda1549_{\rm NC}$ FWHM was less than FWHM(H$\beta_{\rm BC}$).

4.1. *The Narrow Cores of* C IV *λ1549 Do Not Reverberate*

An ideal check on our NLR results would involve reverberation mapping where any NLR component would be expected to remain stable. One *International Ultraviolet Explorer* (*IUE*) based study (Turler & Courvoisier 1998) reported PCA analysis on 18 AGNs with 15 or more independent spectra. Ten of the sources are included in our sample. The principal component in their study was interpreted to involve the parts of the C IV λ1549 line profile that varied with zero lag time. The approach of Türler & Courvoisier was to isolate the principal component dominated by continuum and broad-line variability. This was then subtracted from the mean spectrum to isolate the remaining information content (rest spectrum). Two things are seen in the rest spectrum: a narrow unshifted peak and more complex and extended wings. The nature of the wings will depend on the complexity and timescale of variations as well as the number and temporal spacing of source spectra. Component 1 can be reasonably argued to be the NLR component of the line, the correlated intensity component that dominated our two-dimensional analogy above.

In the case of 3C 273, only the continuum was present in the principal component. We identified and subtracted an NLR component in all 10 overlap cases. A narrow component of similar strength and width is seen in the second principal component spectra for nine of these cases (except 3C 273). The least ambiguous case involves 3C 390.3, where there is a clear inflection between NLR and BLR. In that case agreement is perfect. Other sources like GQ Com, NGC 3783, and NGC 5548 also show strong agreement. The range of FWHM for the second principal component C IV λ1549 profiles 1–5000 km s^{-1}, suggesting that the NLR is often blended with additional broad-line emission. However, the overall agreement between the central cores and our own estimates of NLR C IV λ1549 emission gives us confidence that we have developed a reasonable approach to correcting the C IV λ1549 line profiles. The alternative is to ignore the problem which we argue will lead to spurious results.

4.2. *Comparison with Previous Work*

Other recent studies of the C IV λ1549 profile, using the same *HST* archival spectra, subtracted little (Baskin & Laor 2005) or no (Wills et al. 1993; Corbin & Boroson 1996; Vestergaard 2002; Kuraszkiewicz et al. 2002, 2004; Warner et al. 2004) NLR component. Figure 5 compares our C IV $\lambda1549_{\rm BC}$ FWHM and centroid shift $\left[c(\frac{1}{2})\right]$ measures with equivalent values for sources in common with some of these studies. The bottom left panel of Figure 4 shows that Baskin & Laor (2005) subtracted a ($\sim$2–4 times) smaller and more constant NLR component. Direct comparison with Kuraszkiewicz et al. (2002, 2004) is not possible, because they model the C IV λ1549 profile with multiple Gaussian components that do not correspond to our NLR and BLR interpretation. FWHM measures are strongly affected by undersubtraction of C IV $\lambda1549_{\rm NC}$. The top left panel of Figure 5 compares our FWHM C IV $\lambda1549_{\rm BC}$ measures with those of Baskin & Laor (2005) and Warner et al. (2004). Symbols for comparisons with Baskin & Laor (2005) (and Corbin & Boroson 1996) retain the Population A-B and RQ-RL distinctions used in

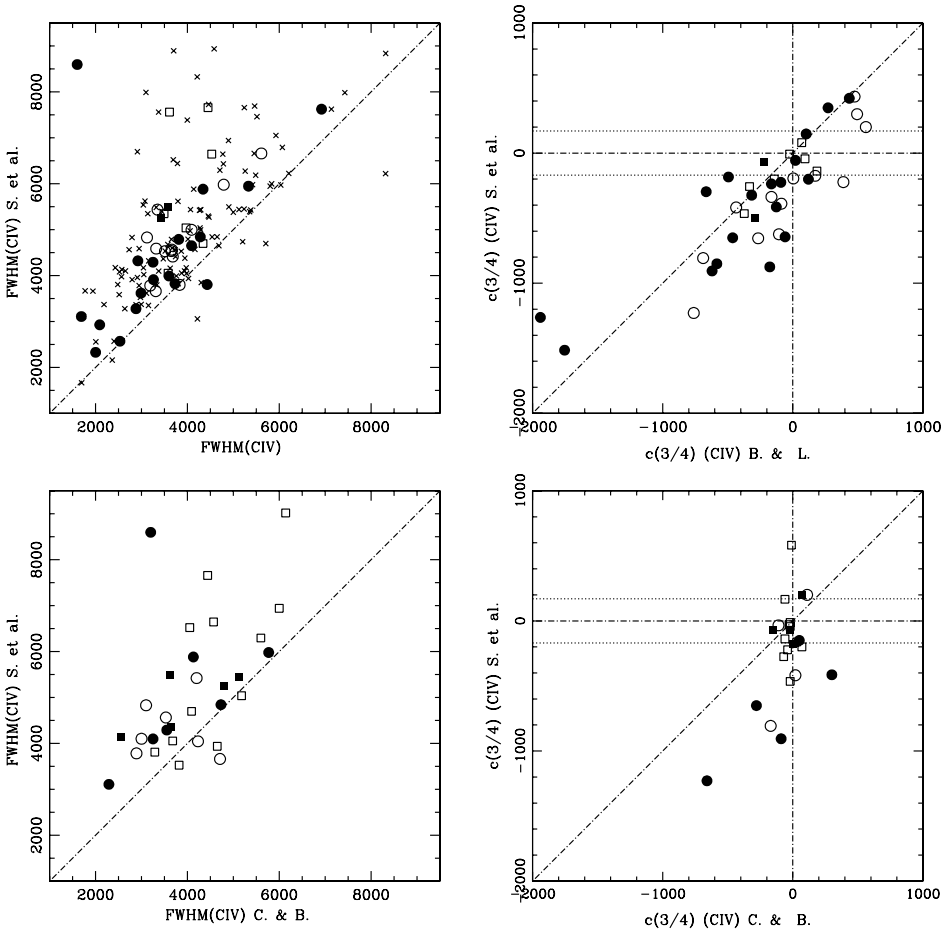

FIG. 5.—Comparison of our C IV $\lambda 1549_{BC}$ measures with those of Baskin & Laor (2005) and Warner et al. (2004) (*top*) and Corbin & Boroson (1996) (*bottom*). *Left*: FWHM(C IV $\lambda 1549_{BC}$) comparison, in units of km s^{-1}. Small crosses compare with FWHM(C IV λ1549) data of Warner et al. (2004). The same symbols used in Fig. 2 were used for comparisons with Baskin & Laor (2005) and Corbin & Boroson (1996). *Right*: Comparison C IV λ1549 line centroid at 3/4 intensity [$c(\frac{3}{4})$], in km s^{-1}. Our $c(\frac{3}{4})$ confidence intervals are shown in the right panels. The source with the largest blueshift (Population A quasar PG 1259+593) falls outside the boundary of the plot [$c(\frac{1}{2}) \approx 4000$ km s^{-1}]. Data point for PG 0026+129 is not shown to avoid *x*-scale compression. Parity diagonal line is shown in all panels. Dotted lines indicate $\pm 2\,\sigma$ confidence intervals for $c(\frac{3}{4})$ (see § 2.2).

earlier figures. Our measures are systematically larger with the amplitude of ΔFWHM increasing systematically with FWHM C IV $\lambda 1549_{BC}$. The bottom left panel compares our FWHM measures with Corbin & Boroson (1996) and shows similar disagreement. Correlations such as FWHM Hβ versus FWHM C IV λ1549 (Corbin 1991; Baskin & Laor 2005; Warner et al. 2004) found using uncorrected C IV λ1549 measures will likely be spurious, except possibly for the Population B sources. The most striking evidence for correlation is found in Figure 7 (*right*) of Corbin & Boroson (1996) involving NC-corrected Hβ_{BC} and uncorrected C IV $\lambda 1549_{BC}$ measures. One sees two groups of sources (Population A and B) each showing a positive trend but with different slopes for the two trends. The trends are displaced by ΔFWHM(C IV $\lambda 1549_{BC}$) = 3000 km s^{-1} at about FWHM(Hβ_{BC}) = 4000 km s^{-1}. The "Population B" trend can be described as displaced toward smaller values of FWHM(C IV $\lambda 1549_{BC}$). Since narrow-line emission is systematically stronger in Population B (especially RL) sources we might expect those FWHM(C IV $\lambda 1549_{BC}$) measures to be more strongly affected by NC subtraction. Is the displacement entirely due to the lack of NC-corrected FWHM(C IV $\lambda 1549_{BC}$) measures? Much of the displacement disappears in our equivalent FWHM-FWHM plot, but the correlation seen for Population B sources ($r_S \approx 0.5$) is stronger than for Population A ($r_S \sim 0.3$; not significant) and its extrapolation into the Population A domain predicts much smaller (3000 km s^{-1}) values for FWHM(C IV $\lambda 1549_{BC}$) than are observed.

The right panels of Figure 5 compare our $c(\frac{3}{4})$ measures with those from Baskin & Laor (2005; see also our Fig. 5, *top*) and Corbin & Boroson (1996; see also our Fig. 5, *bottom*). There is a systematic displacement of uncorrected shift measures toward smaller or even redshifted values in both comparisons. This will tend to diminish the Population A-B (or RQ vs. RL) differences that are highlighted in this paper. The systematic C IV λ1549 blueshift for Population A sources becomes much less obvious using NC-uncorrected C IV λ1549 measures and especially using shift measures taken closer to the profile peak [e.g., $c(0.9)$]. Figure 5 shows systematic differences between corrected and

uncorrected measures that will erase or obscure important C IV λ1549 results like the ones discussed in this paper.

5. M_{BH} CALCULATIONS USING C IV λ1549 WIDTH

C IV λ1549 has become the line of choice for black hole mass estimation in high-z quasars. It is a dangerous choice for at least two reasons: (1) it shows a systematic blueshift in many sources, and (2) FWHM C IV $\lambda1549_{BC}$ does not correlate strongly or monotonically with FWHM Hβ_{BC}, the line of choice for low-redshift M_{BH} estimation. Reason (1) does not necessarily rule out a virialized distribution of emitting clouds, but it certainly motivates caution when using the line to infer black hole mass. Blueshifted C IV λ1549 profiles are thought to arise in a high-ionization wind resulting in a velocity flow that is not negligible relative to any rotational component (Murray et al. 1995; Proga & Kallman 2004). We think use of C IV λ1549 warrants even more caution, because we see different line properties for Population A and B (or alternatively RQ and RL) sources. This raises the possibility that the geometry/kinematics of the C IV λ1549 emitting region may be fundamentally different in Population A and B sources. The population distinction is at least useful and possibly fundamental, because it maximizes source differences. FWHM Hβ_{BC} and C IV $\lambda1549_{BC}$ are most similar (Table 3) for RQ sources that show mean FWHM(C IV $\lambda1549_{BC}$) only $\approx$600 km s^{-1} larger than FWHM(Hβ_{BC}). The RQ source distinction will therefore yield reasonable agreement between the two M_{BH} estimators. The same is true for sources under the RL distinction where FWHM(C IV $\lambda1549_{BC}$) is $\approx$900 km s^{-1} broader. Both differences are approximately 15%–16% of the mean RQ and RL profile widths, respectively.

The two lines show larger difference when sources are divided using the Population A-B distinction where ΔFWHM(Hβ_{BC}) $-$ FWHM(C IV $\lambda1549_{BC}$) ≈ -1900 km s^{-1} and $\approx$+1400 km s^{-1} for Population A and B, respectively. These discrepancies amount to $\sim$56% and $\approx$21% of FWHM(C IV $\lambda1549_{BC}$) + FWHM(Hβ_{BC})/2 for Population A and B, respectively. This is larger than the measurement uncertainties for FWHM measures of both lines and further supports the utility of the Population A-B concept. The two estimators will yield M_{BH} estimates that are more discrepant. Adopting the Population A-B distinction as more useful than the RQ-RL one then finds the largest Population A-B differences using FWHM(Hβ_{BC}) where ΔFWHM(A-B) ≈ -4600 km s^{-1} compared to -1400 km s^{-1} using FWHM(C IV $\lambda1549_{BC}$). The corresponding differences for the RQ-RL distinction are ΔFWHM(RQ-RL) ≈ -2800 km s^{-1} (Hβ_{BC}) and -1200 km s^{-1} (C IV $\lambda1549_{BC}$).

As already pointed out (e.g., Marziani et al. 1996) the intrinsic dispersion of FWHM C IV $\lambda1549_{BC}$ is less than for FWHM Hβ_{BC} making it less sensitive to differences between source populations. Since FWHM C IV $\lambda1549_{BC}$ measures are less accurate than FWHM Hβ_{BC} values derived from BH masses, using the former will blur out any trends obtained with Hβ_{BC} measures. FWHM C IV $\lambda1549_{BC}$–derived masses will yield much larger M_{BH} estimates for Population A and smaller values for Population B. If one prefers to avoid the Population A-B distinction then one will find smaller C IV $\lambda1549_{BC}$–Hβ_{BC} differences using the RQ-RL distinction perhaps encouraging the incorrect assumption that a simple correlation exists between the two sets of M_{BH} measures. The smaller difference between mean FWHM values has also caused some to conclude that RQ and RL sources have similar M_{BH} distributions and mean values. Even if FWHM(C IV $\lambda1549_{BC}$) could be measured with equal accuracy and confidence about viriality, like FWHM(Hβ_{BC}), it would be a less useful M_{BH} estimator, because it shows less dispersion. The main source of disagreements about M_{BH} similarities and differences among AGN samples involves Population B RQ sources. Combining them with narrower lined RQ sources will raise the mean value of M_{BH} for that population with only a small effect on the RL results. It will tend to equalize the means.

Estimates of M_{BH} were obtained from the UV flux density and FWHM C IV $\lambda1549_{BC}$ reported in Table 2, as well as for the corresponding data from Baskin & Laor (2005, their Table 1), assuming Hubble constant $H_0 = 70$ km s^{-1} Mpc^{-1} and relative energy density $\Omega_\Lambda = 0.7$ and $\Omega_M = 0.3$. Values of M_{BH} were derived following the latest normalization of Vestergaard & Peterson (2006) which uses the same cosmological parameters. The top panel of Figure 6 compares C IV λ1549–based M_{BH} estimates of Baskin & Laor (2005; based on slightly C IV $\lambda1549_{NC}$–corrected C IV λ1549 measures) with the NC-corrected estimates derived from this paper. We see that Baskin & Laor (2005) measures are systematically low and that the difference from our results increase with M_{BH}. This comparison involves only sources in common between the two studies and involves only a 2 dex range in M_{BH}. The differences between our measures and completely uncorrected C IV λ1549 profiles will be larger. We note that both Population A and B sources show this disagreement. The middle panel of Figure 6 compares M_{BH} measures based on FWHM C IV $\lambda1549_{BC}$ and Hβ_{BC}. We show the ratio of C IV $\lambda1549_{BC}$/Hβ_{BC}–derived M_{BH} measures as a function of Hβ_{BC}–derived M_{BH}. The Hβ_{BC} and continuum flux density measures come from Marziani et al. (2003a). The latest normalization of Vestergaard & Peterson (2006) was applied to these data, too.

We suggest a corrected FWHM(Hβ_{BC}) measure [reduced by a fraction dependent on FWHM(Hβ_{BC})] as likely to be the most reliable virial estimator for reasons described in Sulentic et al. (2006a). The middle panel of Figure 6 suggests that (NC-corrected) C IV λ1549–based M_{BH} estimates for Population B sources are more consistent with ones computed from the corrected Hβ_{BC} width. However, the scatter is large and our C IV λ1549 regression line is 0.2 dex higher than for M_{BH} derived from Hβ_{BC}. The most serious disagreement involves Population A sources ($\approx$60% of RQ sources) which show a trend where the M_{BH} ratio increases with decreasing M_{BH}. This does not allow one to easily correct C IV λ1549–computed M_{BH} to Hβ_{BC} values unless information on the optical spectrum (rest-frame and Hβ_{BC} line width) is available. We made several attempts to deduce a correction for C IV λ1549–derived M_{BH} values from properties intrinsic to the C IV λ1549 profile shape (i.e., width, asymmetry, and kurtosis) but were unable to find an effective relationship. Perhaps the most effective relationship we found involves the one shown in the bottom panel of Figure 6, which shows that the ratio of M_{BH} derived from C IV λ1549, and Hβ_{BC} is loosely correlated with W(C IV $\lambda1549_{BC}$) [for W(C IV $\lambda1549_{NC}$) $\lesssim$ 100 Å]. C IV $\lambda1549_{BC}$ and Hβ_{BC} estimates of M_{BH} show better agreement for larger values of W(C IV $\lambda1549_{BC}$). Caution is advised because equivalent width measures may be affected by continuum reddening. We also suffer from a relatively small sample of sources with W(C IV $\lambda1549_{BC}$) $\gtrsim$ 100 Å. Our fears about C IV λ1549–derived estimates for M_{BH} have motivated us to pursue Hβ to the highest possible redshift, and we have recently presented Hβ_{BC}-derived M_{BH} estimates out to $z \approx 2.5$ (Sulentic et al. 2004 2006a).

If NLR C IV λ1549 follows [O III] λ5007, then we expect the strongest and most frequent C IV λ1549 NLR to affect Population B sources. Uncorrected C IV λ1549 profiles in Population B sources will then be measured with systematically narrow FWHM C IV λ1549. Using this measure for M_{BH} estimation will result in systematic underestimation. This explains why many previous studies found little or no difference in M_{BH} estimates for RQ and

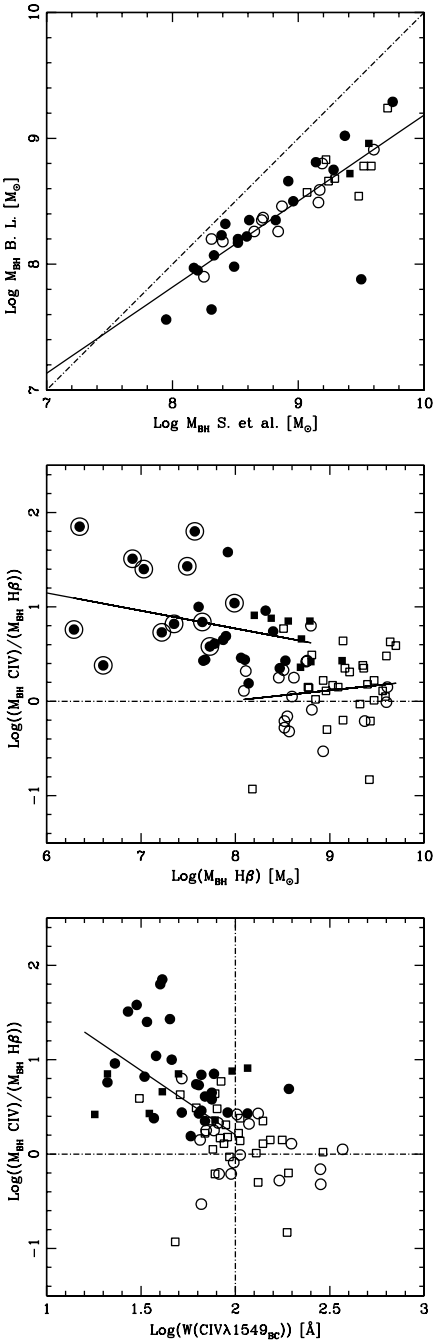

FIG. 6.—*Top*: Comparison of our log M_{BH} estimates for sources in common with Baskin & Laor (2005). "Virial" velocity values derived from FWHM C IV $\lambda1549_{BC}$ measures in both samples. Dot-dashed line indicates the parity line. The thin line shows an unweighted least-squares best fit for all sources. *Middle*: Log ratio of M_{BH} estimated from C IV $\lambda1549$ and "corrected" Hβ_{BC} (see text in § 5) vs. log M_{BH} for sources in common with Marziani et al. (2003a). Thin lines show independent best fits (unweighted least-squares) for Population A and B sources. NLSy1 sources are identified among Population A sources by a larger open circle. *Bottom*: Log ratio of M_{BH} estimated from C IV $\lambda1549$ and "corrected" Hβ as in panel above vs. log W(C IV $\lambda1549_{BC}$). Thin line shows a best fit (unweighted least-squares) for all sources with log W(C IV $\lambda1549_{BC}$) < 2.49

RL sources in direct contradiction with derivations based on FWHM Hβ_{BC}. The overall tendency will be to push both ends toward the center, thus reducing the dispersion of M_{BH} derived from uncorrected M_{BH} (see also discussion in Baskin & Laor 2005). M_{BH} underestimates for many sources, especially RL, which tend to be overluminous in an optically selected sample (e.g., BG92), will yield spuriously high L_{bol}/L_{Edd} values (e.g., Warner et al. 2004) for Population B. The insidious effect of uncorrected C IV $\lambda1549$ measures is that it will tend to mix sources of very different empirical and physical properties. The correlation between FWHM C IV $\lambda1549$ and L_{bol}/L_{Edd} (Warner et al. 2004, Fig. 5) is almost certainly driven by biases resulting from use of uncorrected C IV $\lambda1549$ measures.

6. CONCLUSIONS

AGNs are widely compared and contrasted in two ways: (1) RQ versus RL and (2) NLSy1 versus broad-line Seyferts/quasars. We suggest an alternate approach that unites both of these distinctions and that is supported by differences in C IV $\lambda1549$ line measures. We find that sources above and below FWHM H$\beta_{BC} \approx$ 4000 km s^{-1} show the most significant spectroscopic (and broadband) differences. RL sources lie largely above this limit, while NLSy1 lie below it. We find that all or most sources below 4000 km s^{-1} show properties similar to NLSy1s. Figure 2 (*top left*) in this paper particularly reenforces this similarity by showing that almost all sources with FWHM H$\beta_{BC} \lesssim$ 4000 km s^{-1} show a systematic C IV $\lambda1549$ blueshift. Our Population A-B concept simply reflects a unification where Population A sources show NLSy1-like properties and Population B sources show RL-like properties.

This paper addresses two thorny problems involving C IV $\lambda1549$ measures and their interpretation: (1) when and how to correct C IV $\lambda1549$ for NLR contamination and (2) whether C IV $\lambda1549$ measures support previous claims, based on optical spectra (and radio loudness), for two populations (A + B) of broad-line AGNs. The second result actually clarifies the answer to the first problem. Evidence is now ubiquitous at both high and low redshift for significant C IV $\lambda1549$ NLR emission in many sources. If we used [O III] $\lambda5007$ as a line template, then we would find fewer C IV $\lambda1549_{NC}$ components and those found would be narrower and weaker (i.e., lower EW). In several cases we find such an [O III] $\lambda5007$–like component but in many sources our inferred C IV $\lambda1549_{NC}$ component is broader and hence stronger. We argue that empirical evidence (e.g., inflections in some sources and broader C IV $\lambda1549_{NC}$ in type 2 AGNs) as well as simple models support our hypothesis that C IV $\lambda1549_{NC}$ is often not "[O III] $\lambda5007$–like."

We argue that correlations found without NLR correction are very often spurious while real correlations (Figs. 2 and 3) require NLR correction to be seen clearly. We propose a simple recipe for C IV $\lambda1549$ NLR correction. C IV $\lambda1549$ proves to be a valuable 4DE1 space discriminator that provides evidence in support of our two population hypothesis in the sense that the C IV $\lambda1549$ blueshift is ubiquitous only in previously defined Population A sources. These results have strong implications for any attempt to use C IV $\lambda1549$ measures for black hole mass (and L_{bol}/L_{Edd}) estimation. We suggest that any use of C IV $\lambda1549$ line measures can be facilitated by interpreting them within the 4DE1 + Population A-B context.

We thank the referee for thorough readings of the manuscript. D. D. acknowledges support from grant IN100703 PAPIIT UNAM.

This research has made use of the NASA/IPAC Extragalactic Database (NED), which is operated by the Jet Propulsion Laboratory, California Institute of Technology, under contract with NASA. Funding for the SDSS and SDSS-II has been provided by the Alfred P. Sloan Foundation, the participating institutions, the National Science Foundation, the US Department of Energy, the National Aeronautics and Space Administration, the Japanese Monbukagakusho, the Max Planck Society, and the Higher Education Funding Council for England. The SDSS is managed by the Astrophysical Research Consortium for the participating institutions. The participating institutions are the American Museum of Natural History, Astrophysical Institute Potsdam, University of Basel, University of Cambridge, Case Western Reserve University, University of Chicago, Drexel University, Fermilab, the Institute for Advanced Study, the Japan Participation Group, the Johns Hopkins University, the Joint Institute for Nuclear Astrophysics, the Kavli Institute for Particle Astrophysics and Cosmology, the Korean Scientist Group, the Chinese Academy of Sciences (LAMOST), Los Alamos National Laboratory, the Max Planck Institute for Astronomy (MPIA), the Max Planck Institute for Astrophysics (MPA), New Mexico State University, Ohio State University, University of Pittsburgh, University of Portsmouth, Princeton University, the United States Naval Observatory, and University of Washington.

APPENDIX

NOTES ON INDIVIDUAL OBJECTS

Most sources follow the 4DE1 trends described here and in previous papers. However, a few sources appear to be genuinely pathological. We mention a couple of such sources that appear as outliers in 4DE1 space and that are particularly relevant to the discussion involving C IV λ1549 measures.

3C 57.—$c(\frac{1}{2})$ C IV λ1549 and $R_{\rm Fe\,II}$ parameters typical of a Population A (even extreme Population A, NLSy1s) source [$c(\frac{1}{2}) = -1605$ km s^{-1}; $R_{\rm Fe\,II} \approx 1.25$]. The W(C IV λ1549) and profile shape are also typical of Population A (even similar to the ones of I Zw 1). At the same time it is RL, shows no soft X-ray excess, and FWHM(H$\beta_{\rm BC}$) $\approx$ 4700 km s^{-1}, all consistent with Population B.

PG 0026+126.—This quasar is moderate RQ Population A, following the current 4DE1 empiricism, because FWHM(H$\beta_{\rm BC}$) $\approx$ 2400 km s^{-1} and $R_{\rm Fe\,II} \approx 0.28$. There are two possible interpretations of the C IV λ1549 profile: (1) FWHM C IV λ1549 $\approx$ 1860 km s^{-1} and $c(\frac{1}{2}) = +140$ km s^{-1} if the strong narrow peak is *not* subtracted or (2) FWHM C IV λ1549 $\approx$ 7000 km s^{-1} and $c(\frac{1}{2}) \sim -1000$ km s^{-1} if the narrow peak is subtracted as a NLR component. This last approach seems especially appropriate, since FWHM of the C IV λ1549 narrow core only slightly exceeds (10%–20%) FWHM([O III] λ5007). The source is a FWHM C IV λ1549 "outlier," whichever C IV λ1549 measure is adopted, either unusually narrow or unusually broad (see Fig. 3). $R_{\rm Fe\,II}$ and $\Gamma_{\rm soft}$ measures are intermediate for the source and therefore unconstraining. Note that an erroneous rest frame is often assumed for this source (Gelderman & Whittle 1994). The most accurate redshift for the source corresponds to the centroid of the narrow component which is consistent with the NLR interpretation. This also yields a modest blueshift for the broader component which is also unconstraining. The strong profile inflection and small FWHM for the unshifted narrow component lead us to subtract it as NLR emission. RQ sources like NGC 4253 and 4395 show similar NLR-strong profiles.

PKS 1252+119.—Is the highest-z quasar in our sample. Hβ is consequently located at the edge of an excellent SDSS spectrum, making measures of FWHM(H$\beta_{\rm BC}$) uncertain. The reported $R_{\rm Fe\,II}$ is the only upper limit in our sample (marked with an arrow in our Fig. 2). This source may be located in an area of the 4DE1 optical plane where other core-dominated RL sources are found (Fig. 1 of Sulentic et al. 2003), but confirmatory optical data are needed.

REFERENCES

Allen, D. A., Norris, R. P., Meadows, V. S., & Roche, P. F. 1991, MNRAS, 248, 528
Bachev, R., Marziani, P., Sulentic, J. W., Dultzin-Hacyan, D., & Calvani, M. 2004, ApJ, 617, 171
Baldwin, J., Ferland, G., Korista, K., & Verner, D. 1995, ApJ, 455, L119
Barger, A. J., Cowie, L. L., Brandt, W. N., Capak, P., Garmire, G. P., Hornschemeier, A. E., Steffen, A. T., & Wehner, E. H. 2002, AJ, 124, 1839
Baskin, A., & Laor, A. 2004, MNRAS, 350, L31
———. 2005, MNRAS, 356, 1029
Boller, T. 2004, Prog. Theor. Phys. Suppl., 155, 217
Boroson, T. A. 2002, ApJ, 565, 78
Boroson, T. A., & Green, R. F. 1992, ApJS, 80, 109 (BG92)
Bottorff, M., et al. 1997, ApJ, 479, 200
Brotherton, M. S. 1996, ApJS, 102, 1
Brotherton, M. S., & Francis, P. J. 1999, in ASP Conf. Ser. 162, Quasars and Cosmology, ed. G. Ferland & J. Baldwin (San Francisco: ASP), 395
Brotherton, M. S., Wills, B. J., Francis, P. J., & Steidel, C. C. 1994, ApJ, 430, 495
Cirasuolo, M., Celotti, A., Magliocchetti, M., & Danese, L. 2003, MNRAS, 346, 447
Collin, S., Kawaguchi, T., Peterson, B. M., & Vestergaard, M. 2006, A&A, 456, 75
Contini, M., & Viegas, S. M. 2001, ApJS, 132, 211
Corbin, M. R. 1991, ApJ, 371, L51
———. 1997, ApJS, 113, 245
Corbin, M. R., & Boroson, T. 1996, ApJS, 107, 69
Dawson, S., Stern, D., Bunker, A. J., Spinrad, H., & Dey, A. 2001, AJ, 122, 598
Eracleous, M., & Halpern, J. P. 2004, ApJS, 150, 181
Foltz, C. B., Chaffee, F. H., Hewett, P. C., Weymann, R., Anderson, S. F., MacAlpine, G. M. 1989, AJ, 98, 1959
Gelderman, R., & Whittle, M. 1994, ApJS, 91, 491
Giveon, U., Maoz, D., Kaspi, S., Netzer, H., & Smith, P. S. 1999, MNRAS, 306, 637
Grupe, D., Beuermann, K., Mannheim, K., & Thomas, H.-C. 1999, A&A, 350, 805 (G99)
Grupe, D., Thomas, H.-C., & Beuermann, K. 2001, A&A, 367, 470
Hewitt, A., & Burbidge, G. 1980, ApJS, 43, 57
———. 1989, A New Optical Catalog of QSO (Chicago: Univ. Chicago Press)
Jackson, N., & Browne, I. W. A. 1991, MNRAS, 250, 414
Jarvis, M. J., van Breukelen, C., & Wilman, R. J. 2005, MNRAS, 358, L11
Jiang, L., Fan, X., Ivezic, Z., Richards, G. T., Schneider, D. P., Strauss, M. A., & Kelly, B. C. 2007, ApJ, 656, 680
Kaspi, S., Smith, P. S., Netzer, H., et al. 2000, ApJ, 533, 631
Keel, W. C. 1996, ApJS, 106, 27
Kraemer, S. B., Crenshaw, D. M., Filippenko, A. V., & Peterson, B. M. 1998, ApJ, 499, 719
Kraemer, S. B., Wu, C.-C., Crenshaw, D. M., & Harrington, J. P. 1994, ApJ, 435, 171
Kuraszkiewicz, J. K., et al. 2002, ApJS, 143, 257
———. 2004, ApJS, 150, 165
Lynds, C. R. 1967, ApJ, 147, 837
Mainieri, V., et al. 2005, MNRAS, 356, 1571
Marziani, P., Dultzin-Hacyan, D., & Sulentic, J. W. 2006, in New Developments in Black Hole Research, ed. P. V. Kreitler (New York: Nova Science), 123
Marziani, P., Sulentic, J. W., Dultzin-Hacyan, D., Calvani, M., & Moles, M. 1996, ApJS, 104, 37 (M96)
Marziani, P., Sulentic, J. W., Zamanov, R., Calvani, M., Dultzin-Hacyan, D., Bachev, R., & Zwitter, T. 2003a, ApJS, 145, 199 (M03)

Marziani, P., Sulentic, J. W., Zwitter, T., Dultzin-Hacyan, D., & Calvani, M. 2001, ApJ, 558, 553
Marziani, P., Zamanov, R., Sulentic, J. W., & Calvani, M. 2003b, MNRAS, 345, 1133
Meiksin, A. 2006, MNRAS, 365, 833
Murray, N., Chiang, J., Grossman, S. A., & Voit, G. M. 1995, ApJ, 451, 498
Norman, C., et al. 2002, ApJ, 571, 218
Osterbrock, D. E., & Pogge, R. W. 1985, ApJ, 297, 166
Peterson, B. M., et al. 2004, ApJ, 613, 682
Proga, D., & Kallman, T. R. 2004, ApJ, 616, 688
Reichard, T. A., et al. 2003, AJ, 126, 2594
Savage, B. D., et al. 2000, ApJS, 129, 563
Schlegel, D. J., Finkbeiner, D. P., & Davis, M. 1998, ApJ, 500, 525
Severgnini, P., et al. 2006, A&A, 451, 859
Stern, D., et al. 2002, ApJ, 568, 71
Sulentic, J. W., Dultzin-Hacyan, D., Marziani, P., Bongardo, C., Braito, V., Zamanov, R., & Calvani, M. 2006b, Rev. Mex. AA, 42, 23
Sulentic, J. W., & Marziani, P. 1999, ApJ, 518, L9
Sulentic, J. W., Marziani, P., Zamanov, R., Bachev, R., Calvani, M., & Dultzin-Hacyan, D. 2002, ApJ, 566, L71
Sulentic, J. W., Marziani, P., Zwitter, T., Dultzin-Hacyan, D., & Calvani, M. 2000a, ApJ, 545, L15
Sulentic, J. W., Repetto, P., Stirpe, G. M., Marziani, P., Dultzin-Hacyan, D., & Calvani, M. 2006a, A&A, 456, 929
Sulentic, J. W., et al. 2000a, ApJ, 536, L5 (2000b)
———. 2000b, ARA&A, 38, 521 (2000c)
———. 2003, ApJ, 597, L17
———. 2004, A&A, 423, 121
Szokoly, G. P., et al. 2004, ApJS, 155, 271
Tadhunter, C. N., Morganti, R., di Serego-Alighieri, S., Fosbury, R. A. E., & Danziger, I. J. 1993, MNRAS, 263, 999
Turler, M., & Courvoisier, T. J.-L. 1998, A&A, 329, 863
Turner, T. J., George, I. M., Nandra, K., & Turcan, D. 1999, ApJ, 524, 667
Véron-Cetty, M.-P., Véron, P., & Gonçalves, A. C. 2001, A&A, 372, 730
Vestergaard, M. 2002, ApJ, 571, 733
Vestergaard, M., & Peterson, B. M. 2006, ApJ, 641, 689
Wang, T., et al. 1996, A&A, 309, 81
Warner, C., et al. 2004, ApJ, 608, 136
Wills, B. J., Laor, A., Brotherton, M. S., Wills, D., Wilkes, B. J., Ferland, G. J., & Shang, Z. 1999, ApJ, 515, L53
Wills, B. J., et al. 1993, ApJ, 415, 563
———. 1995, ApJ, 447, 139
Wisotzki, L., Christlieb, N., Bade, N., Beckmann, V., Köhler, T., Vanelle, C., & Reimers, D. 2000, A&A, 358, 77
Yuan, M. J. & Wills, B. J. 2003, ApJ, 593, L11
Zamanov, R., Marziani, P., Sulentic, J. W., Calvani, M., Dultzin-Hacyan, D., & Bachev, R. 2002, ApJ, 576, L9

Capítulo 3

Condiciones físicas de la Región de Líneas Anchas para Cuasares a $z < 1$ a lo largo del Eigenvector 1.

Del resultado del capítulo anterior, nos dimos cuenta de que en el estudio espectroscópico de los cuasares es muy importante la separación de las distintas componentes de una misma línea producidas en diversas regiones. En este capítulo hacemos un estudio comparativo de seis espectros de cuasares representativos de la secuencia del E1. Usamos la tarea *specfit* de IRAF (*Image Reduction and Analysis Facility*) para ajustar, cuando aplica, tres componentes a cada línea seleccionada: Hβ, MgIIλ2800, SiIII]λ1892, AlIIIλ1860, CIVλ1549, HeIIλ1640 y Lyα. La primera componente es la línea central ancha (BC), presente en todos los espectros de cuasares de tipo 1, que suponemos no tiene ningún corrimiento. Primero ajustamos el perfil de H$\beta_{\rm BC}$, lorentziano con FWHM $\leqslant$ 4000 km s^{-1} para la Población A y gaussiano con FWHM $>$ 4000 km s^{-1} para la B (para más detalle de la fenomenología de los perfiles de líneas véase Sulentic et al.2002) y para ajustar las otras seis líneas simplemente lo escalamos. La segunda componente está corrida al azul y se piensa está siendo emitida en un viento saliente. Esta componente es visible en las líneas de alta ionización, como por ejemplo CIVλ1549, en objetos de Población A.

La última componente es la muy ancha. Está corrida al rojo y es la menos entendida. Se encuentra en no más de la mitad de los cuasares, en su mayoría radio fuertes. Es así como podemos decir que el 4DE1, explicado ampliamente en el capítulo anterior, es muy útil en la unificación de la diversidad espectral de los cuasares de líneas anchas.

Trabajo publicado en *Monthly Notices of the Royal Astronomical Society*, Marziani et al. 2010, 409, 1033.

Monthly Notices
of the
ROYAL ASTRONOMICAL SOCIETY

Mon. Not. R. Astron. Soc. **409,** 1033–1048 (2010) doi:10.1111/j.1365-2966.2010.17357.x

Broad-line region physical conditions along the quasar eigenvector 1 sequence

P. Marziani,[1⋆] J. W. Sulentic,[2]† C. A. Negrete,[3] D. Dultzin,[3] S. Zamfir[4] and R. Bachev[5]

[1]*INAF, Osservatorio Astronomico di Padova, Vicolo dell' Osservatorio 5, IT 35122, Padova, Italy*
[2]*Instituto de Astrofísica de Andalucía (CSIC), C/ Camino Bajo de Huétor 50, 18008 Granada, Spain*
[3]*Instituto de Astronomía, Universidad Nacional Autónoma de México, DF 04510, Mexico*
[4]*Department of Physics & Astronomy, University of Alabama, Tuscaloosa, AL 35487, USA*
[5]*Institute of Astronomy, Bulgarian Academy of Sciences, 72 Tsarighradsko Shousse Blvd., 1784 Sofia, Bulgaria*

Accepted 2010 July 13. Received 2010 July 13; in original form 2010 April 29

ABSTRACT

We compare broad emission-line profiles and estimate line ratios for all major emission lines between Lyα and Hβ in a sample of six quasars. The sources were chosen with two criteria in mind: the existence of high-quality optical and ultraviolet spectra and the possibility of sampling the spectroscopic diversity in the 4D eigenvector 1 (4DE1) context. In the latter sense, each source occupies a region (bin) in the full width at half-maximum (FWHM)(Hβ) versus Fe II$_{\rm opt}$ strength plane that is significantly different from the others. High signal-to-noise ratio Hβ emission-line profiles are used as templates for modelling the other lines (Lyα, C IVλ1549, He IIλ1640, Al IIIλ1860, Si III]λ1892 and Mg IIλ2800). We can adequately model all broad lines assuming the existence of three components distinguished by blueshifted, unshifted and redshifted centroids [indicated as a blue component (BLUE), broad component (BC) and very broad component (VBC), respectively]. BC (electron density $n_{\rm e} \sim 10^{12}$ cm^{-3}, ionization parameter $U \sim 10^{-2}$ and column density $N_{\rm c} \gtrsim 10^{23}$ cm^{-2}) is present in almost all type-1 quasars and therefore corresponds most closely to the classical broad-line emitting region (the reverberating component). The bulk of Mg IIλ2800 and Fe II emission also arises in this region. The BLUE emission ($\log n_{\rm e} \sim 10$, $\log U \sim -1$ and $\log N_{\rm c} < 23$) arises in less optically thick gas; it is often thought to arise in an accretion disc wind. The least understood component involves the VBC (high ionization and large column density), which is found in no more than half (but almost all radio-loud) type-1 quasars and luminous Seyfert nuclei. It is perhaps the most distinguishing characteristic of quasars with FWHM (Hβ) $\gtrsim$ 4000 km s^{-1} that belong to the so-called population B of our 4DE1 space. Population A quasars [FWHM (Hβ) $\lesssim$ 4000 km s^{-1}] are dominated by BC emission in Hβ and BLUE component emission in C IVλ1549 and other high ionization lines. 4DE1 appears to be the most useful current context for revealing and unifying spectral diversity in type-1 quasars.

Key words: line: formation – line: profiles – galaxies: quasars – quasars: general – galaxies: Seyfert – quasars: individual: I Zw 1 – quasars: individual: Mrk 478 – quasars: individual: Mrk 335 – quasars: individual: Fairall 9 – quasars: individual: 3C 249.1 – quasars: individual: 3C 110.

1 INTRODUCTION

1.1 Diversity of quasar spectra

Quasar spectra are not self-similar even if we restrict ourselves to active galactic nuclei (AGN) that show broad emission lines (type-1 AGN). Examination of the same broad emission line in many different sources reveals a striking diversity. This diversity begins with the profile width but extends to every other measurable property [e.g. shape, line shift, equivalent width (EW)]. The H I Balmer line Hβ is a good place to start a line profile characterization because a lot of data exist on this line. It can be observed from the ground out to $z \sim 0.9$ and through numerous infrared (IR) windows to $z \gtrsim 3$. Thus, one can compare the line over a wide range of redshifts and source luminosities. It is usually a strong line and suffers only moderate

⋆E-mail: paola.marziani@oapd.inaf.it
†Professor Emeritus at the University of Alabama.

© 2010 The Authors. Journal compilation © 2010 RAS

contamination falling in a gap between strong optical Fe II blends. At this time, good signal-to-noise ratio (S/N) and moderate resolution spectra exist for more than 600 low-*z* sources [including the brightest ≈400 Sloan Digital Sky Survey (SDSS) quasars; Marziani et al. 1996, 2003b; Zamfir, Sulentic & Marziani 2008; Zamfir et al. 2010]. Table 2 in Sulentic, Marziani & Dultzin-Hacyan (2000a) shows earlier references with high S/N spectra. Comparable quality IR spectra of the Hβ region now exist for more than 50 sources in the range $z = 0.9$–3.1 (Sulentic et al. 2004, 2006; Marziani et al. 2009).

The C IV line at λ1549 is the other current broad line of choice providing a high ionization line (HIL) counterpoint to low ionization line (LIL) Hβ. High-quality C IVλ1549 spectra for low-*z* sources are more difficult to obtain with the *Hubble Space Telescope* (*HST*) archive providing ultraviolet (UV) spectra of the C IVλ1549 region for ∼130 sources (Bachev et al. 2004). Above $z \sim 1.5$, C IVλ1549 is accessible at optical wavelengths out to $z \sim 4.8$. The largest compilation of high-quality and high-*z* C IVλ1549 spectra came from the Palomar surveys almost 20 yr ago (Young, Sargent & Boksenberg 1982; Sargent, Steidel & Boksenberg 1989; Barthel, Tytler & Thomson 1990). A uniform study of the Palomar and other good quality HIL spectra can be found in Tytler & Fan (1992). Unfortunately, most of sources with good Hβ spectra lack a corresponding C IVλ1549 spectrum and vice versa. Many of the other broad lines have been studied individually without the coverage of other broad lines in the same source. A fundamental desideratum involves strong narrow lines that provide a reliable determination of the quasar rest frame (e.g. [O III]$\lambda\lambda$4959, 5007 and especially [O II]λ3727). Full exploitation of the Palomar spectra is impeded by the lack of rest-frame determinations for the sources and the lack of matching Hβ spectra.

Broad-line profiles provide some of the most direct clues about the nature, structure and kinematics of the central regions in quasars. Interline profile comparisons for individual sources [Seyfert 1 nuclei as well as radio-quiet (RQ) and radio-loud (RL) quasars] have been carried out for a long time although there has been little agreement on the systematics (Gaskell 1982; Wilkes 1986; Espey et al. 1989; Corbin 1990; Carswell et al. 1991; Tytler & Fan 1992; Marziani et al. 1996; Richards et al. 2002). Most of these studies have sampled (i) small numbers of sources, (ii) only a few of the broad lines in each source and/or (iii) specks of less than ideal S/N (see Shang et al. 2007 for a notable exception). If we consider the best-studied HIL and LIL features (C IVλ1549 and Hβ), we find little evidence for profile (shape/shift/EW) similarity for sources with full width at half-maximum (FWHM)(Hβ) $\lesssim$ 4000 km s^{-1} while above this value the profiles appear to be more similar, after proper correction for narrow-line C IVλ1549 emission is made (Marziani et al. 1996; Sulentic & Marziani 1999; Bachev et al. 2004; Sulentic et al. 2007). Ideally, we would like to have spectral coverage for all of the principal broad lines in each sample of sources that reflect the impressive source-to-source diversity now known. It would also be ideal if we could achieve a consensus on how many distinct components each line contains. This paper will address both of these desiderata.

1.2 Eigenvectors of quasars

We are never satisfied with the S/N and resolution of the available quasar spectra even though the current best data exceed our ability to explain them theoretically. The minimum acceptable values for good spectra are arguably 20–30 in the continuum and $\lambda/\Delta\lambda \sim 1000$. We are tempted to indiscriminately average line profiles in order to improve even more the S/N, but a composite spectrum generated from a large sample obscures most of the important astrophysical information. Such composite spectra have a heuristic value since they provide a wide spectral coverage and give a global view of the continuum shape (Vanden Berk et al. 2001). Different lines represent averages of different sources making comparison impossible unless all quasar spectra are fundamentally similar. In the context of broad-line physics, indiscriminate averaging obscures rather than revealing profile differences. It is the 'why' of differences that yields physical insight. Not only do quasar spectra show significant diversity, but measured line parameters do not scatter symmetrically around an average. Eigenvector analysis showed that the diversity of optical and UV spectra is not entirely random but that there are systematic trends (Boroson & Green 1992; Sulentic et al. 2000c). We expanded the original optically based eigenvector 1 parameters to include C IVλ1549 and soft X-ray photon index (see also Wang, Brinkmann & Bergeron 1996) in an effort to enhance our ability to identify profile differences (4D eigenvector 1 ≡ 4DE1; Sulentic et al. 2000a,c, 2007). As examples of the lack of symmetric scatter, we note that sources occupy well-defined non-random sequences in e.g. FWHM(Hβ) versus normalized Fe IIλ4570 strength (see Fig. 1) or versus normalized C IVλ1549 line shift (fig. 2d in Sulentic et al. 2007).

Profile diversity persists when composite spectra are generated in some fundamental context like 4DE1. For example, sources in a restricted region of the 2D parameter space involving FWHM (Hβ) and Fe II$_{\rm opt}$ strength measures show considerable profile diversity (Fig. 1 which is the optical plane of 4DE1). The composite spectrum for sources in a restricted region (bin) presumably reveals the underlying 'stable' emission component(s). The source-to-source diversity within a bin likely reflects minor changes in profile shape connected with profile variability. The bin-to-bin diversity in a contextual space like 4DE1 has the greatest potential to yield clues about broad-line region (BLR) structure and kinematics (convolved with source orientation). Contexts for such binned profile composites can be empirical (e.g. FWHM, Fe II strength) or physical [e.g. black hole (BH) mass $M_{\rm BH}$, Eddington ratio $L_{\rm bol}/L_{\rm Edd}$]. A comparison between e.g. RQ and RL quasars will yield any result that one desires unless the empirical context for profile binning is carefully chosen and is independent of radio properties.

1.3 How many broad-line components?

We would like to compare all principal broad lines in a small sample of sources that reflect the diversity found in the 4DE1 binning. At present, however, adequate multiwavelength data exist for very few sources so studies encompassing all the principal broad lines are rare (e.g. Shang et al. 2007). The most basic question for facilitating such a study involves how many components one can identify in each broad line. This is particularly important for studies that use the widths of broad lines as virial estimators. Empirical studies have made it clear that HIL (e.g. C IVλ1549) and LIL (e.g. Balmer series) show a wide range of strength, shape and shift properties. Our own work in the 4DE1 context has attempted to systematize these properties (Sulentic et al. 2000a, 2007; Marziani et al. 2001, 2003b,c; Marziani, Sulentic & Dultzin 2008) with focus being so far on comparisons of C IVλ1549 and Hβ assumed to be typical HIL and LIL features.

Several authors have considered the degree of stratification that might exist in the BLR including the idea that the innermost part

© 2010 The Authors. Journal compilation © 2010 RAS, MNRAS **409,** 1033–1048

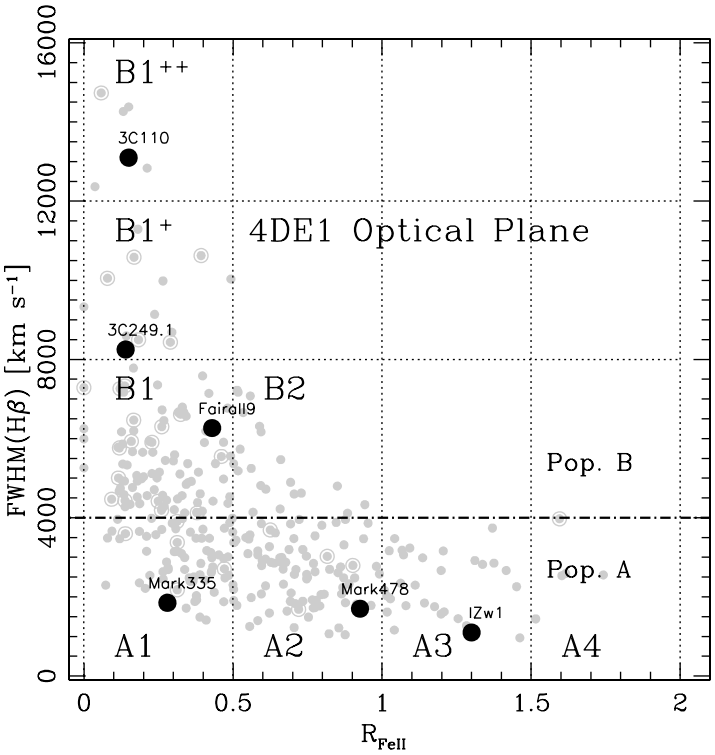

Figure 1. Optical plane of the 4DE1 parameter space, i.e. FWHM(Hβ) versus $R_{\rm Fe\,II}$. $R_{\rm Fe\,II}$ measures the prominence of Fe IIλ4570 with respect to Hβ (see the text for definition). Occupied spectral bins are labelled. Grey dots are from the sample of Zamfir et al. (2008). Large black spots mark the position of the six sources considered in this study.

of the BLR could be emitted in a quasi-distinct very broad-line region (VBLR). The VBLR concept may have originated with the discovery that the core and wings of HIL He IIλ4686 and LIL Hβ in highly reverberated NGC 5548 show different responses to continuum change (Peterson & Ferland 1986). The VBLR concept and/or terminology arose in several additional guises, and this has led to some confusion. Is the very broad component (VBC) present in all quasars? Are there equal numbers of blueshifted and redshifted VBCs (see e.g. Corbin 1995)? Is there no significant narrow emission-line component in C IVλ1549? If one rejects a significant C IVλ1549 narrow component, the 'peakiness' of the C IVλ1549 profile in many sources suggests both narrow intermediate-line region (ILR) and VBLR as the simplest C IVλ1549 profile model (Brotherton et al. 1994). We think that the answer to all of these questions is 'no' (see e.g. Marziani et al. 1996; Sulentic & Marziani 1999; Sulentic et al. 2002, 2007). Our studies show evidence for a VBC *only* in sources with FWHM(Hβ) $\gtrsim$ 4000 km s^{-1} (population B; Sulentic et al. 2000a,c; Marziani et al. 2003c; Zamfir et al. 2010). The Hβ profile in these sources requires both unshifted Gaussian [broad component (BC)] and redshifted VBC components. Narrower [FWHM (Hβ) $\lesssim$ 4000 km s^{-1}] population A sources can often be fitted with a simple Lorentz-like function although a blue asymmetry is seen in the Hβ profiles of some population A sources. Whether FWHM H$\beta \approx$ 4000 km s^{-1} signifies a fundamental change in BLR physics (e.g. critical Eddington ratio) or not, the highly significant changes in profile shape above and below this value cannot be ignored.

1.4 Defining an empirical approach

This paper compares all of the principal broad lines (Lyα, C IVλ1549, C III]λ1909, Mg IIλ2800, Hβ) for a sample of sources where (1) suitably high S/N spectra are available for all or most of the principal broad lines and (2) 4DE1 spectroscopic diversity is sampled. Our approach is empirical and uses the Hβ profile fit for each chosen source to constrain the fits of all other broad lines in that source. High- and low-redshift population B quasars show rather symmetric Lyα and C IVλ1549 profiles (Barthel et al. 1990; Bachev et al. 2004) which is in sharp contrast to the appearance of Hβ in population B sources where a red asymmetry is common. In population A, the situation is reversed with blue asymmetric Lyα and C IVλ1549 and symmetric Balmer line profiles. Comparisons of Hβ and C IVλ1549 profiles suggest that the following three emission components are present in some or all sources.

(i) A 'classical' BC (FWHM = 600–5000 km s^{-1}). The Hβ profile is best modelled with a symmetric Lorentzian function for population A sources (FWHM $<$ 4000 km s^{-1}) and a Gaussian function for population B (FWHM $>$ 4000 km s^{-1}). This component may be weak or, even, absent in some population B sources. The bulk of the optical Fe II emission appears to follow the BC (e.g. Marziani et al. 2003b).

(ii) A VBC (FWHM $\sim$ 10000 km s^{-1}). Hβ is reasonably well modelled with a Gaussian function. It is only observed in population B sources where it shows a redshift (FWHM in the range of

© 2010 The Authors. Journal compilation © 2010 RAS, MNRAS **409**, 1033–1048

Table 1. Selected sources.

IAU code	NED name	z	m_B	A_B	Sp. T.	Comments[a]
J00535+1241	UGC 00545	0.0605	14.4	0.28	A3	≡ I Zw 1, Hα
J14421+3526	Mrk 0478	0.0771	15.0	0.06	A2	
J00063+2012	Mrk 0335	0.0258	14.0	0.15	A1	RM, Hα
J01237−5848	Fairall 9	0.0462	13.5	0.12	B1	RM, Hα
J11042+7658	PG 1100+772	0.3116	15.7	0.15	B1^{+}	≡ 3C 249.1, no Mg II
J04172−0553	3C 110	0.7744	15.8	0.19	B1^{++}	No C III

[a]RM: reverberation mapping data; listed in Peterson et al. (2004).

1000–5000 km s^{-1}). This can be the dominant component in some population B sources.

(iii) BLUE (blueshifted component or blue asymmetric profile). This is seen in the Hβ profile of some population A sources with $R_{\rm Fe\,II} = {\rm I(Fe\,II\lambda 4570)/I(H}\beta) > 0.5$. It is more prominent in C IVλ1549 where it can be defined as the residual emission after subtraction of an unshifted Lorentzian BC in population A sources. In this paper, we model this component with a Gaussian.

If there is a semicoherent structure that gives rise to all or most of the broad-line emission, then all broad lines in a source should show similar properties allowing for some degree of stratification. Hβ apparently does not show the same components in all sources motivating the population A–B nomenclature (Sulentic et al. 2000a,c, 2007) as an effective way to highlight this difference. We assume that the distribution of sources in the optical plane of 4DE1 has a physical meaning in the sense that source occupation is driven by both physics and line-of-sight orientation. This assumption is reinforced by the discovery that sources in different regions of the optical plane (and especially population A and B regions) show differences in almost all other multiwavelength measures. The sources chosen for this study allow us to test the hypothesis that the same three components observed in Hβ and C IVλ1549 can account for the diverse line profiles of Lyα, C IVλ1549, He IIλ1640, Si III]λ1892, Al IIIλ1860, C III]λ1909, Mg IIλ2800, Hβ and Hα. After testing this hypothesis (Section 4.1), we measure line intensities of the components (Section 4.3). Analysis of the properties of each line component yields insights into differences in physical conditions of the three identified emitting regions (Section 4.4).

2 SOURCE SELECTION AND OBSERVATIONS

Sources were selected to be representative for the spectral diversity in the 4DE1 context. We selected six sources that include one quasar in each of the six most populated 4DE1 spectral bins (A1, A2, A3, B1, B1^{+} and B1^{++}; Sulentic et al. 2002). Fig. 1 marks the location of these sources in the optical plane relative to the distribution of the brightest 400+ SDSS DR5 quasars (Zamfir et al. 2010). We remark that the validity of the analysis presented in this paper is not restricted to six objects only. Each object has been chosen as representative of each bin in the E1 plane of Fig. 1. These bins are occupied by 90 per cent of low-z quasars (Zamfir et al. 2010). While high S/N and moderate resolution spectral coverage from Lyα to Hβ exists for very few quasars, we were fortunate to find representative sources for these six bins. UV coverage from Lyα to Mg IIλ2800 comes from the *HST* archive for these low-z sources save for 3C 110 where Mg IIλ2800 is covered in our optical spectrum. A list of the available *HST* spectra can be obtained at the *HST* archive. A list with the data sets actually employed to build the UV spectra can be obtained from the authors.[1] Optical spectra come from Marziani et al. (2003b); a log of observation can be easily retrieved from their table 2. UV and optical observations are generally not simultaneous, with a time mismatch of less than 3 yr in all cases save Mrk 478; in this last case, the UV observations were collected more than 5 yr after the optical ones.

We make use of composite spectra for each of these bins (Sulentic et al. 2002; Bachev et al. 2004; Zamfir et al. 2010) computed from the bright SDSS sample or from our spectroscopic atlas (Marziani et al. 2003b). The C III]λ1909 blend is unavailable for 3C 110 and the region of Mg IIλ2800 has not been observed in 3C 249. Hα spectra are only available for three sources. Our composite spectra are used as surrogates for these gaps in our source data.

Table 1 identifies the selected sources where Column 1 gives the IAU code name, Column 2 the common name recognizable by NASA/IPAC Extragalactic Database (NED), Column 3 the adopted redshift, Column 4 the B magnitude, Column 5 the Galactic B-band absorption from NED, Column 6 the spectral type following Sulentic et al. (2002) and Column 7 additional information. Two sources have been reverberation mapped (RM; Peterson et al. 2004). Galactic absorption values A_B are from Schlegel, Finkbeiner & Davis (1998); if $R_V = 3.1$, then $A_V \approx 0.756 A_B$. This value has been used with the task DEREDDEN of IRAF. No internal extinction correction was applied to our sources.

3 DATA ANALYSIS

Data used in this paper are wavelength and flux calibrated. Spectra and spectral measures were shifted to rest-frame wavelength and flux using the redshift listed in Table 1 after correction for Galactic extinction.

The regions around Lyα, C IVλ1549 (including He IIλ1640), the blend at ≈1900 Å (including Al IIIλ1860, Si III]λ1892, C III]λ1909), Mg IIλ2800, Hβ (including the Fe IIλ4570 blend) and Hα were analysed using the SPECFIT task of IRAF (Kriss 1994). We used an Fe II template based on a European Southern Observatory spectrum of I Zw 1 to correct for Fe II contamination. This template was already employed for data analysis in Marziani et al. (2003b,c) with improvements described in Marziani et al. (2009). It is basically the Boroson & Green (1992) template with two major modifications. First, the Fe II emission underlying Hβ was set according to a model simulation, due to the difficulty in distinguishing between Hβ proper and underlying Fe II$_{\rm opt}$ features (Marziani et al. 2009). Secondly, our spectrum shows a significant feature at 6446 Å in the red. In any case, the Fe II$_{\rm opt}$ correction in the red is so small that it would not affect any of our results concerning the Hα line shape. In the UV, Fe II emission around Mg IIλ2800, C III]λ1909 and C IVλ1549

[1] It is available at http://web.oapd.inaf.it/marziani/uvlog.pdf

© 2010 The Authors. Journal compilation © 2010 RAS, MNRAS **409,** 1033–1048

is corrected applying a template obtained from a CLOUDY (Ferland et al. 1998) simulation, assuming an ionization parameter of $10^{-2.25}$ and an electron density of $10^{12.25}$ cm^{-3}. Fe III emission, especially prominent around the 1900-Å line blend, was modelled using a template build following Vestergaard & Wilkes (2001). There is considerable uncertainty regarding the intensity of the Fe III feature at 1914 Å; this feature is heavily blended with C III]λ1909 making a reliable estimate of the intensity of both lines in population A sources impossible (i.e. in any case, the iron spectrum is strong).

The three previously described line components were simultaneously fitted along with a power-law continuum and appropriate Fe II (and Fe III around 1900 Å) template solution employing χ^2 minimization techniques. The relative intensity of the components was left free to vary although we imposed the condition that velocity shifts and widths roughly match those measured in Hβ and C IVλ1549 (BLUE only).

4 RESULTS

4.1 Multicomponent fits

Fig. 2 shows the resultant fits to the line profiles of Lyα, C IVλ1549+He IIλ1640, 1900-Å blend, Mg IIλ2800 and Hβ for each source. Hα is not included since it does not add information to the line profile interpretation based on Hβ. Residuals are shown below each panel. Table 2 reports the total flux in the C IVλ1549 line and the normalized intensity ratios of BC, VBC and BLUE; individual sources are discussed in Appendix A. The following results are consistent with trends visible in median composite spectra for the same bins (Sulentic et al. 2002; Bachev et al. 2004; Zamfir et al. 2010).

Broad component. The BC dominates LIL (Balmer lines, Fe II, Mg IIλ2800) emission in population A sources, while it becomes less prominent in population B. The fraction of BC Hβ flux decreases for population B sources from bin B1 to B1$^+$ and from B1$^+$ to B1^{++}. The 4DE1 sequence can be described as a sequence of decreasing Hβ BC prominence and may even involve BC demise. Evidence exists for AGN with a very weak or absent BC, some showing no emission lines (e.g. BL Lacs) or only narrow emission lines (type-2 AGN). Others more relevant to this study show lines with strong VBC emission that can be mistaken for a typical type-1 AGN (Sulentic et al. 2000b; e.g. PG 1416−129). We suspect that 3C 110 (also discussed in Appendix A) may be an example of this situation. Rather than the two-component BC+VBC fits shown in Figs 2 and 3, the correct interpretation for 3C 110 may involve a single redshifted VBC component. FWHM $\sim 10\,000$ km s^{-1} would be unprecedented for the BC.

In population A sources I Zw I and Mrk 478 C III]λ1909 is closely blended with Fe III emission leaving open the possibility that BC C III]λ1909 may be very weak or absent (for this reason, no C III]λ1909 ratios are reported in Table 3). Nearby, Al IIIλ1860 and Si III]λ1892 are also very prominent in these two population A sources. Conversely, bin A1 source Mrk 335 shows stronger C III]λ1909 emission and Al IIIλ1860 intensity more similar to population B sources.

BLUE. Fig. 3 provides the justification for including BLUE in the Fig. 2 fits by showing the residual that arises from a two-component fit to C IVλ1549 (BC+VBC) for all six sources. Population A sources show a strong residual reflecting the well-known BLUE/asymmetric component. BLUE is present in the Lyα and C IVλ1549 emission of all sources but 3C 110, with typical shifts and widths $\Delta v \sim -2000$ km s^{-1} and $\sim$7000 km s^{-1}, respectively. Population A and B sources show similar shift and width values. Only bin A3 source I Zw 1 may show a possible hint of this BLUE in the Hβ line. BLUE is not seen in Mg IIλ2800 while the 1900-Å blend is too complex to allow any conclusion to be made.

Very broad component. A VBC is one of the defining properties of the broad-line spectrum in population B sources. A VBC is not observed in NLSy1 or even less extreme population A quasars (see the cautionary note regarding very high-luminosity quasars; Marziani et al. 2009). Using Hβ as a template, we therefore fit only two components (BLUE + BC) in population A sources. The residuals of these fits show no excess flux on the red wing of Hβ that might be interpreted as a weak VBC signature. This reinforces the earlier proposed ideas that FWHM ≈ 4000 km s^{-1} reflects some fundamental change in the structure and/or kinematics of the line-emitting region – perhaps connected to a critical value of the Eddington ratio.

Restricting attention to our three population B sources that show a VBC, shifts and widths are $\sim$2000 and $\sim$10 000 km s^{-1}, respectively (3C 110 has two entries in Table 5: the second one refers to the assumption of no BC presence in the emission lines; see Appendix A). These values are consistent with those derived for median spectra of more than 150 population B sources in the SDSS bright sample (Zamfir et al. 2010). Using Hβ as the model we conclude that a VBC is also present in the C IVλ1549 profiles of Fairall 9 and 3C 249.1, giving rise to the extended red wings visible in Fig. 3. These profiles look deceptively symmetric, but both our empirical fits argue that C IVλ1549 counterparts to the Hβ VBC should be present.

4.2 The He IIλ1640 profile

The EW of He$^+$ lines is an eigenvector 2 parameter involving an apparent anticorrelation with source luminosity (Boroson & Green 1992). The He IIλ1640 profile of population B sources is customarily flat-topped and rather extended on the blue side. The profile can be interpreted as due to the sum of the same components observed in C IVλ1549. An unambiguous decomposition of the He IIλ1640+O III]λ1663 blend for population A sources is difficult. A fit of the He IIλ1640 + C IVλ1549 profile reproduces the shape of the entire blend assuming that He IIλ1640 is due to BLUE + BC. In population B sources, the analysis is even more complex because He IIλ1640 is blended with the red wing (VBC) of C IVλ1549. The presence of BLUE and VBC He IIλ1640 emission creates the apparent flat extension on the red side of C IVλ1549 that has not been satisfactorily explained as yet. This extension is visible in the spectra of several RL sources at both low and high redshift (Marziani et al. 1996; Barthel et al. 1990). This 'plateau' effect is especially well seen on the red side of C IVλ1549 in 3C 249.1 (Fig. 4) where the best fits for He IIλ1640 are obtained assuming the BLUE and VBC as for C IVλ1549 and Lyα. The same interpretation seems to apply to He IIλ4686: a good supporting case involves the low-luminosity quasar PG 138+22 (Marziani & Sulentic 1993).

4.3 Intensity ratios

Tables 3–5 provide flux ratios for the three line components in each of the six sources. The rest-frame EW for Lyα is reported for each emission component in the last column of each table. Ratios are reported with two significant digits to avoid roundoff errors. Uncertainties on ratios are estimated from the errors in the individual

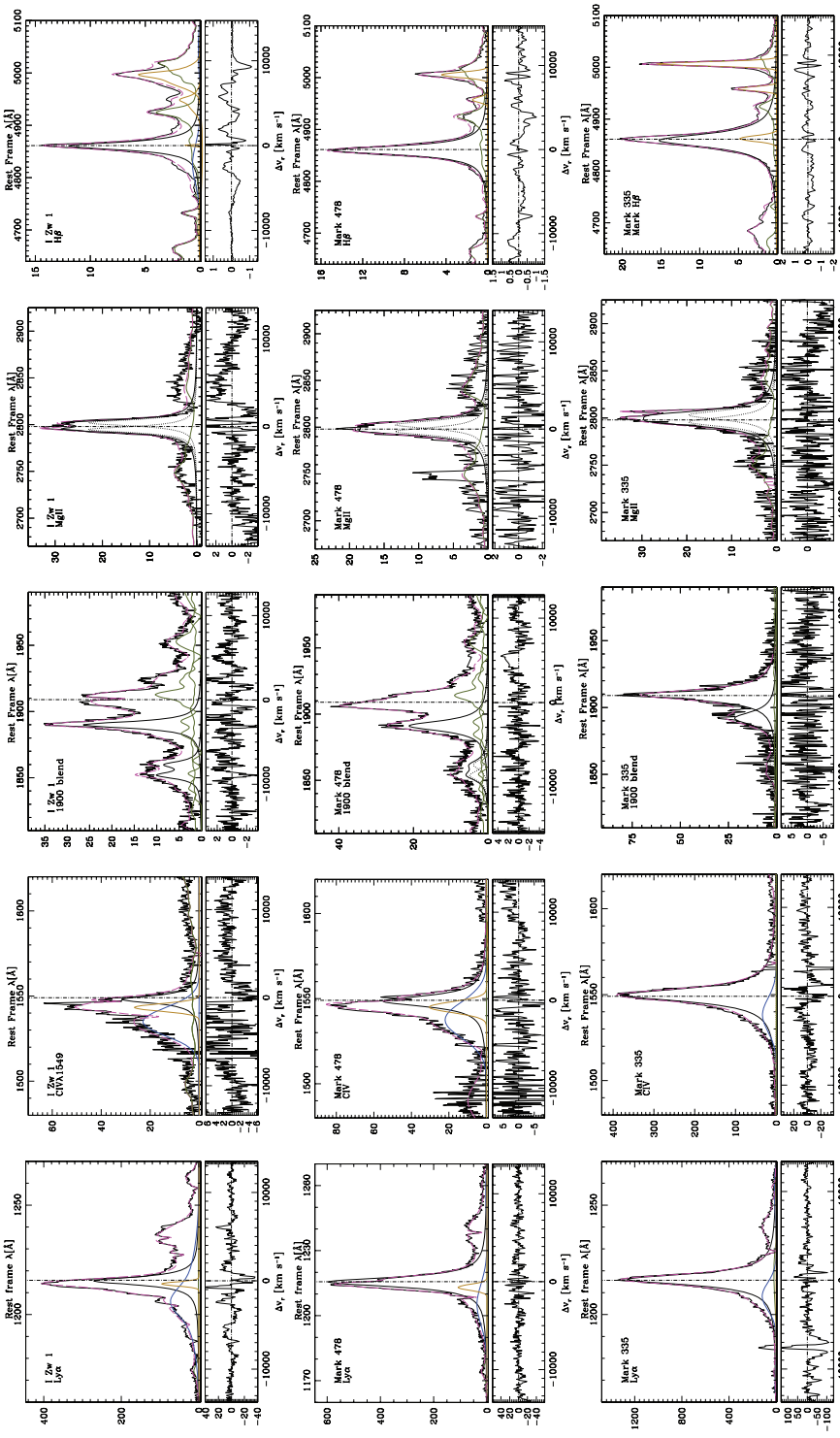

Figure 2. Multicomponent fits of the Lyα, C IVλ1549, 1900-Å, Mg IIλ2800, Hβ spectral regions for the six objects of this work ordered along the E1 sequence. All spectra are reduced to rest frame and continuum subtracted. The ordinate is specific flux in units of 10^{-15} erg s^{-1} cm^{-2} Å^{-1}. The lower part of each panel shows residuals as a function of radial velocity. Thin black line: continuum-subtracted rest-frame spectrum; thick dashed (magenta) line: multicomponent fit result. Thick continuous lines: BLUE (blue), BC (black) and VBC (red). Thin orange line: narrow-line components; thin dark green line: Fe II template emission. In the 1900 blend panel, the thick dark green line shows the adopted Fe III template. In the case of severe Fe III contamination, the C III]λ1909 line is not shown.

© 2010 The Authors. Journal compilation © 2010 RAS, MNRAS **409,** 1033–1048

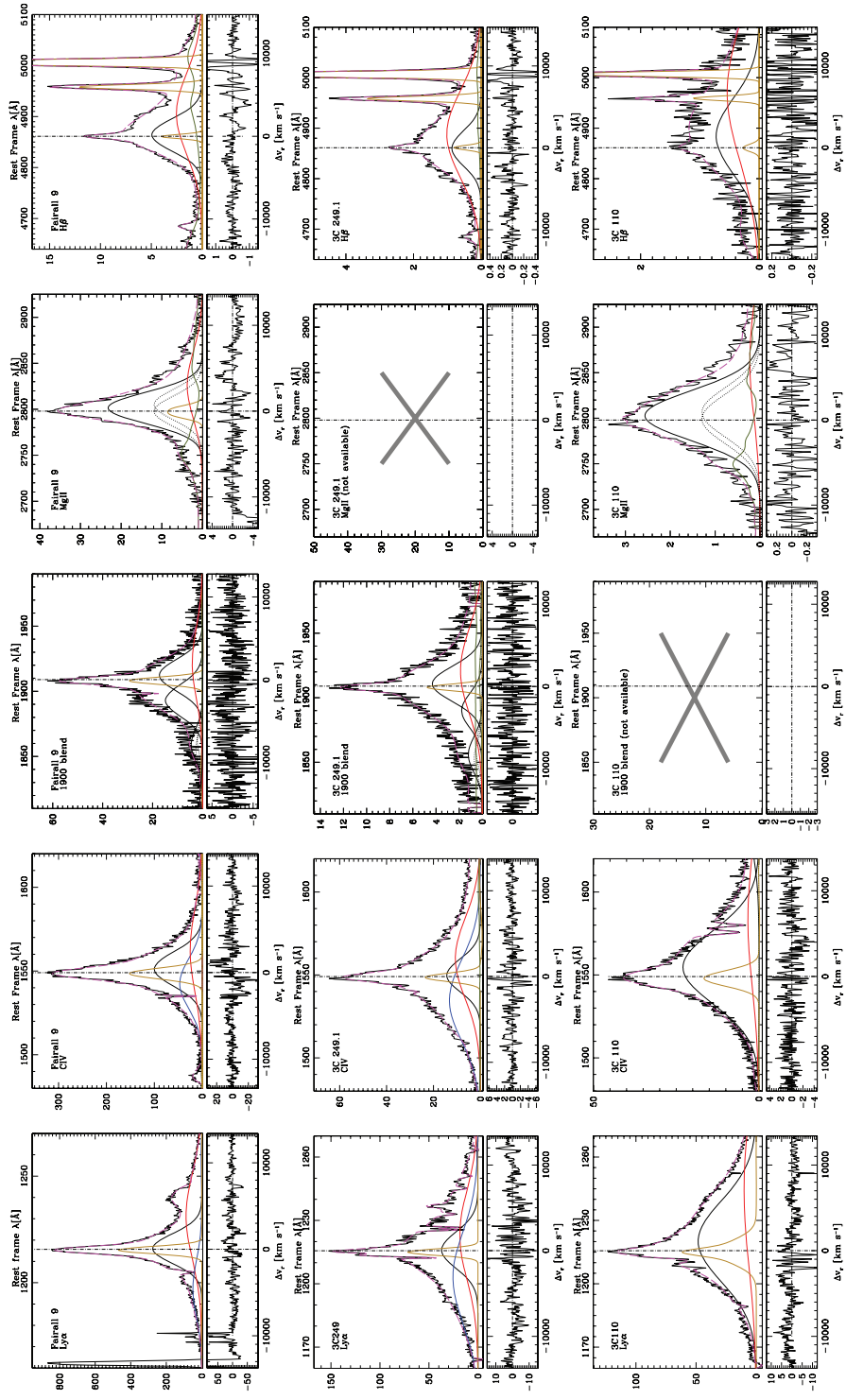

Figure 2 – *continued*

Table 2. Relative intensity of BLUE, BC and VBC in the C IVλ1549 line.

Sp. T.	Name	F(C IVλ1549)[a] (erg s^{-1} cm^{-2})	BC(C IV)/ F(C IV)	VBC(C IV)/ F(C IV)	BLUE(C IV)/ F(C IV)
A3	I Zw 1	0.74E−12	0.36	0.00	0.74
A2	Mrk 478	1.17E−12	0.61	0.00	0.39
A1	Mrk 335	6.31E−12	0.87	0.00	0.13
B1	F 9	5.84E−12	0.43	0.27	0.30
B1^{+}	3C 249.1	2.11E−12	0.17	0.31	0.38
B1^{++}	3C 110	1.60E−12	0.44	0.56	0.00
	3C 110[b]	1.60E−12	0.00	1.00	0.00

[a]F(C IV) = BLUE + BC + VBC.
[b]VBC only; see text for details.

component intensity which are typical ±20 per cent for the strongest components (those of Lyα and C IVλ1549, Mg IIλ2800 BC, Hβ BC in population A) or for individual or unblended features (Fe II) and ±50 per cent for the weakest or most blended features (He IIλ1640, Si III]λ1892, Mg IIλ2800 VBC). Applying simple error propagation yields, for the intensity ratio of two components, labelled 1 and 2, $\Delta(I_2/I_1) = (I_2/I_1)\sqrt{(\Delta I_1/I_1)^2 + (\Delta I_2/I_2)^2}$. For a typical error ≈40% on line intensity, the error on ratio is $\Delta(I_2/I_1) = 0.56(I_2/I_1)$.

BC. The 'classical' and almost ubiquitous broad-line component shows some line ratios that yield important constraints on the physical conditions: Lyα/Hβ ∼ 10 (see also Netzer et al. 1995), compared to an expectation of ∼35 for pure recombination; Mg IIλ2800/Lyα ≈ 0.1–0.3; relatively large $R_{\rm Fe\,II}$ ($\gtrsim$0.3). The Fe II/Hβ$_{\rm BC}$ values assume that all or most Fe II arises in the same region as Hβ BC. Removal of the VBC part of Hβ in the $R_{\rm Fe\,II}$ estimation increases values over the previously published ones where no Hβ VBC correction was made, yielding $R_{\rm Fe\,II} \sim 0.5$ for Fairall 9 and 3C 249.1. C IVλ1549/Lyα estimates range from ≈0.15 for I Zw 1 and Mrk 478 to ≈0.5 for Mrk 335 and all population B sources. An apparent anticorrelation between C IVλ1549/Lyα and $R_{\rm Fe\,II}$ as well as a positive correlation between Si III]λ1892/C IVλ1549 and $R_{\rm Fe\,II}$ for population A sources is visible in median composite spectra of Bachev et al. (2004). Our data in Table 3 confirm a positive trend between Si III]λ1892/C IVλ1549 and $R_{\rm Fe\,II}$ for the three population A sources, although low Si III]λ1892/C IVλ1549 values are observed for $R_{\rm Fe\,II} \approx 0.5$. The largest Si III]λ1892/C IVλ1549 (and lowest C IVλ1549/Hβ) ratios are associated with the largest $R_{\rm Fe\,II}$ ($\gtrsim$0.5) estimates, probably implying metal enrichment (Section 4.4.1).

BLUE. The blueshifted component is less constrained due to its weakness in many lines/sources. The only ratios that can be measured involve Lyα, C IVλ1549 and, with greater difficulty, He IIλ1640. Given the importance of the Lyα/Hβ ratio, we made a special effort to derive an upper limit for it. They are estimated assuming that any Hβ emission is peaking at less than 3σ the noise level, meaning that the upper limit to the line flux can be written as $I_{\rm p}\sqrt{2\pi}\sigma \approx 1.067 I_{\rm p}$FWHM, where $I_{\rm p}$ is the peak line intensity. The lower limits indicate that BLUE values of Lyα/Hβ are much higher than those of BC and VBC. This has important physical consequences (Section 4.4).

VBC. Visually, the observed Fe II$_{\rm opt}$ emission is fully consistent with an origin in the BC (i.e. no obvious evidence for any Fe II VBC). Even if we measure an FWHM of Fe II consistent with that of Hβ$_{\rm BC}$ for our three population B sources, the VBC large width of $\gtrsim$10 000 km s^{-1} could create a pseudo-continuum underlying Hβ. To settle the issue of a possible Fe II VBC, we attempted to fit a VBC of Fe II$_{\rm opt}$ to the B1 and B1^{+} composites from the bright SDSS sample of Zamfir et al. (2010, S/N $\gtrsim$ 200). The assumption of an Fe II VBC with the same shift and width of Hβ$_{\rm VBC}$ leads to implausible results

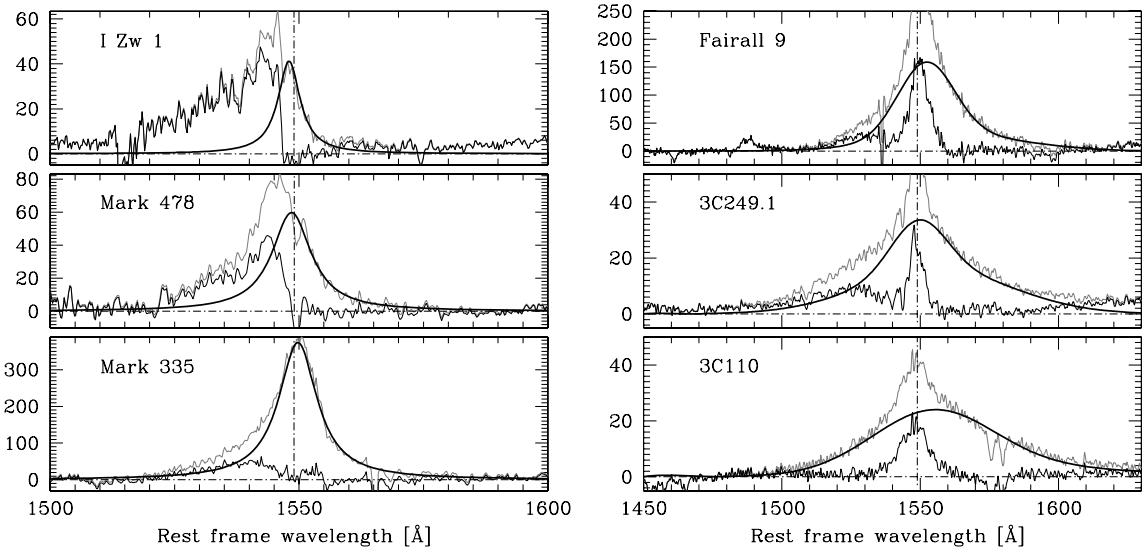

Figure 3. C IVλ1549 profile (grey line), after continuum subtraction for the six sources considered in this study. The scaled profile of Hβ (Hβ$_{\rm BC}$ + Hβ$_{\rm VBC}$) is shown as a thick line and the residuals as a thin continuous line. For Fairall 9 and 3C 249.1 it is possible to identify two major contributions to the residuals, namely one due to C IVλ1549$_{\rm NC}$ and one broad and shifted to the blue with respect to the source rest frame. The scaling is meant to show a maximum possible Hβ contribution to the C IVλ1549 profiles; the actual C IVλ1549 retrieved from the multicomponent fits (see the text) can be somewhat different from that shown in this figure.

© 2010 The Authors. Journal compilation © 2010 RAS, MNRAS **409,** 1033–1048

Table 3. BC: 1000 km s^{-1} $\lesssim$ FWHM $\lesssim$ 5000 km s^{-1}, $\Delta v_r \sim 0$ km s^{-1}.

Sp. T.	Name	Intensity ratio								W^a
		C IV/ Lyα	Al III/ Si III	Si III/ C IV	Mg II/ Lyα	Fe II/ Hβ	Hα/ Hβ	Lyα/ Hβ	Mg II/ Hβ	Lyα
A3	I Zw 1	0.14	0.61	0.97	0.31	1.80	4.2	5.5	1.70	61
A2	Mrk 478	0.14	0.41	0.47	0.09	0.95	–	10.3	0.94	87
A1	Mrk 335	0.45	0.33	0.07	0.07	0.47	4.6	15.8	1.03	102
B1	Fairall 9	0.53	0.32	0.18	0.21	1.04	$\lesssim$6.1	12.3	2.54	158
B1$^+$	3C 249.1	0.44	0.68	0.17	–	0.54	–	10.7	–	32
B1^{++}	3C 110	0.55	–	–	0.08	$\lesssim$0.36^b	–	17.0	1.3	71

[a]EW in Å.
[b]Assigned following the criterion that related FWHM – S/N and minimum detectable intensity, as in Marziani et al. (2003b).

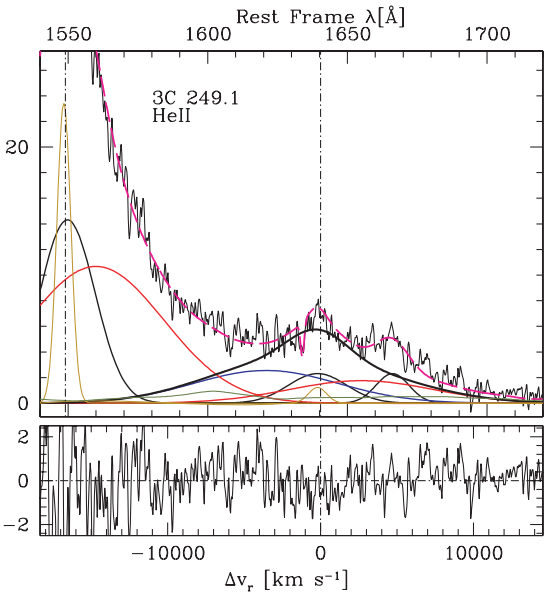

Figure 4. The interpretation of the He IIλ1640 profile of 3C 249.1. The 'plateau' appearance of the far red wing of C IVλ1549 is accounted for by a BLUE (blue) and a redshifted VBC (red) of He IIλ1640, whose shifts and widths match those of C IVλ1549. The resulting profile is shown as the thickest black line. Units are as for Fig. 2. The dashed magenta lines trace the fit with all components added up. Other line styles have the same meaning as Fig. 2.

with very large χ^2 unless Fe II VBC is negligible. We conclude that we have no strong evidence of a significant Fe II VBC emission.

The red wing of the λ1900 blend is ascribed to C III]λ1909 VBC emission, as the iron spectrum of population B sources is always weak.

4.3.1 *The Mg IIλ2800/Hβ ratio*

With the goal of verifying whether the values of Mg IIλ2800/Hβ reported in Tables 3 and 5 are typical, we selected a sample of quasars brighter than $g = 19.0$ with SDSS spectra that included both Hβ and Mg IIλ2800 (redshift range $z = 0.40$–0.75). While most of these spectra show moderate–low S/N, they are good enough to allow one to assign the sources to 4DE1 bins in which context high S/N composite spectra can be computed (normalized to specific flux at 5100 Å). We obtained 160 sources in bin B1 and 58 in B1$^+$. The VBC Mg IIλ2800/Hβ ratios we derive from bin B1 and B1$^+$ composite spectra are 0.7 and 0.5, respectively. Given population A values in Table 5 and the consistent value Mg IIλ2800/H$\beta \approx 1.5$ computed on the median spectra, we conclude that the VBC shows Mg IIλ2800/Hβ ratios two to three times lower than the BC. Due to the lesser prominence of the VBC in population B sources, the FWHM of Mg IIλ2800 becomes significantly lower than that of Hβ (Wang et al. 2009).

Table 4. BLUE: FWHM $\sim$ 7000 km s^{-1}, $\Delta v_r \sim -3000$ km s^{-1}.

Sp. T.	Name	Intensity ratio				W^a
		C IV/ Lyα	He II/ C IV	Hα/ Hβ	Lyα/ Hβ^b	Lyα
A3	I Zw 1	0.25	0.41	4.2	$\sim$18	60
A2	Mrk 478	0.66	0.17	–	$\gtrsim$46	15
A1	Mrk 335	0.45	0.67	–	$\gtrsim$32	16
B1	Fairall 9	1.05	0.14	–	$\gtrsim$46	30
B1$^+$	3C 249.1	0.59	0.17	–	$\gtrsim$32	53
B1^{++}	3C 110^c	–	–	–	–	0

[a]EW in Å.
[b]Lower limits to Lyα/Hβ are estimated by the maximum contribution expected by a component of the same shift and width if peaking at 3σ the noise level. See the text for a detailed explanation.
[c]Consistent with 0 intensity in all lines.

4.4 Physical conditions

We generated a multidimensional grid of CLOUDY (Ferland et al. 1998) simulations in order to infer ionization parameter U and electron density n_e values from our spectral measurements. Simulations span the density range $7.00 \leq \log n_e \leq 14.00$, and $-4.50 \leq \log U \leq 00.00$ with an interval of 0.25 in both $\log U$ and $\log n_e$ (cf. Korista et al. 1997). Each simulation was computed for a fixed ionization parameter and density assuming plane-parallel geometry. Part or all of this 2D grid of simulations was repeated assuming $N_c = 10^{21}, 10^{22}, 10^{23}, 10^{24}, 10^{25}$ cm^{-2}. Metallicity was assumed to be either solar or five times solar. Two alternative input continua were employed: (1) one assumed to be the standard AGN continuum by CLOUDY, which is equivalent to the continuum described in Mathews & Ferland (1987), and (2) the low-z quasar continuum of Laor et al. (1997a). We exploit the simulations to deduce constraints on U, N_c and n_e from the most reliable intensity ratios we derived in this paper.

Table 5. VBC: FWHM $\sim 10\,000$ km s^{-1}, $\Delta v_r \sim +2000$ km s^{-1}.

Sp. T.	Name	Intensity ratio							W^a
		C IV/ Lyα	He II/ C IV	C III/ C IV	Mg II/ Lyα	Hα/ Hβ	Lyα/ Hβ	Mg II/ Hβ	Lyα
A3	I Zw 1	–	–	–	–	–	–	–	0
A2	Mrk 478	–	–	–	–	–	–	–	0
A1	Mrk 335	–	–	–	–	–	–	–	0
B1	Fairall 9	0.36	0.13	0.18	0.08	1.26	9.0	0.68	88
B1$^+$	3C 249.1	0.67	0.17	0.17	–	–	4.5	–	41
B1^{++}	3C 110	0.37	0.10	–	0.04	–	5.0	0.2	27
	3C 110^b	0.50	0.10	–	0.07	–	12.6	0.83	97

[a]EW in Å.
[b]VBC only; see the text for details.

BC. The BC is the better constrained component with relatively large $R_{\rm Fe\,II}$ and ratios Al IIIλ1860/Si III]λ1892, Si III]λ1892/C IVλ1549 requiring high density ($\log n_{\rm e} \sim 12$), low ionization ($-3 \lesssim \log U \lesssim -2$) and large column density ($N_{\rm c} \gtrsim 10^{23}$ cm^{-2}). These conditions yield values of the important Lyα/Hβ and Mg IIλ2800/Lyα ratios that are consistent with those observed and explain $R_{\rm Fe\,II} \lesssim 0.5$–1.0 as well. Larger $R_{\rm Fe\,II}$ values suggest super-solar metallicity (Section 4.4.1). Hereafter, we will refer to the BC-emitting region as the LIL BLR while we will retain the term BLR in its more general meaning, i.e. as the region where all of the broad emission is produced.

BLUE. The very large Lyα/Hβ ratio suggests radically different conditions including lower optical depth and consistency with $N_{\rm c} < 10^{23}$ cm^{-2} (see Section 5.2) . The Lyα/Hβ and the He IIλ4686/ C IVλ1549 ratios suggest high ionization $\log U \sim -1$ and densities in the range $n_{\rm e} \sim 10^{9.5}$–$10^{10.5}$cm^{-3}. There is no detection of C III]λ1909 BLUE in the λ1900 blend, but this is consistent with high ionization gas at density $\log n_{\rm e} \sim 10$: the expected C III]λ1909/C IVλ1549 ratio for $\log U \sim -1$ is $\approx$0.1, and any blueshifted C III]λ1909 emission would be lost in the 1900-Å blend. We included a component with the same shift and width derived for C IVλ1549 in the fits of F9 and 3C 249.1, but SPECFIT yielded 0 or negative values in the final fit.

VBC. If $R_{\rm Fe\,II} \sim 0$ in the VBC and given the low Mg IIλ2800/Lyα ratio, we infer a high ionization parameter $\log U \gtrsim -1$. However, results for VBC are contradictory with all ratios consistent with high ionization but some ratios indicating high and others low density.

We observe C III]λ1909/C IVλ1549 $\sim$ 0.1–0.2 which indicates a relatively low density emitting region with $n_{\rm e} \sim 10^9$–10^{10} cm^{-3}. The observed He IIλ4686/C IVλ1549 ratio (0.1–0.2) is also consistent with this picture. Much higher density would collisionally quench C III]λ1909 to undetectable levels. Not all VBC line ratios are consistent with the moderate density picture. If the Balmer decrement is very flat, and the Lyα/Hβ ratio is between 5 and 10, then very high density gas ($n_{\rm e} \sim 10^{13}$ cm^{-3}) is required (Netzer et al. 1995) as well as a very large optical depth if photoionization is assumed. A large column density $N_{\rm c} > 10^{23}$ cm^{-2} yields conditions consistent with these line ratios measured for the VBC. Snedden & Gaskell (2007) computed line profile ratios Lyα/Hα and Hα/Hβ for several luminous Seyfert 1 nuclei (mainly population B) and reached similar conclusions in favour of large $n_{\rm e}$ and $N_{\rm c}$.

4.4.1 *Chemical abundances and Fe III contribution*

The LIL BLR is the only region allowing for tentative abundance considerations; results should obviously be applicable to the other emitting regions. Ratios involving metal lines should be considered the most robust for deriving physical inferences. Intermediate-ionization lines (such as Al IIIλ1860 and Si III]λ1892) are produced in a fully ionized region which makes them less dependent on column density than the LILs (Negrete et al. 2010). From the simulations, we find that the ratio Al IIIλ1860/Si III]λ1892 is not strongly dependent on Z: the ratio increases by about 40 per cent passing from $Z = 1\,{\rm Z}_\odot$ to $Z = 5\,{\rm Z}_\odot$, for $\log n_{\rm e} \approx 12$ and $\log U \approx -2$. However, C IVλ1549/Si III]λ1892 (or, equivalently, C IVλ1549/Al IIIλ1860) is much more affected. The low Si III]λ1892/C IVλ1549 and the other line ratios we measure for Mrk 478 can be all accounted for with $Z = 5\,{\rm Z}_\odot$, $\log n_{\rm e} \approx 11.6$ and $\log U \approx -2.4$. No solution with a well-defined value of $n_{\rm e}$ and U is found if $Z = {\rm Z}_\odot$ is assumed. Even higher metallicity, $\sim$10 Z$_\odot$, is strongly suggested for I Zw 1. The assumption of metallicity above solar is consistent with observations of high-z quasars (e.g. Hamann & Ferland 1999; Juarez et al. 2009), and the two sources where the evidence of higher abundance is strong also show the most prominent N Vλ1240 line in the Lyα panels of Fig. 2, as expected.

In the cases of high metallicity, we expect that Fe III should be especially prominent in the λ1900 spectral region. The physical conditions derived for the LIL BLR remind us of the 'Weigelt blobs' of η Carinæ, located in the equatorial plane of the system, perpendicular to the symmetry axis of the bipolar lobes forming the 'Homunculus' nebula. The Weigelt blobs are believed to be dense gas photoionized by the radiation associated with the central, massive star and with a possible companion (e.g. Johansson et al. 2000; Davidson 2005). The spectrum of the Weigelt blobs shows very weak C III]λ1909 along with a prominent line at λ1914, ascribed to the $z^7{\rm P}^0_3 \rightarrow a^7{\rm S}_3$ Fe III transition. Although this is not a resonant line (the lower level is $\approx$3 eV above ground), the line appears very strong because the upper level is populated by Lyα fluorescence. Indeed, in I Zw 1 where lines are narrow, the peak emission at λ1914 is actually visible, and the Fe III emission around 1900 Å may resemble that of Model 3 of Vestergaard & Wilkes (2001).

5 DISCUSSION

In the following, we will discuss measurements in fixed interpercentile velocity ranges (Section 5.1) as an approach complementary to our multicomponent analysis. After considering the properties of

© 2010 The Authors. Journal compilation © 2010 RAS, MNRAS **409,** 1033–1048

the BLUE (Section 5.2), we will show how our results on the physical properties of the different emitting regions do not favour a predominance of line emission from an accretion disc (Section 5.3.1) or from a binary BLR (Section 5.3.2). We suggest that the properties of the BLUE, BC and VBC emitting regions as well as their trends along the E1 sequence can be explained by the interplay of gravitational and radiation forces (Sections 5.4 and 5.5). Finally, we will discuss our interpretation of the BLR and compare it to past work (Section 5.7).

5.1 Interpercentile velocity measurements

The true profile shapes of the various line components are uncertain. The Lorentz-like shape of population A Hβ profiles can be considered the most accurate assuming that the peak and the wings do not represent independent emission components (e.g. La Mura et al. 2009). The lack of inflections in even the highest S/N composite profiles (Zamfir et al. 2010) motivated us to favour the single-component Lorentz fits. Uncertainties in our decompositions force us to restrict the analysis to estimates of the relative component intensities, average line shifts and widths. A double Gaussian function is a good approximation, but the individual Gaussian fits may provide uncertain estimates of the relative BC and VBC fluxes in the core of the line where the two components overlap in radial velocity. It is difficult to say whether a stronger core component and a less broad, fully redshifted VBC provide a worse fit, although the SDSS composite spectra of Zamfir et al. (2010) and earlier work on PG 1416−129 (Sulentic et al. 2000b) favour our BC–VBC decompositions. Also, if our interpretation of some sources showing Hβ that is almost pure VBC Hβ (3C 110 in this paper) is correct, then the Gaussian functions that we employ represent a reasonable description of the VBC profile shape. Measuring line ratios at fixed interpercentile velocities is an alternative approach that might have a more direct physical meaning if the BLUE and VBC matter only in the highest radial velocity ranges. We therefore report emission-line fluxes measured in three radial velocity ranges of $\Delta v_{\rm r} = 2000\,{\rm km\,s^{-1}}$ centred at 0 $\rm km\,s^{-1}$ ('0' range) and ± 4000 $\rm km\,s^{-1}$ (*B* and *R* ranges for population A sources) and 0 and ± 6000 $\rm km\,s^{-1}$ (population B sources) in Table 6. The reported measurements were carried out after subtraction of Fe II, Fe III and of contaminating narrow lines. Errors are estimated at a 2σ confidence level as twice the rms scatter in the radial velocity range times the $\Delta\lambda$ in Å. Two different centrings of the radial velocity ranges are needed to account for the linewidth difference of population A and B sources. The overall interpretation as deduced from the multicomponent fit is confirmed. In particular, the data of Table 6 indicate that there is no evidence of an additional red component for population A objects. There is also no convincing evidence of BLUE in Hβ of population B sources. The large error bars associated with the Lyα/Hβ ratios support the same conclusion motivated by the multicomponent fits for the BLUE: the upper limits and the possible detection of I Zw 1 imply Lyα/H$\beta \gg 10$. Line ratios for the *B*, 0 and *R* ranges yield the same qualitative conclusions as the multicomponent fits, with the limitation that we cannot obtain meaningful results for the heavily blended features at λ1900. Also, the large error bars in the Hβ *R* range of population B sources reflect the residuals of [O III]λ4959 subtraction. A comparison of our Lyα/Hβ ratios with those of Netzer et al. (1995) and of our Hα/Hβ ratios (from the multicomponent fits) with those of Snedden & Gaskell (2007) show agreement especially in the redshifted line wings, i.e. for the VBC. This suggests that our approach yields

Table 6. Interpercentile velocity measurements.

Name	Lyα^a			C IVλ1549^a			λ1900^{a,b}			Mg IIλ2800^a			Hβ^a		
	B	0	*R*	*B*	0	*R*	*B*	0	*R*	*B*	0	*R*	*B*	0	*R*
I Zw 1[c]	4.2 ± 0.7	15.5 ± 3.4	1.1 ± 0.9	1.7 ± 0.8	2.4 ± 1.3	$\lesssim 0.4$	$\lesssim 0.2$	0.8 ± 0.3	$\lesssim 0.4$	$\lesssim 0.3$	4.2 ± 0.8	0.4 ± 0.3[d]	0.15 ± 0.10	2.4 ± 0.3	$\lesssim 0.1$
Mrk 478[c]	3.4 ± 1.1	33.0 ± 2.4	1.3 ± 1.2	1.6 ± 0.6	5.1 ± 1.0	$\lesssim 0.4$	$\lesssim 0.3$	0.6 ± 0.4	$\lesssim 0.4$	$\lesssim 0.8$	2.8 ± 0.5	$\lesssim 0.4$	$\lesssim 0.1$	3.2 ± 0.2	$\lesssim 0.2$
Mrk 335[c]	7.5 ± 2.2	75.9 ± 4.9	3.9 ± 1.8	3.8 ± 1.2	30.8 ± 2.5	$\lesssim 1.2$[e]	$\lesssim 0.9$	6.1 ± 1.8	$\lesssim 0.8$	$\lesssim 0.7$	4.5 ± 0.7	$\lesssim 0.5$	0.15 ± 0.10	4.0 ± 0.2	0.2 ± 0.1
Fairall 9[f]	4.0 ± 1.5	28.5 ± 3.2	7.2 ± 2.6	2.2 ± 0.7	16.3 ± 2.4	2.7 ± 1.0	$\lesssim 0.8$	2.5 ± 0.9	$\lesssim 0.5$	$\lesssim 0.4$	4.6 ± 0.6	0.5 ± 0.4	$\lesssim 0.1$	2.2 ± 0.2	0.6 ± 0.3
3C 249.1[f]	2.4 ± 0.5	6.0 ± 1.2	1.5 ± 0.7	1.4 ± 0.2	3.6 ± 0.6	1.1 ± 0.3	$\lesssim 0.2$	0.8 ± 0.2	0.2 ± 0.1	–	–	–	0.15 ± 0.05	0.6 ± 0.1	0.3 ± 0.1
3C 110[f]	1.4 ± 0.3	4.2 ± 0.8	3.0 ± 0.2	0.7 ± 0.2	2.4 ± 0.4	1.5 ± 0.2	–	–	–	$\lesssim 0.1$	0.5 ± 0.1	0.15 ± 0.01	0.1 ± 0.1	0.4 ± 0.1	0.3 ± 0.2

[a] Fluxes in units of 10^{-12} erg $\rm s^{-1}$ $\rm cm^{-2}$.
[b] Al III]λ1860 is measured for I Zw1 and Mrk 478; C III]λ1909 for the remaining objects.
[c] *B*: $-5000\,{\rm km\,s^{-1}} \leq v_{\rm r} \leq -3000\,{\rm km\,s^{-1}}$; 0: $1000\,{\rm km\,s^{-1}} \leq v_{\rm r} \leq 1000\,{\rm km\,s^{-1}}$; *R*: $3000\,{\rm km\,s^{-1}} \leq v_{\rm r} \leq 5000\,{\rm km\,s^{-1}}$.
[d] Strong Fe II residual.
[e] *R*: $3500\,{\rm km\,s^{-1}} \leq v_{\rm r} \leq 5500\,{\rm km\,s^{-1}}$ due to a blemish in the spectrum.
[f] *B*: $-7000\,{\rm km\,s^{-1}} \leq v_{\rm r} \leq -5000\,{\rm km\,s^{-1}}$; 0: $1000\,{\rm km\,s^{-1}} \leq v_{\rm r} \leq 1000\,{\rm km\,s^{-1}}$; *R*: $5000\,{\rm km\,s^{-1}} \leq v_{\rm r} \leq 7000\,{\rm km\,s^{-1}}$.

© 2010 The Authors. Journal compilation © 2010 RAS, MNRAS **409**, 1033–1048

consistent values although the true shape of the VBC is uncertain especially in the range $-1000 \leq v_r \leq 1000\,\mathrm{km\,s^{-1}}$.

5.2 Optically thin gas?

The weakness of the response to continuum changes in the Hβ wings and interline comparisons e.g. have motivated arguments that the VBC is mainly produced in optically thin gas (Morris & Ward 1989; Zheng 1992; Shields, Ferland & Peterson 1995; Corbin & Smith 2000; Sulentic et al. 2000b). On the other hand, several authors have interpreted the response of the blue wings in C IVλ1549 and Hβ as evidence for predominantly optically thick gas (e.g. Turler & Courvoisier 1997; Korista & Goad 2004; Snedden & Gaskell 2007; Shapovalova et al. 2010, and references therein). Korista & Goad (2004) showed that an optically thick VBLR can explain the stronger core response of Hβ to continuum changes. The small Lyα/Hβ and Hα/Hβ ratios suggest a large column density N_c for both LIL BLR and VBLR. This interpretation may be correct for some transient sources but is unlikely to apply to more stable sources that show a strong redward asymmetry (i.e. population B quasars). In an optically thick medium, the intensity of a recombination line depends on the luminosity of the ionizing continuum; if the medium is optically thin, it depends on the amount of emitting gas. In practice, this places a constraint on the column density N_c. In high-luminosity quasars optically thin gas may not be adequate, even with a covering factor approaching unity, to explain the EW and luminosity of the observed VBC (Marziani, Dultzin-Hacyan & Sulentic 2006; Snedden & Gaskell 2007).

Is the BLUE due to optically thin gas perhaps ejected from the central engine? Fig. 5 shows the predicted EW of Lyα and Lyα/Hβ intensity ratios (thin lines) as a function of the ionization parameter U for $N_c = 10^{21}$ and 10^{22} cm^{-2}. Computations assume total covering, solar metallicity and $n_e = 10^{10}$ cm^{-3}. W(Lyα) remains approximately constant until the optically thin domain is entered at a 'critical' value of U. Beyond this value, W(Lyα) is roughly proportional to the inverse of U: in the optically thin domain the increase in continuum luminosity does not give rise to a corresponding increase in line luminosity. The most stringent observational boundary is set for Mrk 478 and Fairall 9, with Lyα/H$\beta \gtrsim 45$. At the same time, the median C IVλ1549/Lyα and He IIλ1640/C IVλ1549 values suggest $-1.5 \lesssim U \sim -1$ if $\log n_e = 10$. Considering that the observed W(Lyα) is in the range of 15–60 Å, low column density gas at $N_c = 10^{21}$ cm^{-2} can explain the largest observed EWs only if there is substantial covering of the source, i.e. the source is almost completely covered by a geometrically thin shell ($\sim 10^{11}$ cm) of optically thin gas. A smaller covering fraction is required if $N_c = 10^{22}$ cm^{-2} or larger.

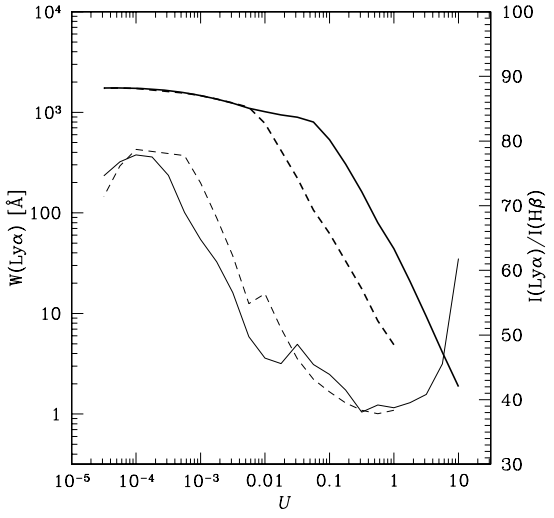

Figure 5. Predicted EW of Lyα in Å (thick lines) and intensity ratio Lyα/Hβ (thin lines) as a function of the ionization parameter U. The dashed lines refer to column density $N_c = 10^{21}$ cm^{-2} and the solid ones to $N_c = 10^{22}$ cm^{-2}.

5.3 Alternative interpretations

5.3.1 Accretion disc contribution

Some population B sources show very broad double-peaked Hβ profiles that have been interpreted as the signature of accretion disc line emission (e.g. Eracleous & Halpern 2003; Strateva et al. 2003). A double-peaked signature has been found for Mg IIλ2800 in Arp 102B (Halpern et al. 1996). Others have argued that double-peaked profiles are too rare and disc model solutions too disparate to justify the disc emission hypothesis (Sulentic 1989). Attempts have been made to find larger samples of double-peaked sources (Strateva et al. 2003; Bon et al. 2009); however, most (90 per cent) of these sources are not double-peaked but rather red or blue asymmetric. A large sample of the highest S/N SDSS spectra binned in the 4DE1 context (Marziani et al. 2009; Zamfir et al. 2010) does not show any hint of a double-peak signature in high S/N ($\approx$250) composites. Broader population B sources unsurprisingly favour red asymmetries. Sources included in a given population B bin of Fig. 1 show a diversity of red/blue bumps and asymmetries; however, bin composite spectra show a BC+VBC blend similar to that observed in e.g. Fairall 9 and 3C 249.1 of this paper. Where is the disc signature? If a significant part of the broad lines is produced in an accretion disc, then it must be obscured or masked by non-disc emission components (e.g. Zhang et al. 2009). For population B sources, one could argue that the *sum* of the BLUE and VBC represents a double-peaked component accounting for the broadest part of the line profile with the BC emitted elsewhere. A difficulty with this interpretation is that the gas in the BLUE and VBC appear to arise in regions with different physical conditions. The BLUE is not consistent with high density and large column density as expected in standard accretion disc models (e.g. Collin-Souffrin & Dumont 1990). In the case of population A sources, the narrower Lorentz-like profiles, interpreted as a disc signature, would require line emission from a disc with outer radius $\sim 10^6$ gravitational radii which is theoretically and observationally disfavoured (Collin & Zahn 1999). The evidence continues to grow weaker for a predominance of accretion disc emission in population A and population B line profiles. Only a minority of very-broad sources whose prototype is Arp 102B remain consistent with accretion disc predictions (Eracleous & Halpern 2003; Strateva et al. 2003; Gezari, Halpern & Eracleous 2007).

5.3.2 Binary BLR

If quasar activity is driven by merger and accretion processes, then we might expect to find some/many sources with evidence for a binary BH. At least, some of these sources might involve two AGN with associated BLRs. It has been proposed that binary BH configurations might give rise to double-peaked line profiles (Gaskell 1985; Halpern & Filippenko 1988; Lauer & Boroson 2009; Shen & Loeb

© 2010 The Authors. Journal compilation © 2010 RAS, MNRAS **409,** 1033–1048

2009; see Gaskell 2009a for a recent review). Two co-orbiting BHs, each with a BLR producing (typical) single-peaked broad lines, could give rise to double- or single-peaked composite line profiles depending on the line-of-sight orientation and radial separation of the BHs. A large peak shift $v_r > 2000$ km s^{-1} is not unphysical since $v_r \approx 2000$ km s^{-1} is less than the typical virial velocity at the reverberation estimated radius of the BLR.

This idea is not easily applicable to population A sources which show quite narrow and symmetric Hβ profiles. The situation for population B sources appears more favourable if one considers, for example, a binary BLR origin of the BLUE and redshifted VBC. The *reductio ad extremum* would view all population B sources as binary population A sources. One problem with this view would involve the fact that virtually all RL sources are population B. However, in some population B sources unshifted BC gas might be associated with a low ionization region at larger radius and distributed around the centre of mass of the two orbiting BHs. The radial velocity of the first component would be $v_{r,1} = \sqrt{GM/d}\sin i \sin(2\pi t/P)m_2/M$, while for the second $v_{r,2} = \sqrt{GM/d}\sin i \sin(2\pi t/P + \pi)m_1/M$ at any given orbital time t. P is the orbital period, m_1 and m_2 are the BH masses, with $M = m_1 + m_2$, and d the BH separation. The inferred properties of the BLUE and VBC lead one to infer that the masses of the two BHs should be roughly equal. The M_{BH} similarity again raises questions about why we find very different Lyα/Hβ ratios and inferred physical conditions for the BLRs around the two BHs. In addition, the broadest profiles should 'narrow' dramatically on a time-scale of $\approx \pi d/2v \approx 10\ d_{16} v_{1000}^{-1}$ yr. Note that the profile presented in fig. 10 of the Shen & Loeb (2009) paper is *not* double-peaked but a prototypical population B source showing the red asymmetry that we suggest is due to a distinct VBC emitting region. If one ascribes a (broader) core component to a more massive BH and the redward asymmetry to a narrower component (less massive BH), then the signs of the two component radial velocities $v_{r,1}$ and $v_{r,2}$ should always be opposite, which is not the case in the majority of population B sources. The expected change in radial velocity is not seen in Arp 102B-like double-peaked sources either (Eracleous et al. 1997; Gezari et al. 2007).

5.4 Role of mass and Eddington ratio

Table 7 reports the M_{BH} and L_{bol}/L_{Edd} values for the sources following the prescription of Vestergaard & Peterson (2006) where Column 1 gives the source name, Column 2 the specific flux at 5100 Å, Column 3 the bolometric luminosity assuming a correction factor of 10 from the observed luminosity at 5100 Å , Columns 4 and 5 the FWHM of the entire Hβ profile and FWHM of Hβ_{BC} as derived from the χ^2 fits and Columns 6–7 and 8–9 present the corresponding BH masses and Eddington ratios, respectively. M_{BH} values are reduced by $\Delta \log M_{BH} \approx 0.3$ when the BC is employed. The effect is larger (factor of 10) if C IVλ1549 is used as a virial proxy for Hβ in population A sources (Sulentic et al. 2007). Sources follow a sequence of increasing mass and especially decreasing L_{bol}/L_{Edd}. Population A sources show the highest Eddington ratios by an order of magnitude or more. A correction by radiation pressure would leave the Eddington ratio trend unaffected (Marconi et al. 2008). It is interesting to note that the VBC occurs only in population B sources where $L_{bol}/L_{Edd} < 0.1$, but BLUE is strong in both Mrk 478 and 3C 249.1 whose L_{bol}/L_{Edd} is different by almost an order of magnitude.

5.5 Gravitational and radiative acceleration

If line emitting gas is optically thick to the Lyman continuum, then the radiation will exert an outward acceleration that is inversely proportional to the column density and proportional to the ionizing luminosity. The ratio of the radiative to gravitational accelerations is

$$r_a = \frac{a_{rad}}{a_{grav}} \approx 0.088 L_{44} M_{BH,8}^{-1} N_{c,23}^{-1}, \quad (1)$$

where M_{BH} is in units of 10^8 M$_\odot$ and L_{44} is the luminosity of the ionizing continuum ($\lambda < 912$ Å) in units of 10^{44} erg s^{-1}. The equation can be written in the convenient form

$$r_a = \frac{a_{rad}}{a_{grav}} \approx 7.2 \frac{L_{bol}}{L_{Edd}} N_{c,23}^{-1}. \quad (2)$$

If $r_a \gg 1$, then radiative acceleration dominates. This may be the case for the BLUE if we interpret the blueshift as a Doppler shift. A condition of equilibrium may be reached at $r_a \approx 1$. If $L_{bol}/L_{Edd} = 1$, the corresponding N_c is $\lesssim 10^{24}$ cm^{-2}, a plausible value for the LIL BLR. Finally if $r_a \ll 1$, the emitting gas may be unable to withstand the central BH gravity and may fall towards the centre giving rise to the observed redshifted VBC. This interpretation is compatible with large N_c values for the VBLR and would naturally explain why the VBC is observed in objects with low $L_{bol}/L_{Edd} \lesssim 0.1$. Of particular relevance to population A sources are emitting clouds moving under the combined effect of gravitation and radiative acceleration (Mathews 1993; Netzer & Marziani 2010) that produce the observed Lorentz-like profiles. If $L_{bol}/L_{Edd} \lesssim 0.1$, as in population B, gas of $\log N_c \sim 22$ would be pushed away while gas of even larger column density could flow out in population A sources.

5.6 Radio loudness

If we compare the Hβ profile of RQ and RL *in population B only,* i.e. where most RL objects are found, there is no major difference although RL objects show a preference towards more extreme redward asymmetries (Marziani et al. 2003c). If we look at HILs of RL

Table 7. BH Mass and Eddington ratio.

Name	f_λ at 5100 Å (erg s^{-1} cm^{-2} Å^{-1})	$\log L_{bol}$ (erg s^{-1})	FWHM Hβ (km s^{-1})	FWHM Hβ_{BC} (km s^{-1})	$\log M_{BH}$ Hβ (M$_\odot$)	$\log M_{BH}$ Hβ_{BC} (M$_\odot$)	$\log L_{bol}/L_{Edd}$ Hβ	$\log L_{bol}/L_{Edd}$ Hβ_{BC}
I Zw 1	8.40E−15	45.5	1100	1100	7.3	7.3	−0.3	−0.3
Mrk 478	7.13E−15	45.7	1300	1300	7.5	7.5	−0.4	−0.4
Mrk 335	9.00E−15	44.8	1500	15000	7.2	7.2	−0.9	−0.9
Fairall 9	7.52E−15	45.3	6500	4550	8.7	8.4	−2.0	−1.7
3C 249.1	3.00E−15	46.5	8300	5050	9.5	9.0	−1.6	−1.2
3C 110	1.50E−15	46.8	14000	10700	10.1	9.9	−1.9	−1.6

objects, the C IVλ1549 profile can show a blueward asymmetry although a redward asymmetry is more frequent (Marziani et al. 1996; Sulentic et al. 2007; Punsly 2010). RQ objects *of population B* show a somewhat different behaviour: C IVλ1549 BLUE is systematically stronger and the profile is more often symmetric or blueward asymmetric. The Sulentic et al. (2007) data suggest that radio loudness may modulate the relative intensity of BLUE and VBC, lowering BLUE, perhaps because radio ejections affect the radial flow seen in RQ quasars (Marziani et al. 1996). BLUE is, however, definitely observed in RL objects (Barthel, Tytler & Thomson 1990; Wills et al. 1995; Small, Sargent & Steidel 1997).

5.7 Previous studies and the present interpretation of the BLR

We are aware of only one other attempt to model all major line profiles in a sample of low-z quasars. Shang et al. (2007) studied 22 sources and modelled all lines using two components – broad and very broad. Their sample is larger and allows for some correlation analysis. However, population A sources are likely overrepresented, a result of their use of an X-ray selection that favours population A sources. The results of Shang et al. (2007) should be therefore related mainly to the population A sources included in our investigation even if some population B present in their data suggest a change in trends at FWHM(Hβ) ≈ 4000 km s^{-1} (their fig. 5). Their major empirical result, namely that C IVλ1549 and Lyα are very different from Hα and Hβ in terms of linewidth, asymmetry and velocity shifts, is confirmed by the present study as far as Hβ is concerned. Our results also suggest, along with Shang et al. (2007), that a simple radially stratified ionization structure of the BLR is unable to explain the different line profiles. A wind component has been isolated through our E1-based approach and three components appear to be a minimum set for the reasons summarized in Section 1. The 4DE1 approach unifies the lines within specific sources and allows for the definition of a trend among the sources. The BLUE and LIL BLR are characterized by well-defined properties. The VBLR is a region that could be defined by virtue of high ionization and, if our considerations are correct, large N_c. Within these constraints, a large range of parameters – especially density – is suggested. The VBLR is therefore the only region where a locally optimally emitting cloud scheme – where a range of properties occurs at every location (Baldwin et al. 1995) – could apply.

Recent reverberation mapping studies attempted to consider the response of lines to continuum changes in bins of radial velocity (Bentz et al. 2008; Denney et al. 2009). Infall is suggested by the observation of a faster response to continuum change in the red wing of Hβ in NGC 3516 and Arp 151. Arp 151 belongs to a perturbed system, and infalling gas can give rise to redward asymmetries on spatial scales much larger than those of the BLR (e.g. Rafanelli & Marziani 1992; Marziani et al. 2003a). Even if it is too early to generalize, these results are consistent with the interpretation of the Hβ redward asymmetry/redshift in population B sources (e.g. Gaskell 2009b). As far as the VBC is concerned, a possible problem with an infall interpretation is related to the line anisotropy. Very high N_c clouds should prevalently emit lines facing the central photoionizing continuum source; this is true also for Hβ (Ferland et al. 1992). Therefore, if line emission is anisotropic, gas should be visible from the far side of the continuum source and infalling gas should yield a net blueshift. However, if emission comes from the non-illuminated side of the cloud (Ferland et al. 2009), and the more distant part of the infalling gas is obscured a net shift to the red is expected as frequently observed in the line profiles.

5.7.1 On the origin of the broad component

The BC may be distinct from the other emitting regions and in many sources (population A) may be the dominant or only visible component in all LILs. Two defining BC properties involve low ionization degree and symmetry of the line profiles. We find BC width FWHM ≤ 5000 km s^{-1} with fractional peak shift Δv_r/FWHM $\lesssim 0.1$. This leads to the conclusion that the LIL BC may be the only Hβ component that is a valid virial estimator. The width of Fe II and especially of Mg IIλ2800 likely offer the next best virial estimators (Sulentic et al. 2006; Wang et al. 2009).

The necessity of a low ionization emitting sub-region within the BLR has been stressed since long, especially by S. Collin and collaborators (Collin-Souffrin et al. 1988). Observational support in favour of this idea came by the realization of the very different profiles of LILs and HILs, as reviewed in Section 1. More recently, the analysis of the Ca II IR triplet suggests that a rather dense gas with density $\log n_e \sim 11.5$ and $\log U \sim -2.5$ is present in the BLR and that this is primarily responsible for the observed O I, Ca II and Fe II lines, based on the resemblance of their profiles (Matsuoka et al. 2007; Matsuoka, Kawara & Oyabu 2008). There is a close agreement between the values derived by Matsuoka et al. (2007) and the values derived in this paper through the ratios Al IIIλ1860/Si III]λ1892 and C IVλ1549/Si III]λ1892 (see Negrete et al. 2010, for a more detailed report).

LIL emission from AGN has been the subject of a controversy related to the ionization mechanism: Collin-Souffrin et al. (1988) and Collin-Souffrin & Dumont (1989) suggested mechanical heating to explain the LIL prominence and especially the Fe II intensity. Explaining strong LIL emission under the assumption of solar abundance has been a challenge for photoionization models. The C IVλ1549/He IIλ1640 and Si III]λ1892/C IVλ1549 intensity ratios lead us to conclude that the assumption of metal enrichment is appropriate. Among population A objects, there could be an important role of metallicity in farther defining the properties of the LIL BLR. We indeed see a trend in the prominence of the N Vλ1240: the most prominent N Vλ1240 is observed in I Zw 1 and Mrk 478. If the N Vλ1240/C IVλ1549 ratio can be used as a metallicity indicator, then our six objects might follow the accretion rate–metallicity relationship pointed out by Shemmer et al. (2004). An increase in iron abundance from a few to several times solar (in agreement with much previous work; e.g. Hamann & Ferland 1999) is suggested for sources with $R_{Fe\,II} \gtrsim 1$ (A2+ bins).

The low ionization BC seems to be preferentially associated with young, or rejuvenated, systems such as NLSy1 galaxies (Mathur 2000; Sulentic et al. 2000a, 2008) whose L_{bol}/L_{Edd} is relatively large ($0.2 \lesssim L_{bol}/L_{Edd} \lesssim 1$). Enhanced star formation in NLSy1s has been recently demonstrated from the analysis of *Spitzer* data (Sani et al. 2010) while clues have existed for a long time (e.g. Sanders et al. 1988; Krongold, Dultzin-Hacyan & Marziani 2001, and references therein). Higher metallicity is likely a consequence of top-heavy starbursts that may be frequent in galaxy nuclei (e.g. Bonnell & Rice 2008). Such starbursts are expected to sustain the high accretion rate typical of population A sources and to provide the enriched LIL-BLR material in extreme population A sources such as I Zw 1.

6 CONCLUSION

Ignoring the composite nature of broad emission lines in quasars will likely result in a poor or erroneous understanding of their emitting regions (as known for 30 yr; e.g. Gordon, Collin-Souffrin & Dultzin-Hacyan 1981). The contextualization of 4DE1 not only

© 2010 The Authors. Journal compilation © 2010 RAS, MNRAS **409,** 1033–1048

shows that quasars are spectroscopically diverse but it provides a way to organize the differences in order to facilitate interpretation of the emitting components in different classes of sources. Analysis of six low-*z* quasars that explore 4DE1 diversity and are believed to be representative of the wide majority of low-*z* quasars suggests that the strongest optical/UV emission lines involve one or more of three different components that can be defined by their shifts with respect to the rest frame of each quasars: a redshifted VBC, an unshifted BC and a BLUE. The three components have been tentatively isolated through models of the strongest lines from Lyα to Mg IIλ2800 and Fe II$_{\rm opt}$ using Hβ as a template, and characterized as follows.

(i) The BC is the broad-line component present in the overwhelming majority of type-1 AGN. Fe II and Mg IIλ2800 emission likely arise in the same region. Other broad lines usually show a BC although there may be exceptions: C III]λ1909 may be very weak in extreme population A sources where metallicity enhancement is most evident. At the other extreme of the 4DE1 sequence, some population B sources may show only weak or even zero BC emission.

(ii) Population A sources show dominant BC emission in LILs and strong BLUE emission in HILs. The BLUE is most prominent in NLSy1s, but is detected in most quasars, including population B sources. The prominence of the BLUE in extreme population A NLSy1s (almost always RQ) suggests that it is not closely related to any relativistic outflow due to radio jets. It has been interpreted as the signature of an accretion disc wind where the receding part of the flow is obscured by the disc (Marziani et al. 1996). If the interpretation of Section 5.5 is correct, then BLUE may be due to gas upon which radiative forces dominate. We are able to constrain the ionization parameter, density and column density of this outflowing region. These quantities are important to assess feedback effects on the interstellar medium of the quasar host galaxy.

(iii) The redshifted VBC can be described as a defining LIL property in population B sources. The BC is distinguished empirically from the VBC by its much larger FWHM and significant redshift. The low Balmer decrement and Lyα/Hβ ratio suggest, if we assume photoionization as the heating source of the gas, high ionization and large column density. The physical conditions in the VBLR are not clear and probably involve a stratification of properties that we are unable to resolve at this time. On the one hand, the C III]λ1909/C IVλ1549 ratio suggests high ionization and moderate density. On the other hand, the strong He IIλ1640 emission, the low Lyα/Hβ ratio and the flat Balmer decrement (Hα/H$\beta \approx 1$) are better explained by extreme density at very high ionization. In this region, a locally optimally emitting cloud scheme (Baldwin et al. 1995) could be appropriated.

ACKNOWLEDGMENTS

DD and CAN acknowledge financial support from PAPIIT UNAM, grant IN111610. PM wishes to thank Professor H. Netzer for discussions on topics closely related to this paper. The authors also thank an anonymous referee for suggesting some necessary additions.

REFERENCES

Bachev R., Marziani P., Sulentic J. W., Zamanov R., Calvani M., Dultzin-Hacyan D., 2004, ApJ, 617, 171
Baldwin J., Ferland G., Korista K., Verner D., 1995, ApJ, 455, L119
Barthel P. D., Tytler D. R., Thomson B., 1990, A&AS, 82, 339
Bentz M. C. et al., 2008, ApJ, 689, L21
Bon E., Gavrilovic N., La Mura G., Popovic L. C., 2009, New Astronomy Reviews, 53, 121
Bonnell I. A., Rice W. K. M., 2008, Sci, 321, 1060
Boroson T. A., Green R. F., 1992, ApJS, 80, 109
Brotherton M. S., Wills B. J., Steidel C. C., Sargent W. L. W., 1994, ApJ, 423, 131
Carswell R. F. et al., 1991, ApJ, 381, L5
Collin S., Zahn J.-P., 1999, A&A, 344, 433
Collin-Souffrin S., Dumont A. M., 1989, A&A, 213, 29
Collin-Souffrin S., Dumont A. M., 1990, A&A, 229, 292
Collin-Souffrin S., Dyson J. E., McDowell J. C., Perry J. J., 1988, MNRAS, 232, 539
Corbin M. R., 1990, ApJ, 357, 346
Corbin M. R., 1995, ApJ, 447, 496
Corbin M. R., Smith P. S., 2000, ApJ, 532, 136
Davidson K., 2005, in Humphreys R., Stanek K., eds, ASP Conf. Ser. Vol. 332, The Fate of the Most Massive Stars. Astron. Soc. Pac., San Francisco, p. 101
Denney K. D. et al., 2009, ApJ, 704, L80
Eracleous M., Halpern J. P., 2003, ApJ, 599, 886
Eracleous M., Halpern J. P., Gilbert A. M., Newman J. A., Filippenko A. V., 1997, ApJ, 490, 216
Espey B. R., Carswell R. F., Bailey J. A., Smith M. G., Ward M. J., 1989, ApJ, 342, 666
Ferland G. J., Peterson B. M., Horne K., Welsh W. F., Nahar S. N., 1992, ApJ, 387, 95
Ferland G. J., Korista K. T., Verner D. A., Ferguson J. W., Kingdon J. B., Verner E. M., 1998, PASP, 110, 761
Ferland G. J., Hu C., Wang J., Baldwin J. A., Porter R. L., van Hoof P. A. M., Williams R. J. R., 2009, ApJ, 707, L82
Gaskell C. M., 1982, ApJ, 263, 79
Gaskell C. M., 1985, Nat, 315, 386
Gaskell C. M., 2010, Nature, 463, E1
Gaskell C. M., 2009b, in Maraschi L., Ghisellini G., Della Ceca R., Tavecchio F., eds, ASP Conf. Ser., Accretion and Ejection in AGNs: a Global View, in press
Gezari S., Halpern J. P., Eracleous M., 2007, ApJS, 169, 167
Gordon C., Collin-Souffrin S., Dultzin-Hacyan D., 1981, A&A, 103, 69
Halpern J. P., Filippenko A. V., 1988, Nat, 331, 46
Halpern J. P., Eracleous M., Filippenko A. V., Chen K., 1996, ApJ, 464, 704
Hamann F., Ferland G., 1999, ARA&A, 37, 487
Johansson S., Zethson T., Hartman H., Ekberg J. O., Ishibashi K., Davidson K., Gull T., 2000, A&A, 361, 977
Juarez Y., Maiolino R., Mujica R., Pedani M., Marinoni S., Nagao T., Marconi A., Oliva E., 2009, A&A, 494, L25
Korista K. T., Goad M. R., 2004, ApJ, 606, 749
Korista K., Baldwin J., Ferland G., Verner D., 1997, ApJS, 108, 401
Kriss G., 1994, in Crabtree D. R., Hanisch R. J., Barnes J., eds, ASP Conf. Ser. Vol. 61, Astronomical Data Analysis Software and Systems III. Astron. Soc. Pac., San Francisco, p. 437
Krongold Y., Dultzin-Hacyan D., Marziani P., 2001, AJ, 121, 702
La Mura G., Di Mille F., Ciroi S., Popović L. Č., Rafanelli P., 2009, ApJ, 693, 1437
Laor A., Fiore F., Elvis M., Wilkes B. J., McDowell J. C., 1997a, ApJ, 477, 93
Laor A., Jannuzi B. T., Green R. F., Boroson T. A., 1997b, ApJ, 489, 656
Lauer T. R., Boroson T. A., 2009, ApJ, 703, 930
Marconi A., Axon D. J., Maiolino R., Nagao T., Pastorini G., Pietrini P., Robinson A., Torricelli G., 2008, ApJ, 678, 693
Marziani P., Sulentic J. W., 1993, ApJ, 409, 612
Marziani P., Sulentic J. W., Dultzin-Hacyan D., Calvani M., Moles M., 1996, ApJS, 104, 37
Marziani P., Sulentic J. W., Zwitter T., Dultzin-Hacyan D., Calvani M., 2001, ApJ, 558, 553
Marziani P., Dultzin-Hacyan D., D'Onofrio M., Sulentic J. W., 2003a, AJ, 125, 1897
Marziani P., Sulentic J. W., Zamanov R., Calvani M., Dultzin-Hacyan D., Bachev R., Zwitter T., 2003b, ApJS, 145, 199

Marziani P., Zamanov R. K., Sulentic J. W., Calvani M., 2003c, MNRAS, 345, 1133
Marziani P., Dultzin-Hacyan D., Sulentic J. W., 2006, in Kreitler P. ed., New Developments in Black Hole Research. Nova Science Publishers, New York, p. 123
Marziani P., Sulentic J. W., Dultzin D., 2008, Rev. Mex. Astron. Astrofis., 32, 69
Marziani P., Sulentic J. W., Stirpe G. M., Zamfir S., Calvani M., 2009, A&A, 495, 83
Mathews W. G., 1993, ApJ, 412, L17
Mathews W. G., Ferland G. J., 1987, ApJ, 323, 456
Mathur S., 2000, MNRAS, 314, L17
Matsuoka Y., Oyabu S., Tsuzuki Y., Kawara K., 2007, ApJ, 663, 781
Matsuoka Y., Kawara K., Oyabu S., 2008, ApJ, 673, 62
Morris S. L., Ward M. J., 1989, ApJ, 340, 713
Negrete C. A., Dultzin D., Marziani P., Sulentic J. W., 2010, ApJ, submitted
Netzer H., Marziani P., 2010, ApJ, submitted, preprint (arXiv:1006.3553)
Netzer H., Brotherton M. S., Wills B. J., Han M., Wills D., Baldwin J. A., Ferland G. J., Browne I. W. A., 1995, ApJ, 448, 27
Peterson B. M., Ferland G. J., 1986, Nat, 324, 345
Peterson B. M. et al., 2004, ApJ, 613, 682
Punsly B., 2010, ApJ, 713, 232
Rafanelli P., Marziani P., 1992, AJ, 103, 743
Richards G. T., Vanden Berk D. E., Reichard T. A., Hall P. B., Schneider D. P., SubbaRao M., Thakar A. R., York D. G., 2002, AJ, 124, 1
Sanders D. B., Soifer B. T., Elias J. H., Madore B. F., Matthews K., Neugebauer G., Scoville N. Z., 1988, ApJ, 325, 74
Sani E., Lutz D., Risaliti G., Netzer H., Gallo L. C., Trakhtenbrot B., Sturm E., Boller T., 2010, MNRAS, 403, 1246
Sargent W. L. W., Steidel C. C., Boksenberg A., 1989, ApJS, 69, 703
Schlegel D. J., Finkbeiner D. P., Davis M., 1998, ApJ, 500, 525
Shang Z., Wills B. J., Wills D., Brotherton M. S., 2007, AJ, 134, 294
Shapovalova A. I., Popović L. Č., Burenkov A. N., Chavushyan V. H., Ilić D., Kovačević A., Bochkarev N. G., León-Tavares J., 2010, A&A, 509, A106
Shemmer O., Netzer H., Maiolino R., Oliva E., Croom S., Corbett E., di Fabrizio L., 2004, ApJ, 614, 547
Shen Y., Loeb A., 2009, preprint (arXiv:0912.0541)
Shields J. C., Ferland G. J., Peterson B. M., 1995, ApJ, 441, 507
Small T. A., Sargent W. L. W., Steidel C. C., 1997, AJ, 114, 2254
Snedden S. A., Gaskell C. M., 2007, ApJ, 669, 126
Strateva I. V. et al., 2003, AJ, 126, 1720
Sulentic J. W., 1989, ApJ, 343, 54
Sulentic J. W., Marziani P., 1999, ApJ, 518, L9
Sulentic J. W., Marziani P., Dultzin-Hacyan D., 2000a, ARA&A, 38, 521
Sulentic J. W., Zwitter T., Marziani P., Dultzin-Hacyan D., 2000b, ApJ, 536, L5
Sulentic J. W., Marziani P., Zwitter T., Dultzin-Hacyan D., Calvani M., 2000c, ApJ, 545, L15
Sulentic J. W., Marziani P., Zamanov R., Bachev R., Calvani M., Dultzin-Hacyan D., 2002, ApJ 566, L71
Sulentic J. W., Stirpe G. M., Marziani P., Zamanov R., Calvani M., Braito V., 2004, A&A, 423, 121
Sulentic J. W., Repetto P., Stirpe G. M., Marziani P., Dultzin-Hacyan D., Calvani M., 2006, A&A, 456, 929
Sulentic J. W., Bachev R., Marziani P., Negrete C. A., Dultzin D., 2007, ApJ, 666, 757
Sulentic J. W., Zamfir S., Marziani P., Dultzin D., 2008, Rev. Mex. Astron. Astrofis., 32, 51
Turler M., Courvoisier T., 1997, in Peterson B. M., Cheng F.-Z., Wilson A. S., eds, ASP Conf. Ser. Vol. 113, Emission Lines in Active Galaxies: New Methods and Techniques. Astron. Soc. Pac., San Francisco, p. 191
Tytler D., Fan X.-M., 1992, ApJS, 79, 1
Vanden Berk D. E. et al., 2001, AJ, 122, 549
Vestergaard M., Peterson B. M., 2006, ApJ, 641, 689
Vestergaard M., Wilkes B. J., 2001, ApJS, 134, 1
Wang T., Brinkmann W., Bergeron J., 1996, A&A, 309, 81
Wang J. et al., 2009, ApJ, 707, 1334
Wilkes B. J., 1986, MNRAS, 218, 331
Wills B. J. et al., 1995, ApJ, 447, 139
Young P., Sargent W. L. W., Boksenberg A., 1982, ApJS, 48, 455
Zamfir S., Sulentic J. W., Marziani P., 2008, MNRAS, 387, 856
Zamfir S., Sulentic J. W., Marziani P., Dultzin D., 2010, MNRAS, 403, 1759
Zhang X., Dultzin D., Wang T., Kauffmann G., 2009, MNRAS, 397, 1510
Zheng W., 1992, ApJ, 385, 127

APPENDIX A: NOTES ON INDIVIDUAL SOURCES

I Zw 1 is the prototypical NLSy1 source. Its UV spectrum has been analysed in detail by many workers, notably Laor et al. (1997b). The Mg IIλ2800 fit shows residuals that may be indicating an excess Fe II emission around 2820 Å.

Mrk 478 is spectroscopically rather similar to I Zw 1, with less extreme properties. The very low C IVλ1549 BC intensity value may be in part due to a narrow absorption close to the systemic velocity.

Mrk 335 belongs to bin A1. Its spectrum is consistent with the median spectrum of the bin, with low $R_{\rm Fe\,II}$, weak BLUE. The profile of Hβ is well described by a Lorentzian function, making this object similar to the rest of population A even if $R_{\rm Fe\,II}$ is as low as in population B.

Fairall 9 is a rather typical B1 source, with a relatively modest but appreciable VBC. The Al IIIλ1860/Si III]λ1892 and Si III]λ1892/C IVλ1549 ratios, along with $R_{\rm Fe\,II} \approx 1$, suggest some metal enrichment above solar.

3C 249.1 is a lobe-dominated radio source. It shares many of the properties of several RL quasars at higher redshift, notably the strong C IV$\lambda 1549_{\rm NC}$, and the shape of the Lyα and of the C IVλ1549+He IIλ1640 blend.

3C 110. Some quasars show lines with strong VBC emission that can be mistaken for a BC (Sulentic et al. 2000b; e.g. PG 1416−129). The correct interpretation for 3C 110 may involve a single redshifted VBC. The BC may be completely absent, as there is no Fe II detection with the present data. This suggestion is also motivated by an analysis of 3C 390.3 (Negrete et al. 2010) which is a lobe-dominated RL quasar like 3C 110. Physical conditions inferred for the BC of 3C 390.3 are similar to those of the VBC implying that there may be no BC in 3C 390.3. If the BC is completely suppressed in 3C110, then the entire C IVλ1549 profile in that source may be a VBC. A fit with a single, shifted Gaussian is worse than that shown in Fig. 2, but not dramatically so. Then, shift and FWHM values for a pure VBC C IVλ1549 in 3C 110 would be close to the canonical values (10^3 and 10^4 km s^{-1}, respectively) for the VBC in Hβ. The spectrum of this object does lack a BLUE which might be closely associated with the BC.

This paper has been typeset from a TEX/LATEX file prepared by the author.

© 2010 The Authors. Journal compilation © 2010 RAS, MNRAS **409,** 1033–1048

Capítulo 4

Condiciones físicas en la Región de Líneas Anchas para Cuasares a $z \sim 3$.

En este capítulo uso los criterios descritos en el capítulo anterior acerca del número de componentes que se deben ajustar a cada línea de emisión, en ocho cuasares de tipo 1 a $z \sim 3$. La obtención de los espectros fue mediante la solicitud y asignación de tiempo de telescopio en el VLT (*Very Large Telescope* operado por la ESO, *European Southern Observatory*). Uno de los propósitos de este capítulo es separar todas las componentes involucradas en la emisión de las líneas, para trabajar sólo con la componente central ancha. El rango espectral de estos objetos está en el UV, de modo que las líneas que ajustamos son: CIII]λ1909, SiIII]λ1892, el doblete de AlIIIλ1860, SiIIλ1814, CIVλ1549, SiIVλ1397 y los pseudocontinuos que se forman con las emisiones de FeII$_{UV}$ y FeIII$_{UV}$. Por otro lado, realizamos simulaciones con CLOUDY con las que conseguimos mallas de valores de la densidad de hidrógeno $N_{\rm H}$ y el parámetro de ionización U, para las líneas consideradas arriba. Con los flujos obtenidos de las componentes anchas, hicimos cocientes de líneas: AlIIIλ1860/SiIII]λ1892, CIVλ1549/AlIIIλ1860, SiIVλ1397 /SiIII]λ1892, CIVλ1549/SiIVλ1397 y SiIIλ1814/SiIII]λ1892 que usamos para graficar mapas de contornos de $N_{\rm H}$ vs U y así obtener estos dos valores. Lo que nos interesa, en especial, es el producto $N_{\rm H}{\cdot}U$, porque a partir de la definición del parámetro de ionización (ec. 1.19), podemos

conocer la distancia a la región de líneas anchas, r_{BLR}. Las distancias obtenidas con nuestro método las comparamos con las obtenidas de la relación empírica r_{BLR}–luminosidad. Finalmente, usamos la suposición de que la componente central está siendo emitida en un sistema virializado para calcular la masa del hoyo negro.

Trabajo enviado a *The Astrophysical Journal* y en proceso de revisión.

To appear in The Astrophysical Journal
Preprint typeset using LaTeX style emulateapj v. 11/10/09

PHYSICAL CONDITIONS IN THE BROAD LINE REGION OF $Z \sim 3$ QUASARS: A PHOTOIONIZATION METHOD TO DERIVE $r_{\rm BLR}$ AND $M_{\rm BH}$ ♣

C. Alenka Negrete[1] and Deborah Dultzin[1]
Instituto de Astonomía, Universidad Nacional Autónoma de México, Mexico

Paola Marziani[2]
INAF, Astronomical Observatory of Padova, Italy

Jack Sulentic[3]
Instituto de Astrofísica de Andalucía, Spain
To appear in The Astrophysical Journal

ABSTRACT

We present high S/N UV spectra for eight quasars at $z \sim 3$ obtained with VLT/FORS. The spectra enable us to analyze in detail the strongest emission features in the rest-frame range 1400-2000 Å of each source (CIII]λ1909, SiIII]λ1892, AlIIIλ1860, SiIIλ1814, CIVλ1549 and SiIVλ1397). Previous work indicates that a component of these lines is emitted in a region with well-defined properties i.e., a high density and low ionization emitting region). Flux ratios AlIIIλ1860/SiIII]λ1892, CIVλ1549/AlIIIλ1860, SiIVλ1397/SiIII]λ1892, CIVλ1549/SiIVλ1397 and SiIIλ1814/SiIII]λ1892 for this region permit us to strongly constrain electron density, ionization parameter and metallicity through the use of diagnostic maps built from CLOUDY simulations. Reliable estimates of the product density times ionization parameter allow us to derive the radius of the broad line region $r_{\rm BLR}$ from the definition of the ionization parameter. The $r_{\rm BLR}$ estimate and the assumption of virialized motions in the line emitting gas yields an estimate for black hole mass. We compare our results with estimates obtained from the $r_{\rm BLR}$ – luminosity correlation customarily employed to estimate black hole masses of high redshift quasars.

Subject headings: galaxies: active — galaxies: high-redshift — quasars: general — quasars: emission lines

1. INTRODUCTION

1.1. *Interpreting Quasar Spectra*

Measuring relevant physical parameters from the observed broad-line spectra of quasars is still an open challenge. Identification and intensity measurements of the strongest emission lines has made possible a rough inference of the typical conditions of the emitting gas since the earliest days of quasar spectroscopy. The very first quasars of intermediate redshift discovered in the 1960s showed a fairly high ionization spectrum, with prominent lines of CIVλ1549, and HeIIλ1640 in addition to strong Balmer lines of the low-redshift quasars. Photoionization by the central continuum source was considered the preeminent heating mechanism of the emitting gas. Significant CIII]λ1909 emission suggested electron densities ($n_{\rm e}$) in the range $10^9 - 10^{10}$ cm^{-3}. The observed intensity ratio CIII]λ1909/CIVλ1549 indicated ionization parameter (defined by Eq. 1 later in this paper) values of the order of 10^{-1}. This photoionization scenario was successful in explaining at least some quasar optical and UV spectra (see the review by Davidson and Netzer 1979 for a synopsis). More recent work emphasized the existence of several problems with this simple scenario. Low ionization lines (LILs), and especially FeII are too strong to be explained by a photoionized region of moderate density and column density (see for example Dumont and Mathez 1981; Joly 1987; Collin-Souffrin et al. 1988; Dumont and Collin-Souffrin 1990). These authors stressed that the LILs required a denser, low-temperature environment.

We unfortunately lack a simple well-defined diagnostic measure of physical conditions in the broad line region. One strategy for estimating electron density in astrophysical sources involves using two emission lines of the same ion, and with similar energies above the ground level, but with different radiative transition probabilities A_{ki}. In practice one often chooses two lines from the same term where one forbidden/semi-forbidden transition is associated with another that is semi-formidden/permitted in order to ensure very different values of A_{ki} (for example, [SiIII]λ1882 and SiIII]λ1892). This technique is not straightforwardly applicable to the broad lines of quasars, precisely because the lines are broad, suitable candidates are too closely spaced in wavelength, and density is at least an order of magnitudes higher than the critical density for the forbidden transitions used in spectra of planetary nebulæ and HII regions. In addition the S/N and the resolution of quasar spectra are usually not very high.

Feibelman and Aller (1987) used the

[0] Based on observations made with ESO Telescopes at Paranal Observatory under programme ID 078.B-0109(A)

[1] anegrete@astroscu.unam.mx, deborah@astroscu.unam.mx
[2] paola.marziani@oapd.inaf.it
[3] sulentic@iaa.es

CIII]λ1909/SiIII]λ1892 ratio to study the rather high-density environment typical of symbiotic stars ($n_e \sim 10^{7-10}$ cm^{-3}). In this case we have two semi-forbidden (intercombination) resonance lines with significantly different transition probabilities (see Table 1). The lines are emitted by two iso-electronic species with somewhat different ionization potentials (11 eV for C^+ vs. 8 eV for Si^+). The ionic fraction is dependent on the relative abundance of silicon-to-carbon (to be assumed) as well as on the ionization structure within the emitting region (to be computed). Using lines of different ions introduces additional potentially serious sources of uncertainty. It is perhaps not surprising that most workers believe that n_e in the BLR cannot be reliably estimated using quasar spectra. Strong CIII]λ1909 emission would imply that n_e cannot be very high ($n_e \sim 10^{11-13}$cm^{-3}). Very high density was invoked to explain the rich low ionization spectrum (especially FeII) seen in the spectra of most quasars. Several lines in the UV spectrum of I Zw 1 point towards high density at least for the LIL emitting zone: prominent FeII, relatively strong AlIIIλ1860, and detection of CIIIλ1176 (Baldwin et al. 1996; Laor et al. 1997b). The region where these lines are produced cannot emit much CIII]λ1909. But is CIII]λ1909 really so strong in most quasars? BLR conditions are certainly complex and a single emitting region is not sufficient to explain both LILs and high ionization lines (HILs).

1.2. *Quasar Systematics*

Quasar spectra are not all alike. There are significant differences in line intensity ratios and broad line profiles from object to object (Bachev et al. 2004; Marziani et al. 2010). More importantly, these differences can be organized in a systematic way as has been realized since the early 1990s (Boroson and Green 1992). Since then several authors stressed the importance of the so-called eigenvector 1 (E1) of quasars (e.g. Gaskell et al. 1999). Sulentic et al. (2000, 2007) expanded the E1 trends into a 4-dimensional space involving optical, UV and X-ray measures. They also defined spectral types along a sequence occupied by AGN in an optical plane involving FeII and FWHM Hβ parameters. Objects at extreme ends of the E1 sequence are very different at almost all wavelengths and median spectra computed in spectral bins within this plane emphasize systematic changes in broad line properties (Sulentic et al. 2002, 2007). The differences have motivated the suggestion of a possible dichotomy between Narrow Line Seyfert 1 (NLSy1s) like sources and broader line objects that include almost all radio-loud quasars. The most effective divider of the two quasar types appears to be at FWHM of the Hβ broad component H$\beta_{\rm BC} \approx 4000$ km s^{-1} for low-to-moderate luminosity sources (Marziani et al. 2009). This corresponds to to Eddington ratio $L/L_{\rm Edd} \sim 0.2 \pm 0.1$ (Marziani et al. 2003b).

The distinction between NLSy1-like objects (hereafter Population A sources with FWHM(Hβ) $\leq$ 4000 km s^{-1}) and the rest of quasars (Population B with FWHM(Hβ) $\gtrsim$ 4000 km s^{-1}) is of special relevance here. Pop. A sources show relatively low equivalent width lines with e.g. the λ1900 blend ∼30 Å. A close analysis of the CIII]λ1909 blend in the prototypical NLSy1 I Zw 1 shows strong SiIII]λ1892, and AlIIIλ1860 blended with rather weak CIII]λ1909 along with prominent FeIII(UV34)(λ1895.5, λ1914.0, and λ1926.3) and FeII blends (Laor et al. 1997b; Vestergaard and Wilkes 2001). The CIII]λ1909 line is apparently so weak that FeIIIλ1914 may be the most prominent feature at $\lambda \approx$ 1910Å (cf. Hartig & Baldwin 1986). This interpretation is confirmed by detailed deblending of a source (SDSS J120144.36+011611.6) that can be considered a high luminosity analog of I Zw 1 (§7.1).

Median composite UV spectra of low-z quasars show that AlIIIλ1860 and SiIII]λ1892 are more prominent in 4DE1 spectral types A2 and A3. Bins A1, A2, A3 are defined in terms of increasing FeIIλ4570 (see Fig. 1 of Sulentic et al. 2002). I Zw 1, although belonging to the extreme type A3 (Bachev et al. 2004) is not unique as a NLSy1, since the fraction of Pop. A sources in bin A3 and A4 is ≈ 20 % of all Pop. A sources in the sample of Zamfir et al. (2010). A significant number of extreme NLSy1 are not classified as quasars in SDSS and must be collected from the galaxy catalog (Hu et al. 2008).

1.3. *Emission Line Diagnostics and BLR Properties*

Emission lines and line ratios are used in diagnostic maps to estimate temperatures and electronic densities in galactic and extragalactic photoionized regions. Examples include HII-regions and galaxies with HII-region nuclear spectra where electron densities are less than $n_e \approx 10^4$ cm^{-3}. This method has been successfully applied to the narrow line region (NLR) in AGN. Application to the broad line quasars has yielded results that are difficult to interpret. One recent exception is the work by Maksuoka et al. (2008) who succeeded in analyzing the partly ionized region thought to emit most of the LILs in quasar spectra. They suggest that OI 8446 and the CaII triplet are emitted by dense, low ionization gas probably located in the periphery of the BLR. If the electron density and ionization conditions are known it is possible to derive, with additional assumptions, the distance of the BLR emitting region from the central continuum source (as stressed earlier also by Baldwin et al. 1996).

The physical conditions of photoionized gas can be described by electron density n_e, hydrogen column density N_c, metallicity (normalized to solar), shape of the ionizing continuum, and the ionization parameter U. The latter represents the dimensionless ratio of the number of ionizing photons and the electron density n_e or, equivalently, the total number density of hydrogen n_H, ionized and neutral.[5] Both U and n_H are related through the equation

$$U = \frac{\int_{\nu_0}^{+\infty} \frac{L_\nu}{h\nu} d\nu}{4\pi n_{\rm H} c r^2} \quad (1)$$

where L_ν is the specific luminosity per unit frequency, h is the Planck constant, ν_0 the Rydberg frequency, c the speed of light, and r can be interpreted as the distance between the central source of ionizing radiation and the line emitting region. Note that $U n_{\rm H} c$ is the ionizing photon flux

$$\Phi(H) = \frac{Q(H)}{4\pi r^2}. \quad (2)$$

[5]In a fully ionized medium $n_e \approx 1.2\ n_{\rm H}$. We prefer to adopt the definition based on $n_{\rm H}$ because it is the one employed in the CLOUDY computations.

TABLE 1
LINE COMPONENTS IN THE λ1900 BLEND.

Ion	λ Å	X eV	$E_l - E_u$ eV	Transition	A_{ki} s^{-1}	n_c cm^{-3}	Note
Si II	1808.00	8.15	0.000 - 6.857	$^2D^o_{3/2} \rightarrow {}^2P_{1/2}$	$2.54 \cdot 10^6$	···	1
Si II	1816.92	8.15	0.036 - 6.859	$^2D^o_{5/2} \rightarrow {}^2P_{3/2}$	$2.65 \cdot 10^6$	···	1
Al III	1854.716	18.83	0.000 - 6.685	$^2P^o_{3/2} \rightarrow {}^2S_{1/2}$	$5.40 \cdot 10^8$	···	1
Al III	1862.790	18.83	0.000 - 6.656	$^2P^o_{1/2} \rightarrow {}^2S_{1/2}$	$5.33 \cdot 10^8$	···	1
[Si III]	1882.7	16.34	0.000 - 6.585	$^3P^o_2 \rightarrow {}^1S_0$	0.012	$6.4 \cdot 10^4$	1,2,3
Si III]	1892.03	16.34	0.000 - 6.553	$^3P^o_1 \rightarrow {}^1S_0$	16700	$2.1 \cdot 10^{11}$	1,4,5
[C III]	1906.7	24.38	0.000 - 6.502	$^3P^o_2 \rightarrow {}^1S_0$	0.0052	$7.7 \cdot 10^4$	1,2,6
C III]	1908.734	24.38	0.000 - 6.495	$^3P^o_1 \rightarrow {}^1S_0$	114	$1.4 \cdot 10^{10}$	1,2,4,5
Fe III	1914.066	16.18	3.727 - 10.200	$z^7P^o_3 \rightarrow a^7S_3$	$6.6 \cdot 10^8$	···	7

NOTE. — All wavelengths are in vacuum. (1) Ralchenko, Yu., Kramida, A.E., Reader, J., and NIST ASD Team (2008). NIST Atomic Spectra Database (version 3.1.5). Available at: http://physics.nist.gov/asd3. 2: Feibelman & Aller (1987). 3: n_c computed following Shaw & Dufour (1995). 4: Morton (1991). 5: Feldman (1992). 6: Zheng (1988). 7: Wavelength and A_{ki} from Ekberg (1993), energy levels from Edlén and Swings (1942).

If we know *the product of* $n_{\rm H}$ and U, we can estimate the radius r of the BLR from Eq. 1. The dependence of U on $r_{\rm BLR}$ was used by Padovani & Rafanelli (1988) to derive central black hole masses assuming a plausible average value of the product $n_{\rm H}{\cdot}U$. The typical value of $n_{\rm e}$ was derived at that time from semiforbidden line CIII]λ1909 which implied that the density could not be much higher than $n_{\rm e}{\approx}\ 10^{9.5}$ cm^{-3} (Osterbrock & Ferland 2006). Padovani (1988) derived an average value $< U{\cdot}\ n_{\rm e}> {\approx}\ 10^{9.8}$ from several sources where $r_{\rm BLR}$ had been determined from reverberation mapping, and for which the number of ionizing photons could be measured from multiwavelength observations. The average value was then used to compute black hole masses for a much larger sample of Seyfert 1 galaxies and low-z quasars (Padovani & Rafanelli 1988; Padovani, Burg & Edelson 1989). Wandel, Peterson & Malkan (1999) compared the results of the photoionization method with the ones obtained through reverberation mapping, found a very good correlation for the masses computed with the two methods, and concluded that "both methods measure the mass of the central black hole."

1.4. *Outline of the paper*

The importance of the product $U{\cdot}n_{\rm H}$ goes beyond knowledge of the physical conditions in the BLR if it can lead to estimates of BLR radius and black hole mass. This paper identifies suitable emission line ratios that overcome some of the major problems in the analysis of emission lines of quasars. It also defines a photoionization method that can be applied to even the highest redshift quasars making use of high S/N near-IR spectroscopic data. In §2 we present the spectra of 8 pilot sources obtained with the VLT/FORS; in §3 we discuss data reduction; In §4 we describe our method of fitting broad emission line profiles; in §5 we give a phenomenological interpretation of the profile fits; in §6 we describe a method for deriving BLR physical conditions and give the results of our fits; in §7 we discuss two sources not belonging to our sample that show extreme behavior and that are helpful to understand more common quasar spectra; in §8 we give the results for the photoionization method; in §9 we derive the radius of the BLR (its distance from the ionizing source) and the mass of the black hole for each quasar in our sample; in §10 we discuss our results; finally, in §11 we summarize our results and the prospect of a more extended application of our method. All the computations were made considering H_0 =70 km s^{-1} Mpc^{-1} and a relative energy density $\Omega_\Lambda = 0.70$ and $\Omega_{\rm M} = 0.3$.

2. OBSERVATIONS

Data were obtained between Nov. 2006 and Jan. 2007 using the VLT2/FORS1 telescope operated in service mode. FORS1 is the visual and near UV focal reducer and low dispersion spectrograph of the Very Large Telescope (VLT) operated by European Southern Observatory (ESO) (Appenzeller et al. 1998). Our VLT sample consists of 8 quasars with $z \sim 3$. In Figure 1 we show the spectra uncorrected for redshift. Tab. 2 provides a log of observations that is organized as follows.

Column 1: object name, Col. 2: apparent B magnitude, Col. 3 redshift, Col. 4: line(s) used for redshift estimation: a) OIλ1304.8, b) CIII]λ1909; Col. 5: absolute B magnitude, Col. 6 flux at 6 cm taken from FIRST (Far InfraRed and Submillimetre Telescope), Col. 7: date (refers to time at start of exposure), Col. 8: Digital Integration Time, Col. 9: number of exposures with integration time equal to DIT, Col. 10: airmass at the beginning of each exposure, Col. 11 S/N in the continuum around 1700Å.

The observation of one of our 8 quasars, J00521-1108, yielded only a low S/N spectrum which weretain because observed features in the blend at $\sim$ 1900 Å are clear enough to fit the individual lines. Two sources, J01225+1339 and J02287+0002, are BAL quasars. We will keep them separate because CIVλ1549 is severely affected by absorption.

3. DATA REDUCTION

Data were reduced using standard IRAF tasks. All spectra were wavelength and flux calibrated in the observed frame and then corrected for Galactic extinction. Flux correction was applied using meteorological data provided by ESO. The observed flux was multiplied by the inverse of the light lost computed from the ratio seeing over slit width in arcsec. Correction to rest frame

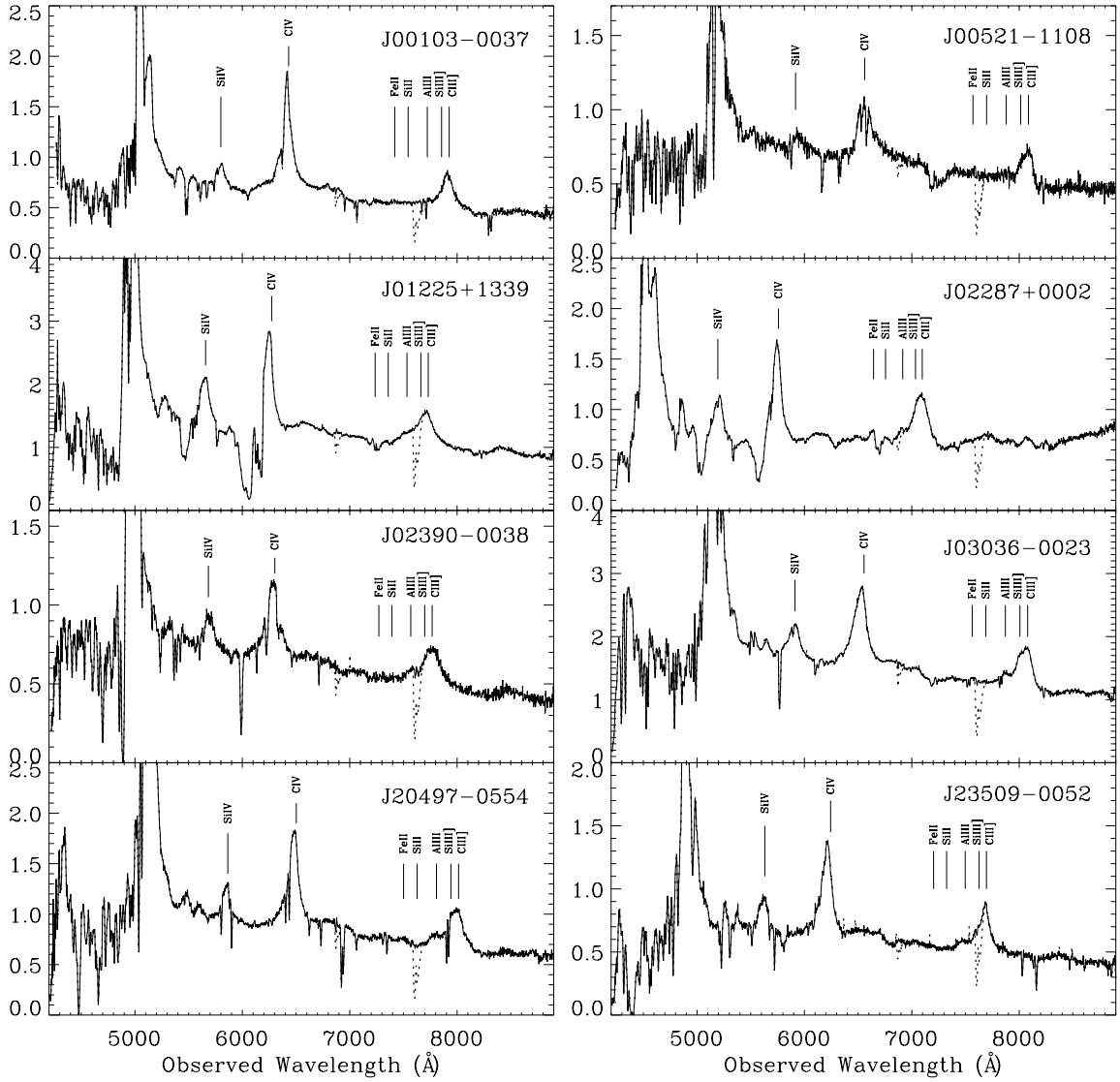

FIG. 1.— Sample of 8 VLT spectra. Abscissa is obseved wavelength in Å, ordinate is specific flux in units 10^{-16} ergs s^{-1} cm^{-2} Å^{-1} corrected for Milky Way Galactic extinction. The superimposed dotted line is before atmospheric bands subtraction. We show the positions of the lines of our interest CIII]λ1909, SiIII]λ1892, AlIIIλ1860, SiIIλ1814, FeIIλ1787, CIVλ1549 and SiIVλ1397. J01225+1339 and J02287 are BAL quasars.

requires estimating the redshift z which is not a trivial task as outlined below. Rest frame correction also involved scaling the specific flux in flux per unit wavelength interval by a factor $(1+z)^3$. Measurements were carried out on the rest-frame spectra. It is necessity to describe below two important aspects of the data reduction.

3.1. *A & B Atmospheric Bands Correction*

The A or B atmospheric band falls on top of the 1900Å blend in many of the spectra. This is an important region for this study especially because it involves SiIII]λ1892, AlIIIλ1860, and SiIIλ1814. In order to remove these absorption features we created an A+ B band template from standard star spectra used as specific flux calibrators. We scaled this template to find a best fit. Fig. 1 shows the A and B absorption correction where we make a line identification to illustrate which lines are affected. In cases where the A or B bands overlap a

TABLE 2
Basic Properties of Sources and Log of Observations.

Object name (1)	m_B (2)	z (3)	Line (4)	M_B (5)	Flux 6cm (mJy) (6)	Date (7)	DIT (8)	N_{exp} (9)	Airmass (10)	S/N (11)
J00103-0037	18.39	3.1546	1	-25.68	0.40	2006-11-08	1139	3	1.16, 1.13, 1.11	60
J00521-1108	18.70	3.2364	2	-25.39	0.43	2007-01-01	1199	3	1.15, 1.21, 1.29	41
J01225+1339	18.24	3.0511	1	-25.80	*	2006-11-08	1259	2	1.36, 1.32	92
J02287+0002	18.20	2.7282	1	-25.72	0.35	2006-12-16	1259	2	1.10, 1.12	67
J02390-0038	18.68	3.0675	1	-25.36	0.43	2006-11-07	1199	3	1.35, 1.46, 1.60	57
J03036-0023	17.65	3.2319	1	-26.44	0.34	2006-12-16	1259	2	1.11, 1.14	88
J20497-0554	18.29	3.1979	1	-25.79	*	2006-11-04	1259	2	1.52, 1.70	54
J23509-0052	18.67	3.0305	1	-25.36	0.41	2006-11-07	1199	3	1.10, 1.11, 1.14	62

* Not in FIRST

weak line like SiIIλ1814 the effect is considerable and measures of SiIIλ1814 should not be considered at all or with extreme care. This happens for sources J00103-0037, J03036-0023, and J20497-0554. In cases where one of the bands overlaps a stronger line like SiIII]λ1892 or AlIIIλ1860, the correction was good enough to permit accurate measures.

3.2. *Redshift Estimate*

Normally one uses strong narrow emission lines to set the rest frame in a quasar. In our case no strong narrow lines are available so we consider the peaks of Lyα, CIVλ1549 and CIII]λ1909. The Lyα peak is affected by absorption and CIVλ1549 is a HIL feature often showing blueshifts and/or asymmetries (Gaskell 1982, Espey et al. 1989, Corbin 1990, Tytler & fan 1992; Marziani et al. 1996; Richards et al. 2002, Baskin & Laor 2005; Sulentic et al. 2007). This is especially true in Pop. A sources. CIII]λ1909 is blended with SiIII]λ1892 and FeIII that is especially prominent in this region and could well affect the peak. Pop. B sources show a rather weak Fe spectrum making the CIII]λ1909 peak a more reliable z estimator.

Our best option is to use the low ionization line OIλ1304 whenever it is strong. However it is blended with low ionization SiII$\lambda\lambda$1304,1309 ($^2P^0_{3/2,1/2} - ^2 S_{1/2}$). Both OI$\lambda$1304 and SiII$\lambda\lambda$1304,1309 are broad lines and in Pop. B sources might show large redshifts or even significant blueshifts. Simulations in the ($n_{\rm H}$, U) region of interest show OIλ1304 $\approx$ 2 SiIIλ1304,1309 and this is confirmed in the spectrum I Zw 1 where OIλ1304 and SiII$\lambda\lambda$1304,1309 are resolved. The two components of the SiII$\lambda\lambda$1304,1309 doublet are set to the same intensity (i.e., we assume an optically thick case). We model the blend OIλ1304 + SiII$\lambda\lambda$1304,1309 with 5 Gaussians; the three components of the OI feature are produced by Bowen florescence mechanism, and should show ratios consistent with their transition probabilities. Generating a model spectrum in IRAF (lines broadened to 4000 km s^{-1}) yields a rest frame peak wavelength of 1304.8 $\pm$ 0.2 Å (in vacuum) which we use as a reference for our VLT spectra assuming that there is no hint of systematic BC shifts as is the case for all Pop. A sources (the majority in our sample) and many Pop. B sources (Marziani et al. 2003a).

Examination of Fig. 2 reveals that the peak of OIλ1304 in source J00521-1108 is not observed clearly. We use CIII]λ1909 to set the rest frame in this case. There are other sources J00103-0037, J02287+0002, J02390-0038 and J20497-0554 where the redshift estimation using both OIλ1304 and CIII]λ1909 are not in good agreement. The largest disagreement was found for J02287+0002. Redshifts obtained for the three remaining quasars, J01225+1339, J03036-0023 and J23509-0052, were obtained from OIλ1304. Fig. 3 shows the deredshifted VLT-FORS spectra for our sample of 8 quasars.

4. DATA ANALYSIS

4.1. *Methodological Considerations on Multicomponent Fits*

The SPECFIT IRAF task (Kriss 1994) allows us to fit the continuum, emission and absorption line components, FeII and FeIII blends, etc. We fit two spectral ranges: (1) 1450–1680 Å for analysis of CIVλ1549 and (2) 1750–2050 Å for analysis of the 1900 Å blend. Significant FeII and FeIII emission are expected close to and underlying the 1900 Å blend. Study of the 1900 Å blend is especially difficult in quasars because the lines are broad and the blending severe. We therefore need to take advantage of several previous results.

4.2. *FeII and FeIII Emission*

Our approach is completely empirical and employs an FeII + FeIII template taken from templates successfully used in previous works. Our FeII template is based on a CLOUDY simulation and is not very far from the preferred model of Bruhweiler & Verner (2008).

FeIII lines are common and strong in the vicinity of CIII]λ1909 as is evidenced by their presence in average LBQS (Francis et al. 1991) and SDSS (Vanden Berk et al. 2001) spectra. They appear to be strong when AlIIIλ1860 is also strong (Hartig and Baldwin 1986). Vestergaard & Wilkes (2001) produced an FeIII template based on the UV spectrum of I Zw 1. Since then, Sigut et al. (2004) have modeled the FeIII BLR spectrum. See also Verner et al. (2003) for a plot of emission around 1900 Å. Lyα pumping enhances FeIII (UV 34)λ1914.0 (Johansson et al. 2000) and this line can be a major contributor to the blend right on the red side of CIII]λ1909 (see Fig. 2 of Vestergaard & Wilkes). We reproduced the option B of the empirical FeIII template of Vestergaard & Wilkes (2001), taking advantage of the line identifications from Ekberg (1993). When detected we can use FeII UV 191 to set a rough FeII level while the feature at 2080 Å is helpful for a more precise estimation of the intensity of FeIII. The continuum was fitted using the regions around 1450Å (1750 and 1960Å) that are relatively

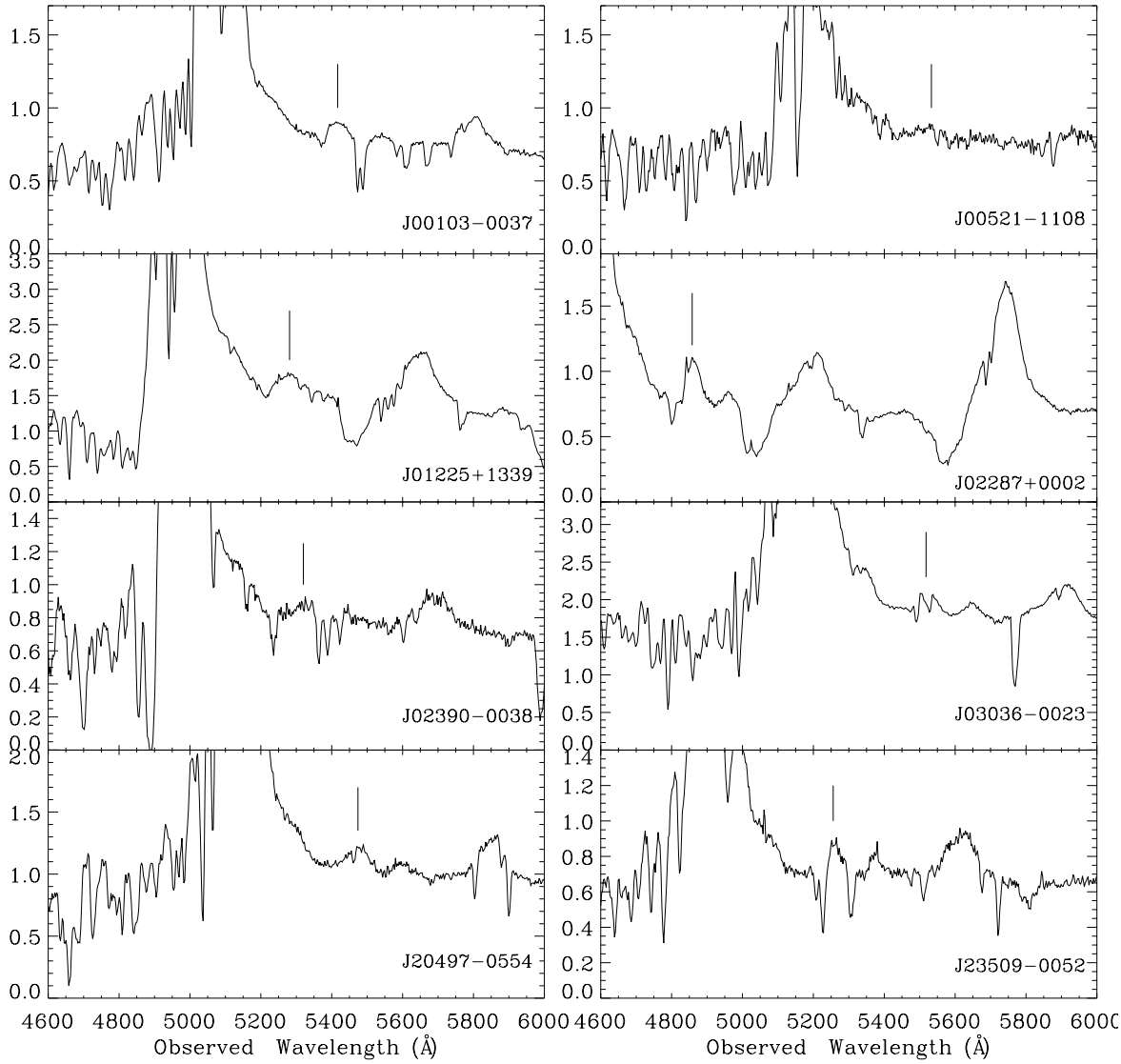

FIG. 2.— OIλ1304.8 used to place the restframe showed by the mark. Abscissa is rest frame wavelength in Å, ordinate is specific flux in units 10^{-16} ergs s^{-1} cm^{-2} Å^{-1} corrected for Milky Way Galactic extinction. In J00521-1108 and J02390-0038 the peak of OIλ1304.8 is not observed clearly. In J00103-0037, J02287+0002 and J20497-0554, the redshift results, using both OIλ1304.8 and CIII]λ1909, are ambiguous. In J01225+1339, J03036-0023 and J23509-0052, the redshifts obtained using OIλ1304.8 or CIII]λ1909 are consistent.

free of FeII emission (Vanden Berk et al. 2001). We used the same power-law to describe the continuum at both the CIVλ1549 and 1900Å regions.

4.3. *Line Components*

We base our SPECFIT analysis on several previous observational results. The most important ones are as follows:

- Sulentic et al. (2002) gridded the broad component of FWHM Hβ_{BC} versus $R_{\rm FeII}$=W(FeIIλ4570blend)/W(H$\beta_{\rm BC}$) parameter plane into bins of fixed Δ FWHM = 4000 km s^{-1} and Δ $R_{\rm FeII}$= 0.5. Quasar spectra in different bins are different in many measures. As mentioned earlier, the largest differences are found between NLSy1-like objects, Pop. A, and broader sources of Pop. B with FWHM(Hβ) $\gtrsim$ 4000 km s^{-1}. The gridding of Sulentic et al.

(2002) is valid for low z (<0.7) quasars. At higher z an adjustment must be made since no sources with FWHM Hβ_{BC} < 3500 km s^{-1} exist above luminosity $\sim 10^{48}$ ergs s^{-1} (Marziani et al. 2009).

- Median spectra were computed for spectral bins from the atlas of Marziani et al. (2003a) who found that Hβ can be described by a Lorentz function in Pop. A sources and by the sum of 2 Gaussians in Pop. B sources (unshifted + broader redshifted components) (Zamfir et al. 2010; Marziani et al. 2010).

- A careful FeII subtraction reveals a blue-shifted Hβ component in some bin A3 sources (i.e. the stongest FeII emitters; Zamfir et al. 2010).

- CIVλ1549 (HIL) and Hβ (LIL) profiles show significant differences in Pop. A. Large CIVλ1549 blueshifts ($\lesssim -1000$ km s^{-1}) are observed in Pop. A *only* (Sulentic et al. 2007). HIL and LIL profiles are more similar in Pop. B sources.

- We do not have Hβ observations for our high-z objects since there are no near IR spectra. We use the results of Marziani et al. (2003b, 2010): they show that the BC of SiIII]λ1892, AlIIIλ1860 and CIVλ1549 lines is similar to the one of Hβ, including the FWHM and profile shape, either Gaussian or Lorentzian. The similarity helps us to define whether an object is Population A or B in this paper.

These observational results point toward three different components in broad line profiles (see Marziani et al. 2010) which can be described as follows:

1. A broad component (BC) showing a roughly symmetric profile with FWHM in the range 1000-5000 km s^{-1}. It is consistent with the component identified by Matsuoka et al. (2008). This broad component dominates LILs in Balmer lines of Pop. A sources while it becomes less prominent in Pop. B. The profile is best modeled by a Lorentzian function in Pop. A sources while Pop. B profiles are better described by a Gaussian (Marziani et al. 2003b).

2. A very broad component (VBC), as seen in LILs and HILs of most pop B sources but is absent from Pop. A profiles. The VBC can be modeled as a Gaussian (FWHM $\sim$ 10000 km s^{-1}) often with a significant shift to the red. It can be called a defining property of Pop. B sources (Marziani et al. 2010). This component is clearly identified in the CIVλ1549 line of Pop. B objects, and is also appreciable on the red side of CIII]λ1909 of Pop. B objects J00103-0037 and J02390-0038.

3. A blueshifted broad component (BBC), defined as the residual emission in the CIVλ1549 line after subtracting a scaled BC Lorentzian profile (Marziani et al. 2010). This blueshifted component is often prominent in CIVλ1549 and Lyα of Pop. A sources. It is much less intense in radio-loud Pop. B sources (Marziani et al. 1996; Punsly 2010; Richards et al. 2010). We model this profile as a blueshifted Gaussian. The Gaussian approximation is probably inappropriate especially if the BCC is strong: this component is believed to be produced in a partially-obscured radial flow, not in a virialized emitting system. In the present work we do not even try to fit the blueshifted in the doubly ionized lines. It is quite obvious from the fits that a possible contribution of this component would be negligible.

Baldwin et al. (1996) presented a similar analysis. Their Fig. 2 organizes spectra in a sequence that is roughly corresponding to E1, going from AlIIIλ1860-strong sources to objects whose spectra show prominent CIII]λ1909 along with weak AlIIIλ1860 (Bachev et al. 2004). Two of the three line components they isolated correspond to the ones we consider in this paper: a blueshifted feature, and a more symmetric, unshifted and relatively narrow component that we call LIL-BC. Less obvious is the correspondence of a third feature, although it appears to be the redshifted part of what we call the VBC.

Several improvements have been introduced since the paper of Baldwin et al. 1996. These improvements are expected to make our analysis easier. First, the definition of a template of FeIII emission (Vestergaard & Wilkes 2001), along with the possibility to model FeII in the 1400–2000 Å spectral region with CLOUDY (Verner et al. 1999, 2004). The analysis of spectra along the E1 sequence allows one to see trends that make the interpretation of the emission line blends easier (Marziani et al. 2010).

4.4. *Expected emission from the various components*

We looked for evidence of three possible components as described above: BC, VBC and BBC only for the most intense HILs: CIVλ1549 and SiIVλ1397. We did not include the contributions of the BBC for the doubly-ionized lines. In the case of Pop. A sources, we indeed assume that the BC contains the vast majority of the light. In the case of Pop. B sources we consider the contribution of the VBC. The AlIIIλ1860 doublet shows no evidence of either a BBC or VBC. There is no obvious BBC for SiIII]λ1892 in the blend. There is evidence of a VBC of CIII]λ1909 extending on the red side of the blend, and this is taken into account. Moreover, we expect that the AlIIIλ1860 doublet is emitted exclusively in the BC, the region where FeII is also emitted. This is empirically confirmed by the aspect of the 1900 blend in many sources, where we do not see any evidence of BBC nor VBC. We remark that the AlIIIλ1860 doublet is relatively unblended, and that a BBC feature as strong as in CIVλ1549 would not easily escape visual detection.The same is also true for SiIII]λ1892. Several fits that included BBC in CIII]λ1909 yielded 0 intensity, implying a large CIVλ1549/CIII]λ1909 (Marziani et al. 2010). The SiIVλ1397 + OIV]λ1402 blend closely resembles the shape of CIVλ1549, suggesting that BBC is relevant, especially for SiIVλ1397 (OIV]λ1402 is expected to give a minority contribution to line emission at the high density derived for the BC; any OIV]λ1402 contribution to the BBC is not relevant to our method). BBC is very

weak or undetectable in the vast majority of the Hβ profiles analyzed in Marziani et al. 2010 (but see Zamfir et al. 2010 for several cases of Hβ BBC), while prominent in Lyα; the Lyα/Hβ ratio in this component is high. In summary, BBC is visually strong in Lyα, CIVλ1549, and SiIVλ1397. HeIIλ1640 in BBC is needed for a self-consistent fit of the CIVλ1549+HeIIλ1640 blend. The VBC of SiIII]λ1892 is poorly constrained, but in the fits where CIII]λ1909 VBC is visible, we always find SiIII]λ1892 < CIII]λ1909, consistent with the high ionization level expected in the VBC region. Some SiIVλ1397 VBC emission is assumed in the Pop. B fits. No VBC emission is expected in AlIIIλ1860 and FeII. These constraints help also to make the fits less ambiguous.

The absence of a VBC makes the decomposition of Pop. A spectra easier. As said earlier, the FeII intensity scale of the template (but FeII is in general weak) is anchored to the UV 191 intensity; similarly the FeIII intensity is set by a feature external to the 1900 Å blend (2080 Å). There is no evidence of BBC of AlIIIλ1860 and SiIII]λ1892; the AlIIIλ1860 doublet profile is mostly unblended and defines the LIL-BC. The additional complication here is the FeIII 1914 line whose intensity is affected by Lyα pumping. Since the shift and FWHM are assumed the same for all lines (and templates) in the 1900 blend, the only free parameters in addition to shift and FWHM are the intensities of 6 components, including the two from the templates, and SiIIλ1814 and AlIIIλ1860 that are not heavily blended. The SPECFIT analysis is especially helpful to measure in a non-subjective way, taking all constraints into account, the two parameters that are most affected by the blend: the intensity of SiIII]λ1892 and CIII]λ1909 (we repeat that any FeIII λ1914 contribution in excess to the one of the adopted template is included in the estimated CIII]λ1909 intensity).

In the case of Pop B, the presence of a VBC does not really complicate the fit as a matter of fact. The CIII]λ1909 line undeniably shows a VBC protruding on the red side of the 1900 blend. In any case, considering that we can expect the VBC to be assimilable to a shifted Gaussian with FWHM $\sim$ 10000km s^{-1}, the unblended part of the CIII]λ1909 VBC provides a strong constraint. The SiIII]λ1892 VBC is certainly the most difficult feature to ascertain, as it buried under SiIII]λ1892 and CIII]λ1909 emission. We rely on the SPECFIT results. that indicate negligible SiIII]λ1892 VBC.

4.5. *Errors*

We identify five sources of error from the conditions for data reduction and methodological considerations described above:

1. A & B atmospheric bands correction (already described in §3.1).

2. Line profile shape, Gaussian or Lorentzian (Pop. A or B). The distinction between Pop. A and B is based on line width with the boundary at FWHM H$\beta \approx$ km s^{-1} in low luminosity quasars and around $\approx$ 5000 km s^{-1} at higher luminosity such as the eight sources presented here. Most of our quasars are unambiguously Pop. A or B because of line width and because Pop. B sources show an Hβ VBC and pop A sources a prominent CIVλ1549 BBC. In these cases only one profile shape (Gaussian or Lorentzian) was fitted.

3. Rest-frame determination using OIλ1304 or CIII]λ1909. In some cases the redshift estimates derived from the two lines do not agree, most likely because of absorptions present in OIλ1304.8 and because this is not a very intense line. The principal impact of uncertainty in the rest frame placement is estimation of the peak wavelength of CIVλ1549. If the line peak differs from λ1549Å, the BC intensity is diminished and we infer a greater contribution from the blue (BBC) component. Similarly, for the blend 1900Å, the rest frame shift may increase or decrease our estimate for the strength of CIII]λ1909 with consequent decrease or increase of the SiIII]λ1892 contribution. This additional source of uncertainty affects J00103-0037, J02287+0002 and J20497-0554.

4. FeII intensity (continuum placement). Broad FeII emission can produce a pseudo-continuum affecting our estimates of emission line intensities. SiIIλ1814 is especially affected in our spectra because it is weak. AlIIIλ1860 is similarly affected when it is weak. The effect is less noticeable for CIVλ1549 since expected FeII emission underlying the CIVλ1549 line is weak also for strong FeII emitters.

5. Broad absorption lines (BALs) in quasars principally affect the blue side of CIVλ1549. We also find an absorption feature between FeIIλ1787 and SiIIλ1814 (eg. Fig. 6). In sources J01225+1339 and J02287+0002 we can only set upper limits for line intensities (since we fit unabsorbed components).

There are other sources of error such as small BC shifts and FWHM variations. We assume that the BC of the SiIII]λ1892, AlIIIλ1860, SiIIλ1814 and CIVλ1549 line has the same FWHM and wavelength shift, although we allow for variations in their relative flux strengths and adopted profile type (Lorentzian for Pop. A and Gaussian for Pop. B). For FeIII(UV34) and FeII we slightly relax this constraint. The FeIII(UV34) and FeII emission is not very strong and the FWHM of individual features is poorly constrained by SPECFIT. In the case of CIII]λ1909 we need to consider the possibility that the profile is narrower because there might be a contribution from different regions: indeed, the SPECFIT routine usually converges toward a narrower profile if the CIII]λ1909 width is not constrained. The effect depends on the strength of the FeIII λ 1914 feature.

The goal of this study is to estimate diagnostic line ratios. A posteriori, we can say that the estimated line ratios are rather insensitive to the emission component profile shape: assuming a Gaussian or Lorentzian profile yields the same ratio for the strongest lines (i.e., CIVλ1549, SiIII]λ1892, AlIIIλ1860) upon which our analysis is based (with an uncertainty of $\sim$10%). The same conclusion applies to the redshift uncertainty. Only in the case of J02287+0002 the redshift difference produces

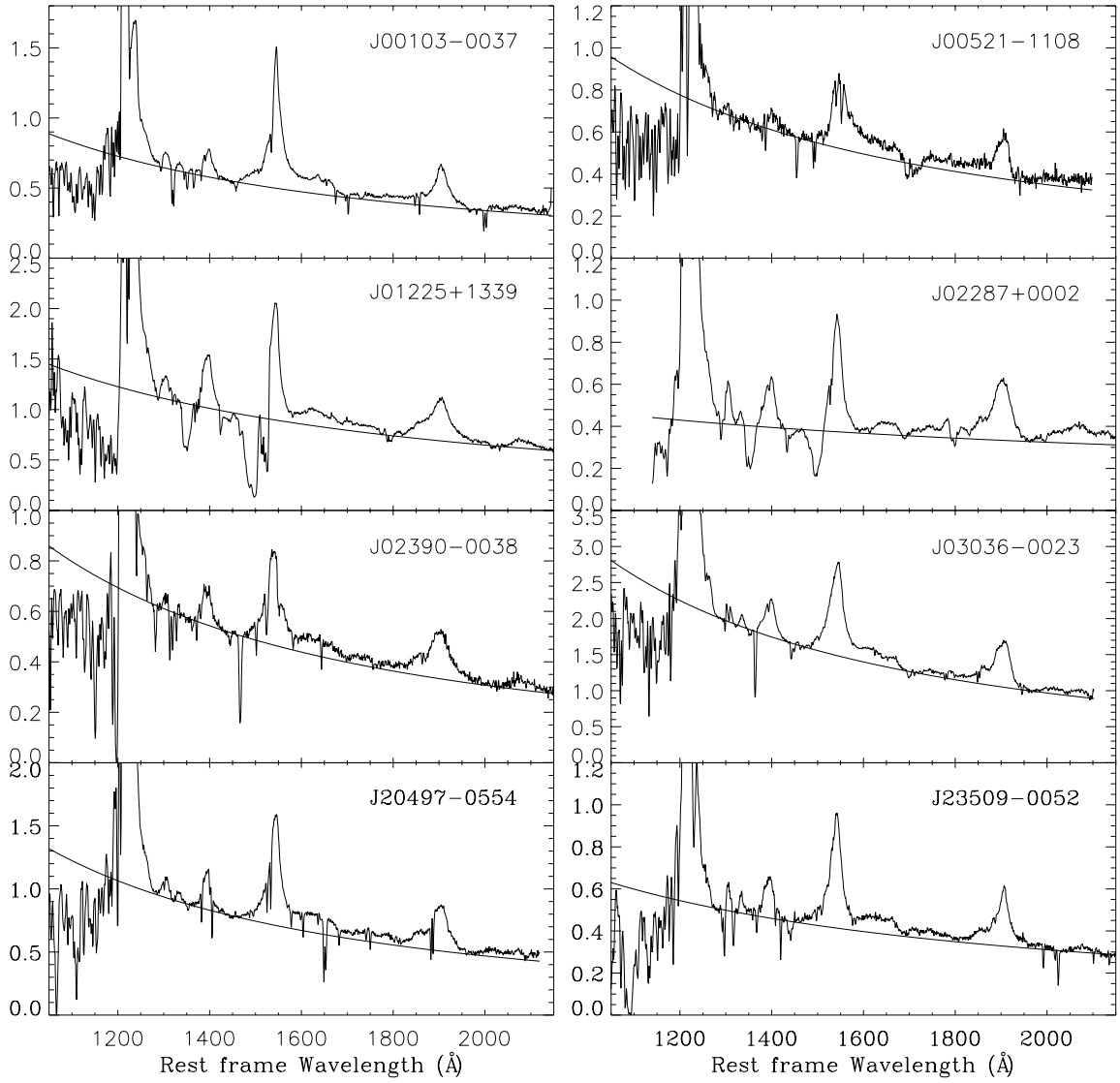

FIG. 3.— Sample of 8 VLT spectra in rest frame wavelength. Abscissa is rest frame in Å, ordinate is specific flux in the rest frame in units 10^{-13} ergs s^{-1} cm^{-2} Å^{-1}.

a significant effect due to a $\Delta z \approx 0.16$. However, we adopt the fit based on OIλ1304: the alternative fit produces line ratios that are of not obvious interpretation and at variance with respect to the other sources. The most serious sources of error remain effects of A/B band overlap for SiIIλ1814 and the presence of a BAL for CIVλ1549.

5. RESULTS OF LINE COMPONENT ANALYSIS ON INDIVIDUAL OBJECTS

In Figures from 4 to 6 we show our best fits for the VLT sample taking into account the considerations described in §4. The fits of SiIVλ1397 are shown in Fig. 7 and the intensity values and equivalent widths are in Tables 3 and 4. We present here a phenomenological description of the fits. The line profiles, intensities and line ratios usually follow the trends of Pop. A or B sources, although in some objects there are features that are ambiguous (for example the line shape). In these cases however, we have assigned Pop. A or B type on the basis of the FWHM (see Cols. 5 and 6 of Table 7).

5.1. *Pop. A Objects*

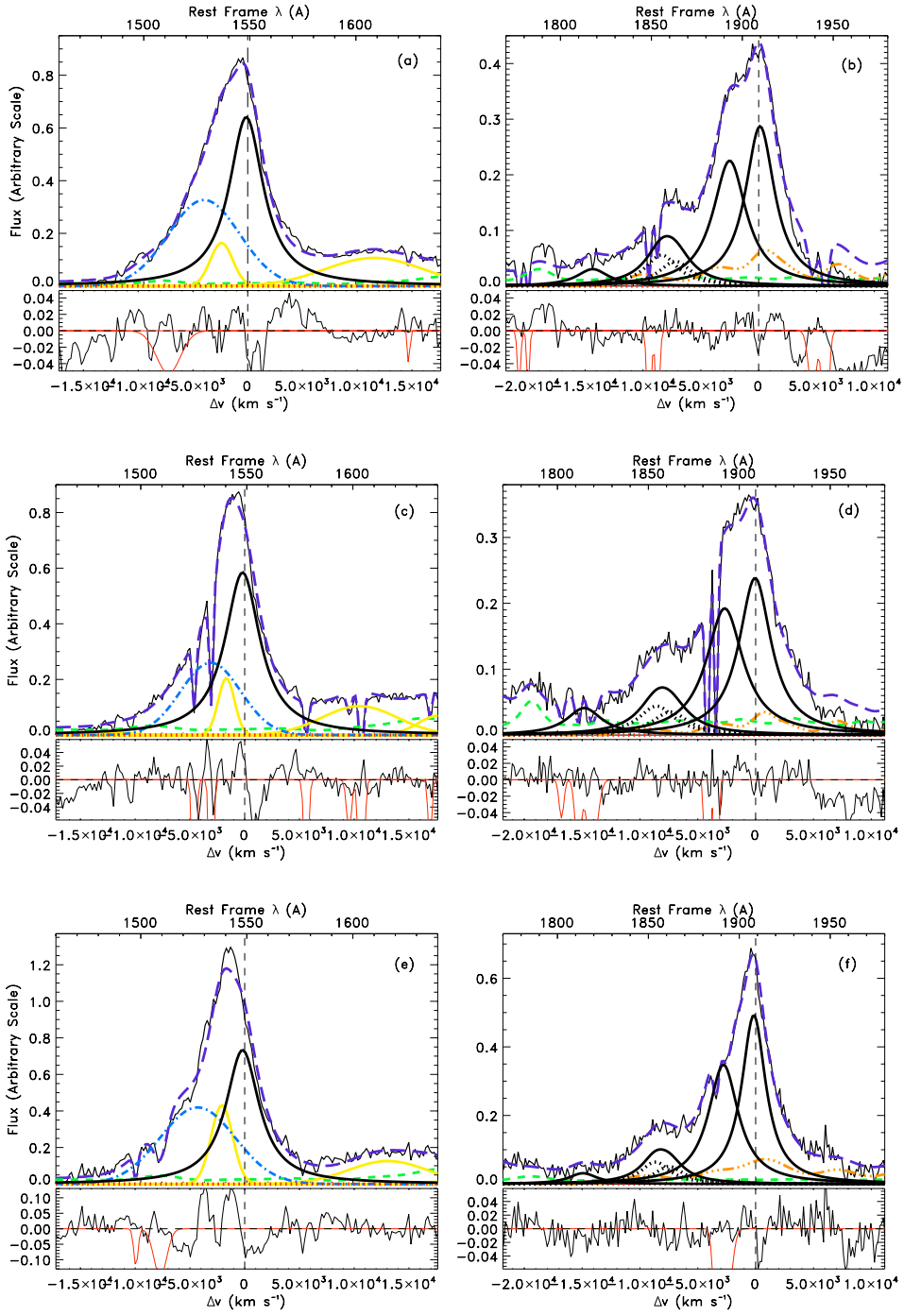

FIG. 4.— Fits for Pop. A objects: up J03036-0023, middle J20497-0554, low J23509-0052. Upper panels show the fits and the lower pannels under the fits show the residuals and also the fitted absorptions lines. Upper abscissa is rest frame wavelength in Å, lower abscissa is in velocity units, ordinate is specific flux in arbitrary units. Vertical dashed line is the restframe for CIVλ1549 and CIII]λ1909. Long dashed line is the fit, solid dark lines are the broad components: CIVλ1549 in left panels and CIII]λ1909, SiIII]λ1892, AlIIIλ1860, SiIIλ1814 in right panels. Dotted dark lines under AlIIIλ1860 show the doublet. Short dashed line is FeII. FeIII is shown in dash-triple-dot line in the right panels. Dash-dot line in the left panels is the blue-shifted component of CIVλ1549 while dotted line is the very broad component, present also in CIII]λ1909 for Pop. B objects. In the left panels we show with faint lines the contribution of NIVλ1486, SiIIλ1533 and HeIIλ1640 core and blue-shifted components. For colors see online figures.

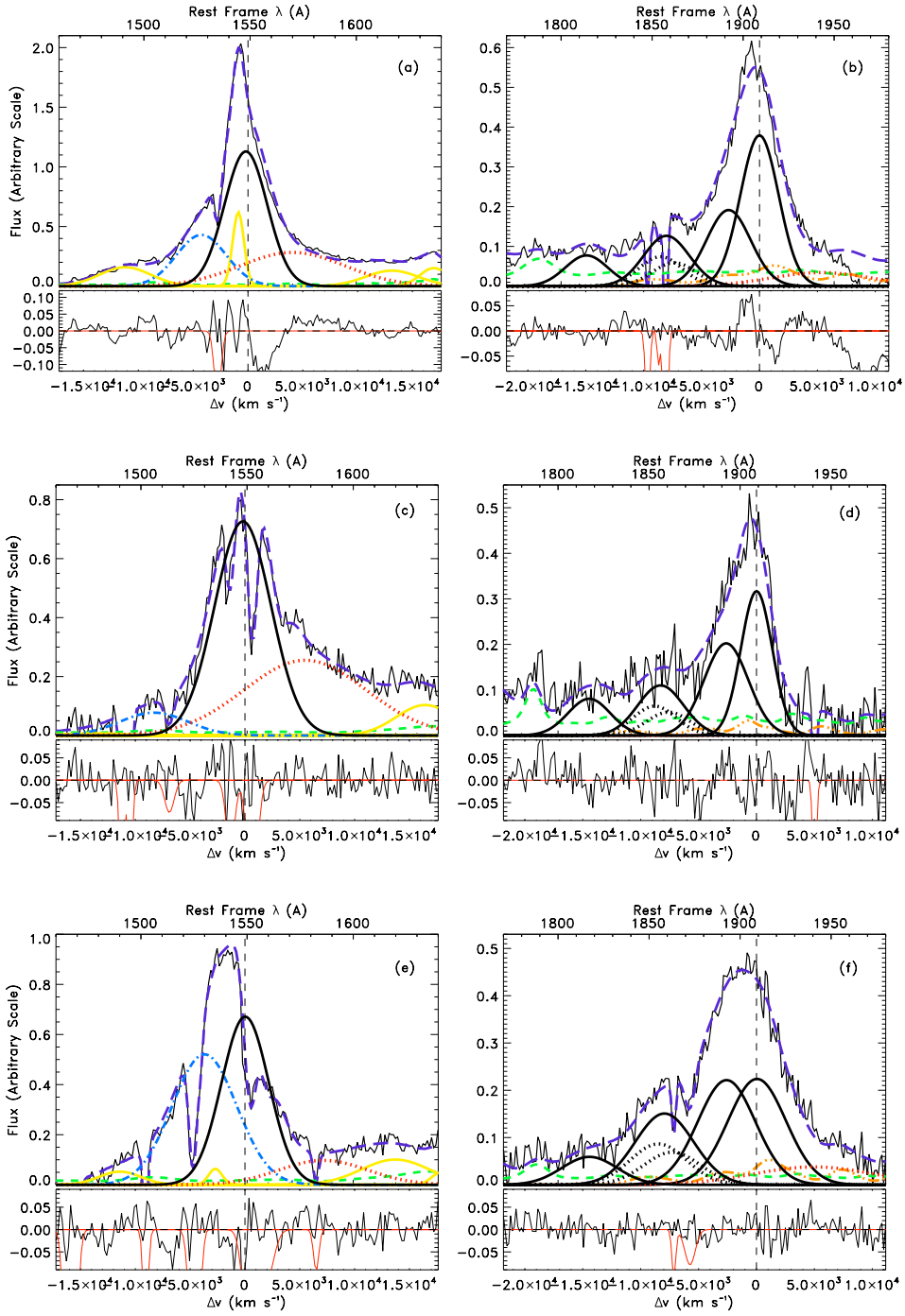

FIG. 5.— Fits for Pop. B objects: up J00103-0037, middle J00521-1108, low J02390-0038. Units and meaning of symbols are the same of Fig. 4.

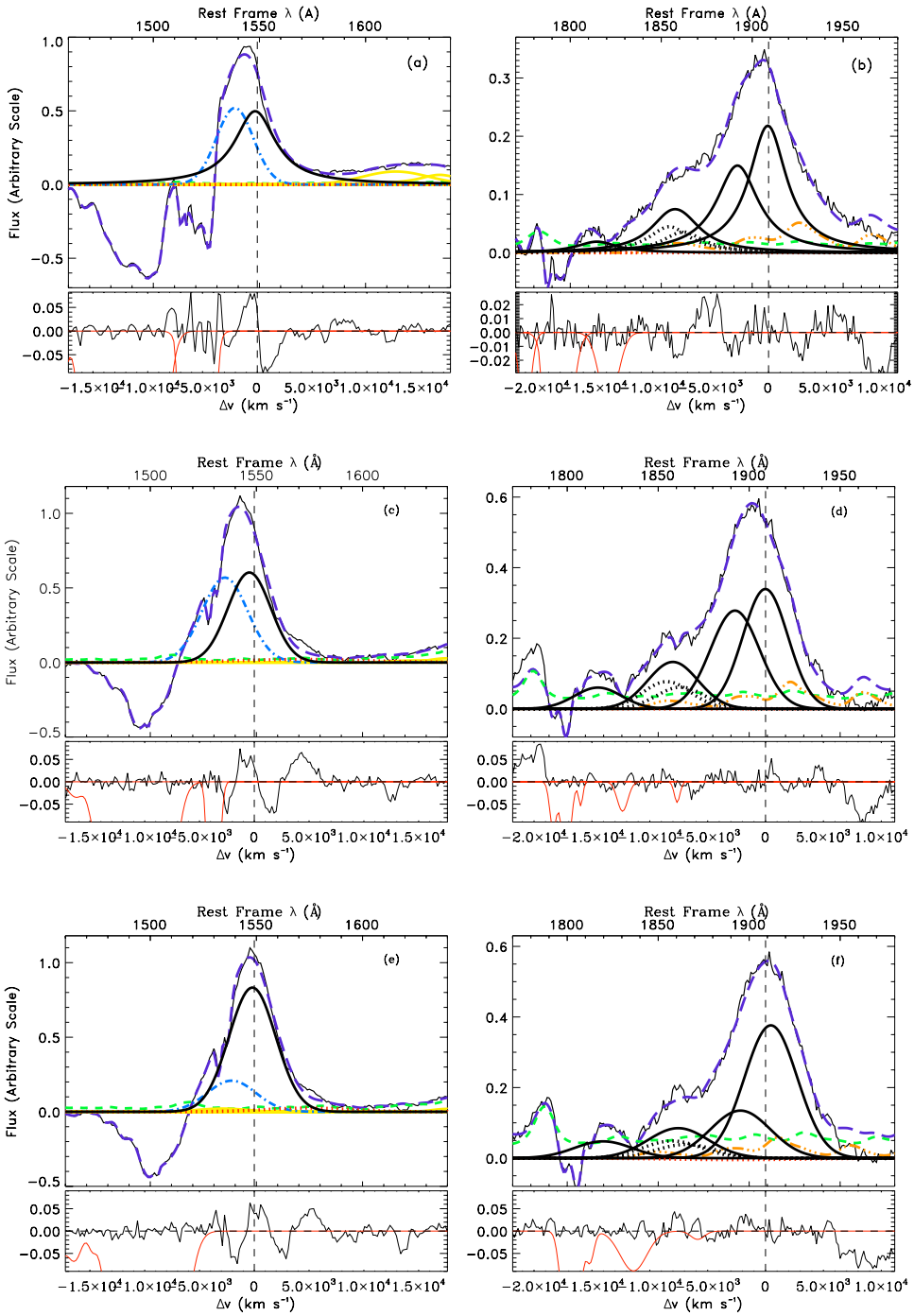

FIG. 6.— Fits for BAL quasars: up J01225+1339, middle J02287+0002 using $z_{OI\lambda1304}$ rest frame, low J02287+0002 using $z_{CIII\lambda1909}$ rest frame. Note in J02287+0002 the line displacement with the consequently line intensity changes, specially in CIII]λ1909, SiIII]λ1892 and CIVλ1549 broad and blue-shifted components. Units and symbols are the same as in Fig. 4.

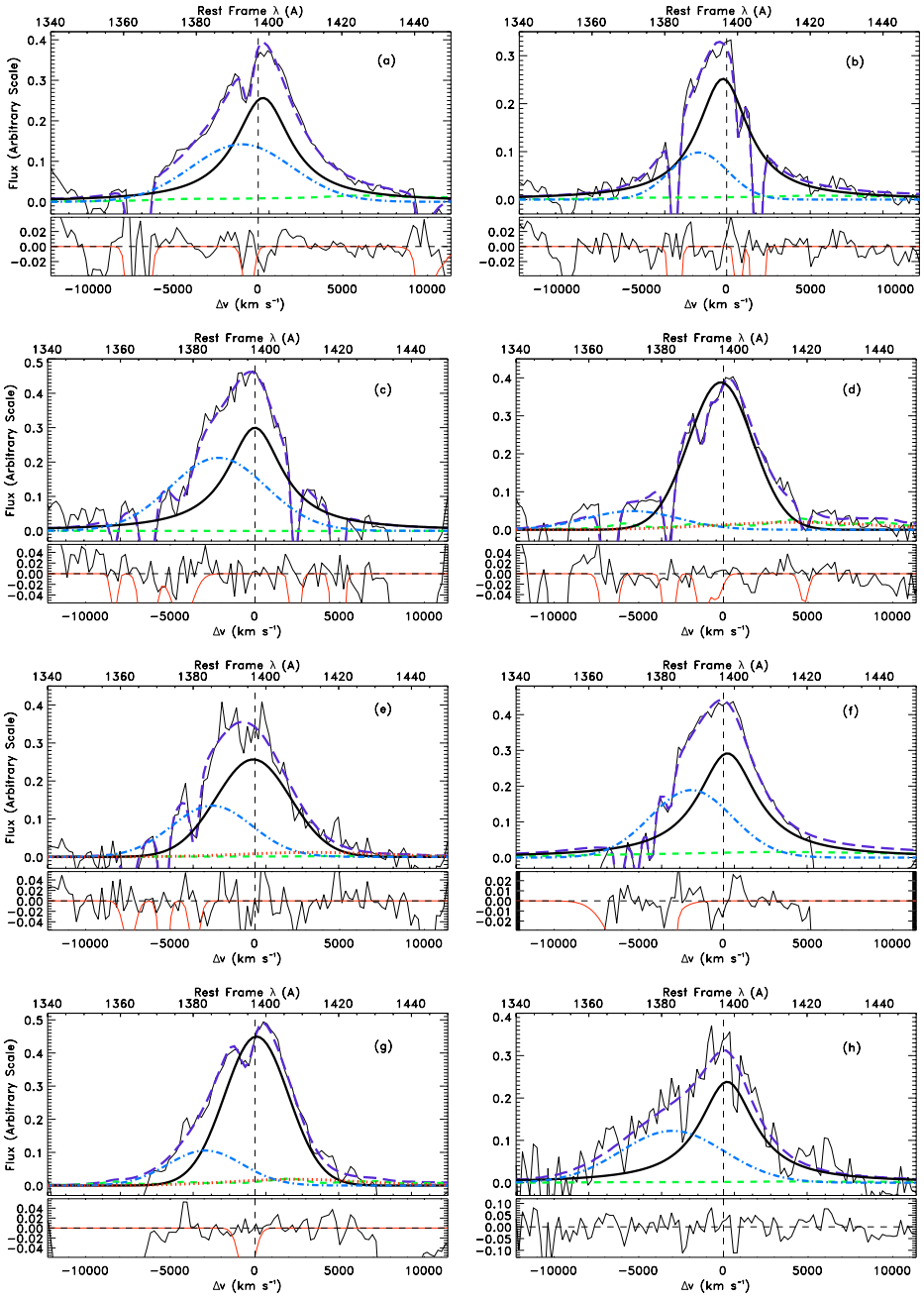

FIG. 7.— Fits for SiIVλ1397: (a) J03036-0023, (b) J20497-0554, (c) 23509-0052, (d) J00103-0037, (e) J02390-0038, (f) J01225+1339, (g) J02287+0002 and (h) J12014+0116. We do not measure SiIVλ1397 for J00521–1108 and 3C 390.3 because they have low S/N. We asume that the profile of SiIVλ1397 can be fitted with the same three possible components (core, blue-shifted and red-shifted) as in the case of CIVλ1549. Units and symbols are the same as in Fig. 4.

TABLE 3
Line Fluxes [a]

Object	CIII]λ1909		SiIII]λ1892	AlIIIλ1860	SiIIλ1814	CIVλ1549			
	BC	*VBC*				*BC*	*blue*	*VBC*	
J00103-0037	4.99 ± 2.11	1.18 ± 1.38 *	2.91 ± 1.03	1.99 ± 0.81	1.13 ± 0.82 :	14.25 ± 8.34	6.32 ± 1.80	8.71 ± 8.24	4
J00521-1108	3.08 ± 0.36	0.01 ± 0.12 *	2.77 ± 0.66	1.55 ± 0.85	1.06 ± 0.90	10.89 ± 2.37	1.40 ± 2.23	8.27 ± 2.63	
J01225+1339	10.71 ± 1.35	...	8.26 ± 1.33	4.35 ± 2.09	1.01 ± 0.98	22.73 ± 6.04	14.21 ± 1.52	...	1
J02287+0002 (1)	5.28 ± 1.56	0.01 ± 0.02 *	4.70 ± 2.01	2.29 ± 1.13	0.98 ± 0.79	7.64 ± 5.00	7.66 ± 2.32	0.77 ± 1.63 *	4
J02287+0002 (2)	6.86 ± 1.56	0.02 ± 0.02 *	2.78 ± 2.01	1.77 ± 1.13	0.94 ± 0.79	11.48 ± 5.00	2.99 ± 2.32	0.64 ± 1.63 *	4
J02390-0038	3.57 ± 0.78	1.26 ± 0.88	3.50 ± 0.40	2.41 ± 0.64	0.90 ± 0.83	7.51 ± 1.25	7.92 ± 1.37	2.04 ± 1.52	2
J03036-0023	13.24 ± 1.09	...	11.82 ± 1.21	5.17 ± 1.48	1.53 ± 1.16 :	29.46 ± 3.54	20.60 ± 3.34	...	1
J20497-0554	8.04 ± 1.09	...	7.43 ± 0.56	3.01 ± 1.25	1.52 ± 1.51 :	18.39 ± 2.17	9.23 ± 2.24	...	6
J23509-0052	5.24 ± 1.21	...	4.61 ± 1.62	1.50 ± 0.50	0.40 ± 0.36	9.24 ± 1.17	7.80 ± 2.36	...	3
Extreme Objects									
J12014+01161	5.52 ± 1.07	...	16.16 ± 5.90	14.03 ± 2.54	4.90 ± 2.95	21.18 ± 12.48	29.37 ± 9.98	...	1
3C 390.3	3.74 ± 1.15	4.30 ± 0.68	2.32 ± 0.43	0.23 ± 0.32 *	0.40 ± 0.48 *	30.04 ± 4.99	...	56.44 ± 10.66	

Note. — (a) Units are 10^{-14} ergs s^{-1} cm^{-2} Å^{-1}. (1) Considering $z_{OI\lambda1304}$. (2) Considering $z_{CIII]\lambda1909}$. (:) SiIIλ1814 approximated values due the line is affected by telluric abs for J00521-1108 and 3c390.3 because they have low S/N. (*) Consistent with no emission.

- J03036-0023 – We estimate for this source a FWHM(BC)∼3700 km s^{-1} and we use a Lorentzian function to fit the broad lines. The peak of CIVλ1549 is blueshifted and requires a strong BBC (Fig. 4(a)). The bump on the red side of CIVλ1549 can be accounted for by HeIIλ4686 BC and BBC. There is no evidence for a red shifted component in CIII]λ1909 (Fig. 4(b)). AlIIIλ1860 is prominent. Unfortunately the blue wing of SiIIλ1814 and the red wing of FeIIλ1787 are affected by A band absorption.

- J20497-0554 – This source shows FWHM(BC)∼3800 km s^{-1}. As for J03036-0023, the CIVλ1549 line can be accounted for by an unshifted BC (assumed Lorentzian) of a considerably contribution of a BBC (Fig. 4(c)). We see a prominent AlIIIλ1860 line and FeIIλ1787 (Fig. 4(d)). SiIII]λ1892 is affected by several narrow absorption lines; however, it is obviously strong. The lack of a red wing on CIII]λ1909 suggests that no VBC is present.

- J23509-0052 – This source has FWHM(BC)∼3600 km s^{-1}. CIVλ1549 shows a slight blue asymmetry with a BBC (Fig. 4(e)) required to model it. The contribution of FeII is small and FeIIλ1787 is weak (Fig. 4(f)). CIII]λ1909 is very strong. AlIIIλ1860 is affected by A band absorption; the profile we fit is probably an upper limit. This object could well belong to spectral type A1 that includes Pop. A sources with the lowest $R_{\rm FeII}(\lesssim 0.5)$.

5.2. *Pop. B Objects*

.

- J00103-0037 – This source has a FWHM(BC)∼4500 kms^{-1}. The red side of CIVλ1549 is blended with HeIIλ4686. Fitting a BC with no shift plus a BBC to CIVλ1549 leaves a very large residual on the red side. A very broad redshifted component (VBC) is needed to model the spectrum (Fig.5 (a)). The faint narrow line under CIVλ1549 can be explained as the narrow component (NC) of CIVλ1549(see Sulentic et al. 2007). The presence of a similar NC in CIII]λ1909 could possible explain the large residual seen ∼1900. We specifically note the prominent CIII]λ1909 emission and weak (but detected) AlIIIλ1860 (Fig. 5(b)). The FeII "bump" at 1787 Å(UV 191) is appreciable. Fainter FeII emission is relatively unimportant because FeII creates a pseudo-continuum. SiIIλ1814 is compromised by A-band absorption. The blend at 1900Å includes a CIII]λ1909 VBC and the fit indicates CIVλ1549/ CIII]λ1909 (VBC) ≈ 7 which is reasonable.

- J00521-1108 – This source shows the noisiest spectrum in the sample. We fit a FWHM(BC) ∼ 5300 km s^{-1} with CIVλ1549 requiring a large VBC to account for the red wing. (Fig. 5(c)). Absorption features seriously affect the CIVλ1549 profile. The profile of CIII]λ1909 is strongly asymmetric due to some sort of absorption on the red side. AlIIIλ1860 is weak consistent with pop. B (Fig. 5(d)).

- J02390-0038 – This objects has a somewhat atypical Pop. B spectrum due to a very strong BBC in CIVλ1549 (Figure 5(e)). This source has a FWHM(BC)∼ 5400 km s^{-1}. Consistent with pop. B we find FeIIλ1787 to be weaker than SiIIλ1814. CIII]λ1909 is flat topped and has a very similar intensity as SiIII]λ1892. Both CIVλ1549 and CIII]λ1909 it show red wings indicating VBC emission. The A band absorption lies between SiIII]λ1892 and AlIIIλ1860 (Fig. 5(f)) producing a possible overestimation of AlIIIλ1860.

5.3. *BAL QSOs*

- J01225+1339 – CIVλ1549 is highly affected by two broad absorption lines (Fig. 6(a)) with blueshifts of 5200 and 10800 km s^{-1} at peak absorption with equivalent widths/FWHM -12Å / 3900 km s^{-1} and -25Å/5200 km s^{-1}, respectively. The blueshift of the CIVλ1549 peak leads us to suspect a large blueshifted BBC emission component. The 1900 Å blend shows absorptions coincident with FeIIλ1787 and the blue side of SiIIλ1814 which is however unambiguously detected (Fig. 6(b)). AlIIIλ1860 is

TABLE 4
EQUIVALENT WIDTHS.

Object	CIII]λ1909$_{BC}$	CIII]λ1909$_{Tot}$	SiIII]λ1892	AlIIIλ1860	SiIIλ1814	CIVλ1549$_{BC}$	CIVλ1549$_{Tot}$	SiIVλ1397$_{BC}$	SiIVλ1397$_{Tot}$
J00103-0037	13.7 ± 5.8	17.1 ± 7.2	7.9 ± 3.0	5.3 ± 2.8	2.9 ± 2.5 :	29.0 ± 16.1	59.6 ± 24.4	7.4 ± 4.32	9.68 ± 6.74
J00521-1108	8.2 ± 1.5	8.2 ± 2.4	7.3 ± 2.5	4.0 ± 2.6	2.6 ± 3.1	21.0 ± 18.9	40.1 ± 26.8	...	...
J01225+1339	15.3 ± 3.5	...	11.6 ± 3.1	6.0 ± 3.6	1.4 ± 2.3	25.5 ± 9.1	41.6 ± 9.7	11.1 ± 3.95	17.74 ± 4.71
J02287+0002 (1)	15.9 ± 5.3	15.9 ± 5.3	14.1 ± 6.6	6.8 ± 4.0	2.9 ± 2.6	20.4 ± 10.5	42.9 ± 16.8	12.7 ± 3.04	17.30 ± 4.03
J02287+0002 (2)	20.5 ± 5.3	20.5 ± 5.3	8.3 ± 6.6	5.2 ± 4.0	2.7 ± 2.6	30.8 ± 10.5	40.6 ± 16.8	12.7 ± 3.04	17.85 ± 4.03
J02390-0038	10.8 ± 3.3	14.7 ± 4.5	10.4 ± 2.0	7.0 ± 2.4	2.5 ± 2.5	16.3 ± 4.1	37.7 ± 7.0	4.9 ± 1.32	11.72 ± 4.15
J03036-0023	12.4 ± 1.8	...	10.9 ± 1.8	4.6 ± 1.6	1.3 ± 1.1 :	19.7 ± 3.7	33.3 ± 4.8	6.4 ± 1.46	10.71 ± 2.94
J20497-0554	15.5 ± 3.5	...	14.1 ± 2.3	5.6 ± 2.9	2.7 ± 2.9 :	25.4 ± 5.6	38.1 ± 7.1	8.0 ± 3.75	10.34 ± 4.04
J23509-0052	15.8 ± 4.0	...	13.7 ± 5.3	4.4 ± 1.8	1.1 ± 0.9	22.0 ± 4.2	40.5 ± 10.6	7.7 ± 3.73	14.02 ± 5.10
Extreme Objects									
J12014+0116	2.9 ± 0.9	...	8.4 ± 4.1	7.1 ± 2.0	2.4 ± 1.9	8.2 ± 5.6	19.4 ± 7.4	6.03 ± 2.76	9.85 ± 4.37
3C 390.3	13.1 ± 4.3	28.4 ± 6.2	7.9 ± 3.3	0.7 ± 0.8	1.2 ± 1.3	49.1 ± 8.1	147.2 ± 19.4	...	...

NOTE. — (1) Considering $z_{OIA1304}$. (2) Considering $z_{CIII]\lambda1909}$. (:) SiIIλ1814 approximated values due the line is affected by telluric absorptions.

prominent which implies that this a Pop. A source. The FWHM(BC) ~ 4400 km s^{-1} is consistent with a high-luminosity Pop. A source. It is also possible that this BAL QSO is an outlier like Mark 231 at low-z (Sulentic et al. 2006), in other words an extreme Pop. A object. The CIII]λ1909 is well fitted with a Lorentzian profile. Broad A band atmospheric absorption lies over SiIII]λ1892.

- J02287+0002 – This object has a very complex spectrum. On one side it has a FWHM(BC) ≈ 4700 km s^{-1} which is typical of low-luminosity Pop. B and the lines profiles are better fitted with Gaussians. On the other side, however, it shows features that are typical of extreme Pop. A sources: prominent FeIIλ1787, strong AlIIIλ1860, no CIII]λ1909 VBC (Fig. 6(d)). Considering that the FWHM limit between Pop. A and B is increasing with luminosity, the FWHM(BC) is within the limit of Pop. A. The CIII]λ1909 line is not very flat topped but the similar intensities of CIII]λ1909 and SiIII]λ1892 remind the case of J02390-0038. Also because it has a strong blue-shifted component in CIVλ1549 atypical to Pop. B objects (Fig. 6(c)).

  The estimated rest frame of this quasar differs by $\sim$ 1400 km s^{-1} using OIλ1304 and CIII]λ1909. This is the largest discrepancy in our sample. In order to evaluate the effect of the z discrepancy we performed two fits using both rest frames. Figs. 6(a) and (b) use the CIII]λ1909 restframe. In the 1900 Å blend, we found a contribution of SiIII]λ1892 similar to CIII]λ1909. If we use the OIλ1304 inferred rest frame we show in Figs. 6(e) and (f) that CIII]λ1909 becomes stronger with a resultant decrease of SiIII]λ1892. A similar effect occurs for CIVλ1549 broad and blue-shifted components.

  The CIVλ1549 BAL shows a blueshift of 9100 km s^{-1}at deepest absorption, a EW of –14 Å and a FWHM of 4600 km s^{-1}.

Summing up, we are able to assign an A/B identification to all sources in our sample. The two BAL QSOs appear as objects of extreme Pop. A. We remind that the identification of CIII]λ1909 in the BAL QSOs and in sources with strong AlIIIλ1860 is debatable (Hartig and Baldwin 1986): strong FeIII 1914 could take the place of most CIII]λ1909 emission.

6. ESTIMATION OF PHYSICAL CONDITIONS IN THE EMITTING REGIONS

6.1. CLOUDY *Simulations*

We computed a multidimensional grid of CLOUDY (Ferland et al. 1998) simulations, (see also Korista et al. 1997) to derive U and $n_{\rm H}$ from our spectral measurements. Simulations span the density range $7.00 \leq \log\, n_{\rm H} \leq 14.00$, and $-4.50 \leq \log U \leq 00.00$, in intervals of 0.25. Each simulation was computed for a fixed ionization parameter and density assuming plane parallel geometry. The 2D grid of simulations was repeated twice assuming $N_{\rm c}= 10^{23}$ and 10^{24} cm^{-2}. Several cases were computed also for $N_{\rm c}= 10^{25}$cm^{-2}. Metallicity was assumed to be either solar or five times solar. Two alternative input continua were used: 1) the standard AGN continuum of CLOUDY which is equivalent to the continuum described by Mathews and Ferland (1987) and 2) the low-z quasar continuum of Laor et al. (1997a). Computed line ratios are almost identical for fixed (U, $n_{\rm H}$). However the ionizing luminosity differs by more than a factor of 2 for a fixed specific continuum luminosity. The contour plots showing the distributions of CIII]λ1909/SiIII]λ1892, AlIIIλ1860/SiIII]λ1892, SiIIλ1814/SiIII]λ1892, SiIVλ1397/SiIII]λ1892, CIVλ1549/AlIIIλ1860and CIVλ1549/SiIII]λ1892 (Fig. 8) are generated from $29 \times 19 = 551$ simulations and assume a standard set of simulations using a Mathews and Ferland (1987) continuum, $N_c = 10^{23}$ cm^{-2}, and solar metallicity. The CLOUDY 08.00 computations included a model of the Fe^{+} ion with 371 levels. The UV FeII template, described in §4.2 is based on a suitable CLOUDY simulation. Even if a relationship is very likely between the dense low ionization gas producing our diagnostic lines and FeII emission (supported observationally) our diagnostics do not use any FeII computation. The weak line OIλ1304 is used only for rest frame estimation and not for diagnostic considerations.

Apart from the hypothesis of plane-parallel geometry, no inferences are made about the actual distribution, location, and kinematics of the line emitting gas. The assumption of constant density is crude. If gas is distributed in clouds then magnetic confinement appears to be unnecessary to avoid cloud dispersion from pressure imbalance or cloud shear associated with a hot confining medium. Magnetic confinement could make density uniform within the cloud (Rees 1987; Bottorff and Ferland 2000).

6.2. *Intermediate Ionization Lines in the Blend at λ1900*

The ratio CIII]λ1909/SiIII]λ1892 is density dependent because the transition probabilities of the two lines are so different: 114 s^{-1} vs 12600 s^{-1} (see Table 1). The forbidden lines at 1883Å and 1907Å have such low transition probabilities that they are collisionally quenched at much lower density and will not be considered. Line ratios like CIII]λ1909/SiIII]λ1892 are useful diagnostics in a rather narrow range of density which depends on the transition probabilities. Above the critical density, emission lines originating from forbidden or semi-forbidden transitions become collisionally quenched, and hence weaker than lines for which collisional effects are still negligible. CIII]λ1909 is clearly unsuitable as a diagnostic for $n_{\rm e} \gg 10^{11}$ cm^{-3}, as the CIII]λ1909/SiIII]λ1892 $\rightarrow 0$. Feldman et al. (1992) gives critical density of SiIII]λ1892 $n_e \sim 2 \cdot 10^{11}$ cm^{-3}. AlIIIλ1860 is a permitted transition with large transition probability ($A \sim 5{\cdot}10^{8}$ s^{-1}) and has very-high critical density (i.e., its equivalent width goes to zero toward thermodynamic equilibrium, which occurs at very high density, when all line emission is collisionally quenched). Our 2D array of CLOUDY simulations shows that the ratio AlIIIλ1860/SiIII]λ1892 is well suited to sample the density range $10^{10} - 10^{12.5}$ cm^{-3}. Within this range the SiIII]λ1892 intensity decreases smoothly by a factor 10; above the upper limit in density, the predicted intensity of SiIII]λ1892 decreases. This corresponds to the densest, low ionization emitting regions

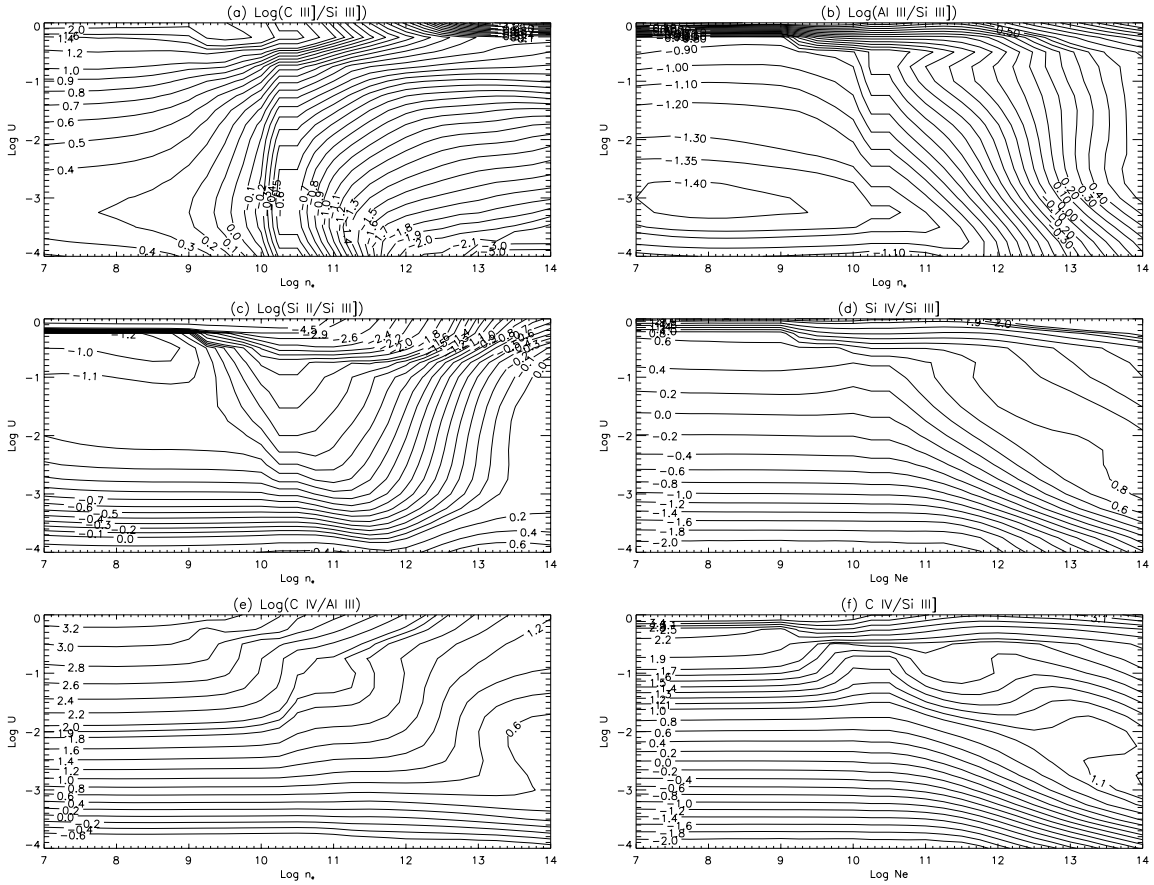

FIG. 8.— Isocontours for the ratios (a) log(CIII]λ1909/SiIII]λ1892), (b) log(AlIIIλ1860/SiIII]λ1892), (c) log(SiIIλ1814/SiIII]λ1892), (d) log(SiIVλ1397/SiIII]λ1892), (e) log(CIVλ1549/AlIIIλ1860), and (f) log(CIVλ1549/SiIII]λ1892) derived from CLOUDY simulations. Abscissa is electron density in cm^{-3}, ordinate is the ionization parameter, both in logarithm scale.

likely associated to the production of FeII.

Intermediate-ionization lines such as CIII]λ1909, AlIIIλ1860, SiIII]λ1892 and SiIVλ1397avoid the issue of collisional ionization (invoked for the production of low-ionization species by S. Collin and collaborators, as mentioned in the introduction).

The widely separated doublet AlIIIλ1860 is expected to be produced entirely in the fully ionized zone (Laor et al. 1997b). CLOUDY simulations confirm this suggestion. Figure 9 (top panel) shows the ionic fraction as a function of the geometrical depth in a cloud (or slab) of fixed column density (N_c= 10^{23} cm^{-2}) and density (n_H= $10^{12.5}cm^{-2}$). As it can be seen, Al^{++}, Fe^{++}, and Si^{++} share a region of dominance deep in the cloud, close to the end of the Strömgren sphere. Beyond, in the partially-ionized zone (PIZ) there is, as by definition, a significant fraction of ionized hydrogen. The dominant ionic stages of Si and Fe become Fe^{+} and Si^{+}. It is very appropriate to consider the AlIIIλ1860/SiIII]λ1892 ratio since the two lines are apparently emitted in the very same zones within the gas slab. Available reverberation mapping results may support this interpretation but are rather difficult to extrapolate since they are limited to an handful of low luminosity objects. The main finding is that CIII]λ1909 responds to continuum changes on timescales much longer than CIVλ1549 and other HILs. This results comes from the analysis of total CIII]λ1909 + SiIII]λ1892 in NGC 3783 (Onken & Peterson 2002), from the CIII]λ1909 of NGC 4151 (Metzroth et al. 2006) and of NGC 5548. It is intriguing that the CIII]λ1909 cross-correlation delay in NGC 5548 (by far the best studied object) is even larger than that of Hβ (32 ld vs. 20 ld; Peterson et al. 2002; Clavel et al. 1991). For fixed density, lines of higher ionization form at higher photon flux. The C^{+}, Al^{+}, Si^{+} ionization potential are 24, 18, and 16 eV respectively. These comparable ionization potentials are well below the one of HILs, $X^{i-1} \gtrsim 50$ eV. However, the much lower CIII]λ1909 critical density implies that the CIII]λ1909 line should be formed farther out than SiIII]λ1892 and AlIIIλ1860 if all these lines are produced under similar ionization conditions.

6.3. *The SiII Contribution to the UV Spectrum of Quasars*

AGN have a rather rich singly-ionized silicon spectrum in the range 1000-2000 Å, due to several resonant tran-

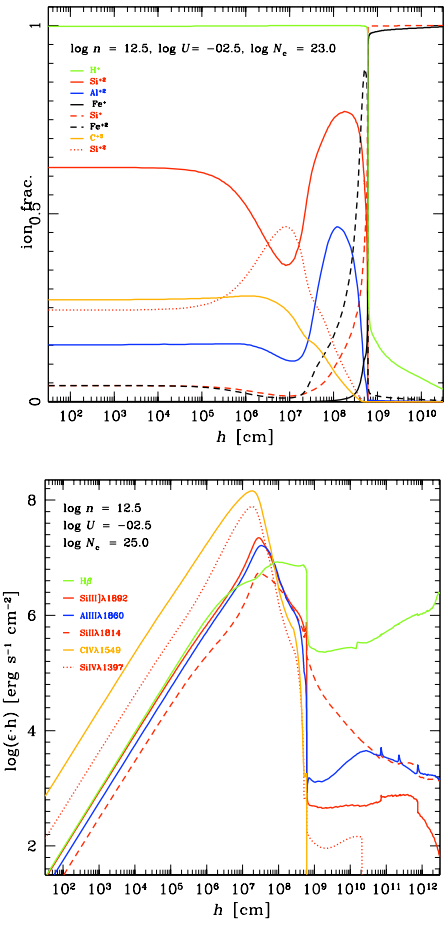

FIG. 9.— Top: Ionic Fractions as a function of the geometric depth h in the gas slab. Bottom: Line emissivity per unit volume in units of ergs s^{-1} cm^{-3} multiplied by depth.

sitions from the ground term $3s^2 3p^{12}P^0$ to terms associated to the $3s^1 3p^2$ (λ1814 and λ1304), $3s^2 4s$ (λ1531), $3s^2 3d$ (λ1263) electronic configurations. A feature on the red side of Lyα, at 1263 Å is detected in several Pop. A sources like I Zw 1 (Marziani et al. 2010).

The λ1309 feature is partially blended with the OI triplet associated with a Bowen fluorescence mechanism from HI Lyβ. The λ1309 line is well resolved in sources like I Zw 1 with the extension of the broad λ1309 feature suggesting significant SiII emission around λ1309. The λ1531 feature is blended with CIVλ1549. High S/N spectra of low redshift sources from HST (Laor et al. 1994) as well as for quasars at $z \approx 4$ (Constantin et al. 2002) indicate that the feature is very weak in most sources.

The SiII feature at λ1814 is detected in at least four of the five quasars studied by Laor et al. (1994). In the 6 objects used for the E1 sequence of Marziani et al. (2010), it is detected without reasonable doubt in I Zw 1 only. However this has to do more with the poor S/N of the 1900 Å region than of anything else; good S/N HST spectra show an unambiguous detection in Akn 120 and Mark 509, for example. Early detection of the UV SiII lines from IUE observations suggested collisional excitation and no relevant fluorescence effects (as observed in type Ia supernovæ; Dumont and Mathez 1981). Fluorescence effects and recombination are revealed by optical lines which are emitted through several cascade routes to the ground state. However, a median spectrum of A2 quasars with S/N $\approx$ 200 (Zamfir et al. 2010) barely detects any expected emission feature in the range 4000-6500 Å. The prominence of the λ1814 feature may then be associated to the relatively low temperature believed to exist in the innermost part of the line emitting "cloud", $T_e \sim 5000 - 8000°$ K. We may consider the equivalent width (W) ratio between the doublet lines at 1264 and at 1814 Å both due to a $^2D_{\frac{5}{2}} \rightarrow^2 P_{\frac{3}{2}}$ transition; in the simplest case we have: $W_{1263}/W_{1814} \approx (N_{\rm u,1264}/N_{\rm u,1814})\,(f_{1264}/f_{1816})\,(\lambda_{1264}/\lambda_{1816})^2 \approx 0.485 \frac{f_{1264}}{f_{1816}} e^{-\frac{\Delta E}{kT}} \approx 0.27$ if $T = 5000°$, where f is the oscillator strength, $N_{\rm u}$ are the density of the upper electronic levels giving rise to the two lines, and the energy difference between the transitions is $\Delta E \approx 3$ eV.

6.4. *Use of SiIVλ1397, CIVλ1549 and SiIIλ1814*

The same caveats mentioned for the ratio CIII]λ1909/SiIII]λ1892 apply to the AlIIIλ1860/SiIII]λ1892 ratio as well. The ground term $^1S_0$ has energy 16 eV and 24 eV for Si^{+2} and C^{+2} respectively. A dependence on the ionization parameter is expected, as already mentioned. However, given the similarity in the ionization structure of the photo-ionized slab, it is after all not surprising that the ratio AlIIIλ1860/SiIII]λ1892 is almost insensitive to the ionization parameter over a wide range of density. We remind that the detection of strong AlIIIλ1860 *alone* already suggests that we are considering very high density emitting gas even if metallicity is super-solar. Simulations indicate that AlIIIλ1860 should increase smoothly with density and be weakest in canonical BLR if the density is $n_{\rm H} \sim 10^9$ cm^{-3} (cf. Korista et al. 1997).

The ratio AlIIIλ1860/SiIII]λ1892 is therefore diagnosing high density gas, while the CIII]λ1909/SiIII]λ1892 ratio covers the domain of $n_{\rm H} \sim 10^{10}$cm^{-3}. The ratio AlIIIλ1860/SiIII]λ1892 alone is, generally speaking, insufficient to determine $n_{\rm H}$. A second diagnostic ratio is needed to constrain U and to unambiguously derive $n_{\rm H}$. We consider SiIIλ1814/SiIII]λ1892, CIVλ1549/SiIII]λ1892, SiIVλ1397/SiIII]λ1892 as three diagnostic ratios suitable for constraining U.

The SiIIλ1814 doublet is conveniently placed, although weak or undetectable in most sources. The SiIIλ1814/SiIII]λ1892 ratio is anti-correlated with U in a regular form, as our CLOUDY simulations show, especially for $\log U \lesssim -2$, and for density not much above the critical density of SiIII]λ1892. The behavior of the ratio SiIIλ1814/SiIII]λ1892 resembles the distribution of CIII]λ1909/CIVλ1549 in the plane ($n_{\rm H}$, U) which shows a very regular dependence and a smooth anti-correlation with U until the collisional quenching of CIII]λ1909 sets on. However, the IP of Si^0 is just 8 eV. The majority of the λ1814 doublet is emitted in the partially ionized

zone (PIZ) near the hydrogen ionization front. Fig 9 (bottom panel) shows the behavior of the volume emissivity ϵ times the geometrical depth within an emitting slab of gas as a function of the depth itself. Since the actual line emission is proportional to $\epsilon \cdot h$ reported in Fig. 9, the emission of the AlIIIλ1860, and SiIII]λ1892 lines is negligible in the PIZ, but the one of Hβ certainly is not, and may be well dominating if $N_c \gg 10^{23}$cm^{-2}. Significant emission in the PIZ is expected also for the SiIIλ1814 doublet. However, for this latter line, total emission should not depend strongly on column density, since the emissivity becomes very low at $N_c \gtrsim 10^{23}$cm^{-2}. If higher N_c are considered (up to 10^{25}cm^{-2}), ratios including SiIII]λ1892, AlIIIλ1860, and SiIIλ1814 show a very weak dependence on column density, with changes a few percent at worst.

We attempted to isolate a CIVλ1549 and a SiIVλ1397 component that corresponds to the AlIIIλ1860 and SiIII]λ1892 lines. This can be a small part of the total CIVλ1549 and of SiIVλ1397 emission, but there is no point to consider the whole CIVλ1549 emission when CIVλ1549 shows a large blueshift and is much broader than Hβ (Fig. 5 of Sulentic et al. 2000) and SiIII]λ1892 and AlIIIλ1860 (Fig. 2 of Marziani et al. 2010). Taking into account various sources of ambiguity (mainly uncertainty in the quasar rest frame, S/N, blending with HeIIλ1640), the CIVλ1549 BC component we measure with our fits is constrained within $\pm$ 50% at worst. Thus we find significant CIVλ1549 emission from the low-ionization gas, and the basic assumption is that its CIVλ1549 profile is the same as the AlIIIλ1860, SiIII]λ1892 lines. If one considers the emissivity behavior, CIVλ1549 and SiIVλ1397 are obviously favored within the fully ionized zone.

The ratio of CIVλ1549 and SiIVλ1397 over CIII]λ1909 or over SiIII]λ1892 increases with ionization parameter in a way that is roughly independent on density until the collisional quenching of the semi-forbidden lines sets on (Fig. 8). The previous considerations are helpful to understand why the CIVλ1549 and SiIVλ1397 ratios provide clear diagnostics of the ionization parameter and seem to be in (at least qualitative) agreement with ratios employing lower ionization lines like SiIIλ1814/SiIII]λ1892 that is also mainly sensitive to U. The striking fact that the CIVλ1549 and SiIVλ1397 emission confirms low-ionization supports the hypothesis that the four lines are emitted by the same region. The ratios involving Si only have the obvious advantage that the the determination of the physical parameters is not dependent on metallicity; the drawback of SiIVλ1397 is that this line is weaker and blended with OIV]λ1402. However, as already pointed out, the SiIVλ1397 BC intensity should be slightly affected by OIV]λ1402.

7. RESULTS ON TWO EXTREME, ELUCIDATING CASES

We analyze two extreme objects – one extreme Pop. A and one extreme Pop. B – with the same methodology we used previously. The aim of this analysis is to help the interpretation of the line components measured on the spectra of the 8 $z \approx$3 quasars.

7.1. *SDSS Weak* CIII]λ*1909 source: SDSS J120144.36+011611.6*

Our project stems from the careful analysis of the I Zw 1 UV spectrum by Laor et al. (1997b), and the evidence of a well-defined trend in the λ1900Å blend along the E1 sequence (**??**Aoki & Yoshida 1999, Wills et al. 1999, Bachev et al. 2004, Marziani et al., 2010). The NLSy1 I Zw 1 is known to be a sort of extremum in the E1 sequence: it shows strong FeII and FeIII, prominent AlIIIλ1860 and SiIII]λ1892 emission. It is an example of the A3 spectral type, whose median 1900Å blend in shown in Fig. 3 of Bachev et al. (2004). Definitely, these sources are present also at intermediate to high redshift. We describe here the analysis of one source, SDSS J120144.36+011611.6 (Fig. 10), which seems to be a high-redshift, high-luminosity replica of I Zw 1, with broader lines (the FWHM limit of NLSy1s and Pop. A sources is luminosity dependent; see Netzer & Trahktenbrot 2007 and Marziani et al. 2009). These sources are Pop. A, and we assume that the profile of the BC is Lorentzian. Hereafter unshifted Lorentzian part of the line is said to be BC. Pop. A sources are also free of any VBC, making the analysis of the blend simpler.

Several considerations can be made from Fig. 10.

AlIIIλ1860 — The lines less ambiguous to measure are the AlIIIλ1860 doublet because the two lines are less blended with other features, and they are remarkably strong. SiIII]λ1892 is more heavily blended with CIII]λ1909 and FeIII. However, the SPECFIT routine allows usually a plausible deconvolution of SiIII]λ1892, making the AlIIIλ1860/SiIII]λ1892 ratio very reliable. FeII and FeIII are obviously strong. We can use FeII UV 191 to set roughly the level of FeII, while the feature at 2080Å is helpful to estimate intensity of FeIII.

FeIII — Our SPECFIT analysis produces a very weak CIII]λ1909 component. A precise measurement of CIII]λ1909 is cumbersome, since its intensity depends on the actual FeIII emission. The strong feature at λ1914 could be dominating, and the template may seriously underestimate it (see Vestergaard and Wilkes 2001 for several alternatives in the empirical FeIII emission of I Zw 1). In any case the residual CIII]λ1909 emission is small, suggesting that the λ1900 blend, once believed to be mostly CIII]λ1909, is actually almost void of CIII]λ1909 emission in these A3-type sources.

SiIIλ1814 — The SiIIλ1814 line is well visible in the spectrum of SDSS J120144.36+011611.6 and can be used as a substitute of CIVλ1549 to measure the ionization parameter. The ratio SiIIλ1814/SiIII]λ1892 is mainly sensitive to the ionization parameters, as it is the ratio CIVλ1549/SiIII]λ1892. The ratio SiIIλ1814/SiIII]λ1892 has the considerable advantage of being weekly dependent on metallicity. If metallicity is known (see also §8.1), the ratio CIVλ1549/AlIIIλ1860 should be in principle preferred since AlIIIλ1860 is emitted through a permitted resonance transition while SiIIλ1814 is emitted in the collisionally excited, partially-ionized zone (PIZ).

CIVλ*1549* — We fit CIVλ1549 with a Lorentzian component that is unshifted + a CIVλ1549 BBC. Note that the lack of shift in AlIIIλ1860 and SiIII]λ1892 imposes a strong, determinant condition on the strength of the Lorentzian-component in CIVλ1549. It is important to stress that some CIVλ1549 BC emission is expected to

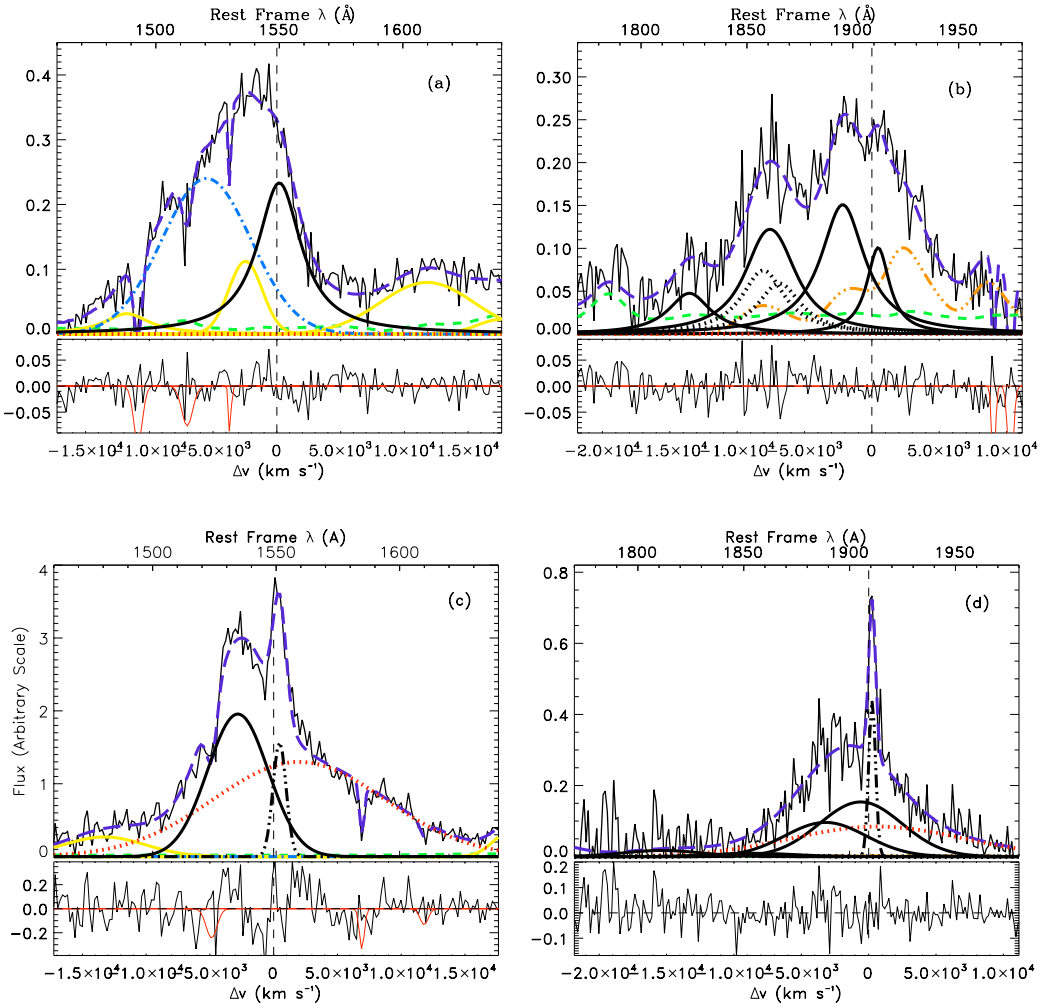

FIG. 10.— Fits for the two extreme objects: up J120144.36+011611.6, low 3C390.3. Units and meaning of symbols are the same of Fig. 4. For 3C390.3 it was needed to fit a narrow unshifted component that we show in dash-dot-dot line. Note for 3C390.3 SiII]λ1814 is almost absent.

be present according to our array of simulations. The ratio CIVλ1549/AlIIIλ1860 is rather modest, as we can easily see even by eye. We note in passing that the with of BCC is ≈ 10000 km s^{-1}, with a peak blueshift indicatively of −6000km s^{-1}, significantly larger than the one measured on the CIVλ1549 of I Zw 1 by Marziani et al. (2009).

SiIVλ1397 — We fit SiIVλ1397 with a Lorentzian component that is unshifted + a BBC (that may include SiIVλ1397 and OIV]λ1402 contribution). Results that are consistent with the ones of CIVλ1549. The ratio SiIVλ1397/SiIII]λ1892 has the advantage that is almost independent on metallicity. In principle, the crossing point between the SiII]λ1814/SiIII]λ1892 and SiII]λ1814/SiIII]λ1892 can set a metallicity independent point in the ($n_{\rm H}$, U) plane. If the accuracy of the SiII]λ1814 intensity is good then this point can be used to retrieve information on metallicity (§8.1).

We consider the measured line ratios in the plane U vs. $n_{\rm H}$ (initally assuming metallicity equal to solar), and see where they cross. We find very high density and low ionization (Fig. 11).

7.1.1. *Along the E1 Sequence: A More Complex Scenario*

Looking at the fit solution (Fig. 10(b)), it seems that our spectrum has almost no CIII]λ1909. In many ways this is not surprising. The physical solutions in the (U, $n_{\rm H}$) plane of Fig. 11, points toward very low ionization ($U \sim 10^{-3} - 10^{-2}$) and high density ($n_{\rm H} \gtrsim 10^{12}$cm^{-3}). At such high values of $n_{\rm H}$ we expect that CIII]λ1909 is collisionally quenched, and no significant emission. The ratio CIII]λ1909/CIVλ1549 is expected to be just $\sim 10^{-2}$ in the dense LIL-BLR. Therefore we can say that sources

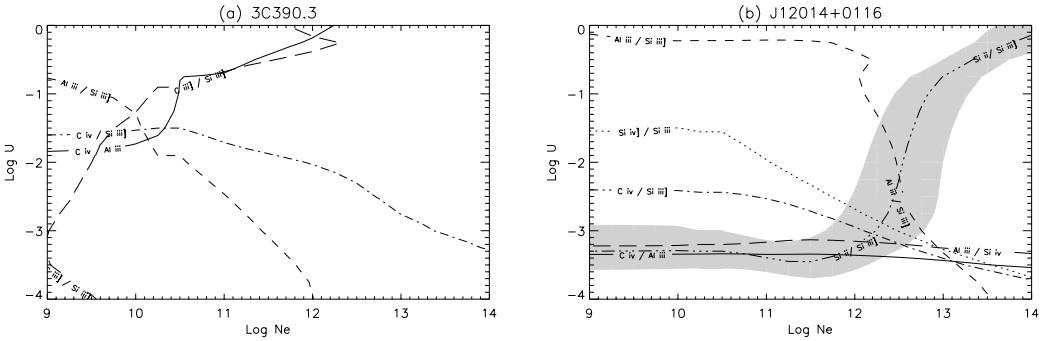

FIG. 11.— Contour plots for the extreme objects (a) 3C390.9 and (b) J12014+0116. Abscissa is electron density in cm^{-3}, ordinate is the ionization parameter, both in logarithm scale. Solid line is for log(CIVλ1549/AlIIIλ1860), dot line is for log(SiIVλ1397/SiIII]λ1892), dash line is for log(AlIIIλ1860/SiIII]λ1892), long dash line is for log(AlIIIλ1860/SiIVλ1397), dash dot line is for log(CIVλ1549/SiIII]λ1892) and dash-triple-dot line is for log(SiIIλ1814/SiIII]λ1892). The point where the isocontours cross determines the values of Logn_e and LogU. The shaded area is the error bands for SiIIλ1814. In 3C390.3 we add a long dash line for log(CIII]λ1909/SiIII]λ1892). In J12014+0116 the shaded area is the error bands for SiIIλ1814. See text for further details.

like SDSS and I Zw 1 are extreme because all of the λ1900Å blend is emitted by very low ionization, dense gas.

However, as soon as we move away from spectral types A3+ along the E1 sequence, we see that the prominence of AlIIIλ1860 diminishes greatly. The emission disappears altogether at the other end of the E1 sequence, where several lobe-dominated radio-loud sources are found. For most quasars we see that CIII]λ1909 is rather strong and unmistakably present. At a first glance this complicates the interpretation of the spectrum. However, one has to consider that CIII]λ1909 can be emitted only by gas of much lower $n_{\rm H}$ than that of the region where the bulk of SiIII]λ1892 and AlIIIλ1860 is emitted. Our simulations show that AlIIIλ1860 intensity grows smoothly as a function of density in the ionization parameter range of interest $-3 \lesssim \log U \lesssim -1$. This said, and considered the smooth trend we see from A3 to B1$^+$, the most reasonable conclusion is that a dense region emits significantly whenever AlIIIλ1860 emission is detected, although the relative prominence of the dense BC changes along the E1 sequence: it accounts for the entire LIL emission *only* in the most extreme Pop. A sources. The sequence of Fig. 3 of Bachev et al. (2004) seems to be mainly a sequence of prominence of AlIIIλ1860+ SiIII]λ1892 vs CIII]λ1909.

So, a very important conclusion is that a very dense, low-ionization region exists in the wide majority of quasars. It is associated with FeII prominence, as such gas is expected to emit a strong low-ionization spectrum. The most extreme FeII emitters are also the most extreme AlIIIλ1860 emitters; in some cases where no AlIIIλ1860 emission is measured, we also fail to detect any FeII emission (Marziani et al. 2010). Where is this region located? Why there are such distinctive line profiles as Lorentzian? The second issue goes beyond the present paper; for the moment our aim is to measure line components of AlIIIλ1860, SiIIλ1814, SiIII]λ1892 and CIVλ1549 that come from this region and to estimate its distance from the central black hole (§9).

7.2. *The Other E1 Extremum: 3C 390.3*

3C 390.3 is a lobe-dominated (LD) RL source, with very broad emission lines and no optical FeII within detection limits (see Marziani et al. 2003, for the criterion used). It also shows a large peak shift in its Hβ profile, and prominent narrow lines ([OIII]λ5007, Hβ), but also narrow components of CIVλ1549 and CIII]λ1909 which are all well separated from the broad Hβ profile.

To deconvolve the blends around CIII]λ1909 and CIVλ1549, we assume the same emission line profiles as for Hβ. The Hβ broad profile can be described as the sum of a BC and a VBC. An unusual property of the BC is its large peak blueshift (it is unusual because of the shift amplitude: even if median spectra of Pop. B sources show a small BC redshift, there is a pretty large scatter with both red- and blueshifted peaks observed in individual sources; Zamfir et al. 2010). Applying in a self consistent way the BC and VBC to the CIII]λ1909 and CIVλ1549 blends, leads to very interesting results as shown in Figure 10:

- AlIIIλ1860 is very weak or even absent within the S/N limits;
- the CIVλ1549 profile is very similar to the one of Hβ: BC+VBC accounts for more than 90% emission, with a possible, very weak contribution of the blueshifted component which is usually dominating in Pop. A sources;
- the red wing observed in the 1900Å blend is accounted for only if there is a strong CIII]λ1909 VBC, FeII and FeIII emission being below the detectability limit in this source;
- there is no evidence of a VBC in AlIIIλ1860;
- the ratio CIVλ1549/CIII]λ1909 BC is $\approx$ 10, a far cry from the ratios observed in extreme Pop. A sources like I Zw 1 and SDSS J120144.36+011611.6;
- even more interesting we find a CIVλ1549/CIII]λ1909 VBC $\approx$10, as for the BC.
- we have a difference of 1600 km s^{-1} between the FWHM of CIVλ1549 and the LIL. In all the previous objects the difference is less than 800 km s^{-1}.

We conclude that this object is fundamentally different from Pop. A sources. The low ionization, high density BC seems to be absent. The similarity in the CIVλ1549/CIII]λ1909 ratios suggest that we are observing a gas in conditions similar to the one associated to the VBC. We predict that FeII will remain undetected or found to be weak even with S/N $\rightarrow \infty$.

In the plane (U, $n_{\rm H}$) of Figure 11, the line ratios converge to a point at $\log U \approx$ -1.5, and $\log n_{\rm H} \approx$ 10.1 (the SiIIλ1814 line cannot be measured accurately since S/N is poor). In this case, the CIII]λ1909/CIVλ1549 ratio also converges toward a (U, $n_{\rm H}$) value consistent with the one indicated by the AlIIIλ1860/SiIIλ1814. In most other cases, this does not happen because the AlIIIλ1860 doublet is too strong to be accounted for by gas of $n_{\rm H} \sim 10^{10}$cm^{-3} even at super-solar metallicity. Emission occurs at pretty high ionization, in conditions that once upon a time were thought to be standard in quasars (Davidson and Netzer 1979). This Pop. A and B difference at the extrema was already pointed out, in a semi-quantitative way, by Sulentic et al. (2000) and Marziani et al. (2001).

It is however important not to generalize the case of 3C 390.3 to the remaining Pop. B sources. In most of them, AlIIIλ1860 is detected, and there is evidence of strong CIII]λ1909. Actually CIII]λ1909 emission seems to be appreciable in all of our VLT quasars. This means that we are in a composite situation, where low-ionization, high-density emission is present, along with significant VBC and other emission. The two extreme cases help us however to understand these more complex cases.

7.3. *The Contribution of Lower Density Gas*

Once the true intensity of the BC components is retrieved, the presence of significant CIII]λ1909 emission complicates the analysis. As pointed out, the photoionization solution for the BC suggests very high density, and in this region no CIII]λ1909 emission is expected. Whenever CIII]λ1909 is observed, we need to reverse the question: how much does any CIII]λ1909 emitting gas contributes to the lines used for diagnostic ratios? Negligible contribution is expected to AlIIIλ1860. However, this is not true for CIVλ1549 and SiIII]λ1892. Especially among Pop. A2 and A3 objects, it is not so obvious that the profile of CIII]λ1909 and SiIII]λ1892 is the same. It could be well that the CIII]λ1909 profile is narrower than the ones of SiIII]λ1892 and AlIIIλ1860 (as found for SDSS J1201+0116), justifying the idea of CIII]λ1909 emission from a disjoint region (§6.2). For the BAL QSOs in our sample and AlIIIλ1860-strong sources most of what we ascribe to CIII]λ1909 could be actually FeIII, as suggested by Hartig and Baldwin (1986).

However, objects like the typical A1 sources show SiIII]λ1892 and CIII]λ1909 with similar profiles, so in the following we will assume the worst condition, that is all CIII]λ1909 emitting gas is contributing to the BC lines.

To estimate the contribution of the CIII]λ1909 emitting gas to SiIII]λ1892 and CIVλ1549, we can consider the trends observed along E1. **SiIII]λ1892 is strong when AlIIIλ1860 is strong**, and the SiIII]λ1892/CIII]λ1909 ratio is lower when CIII]λ1909 is strong, as visible in both Baldwin et al. (1996) and Bachev et al. (2004), as well as in the present paper. The observed SiIII]λ1892/CIII]λ1909 ratio in the A1 median bin seems to be as low as in Mark 335, $\approx$ 0.4. Pop. B sources that often show prominent CIII]λ1909 also show a low SiIII]λ1892/CIII]λ1909 ratio, as also appreciable in the median spectra of Bachev et al. (2004). These trends suggest that most SiIII]λ1892 is emitted where AlIIIλ1860 is also emitted. As a consequence, any correction due to gas in different physical conditions (lower density) emitting SiIII]λ1892 is expected not to be dominant unless CIII]λ1909 is extremely strong. The CIII]λ1909 emitting gas should be at density $\log n \sim$ 9, or lower. Higher density would imply increasing SiIII]λ1892/CIII]λ1909 to values that would exceed the observed ones even if the LIL-BC is not emitting any significant SiIII]λ1892 (see Fig. 12).

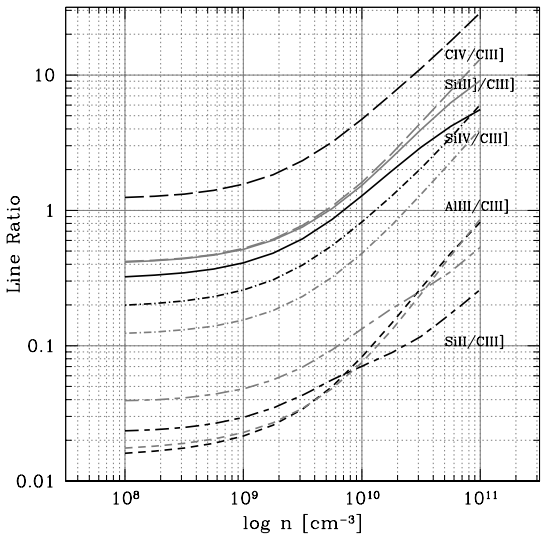

FIG. 12.— Expected contribution from moderate density emitting gas as a function of density for ionization parameters $\log U = -2$ (black lines) and $\log U = 2.5$ (grey lines).

7.3.1. *Preliminary analysis of a low-z sample*

To set these trends on a more quantitative basis we considered the set of pre-COSTAR recalibrated sources, for which CIII]λ1909 and CIVλ1549 data are publicly available (Kuraszkiewicz et al 2002, Evans & Koratkar 2004).We performed measurements (interactively with the task SPLOT of IRAF) for about 30 sources with the highest S/N, holding a CIII]λ1909 blend that could be relatively easily deblended, and following the expectations described in §4.4. The rest frame equivalent width of AlIIIλ1860 and SiIII]λ1892 are found to be highly correlated (Fig. 13). The correlation is due to SiIII]λ1892 being stronger when AlIIIλ1860 is strong, not necessarily because CIII]λ1909 is strong: actually, the SiIII]λ1892/CIII]λ1909 ratio can be low when CIII]λ1909 is strong, and the AlIIIλ1860/SiIII]λ1892 ratio achieves maximum values when CIII]λ1909 is faintest. This is consistent with the bulk of AlIIIλ1860 and SiIII]λ1892 originating in the same region. At the same time the presence of CIII]λ1909 lowers the AlIIIλ1860/SiIII]λ1892, CIVλ1549/SiIII]λ1892 and SiIVλ1397/SiIII]λ1892 because of "excess" SiIII]λ1892 emission associated to the

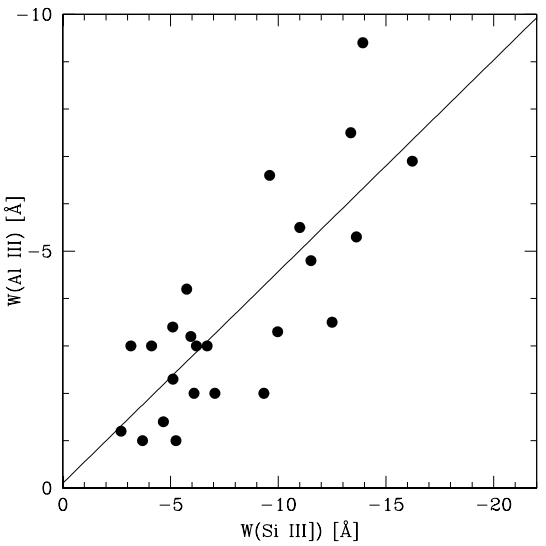

FIG. 13.— Correlation between rest frame equivalent width of AlIIIλ1860 and SiII]λ1892. Line in unweighted least square best fit.

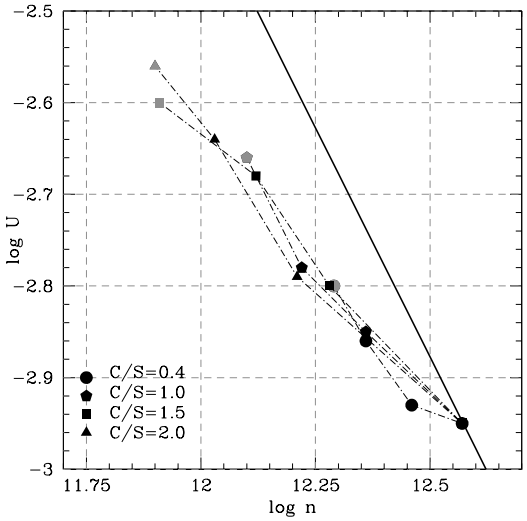

FIG. 14.— Plane $\log U - \log n$ in an expanded scale. The lower-left dot corresponds to a high density solution. Moderate density emitting gas is then added with increasing intensity of a CIII]λ1909 component with the four CIII]λ1909/SiIII]λ1892 ratios reported in the figure. Connected positions corresponds to increasing density of CIII]λ1909 emitting gas, $\log n = 9, 9.5, 10$. Note that the case $\log n = 10$ (grey symbols) is not appropriate for the observed data.

gas emitting CIII]λ1909.

7.3.2. *The effect of low-density gas on the product ($Un_{\rm H}$)*

We expect that any correction will increase density (increase AlIIIλ1860/SiIII]λ1892 lowering SiIII]λ1892) and decrease ionization parameter (lowering CIVλ1549 more than SiIII]λ1892), but that their product will be less affected. To show the amplitude of the effect we performed an experiment, adding to a pure, high-density solution, contribution from moderate density gas (log $n_{\rm H}\sim 9-10$). The Fig. 14 shows the displacement in the density – ionization parameter plane for several values of the CIII]λ1909/SiIII]λ1892 intensity ratio. The values refer to the CIII]λ1909 addition over SiIII]λ1892 in the ideal case, corresponding to observed ratios of 0.34, 0.7, 1.0, 1.1 for an addition of a CIII]λ1909 component whose intensity is 0.4, 1.0 ,1.5 ,2.0 the intensity of the SiIII]λ1892 component associate to the high density gas. As one can see from the figure, even if deviation for U and $n_{\rm H}$ taken separately are significant, deviations for the product are by far less important. The largest change for the product is found to be ≈ 0.15, if we exclude the gray dots corresponding to log $n_{\rm H}$= 10 (an unlikley case, since this would imply a correction SiIII]λ1892/CIII]λ1909 > 1, inconsistent with what we observe when CIII]λ1909 is strong). Following the expected line ratios of Fig.12 we apply a correction to the BC fluxes that is 0.4 and 1.5 CIII]λ1909 for SiIII]λ1892 and CIVλ1549 respectively (Figures 11, 15 and 16) corresponding to $\log U = -2$ and log$n_{\rm H}$= 9. We remark that that if U is lower, the correction will have negligible effect, while assuming a larger U will lead to CIVλ1549 flux in excess to the one observed.

To constrain the ionization parameter we can first consider that, since the CIII]λ1909 gas comes from a (relatively) low density region, the contribution to SiIIλ1814 is small: for $\log n \sim$ 9 and $\log U \approx -2$, the contribution should be $\approx$ 0.03 CIII]λ1909. Second, another powerful feature is the SiIVλ1397 doublet (Baldwin et al. 1996): the SiIVλ1397 doublet is less affected by the CIII]λ1909 correction, the contribution from lower density gas being estimated $\approx$ 0.25 CIII]λ1909. The line ratio SiIVλ1397/AlIIIλ1860 is also sensitive to ionization and less affected by any lower density correction (provided that the relative abundance of S and Al stays the same, as it seems to be the case).

In summary, corrected BC line intensities are computed as follows: $I^{\rm c}$(SiIIλ1814)$_{\rm BC}$ = I(SiIIλ1814)$_{\rm BC}$ – 0.03 I(CIII]λ1909)$_{\rm BC}$; $I^{\rm c}$(SiIII]λ1892)$_{\rm BC}$ = I(SiIII]λ1892)$_{\rm BC}$ – 0.4 I(CIII]λ1909)$_{\rm BC}$; $I^{\rm c}$(SiIVλ1397)$_{\rm BC}$ = I(SiIVλ1397)$_{\rm BC}$ – 0.26 I(CIII]λ1909)$_{\rm BC}$; $I^{\rm c}$(CIVλ1549)$_{\rm BC}$ = I(CIVλ1549)$_{\rm BC}$ – 1.5 I(CIII]λ1909)$_{\rm BC}$.

8. RESULTS ON THE $Z \approx 3$ QUASARS

To estimate log$n_{\rm H}$ and log$U$ values, we use the CLOUDY contour plots of the ratios AlIIIλ1860/SiIII]λ1892, SiIIλ1814/SiIII]λ1892, CIVλ1549/SiIII]λ1892, SiIVλ1397/SiIII]λ1892 showed in Fig. 8[6]. The data points of our objects are in regions were the ratios are well-defined. The ratios CIVλ1549/SiIII]λ1892, SiIVλ1397/SiIII]λ1892, and SiIIλ1814/SiIII]λ1892 are mainly sensitive to the ionization parameter U, while AlIIIλ1860/SiIII]λ1892 and CIII]λ1909/SiIII]λ1892 are mainly sensitive to the electron density. We know that CIII]λ1909 is collisionally

[6]Note that there are regions where the ratio values are actually undefined: close to the high U limit ($\log U \gtrsim -0.3$), ratios AlIIIλ1860/SiIII]λ1892 and SiIIλ1814/SiIII]λ1892(with $n_{\rm H} \lesssim 10^9 {\rm cm}^{-3}$) should not be considered.

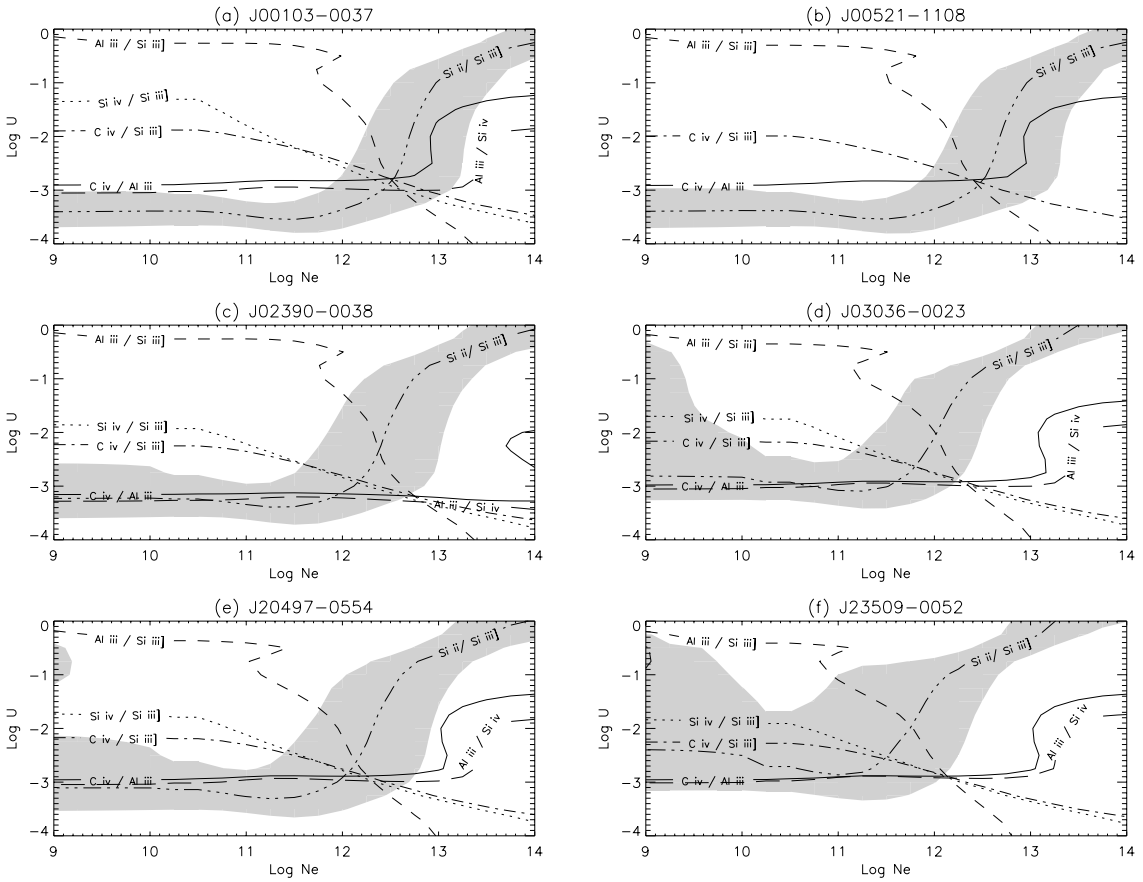

FIG. 15.— Contour plots for (a) J00103-0037, (b) J00521-1108, (c) J02390-0038, (d) J03036-0023, (e) J20497-0554 and (f) 23509-0052. Units and meaning of symbols are the same of Fig. 11. In the case of the objects shown in panels (c) and (f) the SiIIλ1814 line is very weak and thus unreliable. For the objects in panels (a), (d) and (e) the line is also affected by the telluric absorption. For these objects we rely on the SiIVλ1397 line.

quenched at log $n_e \gtrsim 10$ and in the contour plot for CIII]λ1909/SiIII]λ1892 we see a step around this value.

We measure the BC intensity of SiIII]λ1892, AlIIIλ1860, SiIIλ1814, SiIVλ1397 and CIVλ1549; with them we compute the diagnostic ratios (for 3C390.3 we use CIII]λ1909 in place of SiIIλ1814; however there is no object similar to 3C390.3 among the $z \approx 3$ quasars). We present the fluxes of the line components in Tab. 3 and the equivalent width in Tab. 4. Table 5 shows the weak lines around CIVλ1549. For CIVλ1549 line we show the core, blue shifted and the very broad components. Errors are at a 2σ confidence level, and include the sources of uncertainty described in §4.5. Errors are then quadratically propagated according to standard practice to compute intensity ratios and their logarithm.

From Table 3 we can derive the diagnostic ratios. As we see in Fig. 1, SiIIλ1814 is absorbed by telluric B band in J00103-0037, J03036-0023, J20497-0554 (most affected). We will not consider SiIIλ1814 to compute n_H and U on those cases. However, if we take at face value the SiIIλ1814 measure on J00103-0037 and J20497-0554, it will converge close to the point set by the remaining two ratios. We display on a graph a line representing the behavior of each ratio under the assumption of

TABLE 5
WEAK LINES AROUND CIVλ1549. [a]

Object	NIV]λ1486	SiIIλ1533	HeIIλ1640	
			BC	*blue*
J00103-0037	2.4 ± 1.9	1.1 ± 0.8	1.3 ± 0.4	2.0 ± 1.8
J00521-1108	0.1 ± 0.2	1.1 ± 1.1	1.6 ± 1.2	0.1 ± 0.2
J01225+1339	...	1.0 ± 1.8	3.2 ± 3.4	4.3 ± 1.8
J02287+0002 (1)	...	1.0 ± 0.8	0.3 ± 0.1	0.2 ± 0.2
J02287+0002 (2)	...	0.9 ± 0.8	0.2 ± 0.1	0.0 ± 0.2
J02390-0038	0.5 ± 0.9	0.9 ± 0.9	0.2 ± 0.4	1.6 ± 1.1
J03036-0023	...	1.5 ± 1.2	0.5 ± 0.5	9.2 ± 3.4
J20497-0554	0.3 ± 0.6	1.5 ± 1.5	1.8 ± 0.8	4.6 ± 2.7
J23509-0052	...	0.4 ± 0.4	0.2 ± 0.9	2.5 ± 1.6
Extreme Objects				
J12014+01161	3.0 ± 3.5	4.9 ± 5.8	1.5 ± 1.7	10.3 ± 9.2
3C 390.3	5.6 ± 2.7	1.6 ± 1.5	2.8 ± 1.5	...

NOTE. — (a) Units are 10^{-14} ergs s^{-1} cm^{-2} Å^{-1}. (1) Considering $z_{OI\lambda 1304}$. (2) Considering $z_{CIII]\lambda 1909}$.
We do not show HeII$\lambda 1640_{VBC}$ because is very weak, when is considered.

TABLE 6
Hydrogen Density and Ionization Parameter.

Object	Logn_H				Log$U$				Log$n_H \cdot U$		
	$1Z_\odot$	$1Z_\odot$ low dens	$5Z_\odot$	$5Z_\odot$ low dens	$1Z_\odot$	$1Z_\odot$ low dens	$5Z_\odot$	$5Z_\odot$ low dens	$1Z_\odot$	$1Z_\odot$ low dens	$5Z_\odot$
J00103-0037 *	**12.50 ± 0.17**	...	...	...	-2.79 ± 0.19	...	...	...	9.71 ± 0.22	...	
J00521-1108	**12.43 ± 0.26**	12.84 ± 0.23	...	...	-2.86 ± 0.15	-3.00 ± 0.11	...	...	9.58 ± 0.26	9.85 ± 0.23	
J00103-0037 *	**12.50 ± 0.17**	...	...	...	-2.79 ± 0.19	...	...	...	9.71 ± 0.22	...	...
J00521-1108	**12.43 ± 0.26**	12.84 ± 0.23	...	...	-2.86 ± 0.15	-3.00 ± 0.11	...	...	9.58 ± 0.26	9.85 ± 0.23	...
J01225+1339	12.45 ± 0.22	13.24 ± 0.20	**11.47 ± 0.28**	12.62 ± 0.25	-2.96 ± 0.09	-3.42 ± 0.18	-1.83 ± 0.11	-2.79 ± 0.68	9.49 ± 0.21	9.82 ± 0.20	9.64 ±
J02287+0002 (1)	**12.35 ± 0.16**	...	11.64 ± 0.33	12.28 ± 0.28	-2.81 ± 0.28	...	-2.33 ± 0.25	-2.58 ± 0.98	9.55 ± 0.28	...	9.31 ±
J02287+0002 (2)	12.47 ± 0.16	...	...	...	-2.81 ± 0.28	...	...	...	9.67 ± 0.28	...	...
J02390-0038	12.75 ± 0.12	13.42 ± 0.21	11.97 ± 0.15	13.20 ± 0.13	-3.18 ± 0.05	-3.60 ± 0.07	-2.19 ± 0.08	-3.29 ± 0.13	**9.57 ± 0.11**	9.82 ± 0.21	**9.78** ±
J03036-0023	12.32 ± 0.14	12.92 ± 0.15	...	...	-2.92 ± 0.06	-3.34 ± 0.05	...	...	**9.40 ± 0.14**	**9.58 ± 0.15**	...
J20497-0554	**12.26 ± 0.25**	12.82 ± 0.18	...	...	-2.89 ± 0.12	-3.29 ± 0.13	...	...	9.37 ± 0.25	9.53 ± 0.23	...
J23509-0052	12.13 ± 0.24	12.90 ± 0.17	10.86 ± 0.23	12.12 ± 0.58	-2.89 ± 0.09	-3.51 ± 0.21	-1.93 ± 0.13	-2.99 ± 0.82	9.24 ± 0.24	9.39 ± 0.16	8.93 ±
Extreme Objects											
J12014+01161	12.81 ± 0.29	12.95 ± 0.16	**12.34 ± 0.11**	12.90 ± 0.42	-2.85 ± 0.18	-2.87 ± 0.08	-2.41 ± 0.25	-3.20 ± 0.58	9.97 ± 0.30	10.09 ± 0.16	9.93 ±
3C 390.3	**10.05 ± 0.34**	...	...	...	-1.48 ± 0.34	...	...	...	8.57 ± 0.41	...	...

Note. — We also show the values considering the correction by the contribution of low density regions (§7.3), $Z = 5Z_\odot$ (§8.1), and $Z = 5Z_\odot$ with the correction by the contribution of low density regions. (1) Considering $z_{OI]\lambda 1304}$. (2) Considering $z_{CIII]\lambda 1909}$. (*) For J00103-0037 the correction is too large to be reliable. We show in bold numbers the ones that we consider the best.

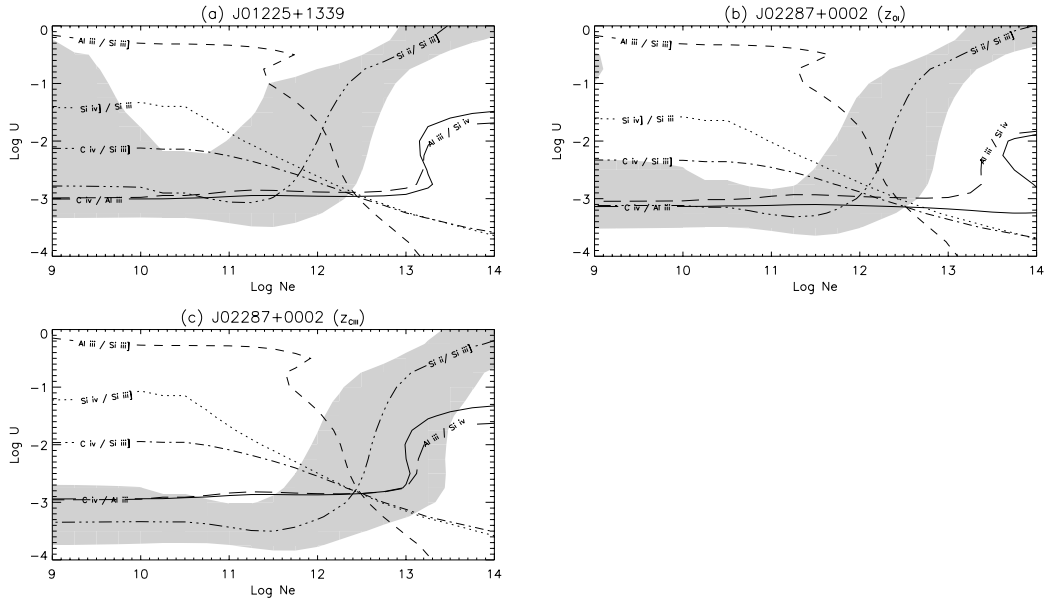

FIG. 16.— Contour plots for BAL quasars (a) J01225+1339 and (b) J01225+1339 using $z_{OI\lambda 1304}$ and (c) J01225+1339 using $z_{CIII]\lambda 1909}$. Units and meaning of symbols are the same of Fig. 11.

solar metallicity; the ideal point where the lines representing different diagnostic ratios cross determines the values of $\log n_{\rm H}$ and $\log U$. Figs. 15 and 16 shows the contour plots were we can see that the diagnostic ratios converge to rather well defined values. The cross point is very precise for the objects J00103-0037, J00521-1108, J02287+0002 (using z_{CIII}), and J20497-0554 ; for the remaining objects J01225+1339, J02287+0002 (using z_{OI}), J02390-0038, J03036-0023, and J23509-0052 the cross point is slightly different. We must not forget the errors involving the fits, such as the changing of the shape profile that makes large the peak intensity if is Lorentzian or it could be less intense if it is Gaussian; the FeII pseudo-continuum contribution that affects principally to SiIIλ1814 or the FeIII that in some cases affects CIII]λ1909.

In principle, the crossing point of the ratios SiIVλ1397/SiIII]λ1892 and SiIIλ1814/SiIII]λ1892 is independent on metallicity. Therefore, any significant disagreement between this crossing point and the ratios based on CIVλ1549 may indicate chemical composition different from the assumed solar one (§8.1). The difficulty here is the large uncertainty of the SiIIλ1814 line. In all contour plots we show the $\pm 2\sigma$ interval as a shaded band. So, it is proper to consider deviations from metallicity only in the case of 4 sources where the crossing point excluding SiIIλ1814 is outside the uncertainty band.

For the objects J00103-0037, J03036-0023 and J20497-0554 we exclude the SiIIλ1814 line from the diagnostic ratios because it is affected by absorption. For the remaining objects, we take the average of the crossing contour plots of log(AlIIIλ1860/SiIII]λ1892) crossing with log(CIVλ1549/SiIII]λ1892) and log(AlIIIλ1860/SiIII]λ1892) crossing with log(SiIIλ1814/SiIII]λ1892). For 3C390.3 we use log(CIII]λ1909/SiIII]λ1892) instead of log(SiIIλ1814/SiIII]λ1892). Table 6 summarizes the $\log n_{\rm H}$ and $\log U$ values including their uncertainty. Since U and $n_{\rm H}$ are not independent quantities (their correlation coefficient is found to be 0.55), we adopt the appropriate formula for the errors on the product $Un_{\rm H}$ (following Bevington 1969). We present average values of the crossing points for extreme objects of Fig. 11 and 18(d). In the SDSS J12014+0116 case we give full weight to the SiIIλ1814 measurement. The crossing points disagree somewhat for SDSS J12014+0116. This could be due to an underestimate of *both* SiIIλ1814 and CIVλ1549 in the fits. On the one hand, SiIIλ1814 is clearly seen and strong but is contaminated by FeII blend; on the other hand, CIVλ1549 is strongly affected by the blue-shifted component and by the assumption that it is of Gaussian shape. An increase by 30% in the measurement of the intensity of the two line would lead to a better agreement but this is somewhat an ad-hoc speculation. Rather, the significant difference between the crossing point of the SiIIλ1814/SiIII]λ1892 and SiIVλ1397/SiIII]λ1892 ratios and the other ones point toward strong metal enrichment. We will show in §8.1 that this is probably the case.

At any rate, the convergence is toward a value of $\log U \approx -3$, lower than for the other $z \approx 3$ quasars. This is reflected in the CIVλ1549 EW of this source, also significantly lower. It is intriguing to note that the correction because of lower density drives the other sources toward values of U and $n_{\rm H}$ that are closer to the ones of SDSS J12014+0116.

Figure 17 shows the contour plots for the corrected ratios considering the low density emission contribution of the CIII]λ1909 region.

Table 7 reports the values of the $r_{\rm BLR}$ and the $M_{\rm BH}$ of our 8 objects and the extreme objects in the last two rows. Column 1 identifies the quasar name; Col. 2 gives the quasar proper distance in mega parsecs [Mpc]; Cols. 3 and 4 are the continuum specific flux value at 1350Å and 1700Å respectively, Col. 5 reports the FWHM in km s^{-1} for the broad components, Col. 6 is the Population designation. Cols. (7) to (10) report the logarithm of the size of the BLR in cm obtained from: a) $1Z_{\odot}$, b) $1Z_{\odot}$ line ratios corrected because of low density emission, c) $5Z_{\odot}$, and d) $5Z_{\odot}$ line ratios corrected because of low density emission. Cols. (11) -(14) list the logarithm of the black hole mass in solar masses in the same order as for $r_{\rm BLR}$. Finally Col. (15) is $M_{\rm BH}$ computed from Vestergaard and Peterson (2006) formula (Equation 10). We will explain in §10 how these quantities are computed.

8.1. *Effects of Metallicity*

The strength of NVλ1240 relative to CIVλ1549 and HeIIλ1640 suggests supersolar chemical abundances (Hamann and Ferland 1993; Hamann & Ferland 1999). Chemical abundances may be well 5 to 10 times solar (Dhanda et al. 2007), with Z $\approx 5Z_{\odot}$ reputed typical of high z quasars (Ferland et al. 1996). The E1 sequence seems to be mainly a sequence of ionization in the sense of a steady decrease in prominence of the low-ionization BC toward Population B (Marziani et al. 2001, 2010). However, this is not to neglect that metal-enrichment also plays a role, especially for the most extreme Pop. A sources i.e., those in bin A3 and higher (Sulentic et al. 2001).

The lines employed in the present study come from carbon, silicon and aluminium; all these element can be significantly depleted from gas if dust grains are formed (e. g., Mathis 1990). However, the emitting regions where our lines are produced are thought too hot to contain significant amount of dust (a definition of broad line region is right the central engine region below the dust sublimation region: e.g., Elitzur 2009). In addition Si and Al are expected to be produced under similar circumstances in the late stage of evolution of massive stars (Clayton 1983, Ch. 7). We note also that the CIVλ1549/SiIII]λ1892 and CIVλ1549/AlIIIλ1860 usually give results that are in perfect agreement in the plane ($n_{\rm H}$,U). These findings support our assumption that, if metallicity variations are present, the relative abundance Al to Si remains constant. We considered two cases for enhanced metallicity: (1) constant solar abundance ratio Al:Si:C with $Z = 5Z_{\odot}$ (5Z) ; (2) an overabundance of Si with respect to carbon by a factor 3, again with $Z = 5Z_{\odot}$ (5ZSA). This condition comes from the yields listed by Woosley and Weaver (1995) from type II Supernovæ. The Si overabundance is also supported by the chemical composition of the gas returned to the interstellar medium by an evolved population with a top-loaded initial mass function simulated using STARBURST 99 (Leitherer et al. 1999). The abundance of Al should scale roughly with the one of Si. While

TABLE 7
THE SIZE OF THE BROAD LINE REGION AND THE BLACK HOLE MASSES.

Object	$d_p[Mpc]$ $X10^{15}$	f(1700Å)[a] $X10^{-15}$	f(1350Å)[a] $X10^{-15}$	FWHM$_{BC}$ [km s^{-1}]	Pop.	Log(r_{BLR}) [cm][b]				Log(M_{BH}) [$M_\odot$][b]			
						original	low dens	$5Z_\odot$	$5Z_\odot$low dens	original	low dens	$5Z_\odot$	$5Z_\odot$low den
(1)	(2)	(3)	(4)	(5)	(6)	(7)	(8)	(9)	(10)	(11)	(12)	(13)	(14)
J00103-0037	6.51	4.8 ± 1.0	6.8 ± 1.4	4500 ± 800	B	18.10 ± 0.12	...	...	...	9.16 ± 0.20	...	...	...
J00521-1108	6.59	6.1 ± 1.5	8.8 ± 2.1	5300 ± 1600	B	18.23 ± 0.14	18.09 ± 0.13	...	...	9.43 ± 0.30	9.29 ± 0.29	...	...
J01225+1339	6.42	8.1 ± 1.6	10.9 ± 2.2	4400 ± 1000	A†	18.32 ± 0.12	18.16 ± 0.13	18.25 ± 0.15	18.15 ± 0.33	9.36 ± 0.23	9.20 ± 0.23	9.29 ± 0.25	9.19 ± 0.3
J02287+0002 (1)	6.09	7.4 ± 2.7	8.4 ± 3.0	4700 ± 1000	A†	18.25 ± 0.16	...	18.37 ± 0.20	18.17 ± 0.48	9.35 ± 0.25	...	9.47 ± 0.27	9.27 ± 0.51
J02287+0002 (2)						18.19 ± 0.16	...	...	...	9.29 ± 0.25	...	...	...
J02390-0038	6.45	6.9 ± 2.1	9.9 ± 3.0	5400 ± 1000	B	18.25 ± 0.09	18.12 ± 0.12	18.14 ± 0.10	18.08 ± 0.10	9.46 ± 0.18	9.34 ± 0.20	9.36 ± 0.19	9.30 ± 0.1
J03036-0023	6.58	20.5 ± 5.7	30.0 ± 8.4	3700 ± 600	A	18.58 ± 0.10	18.49 ± 0.10	...	...	9.47 ± 0.17	9.38 ± 0.17	...	...
J20497-0554	6.55	6.6 ± 1.3	9.5 ± 1.9	3800 ± 600	A	18.34 ± 0.13	18.26 ± 0.11	...	...	9.25 ± 0.19	9.17 ± 0.18	...	...
J23509-0052	6.40	4.8 ± 1.0	6.1 ± 1.2	3600 ± 800	A	18.33 ± 0.13	18.25 ± 0.12	18.49 ± 0.13	18.38 ± 0.43	9.19 ± 0.23	9.12 ± 0.23	9.35 ± 0.23	9.25 ± 0.47
Extreme Objects													
J12014+01161	6.58	21.8 ± 2.3	31.9 ± 3.2	4000 ± 800	A	18.31 ± 0.15	18.25 ± 0.09	18.33 ± 0.13	18.44 ± 0.31	9.26 ± 0.23	9.20 ± 0.19	9.28 ± 0.22	9.40 ± 0.43
3C 390.3	0.24	4.2 ± 0.7	9.9 ± 1.6	6400 ± 2200	B	17.23 ± 0.21	...	...	...	8.60 ± 0.37	...	...	...

NOTE. — (a) Units of the flux at 1350 and 1700Å are in ergs s^{-1} cm^{-2} Å^{-1}. (b) The showed values are the average ± 0.17 dex of the computation using both SED of Laor (1997) and Mathews & Ferland (1987) (see Fig. 20. (c) We show the comparison between our computations and those using the Vestergaard & Peterson (2006) mehtod. They report an uncertainty of 0.66 dex. (†) Acording to the FWHM it is clasified as pop B, but has other spectral caracteristics of pop. A objects. See §5. (1) Considering $z_{OI\lambda1304}$. (2) Considering $z_{CIII]\lambda1909}$

some cases with Al scaling with C are possible from the Woosely and Weaver (1995) yields, they are rarer than cases in which Al scales with Si. This latter case is appropriate for the most massive progenitors. Also, the assumption of Al scaling with C with [Si/C] = 0.477 would yield to implausible high density and lack of convergence to a well-defined solution for $\log n_{\rm H} \lesssim 14$. We therefore assume in the following that Al scales with Si in the two cases listed above.

An array of simulations as a function of ionization parameter and density was computed assuming the conditions (1) and (2) listed in the previous paragraph. As expected, if the solar metallicity is simply scaled by a factor (5Z) we find that the ratio AlIIIλ1860/SiIII]λ1892 is not strongly dependent on Z: the ratio increases by about 40% passing from $Z = 1Z_{\odot}$ to $Z = 5Z_{\odot}$, for $\log n_{\rm H} \approx$ 12 and $\log U \approx$–2. The same is true for the SiIIλ1814/SiIII]λ1892 and SiIVλ1397/SiIII]λ1892 ratios. Since the first ratio sets $n_{\rm H}$, and the last two U, the ratios mentioned in this paragraph should be preferred because they provide $n_{\rm H}$ and U values that are weakly affected by a factor 5 change in metallicity. A posteriori we confirm that the effect on the product $Un_{\rm H}$ derived also with ratios involving CIVλ1549 is negligible in case 5Z (and it should be even more so if a metallicity increase is $Z_{\odot} \lesssim Z \lesssim 5Z_{\odot}$).

The two extreme cases seem to be revealing also as far as metallicity is concerned. Ratios converge to a fairly well defined point in the case of 3C 390.3 (see Fig. 11, left panel, $Z = 1Z_{\odot}$ assumed). In this case there is no major evidence of supersolar metallicity. The converse is true in the case of SDSS J120144.36+011611.6. The ratios involving CIVλ1549 indicate a lower ionization level, with $\log U \sim -3$. This is because C^{3+} changes ionization state to C^{2+} for smaller ionization parameters, and so CIVλ1549 rapidly disappears. The CIVλ1549 intensity depends weakly on Z while the AlIIIλ1860 and SiIII]λ1892 lines are more sensitive. The 5Z case yields values closer to the ones obtained from the Si and Al line ratios, but not yet in concordance. If we pass to case 5ZSA with a factor 3 Si overabundance, then the concordance of the line ratios is good, especially if no correction because of low density emission is applied. As a further confirmation we checked that the metallicity-dependent CIVλ1549/SiIVλ1397 ratio is in very good agreement with the crossing point of the other lines. Therefore, in this case, we have independent measures of metallicity, $n_{\rm H}$, and U. The case of even higher metallicity, say $Z \sim 10Z_{\odot}$, remains to be exploredbut may not be appropriate considering the good agreement with 5ZSA.

In principle, the discrepancy in the intersection point, with SiIII]λ1892/CIVλ1549 and AlIIIλ1860/CIVλ1549 yielding lower U than the Al-Si ratios, should signal a significant enrichment in Si and Al of the BLR gas. In this case the SiIVλ1397/CIVλ1549 ratio should be helpful, as it can be assumed to be dependent mainly on the Si abundance relative to C. Here, more than precisely determining the exact abundance value we are interested in analyzing the effect of large metallicity changes on U, $n_{\rm H}$, and their product. Appreciable discrepancy is visible in the contour plots of the BAL quasar J01225+1339, J03036-0023, J20497-0554 and J23509-0052 if $Z = Z_{\odot}$ is assumed.

In the same plots made for $Z = 5Z_{\odot}$SA, the agreement becomes better (see Fig. 18). High metallicity yields higher U and smaller $n_{\rm H}$ if emission line ratios involving CIVλ1549 are considered. This reflect the increase in abudance of Si and Al with respect to C, and the fact the SiIIλ1814, SiIII]λ1892, AlIIIλ1860 lines are emitted at lower ionization than CIVλ1549. In the case of sources like J02390-0038 and J20497-0554, the discrepancy of the crossing lines might indicate $Z_{\odot} \lesssim Z \lesssim 5Z_{\odot}$, more than the extreme enrichment like the one assumed in 5ZSA, as also suggested by the CIVλ1549/SiIVλ1397 ratio.

In Fig. 18 and 19 the contour plots are shown for the case 5ZSA. We consider uncorrected and corrected line ratios as two independent cases. The halftone bands also show the importance of accurate SiIIλ1814 measurements to infer unambiguous constrain on metallicity (and, by extension, to estimate $n_{\rm H}$ and U independently). The product $n_{\rm H}U$ is however much less affected than $n_{\rm H}$ and U individually (Tab. 6).

A first $r_{\rm BLR}$ and $M_{\rm BH}$ estimate can be obtained considering only the SiIIλ1814/SiIII]λ1892 and AlIIIλ1860/SiIII]λ1892 ratios. We conclude that the effect of scaling the metallicity up to $Z = 5Z_{\odot}$ is within the uncertainty of the method, and particularly small if the ratios SiIIλ1814/SiIII]λ1892, AlIIIλ1860/SiIII]λ1892, and SiIVλ1397/SiIII]λ1892 are considered to compute $n_{\rm H}$ and U. It is significant if strong enrichment of Al and Si over C occurs. A more refined approach could exploit the dependence of AlIIIλ1860/CIVλ1549 (and SiIII]λ1892/CIVλ1549 and SiIVλ1397/CIVλ1549) on Z to build a 3D diagram where $n_{\rm H}$, U, Z along with Si-Al enrichment can be determined independently.

8.2. *Determining the best estimate of $n_{\rm H}$, U*

There are two sets of line ratios for each object: one comes from the SPECFIT results, and the other is the one computed after correcting the SPECFIT results because of low density contributions. Solutions with corrected value usually point toward very high density and low ionization, predicting SiIIλ1814 emission even twice as strong as SiIII]λ1892. However, increasing the metallicity for corrected ratios leads to better agreement among lines and more reasonable $n_{\rm H}$, U values, while leaving the product fairly unaffected. Especially the assumption of Silicon - Aluminium enrichment improves the concordance in the intriguing cases of SDSS J12014+0116, J01225+1339, J02287+0002 (using z_{oi}), the extreme objects and the two BAL QSOs in our sample. However, apart from the case of SDSS J12014+0116, the enrichment is probably excessive. From the discussion above the independent determination of $n_{\rm H}$ and U seems possible only if metallicity is at least roughly known. We exclude metallicity cases where we find a sizeable disagreement in the crossing points (with the exceptions of ratios involving SiIIλ1814: the ionization level can be estimated in a Z-independent way using the SiIVλ1397/SiIIλ1814 and the SiIVλ1397). We consider each individual source with line intensity before and after correction to obtain two independent sets of product $n_{\rm H}U$ values. As mentioned, changing metallicity is not affecting the product $n_{\rm H}U$ as much as $n_{\rm H}$ and U individually. In case of concordance of the crossing points and of high accuracy in the SiIIλ1814 ratio, $n_{\rm H}$ U, and Z can be considered independently determined. In Table 6 we indicate the values that are deemed most appropriate.

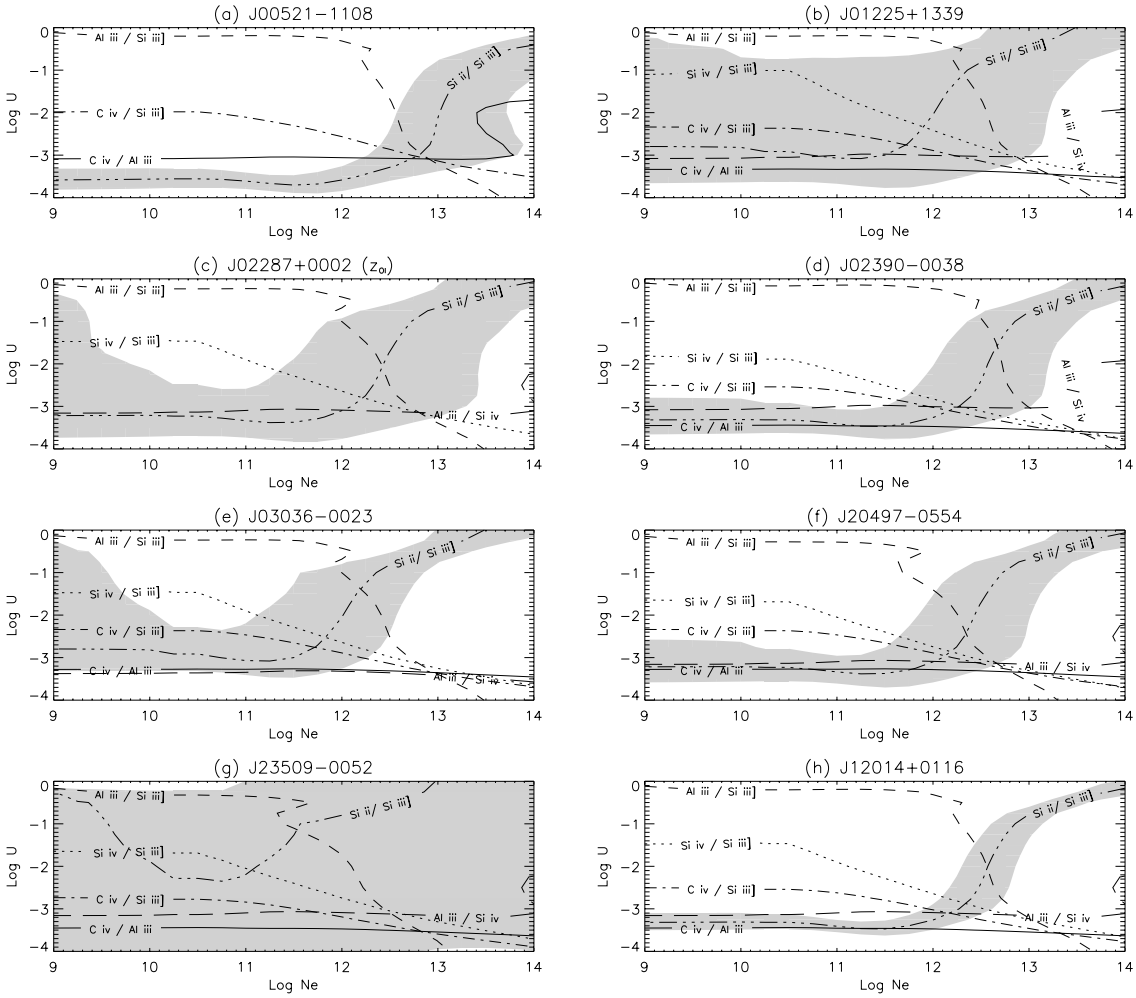

FIG. 17.— Contour plots for corrected values considering the low density emission contribution of CIII]λ1909. Contour plot for J00103-0037 is not shown because the correction is so large to be reliable. For the objects in panels (e) and (f) the SiIIλ1814 line is also affected by the telluric absorption. Abscissa, ordinate and symbols are the same as Fig. 11.

9. A PHOTOIONIZATION METHOD TO COMPUTE THE BROAD LINE REGION DISTANCE AND THE BLACK HOLE MASS.

The distance of the broad line region ($r_{\rm BLR}$) from the central continuum source and the black hole mass ($M_{\rm BH}$) are key parameters that let us understand the dynamics of the gas in the emitting region and the quasar behavior and evolution. In this work we will use a method based on the determination of $n_{\rm H}$ and U to compute $r_{\rm BLR}$. Eq. 1 can be rewritten as

$$r_{BLR} = \left[\frac{\int_{\nu_0}^{+\infty} \frac{L_\nu}{h\nu} d\nu}{4\pi U n_{\rm H} c} \right]^{1/2} \quad (3)$$

and also as

$$r_{BLR} = \frac{1}{h^{1/2} c} (U n_{\rm H})^{-1/2} \left(\int_0^{\lambda_{Ly}} f_\lambda \lambda d\lambda \right)^{1/2} d_p \quad (4)$$

where h is the Plank constant, c is the light speed, $d_{\rm p}$ is the proper distance. The integral is carried out from the Lyman limit to the shortest wavelengths on the *rest frame* specific flux f_λ. For the integral we will use two Spectral Energy Distributions (SEDs): one described by Mathews & Ferland (1987) and one by Laor et al. (1997a), also reproduced in Fig. 20.

Eq. 4 becomes:

$$r_{\rm BLR} \approx 93 \cdot (U n_{\rm e})_{10}^{-\frac{1}{2}} \cdot f_{\lambda_0,-15}^{\frac{1}{2}} \tilde{Q}_{H,0.1}^{\frac{1}{2}} \zeta(z, 0.3, 0.7) \ \ {\rm ld} \quad (5)$$

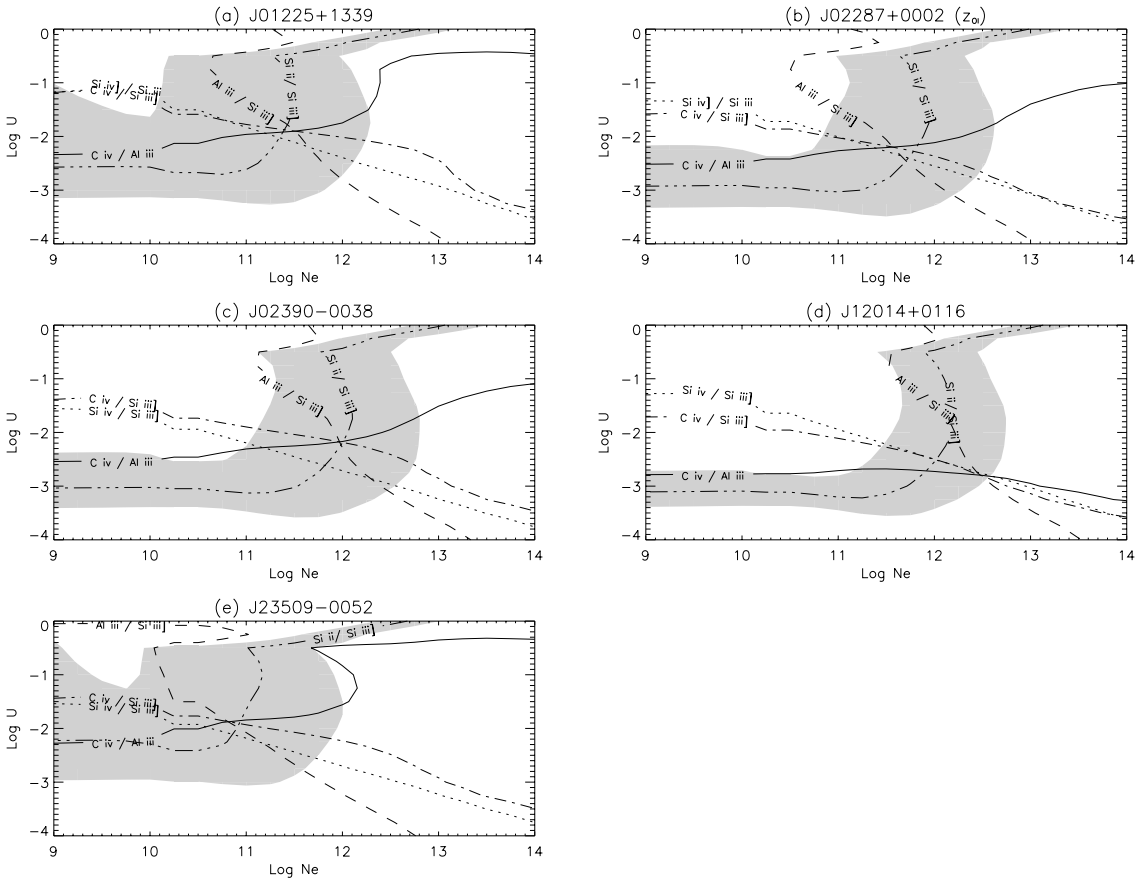

FIG. 18.— Contour plots for (a) J01225+1339, (b) J02287+0002 using $z_{CIII]\lambda1909}$, (c) J02390-0038, the extreme object (d) J12014+0116, and (e) J23509-0052, from the array of simulations computed for $Z = 5Z_{\odot}$. Coordinates and symbols are as for Fig. 11. The intersection point improves in certain cases, but in others is the same.

where $\tilde{Q}_H = \int_0^{\lambda_{Ly}} \tilde{n}_\lambda \lambda d\lambda$, and $\zeta(z, 0.3, 0.7)$ is an interpolation function for $d_{\rm p}$ as a function of redshift.

$\tilde{Q}_H$ is 0.00963 cmÅ in the case the continuum of Laor et al. (1997) is considered; $\tilde{Q}_H$ ≈0.02181 cmÅ for Mathews & Ferland (1987). We use their average value, since the derived U and $n_{\rm H}$ are not sensitive to the two different shapes to a first approximation.[7]

Knowing $r_{\rm BLR}$ we can calculate the $M_{\rm BH}$ assuming virial motions of the gas

$$M_{\rm BH} = f\frac{\Delta v^2 r_{\rm BLR}}{G}. \quad (6)$$

or,

$$M_{\rm BH} = \frac{3}{4G} f_{0.75}(FWHM)^2 r_{BLR} \quad (7)$$

with the geometry term $f \approx 0.75$, corresponding to $f_{0.75} \approx 1.0$ (Graham et al. 2011, see also Onken et al. 2004 and Woo et al. 2010). Collin et al. (2006) suggest that f is significantly different for Pop.A and B sources; we do not consider here their important result for the sake of comparison with previous work (§10.2). The resulting $r_{\rm BLR}$ and $M_{\rm BH}$ are reported in Columns 7 to 14 of Table 7. Errors are at 2σ confidence level and have been computed propagating quadratically the major sources of uncertainty. More precisely, in addition to the error on $\log(n_{\rm H}U)$, the $r_{\rm BLR}$ determination is affected by the uncertainty in the spectrophotometry (specific fluxes of Col. 3 of Tab. 7), and errors on the shape of the ionizing continuum. The two SEDs that we assumed as extreme yield a difference in ionizing photons of a factor 2.2. At a 2σ confidence level this corresponds to an uncertainty of ±0.065 in logarithm. An additional source of uncertainty affects $M_{\rm BH}$ due to the FWHM determination. Errors on FWHM are quadratically added to the uncertainty on $r_{\rm BLR}$ in the values reported as $\log M_{\rm BH}$ errors.

[7]Since the Laor et al. (1997) continuum produces a fewer ionizing photons, the same value of U is obtained at a smaller distance.

10. DISCUSSION

10.1. *Previous work*

There have been several studies aimed at computing $r_{\rm BLR}$ and $M_{\rm BH}$. A direct measure of $r_{\rm BLR}$ through reverberation mapping requires an enormous amount of observational effort and has only been applied to a relatively

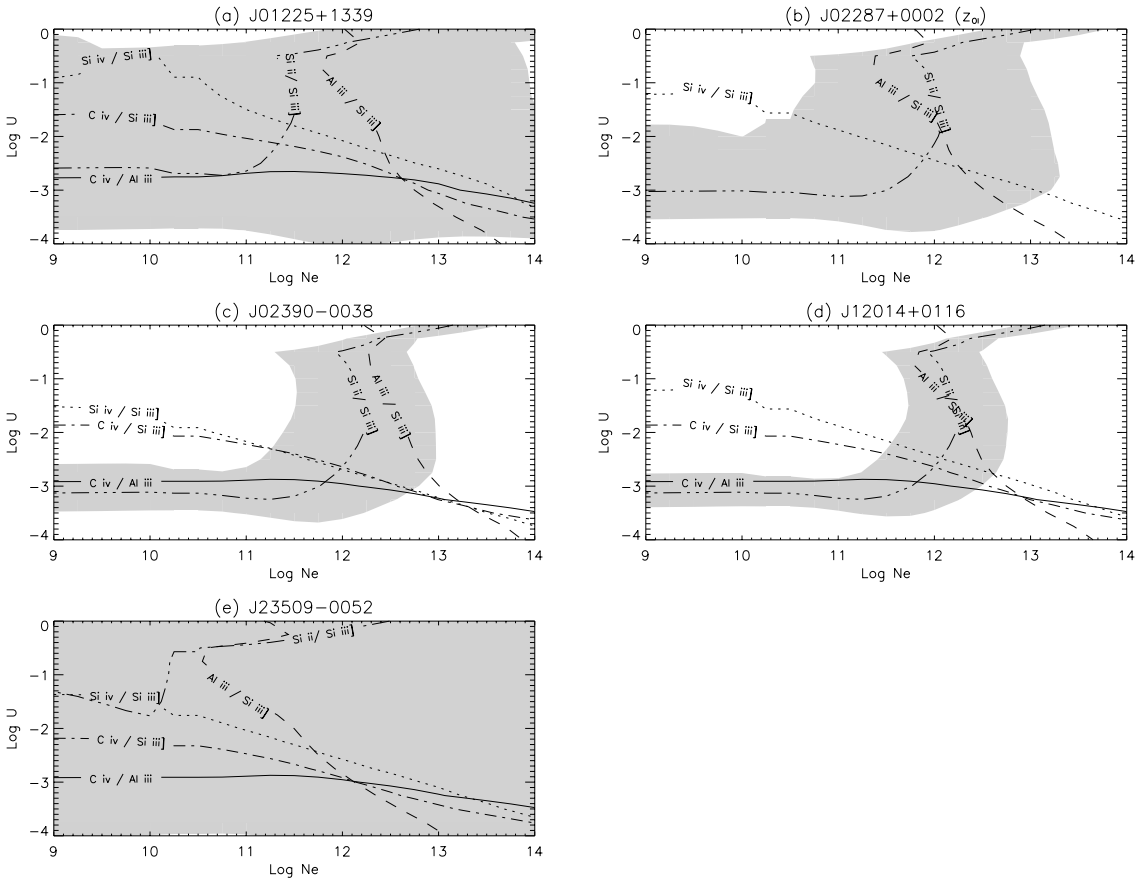

FIG. 19.— Contour plots for the same objects of the previous figure from the array of simulations computed for $Z = 5Z_{\odot}$ with ratios corrected because of low-density emission. Coordinates and symbols are as for Fig. 11.

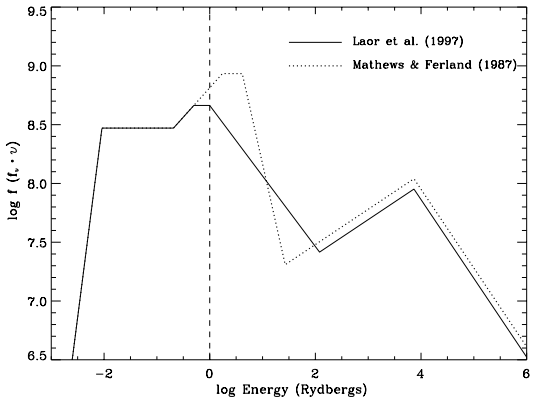

FIG. 20.— Spectral energy distribution used to compute the number of ionizing photons for Laor et al. (1997) in solid line and Mathews & Ferland (1987) in dotted line. Dashed line shows the Lyman limit.

small number of quasars: slightly less than 50 objects with $z \lesssim 0.4$ (Kaspi et al. 2000, 2005, Peterson et al. 2004; Bentz et al. 2010). A second way to measure $r_{\rm BLR}$ uses a less direct method. Kaspi et al. (2000, 2005) and Bentz et al. (2009) used reverberation mapping results to find, in an empirical way, a relationship between $r_{\rm BLR}$ and the optical continuum luminosity at 5100Å,

$$r_{\rm BLR} \propto L^{\alpha} \tag{8}$$

with $\alpha \approx 0.52$. Vestergaard & Peterson (2006) obtained a similar result for the optical continuum luminosity with an $\alpha \approx 0.50$ and for the UV continuum at 1350Å, $\alpha \approx 0.53$. These relationships have been used to compute the $r_{\rm BLR}$ not only for nearby objects, but also for high redshift, high luminosity objects. There are other works that use single epoch spectra and the continuum at 3000Å, obtaining an $\alpha \approx 0.47$ (McLure & Jarvis 2002).

We can rewrite Eq. 6 as

$$M_{\rm BH} \propto f \frac{\rm FWHM^2 L^{\alpha}}{G}. \tag{9}$$

Hβ is a low ionization strong line whose FWHM has been widely used to determine the $M_{\rm BH}$ for objects mainly up to $z \lesssim 0.9$; above this limit IR spectrometers and large telescopes are needed to cover the redshifted

line. For distant objects ($z \sim 2$), an alternative is to use CIVλ1549, a high ionization line emitted in the UV. However, this line should be used with caution because the line is often blueshifted. This means that at least part of this line is likely emitted in an outflow (Sulentic et al. 2007; Richards et al. 2010). Thus the estimation of $M_{\rm BH}$ using FWHM(CIVλ1549) tend to be systematically higher than those using FWHM(Hβ), especially for objects of Population A.

10.2. *Comparison with Vestergaard and Peterson (2006)*

Vestergaard & Peterson (2006) used the relationship $r_{\rm BLR} \propto L^{0.53}$ to obtain the following formula that relates $M_{\rm BH}$ to the FWHM(CIVλ1549) and the continuum luminosity at 1350Å:

$$\log M_{\rm BH}({\rm C\,IV}) = (6.66 \pm 0.01) - s_{\rm f} + \log\left\{\left[\frac{\rm FWHM(C\,IV)}{1000\,{\rm km\,s^{-1}}}\right]^2 \left[\frac{\lambda L_\lambda(1350{\rm \AA})}{10^{44}\,{\rm ergs\,s^{-1}}}\right]^{0.53}\right\}. \quad (10)$$

The scale factor $s_{\rm f} \approx -0.27$ sets the masses to the f value obtained by Graham et al. (2011). In Cols. 11 and 15 of Table 7 and in Fig. 21 we compare our $M_{\rm BH}$ results with those using Eq. 10. We do not apply corrections for radiation-pressure effects that are likely relevant especially for objects radiating at large Eddington ratio (Netzer 2009; Netzer & Marziani 2010). The difference between this computation and the one reported in Sulentic et al. (2007) is that in the latter work the blueshifted component was not separated from the broad component of CIVλ1549 just to show how larger values of FWHM(CIVλ1549) yielded $M_{\rm BH}$ much larger than the ones derived from FWHM(Hβ) in Pop. A objects.

We compare the masses obtained using our photoionization method with those of Vestergaard & Peterson (2006) in Fig. 21. We use the FWHM of the BC as an estimator of the virial line broadening. From our results we can see that the masses agree within less than 1σ uncertainty in the luminosity correlation (0.33). There is a systematic offset of 0.17±0.10 if uncorrected ratios are used. The mass values obtained after correction for low density gas are systematically lower. This happens because the correction increases the product $Un_{\rm H}$, lowering $r_{\rm BLR}$ and hence $M_{\rm BH}$. The $M_{\rm BH}$ obtained after corrections are within the error bars. The systematic offset is then 0.13 ± 0.12. It is important to consider that the computed correction is in many ways a maximum correction. CIII]λ1909 emission is assumed to have the same FWHM of SiIII]λ1892 while it could be significantly narrower; in addition part of the CIII]λ1909 emission could be due to FeIII λ 1914. In many sources of Pop. A the correction could be ignored altogether. The present results indicate that the Kaspi et al. (2000) relationships can be extended to be used in high redshift objects (or at least until z∼3) if the FWHM of the core broad line region can be well determined and measured. In order to do this, we need:

- Spectra with S/N high enough to see the profile shape that allows decomposition of the CIVλ1549 line, especially to separate the blue component from the broad core;
- to follow the methodological considerations explained in §4 .

Fig. 21 should be looked at with two cautions. First, the correlation is dominated by the luminosity dependence of $r_{\rm BLR}$, used to compute $M_{\rm BH}$ in both cases. Second, the spread of $M_{\rm BH}$ values is small, less than one order of magnitude (and most objects have statistically indistinguishable masses). Our estimated error bars are however smaller compared to the spread expected on the basis of the $r_{\rm BLR}$-L correlation which is, according to Vestergaard & Peterson (2006), ±0.66 at a 2σ confidence level. The two shaded bands of Fig. 21 limit the region where we can expect to find data points on the basis of the $r_{\rm BLR}$-L correlation. Clearly, a proper interpretation of the CIVλ1549 profile may help to reduce the scatter. In any case, our method should provide $M_{\rm BH}$ estimates with somewhat lower uncertainty. It is interesting to note that SDSS J12014+0116 appear at the largest $M_{\rm BH}$, and the agreement with the $r_{\rm BLR}$-L is very good. The $r_{\rm BLR}$ value of 3C 390.3 we obtain is fairly uncertain due to the low S/N. The size computed in the present paper is larger than the reverberation mapping derived $r_{\rm BLR}$ for Hβ and CIVλ1549, although consistent with the value derived from Lyα. 3C 390.3 has the unusual property of having a response time longer in CIVλ1549 than in Hβ, although the large error bars do not exclude that the two lines respond with similar time. This behavior might be related to different physical conditions found for this object.

10.3. *The LIL-BLR*

While the existence of high density and low ionization has been invoked since long to explain FeII emission (especially by S. Collin and collaborators, as mentioned in the introduction), we have provided additional evidence that high density and low ionization are indeed diagnosed from emission lines other than FeII blends, and that conditions are the one producing most line emission in extreme Pop. A quasars. Last but not least, both U and $n_{\rm H}$ can be observationally determined with reasonable accuracy from the diagnostic ratios SiIIλ1814/SiIII]λ1892, SiIVλ1397/SiIII]λ1892, AlIIIλ1860/SiIII]λ1892, and CIVλ1549/(AlIIIλ1860 or SiIII]λ1892). Metallicity can be also constrained from the previous ratios as well as from CIVλ1549/SiIVλ1397. These ratios are pretty well defined, while estimating CIII]λ1909 and FeIIIλ1914 relative contribution is not relevant to our method (with the exceptions of sources like 3C 390.3). This low ionization BLR (or LIL BLR) has very similar properties to the OI and CaII emitting region identified by Matsuoka et al. (2008). The LIL-BLR seems to be present in the vast majority of quasars, probably all the ones with significant FeII emission (Marziani et al. 2010). The low values of U could be a consequence of the high density rather than of a far away location of the emitting region. The assumption of a single well defined value of U and $n_{\rm H}$ is probably an idealization even for the LIL-BLR taken alone; however the convergence of emission line ratios toward a well defined point, along with the ability to qualitatively explain FeII and most Hβ emission, indicate that the LIL-BLR might be a region with a small range of low U and high $n_{\rm H}$.

Do density and ionization parameter in the LIL BLR

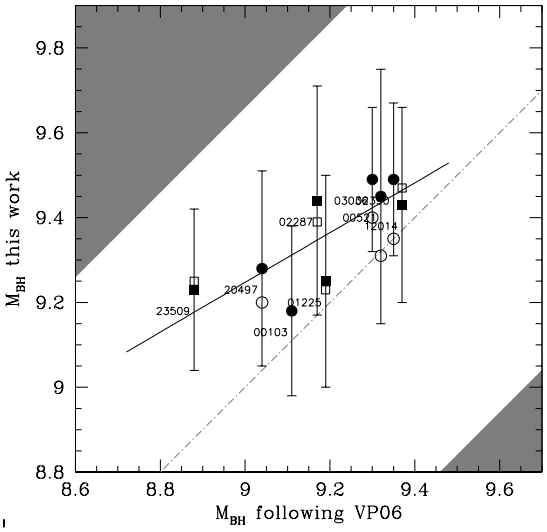

FIG. 21.— $M_{\rm BH}$ comparison for the high-z sample. Filled symbols refer to uncorrected intensity ratios; open symbols are for intensity ratios corrected because of low-density emission. Circles refer to solar metallicity; squares to 5 times solar metallicity and Si-Al enrichment. Abscissa and ordinate are logarithm of $M_{\rm BH}$ in solar masses. Each point is labeled with the object name in short format. In ordinate we report $M_{\rm BH}$ values obtained with the method of this paper; in abscissa those obtained employing the Vestergaard & Peterson relationship described in the text. The shaded bands limit the 2σ confidence level spread expected on the basis of the Vestergaard & Peterson relationship.

converge to a single well defined value with a small dispersion? A tentative answer comes from the values reported in Tab. 6. Excluding 3C390.3, the range U and $n_{\rm H}$ span is not very large (even considering changes in metallicity): less than one order of magnitude around log $n_{\rm H}\sim$ 12.5, and ionization parameter ~ -2.75, and the spread is not much larger than the uncertainties in the individual measurements. The product $U{\cdot}n_{\rm H}$ seems to be fairly stable. We have $< \log(U{\cdot}n_{\rm H})> \approx 9.5$, with a sample dispersion of 0.15 (excluding 3C 390.3). We applied the same method to 14 low-z quasars (Negrete et al. 2010), and we obtain $< \log(U{\cdot}n_{\rm H})> \approx 9.7$, with a dispersion of 0.3. Assuming $\log(U{\cdot}n_{\rm H}) \approx 9.6$ could be a good approach to estimate $M_{\rm BH}$ if elaborate measurements on CIVλ1549 and CIII]λ1909 are not possible, and only a rough estimate of the SiIII]λ1892 BC FWHM is available. On the other hand, there is still a major effect of measurement errors on the uncertainty derived for $\log(U{\cdot}n_{\rm H})$; instrumental improvements may lead to a significant appreciation of object-by-object diversity.

The $U{\cdot}n_{\rm H}$ values reported in Table 6 are not very far from the average value obtained by Padovani and Rafanelli (1988). This is not surprising since the spectra at low and high z seems to show the same diversity, classified through the E1 sequence and the Pop. A/Pop. B distinction. In other words, NLSy1-like sources whose spectrum is similar to I Zw1 appear to be present at high redshift, meaning that the LIL-BLR remains strong and prominent over a wide range of redshifts. A second reason is that Padovani and Rafanelli (1988) considered Hβ. Emission of Hβ can be significant under a much wider range of U and $n_{\rm H}$; however, the AlIIIλ1860, MgIIλ2800, FeII emitting region should be also a strong producer of Hβ. This region with well-defined physical conditions is expected to be the emitter of the core of Hβ, i.e., the part of the line responding more strongly to continuum changes.

10.3.1. *Verification on EW and Line Luminosity*

Considering that we have very low ionization parameter values, a legitimate question is whether we have a sufficient number of photons to explain the EW and luminosity of the emission lines. We made a preliminary check of consistency for the EW from CLOUDY simulations. A second, a-posteriori test was to consider the predicted line luminosity assuming the actual luminosity of the quasar, the density and the distance $r_{\rm BLR}$ derived from our method, and spherical geometry.

A remarkable property common to all spectra is the low EW of the emission lines. The extreme source SDSS J120144.36+011611.6 has total W(CIVλ1549) $\approx$ 19 Å, which becomes $\approx$ 7 Å if only the LIL component is considered. The whole 1900 Å blend has $W \approx$ 20 Å; the individual EWs of SiIII]λ1892 and AlIIIλ1860 are just a few Å. Similar considerations apply to the other high-z quasars, especially for Pop. A sources. In this case we have W(CIVλ1549)$\approx 20-30$ Å, the equivalent width of the whole 1900 Å $30-40$Å including the uncertain contribution of FeIII and CIII]λ1909. This has the important implication that the ionization parameter cannot be very large. From our simulations, we deduce that the LIL-BLR $\log U$ is always $\lesssim -2.0$. On the other hand, toward the low U, high density limit emission lines tend to disappear altogether. The predicted EWs become too low to account for the observed EW with a covering factor $f_{\rm c} \lesssim 0.5$ if $\log U \lesssim -3$. The values obtained after correction $\log U \approx -3.25$ are still possible within the condition of $f_{\rm c} \lesssim 0.5$ since the CIVλ1549 EW is greatly diminished. Cases of very low U are rather indicative of strong metal enhancement than of extremely low ionization level (see §8.1). If we take log $n_{\rm H}\approx$12.5, $\log U = -2.75$, the predicted equivalent width of is W(CIVλ1549)$\approx$37 Å for a covering factor 0.5, close to the largest values observed in our quasars. However, The CIVλ1549 EW of SDSS J12014+0116 can be accounted for by the values of $\log U \approx -3.00$ and log $n_{\rm H}\sim$ 12.75 – 12.50.

If we model the BLR with a spherical geometry where the emitting gas covers a fraction $f_{\rm c}$ of the continuum, CLOUDY computations confirm that the line luminosity can be accounted for. The luminosity at 1700 Å of J00103-0037 is $\log \lambda L_\lambda \approx 46.6$; the predicted luminosity of CIVλ1549 is $\log L$(CIVλ1549) $\approx$ 44.5, under the assumption of $Z = Z_\odot$, $f_{\rm c} = 0.1$, and Mathews & Ferland continuum shape. The observed CIVλ1549 line luminosity of J00103-0037, $\approx 9 \cdot 10^{44}$ ergs s^{-1}, is obtained with $f_{\rm c} \approx 0.3$.

10.3.2. *Analogy with η Carinæ*

The physical conditions we envisage for the BC of quasars find a correspondence in the so-called Weigelt blobs of η Carinæ, located in the equatorial plane of the

system, perpendicular to the symmetry axis of the bipolar lobes forming the homunculus nebula (cf. Marziani et al. 2010). Unlike the gas of the bipolar lobes, predominantly shock heated, the Weigelt blobs are believed to be dense gas photoionized by the radiation associated to the central, massive star and to a possible companion (e.g., Johansson et al. 2000; Davidson 2005). The spectrum of the Weigelt blobs shows very weak CIII]λ1909 along with a prominent line at λ1914, ascribed to the $z^7P^0_3 \rightarrow a^7S_3$ FeIII transition. The line appears very strong because the upper level is populated by Lyα fluorescence. This very same process is expected to be present also in quasars. Indeed, in I Zw 1, where lines are narrow, and in SDSS J120144.36+011611.6 the peak emission at around 1914 Å is actually visible. The amount of Lyα pumping to the upper level ($z^7P^o_3$) of the UV 34 cannot be estimated through the standard edition of CLOUDY (the relevant levels of the UV 34 multiplets of Fe^{+2} ion are not included). Additional photoionization computations including a suitable Fe^{+2} model and line transfer should be considered. This is beyond the aim of the present study; we can conclude in a qualitative fashion that the spectrum of the η Carinæ blobs supports a view of the low-ionization part of the BLR that is not conventional: very high density gas, at very low ionization.

11. CONCLUSIONS

In this paper we presented new observations of eight high redshift quasars. The spectra were meant to provide high S/N, moderate resolution data on which the CIVλ1549, SiIII]λ1892, AlIIIλ1860, and SiIIλ1814 emission line profiles could be accurately analyzed. Line profile fits allowed us to isolate a specific component whose intensity ratios were used to derive consistent values for electron density and ionization parameter. This line component (LIL BC) seems to be emitted predominantly by low ionization, high density gas in the majority of quasars studied thus far by us.

These results permitted us to compute the product $n_{\rm H}{\cdot}U$ and hence the size of the Broad Line Region and the central black hole mass. The method described in this paper rests on the assumption of photoionization as the mechanism of gas heating; on the assumption of isotropic luminosity, and on line ratios predicted by CLOUDY simulations. The photoionization method explored in this paper offers an estimate of $r_{\rm BLR}$ for each quasar, with some advantages on the $r_{\rm BLR}$ valued derived from the luminosity-size correlation. The luminosity correlation suffers from large scatter and is simply extrapolated to very high luminosity without any support since there are, unfortunately, no conclusive results on reverberation of high luminosity quasars even if heroic efforts are underway (e.g., Trevese et al. 2007, Botti et al. 2010). We found that the black hole masses derived from the computed $r_{\rm BLR}$ and from the virial assumption are in good agreement with the ones derived from the luminosity-size relationship. Actually, Fig. 21 suggests that we might have reduced the errors of the $M_{\rm BH}$ by a factor of two with respect to the expectation from the Vestergaard & Peterson (2006) relationship.

We repeat that our $M_{\rm BH}$ and $r_{\rm BLR}$ results are based on the product $n_{\rm H}{\cdot}U$ and not on values of $n_{\rm H}$ and of U taken separately. It seems that this product converges to two typical ranges of values, one of them associated to low-ionization, high density gas (the LIL-BLR). For our $n_{\rm H}$ and U determinations we do not use ratio CIII]λ1909/SiIII]λ1892 except for 3C 390.3. As we discussed in §7.2, this ratio should not be considered at high density because CIII]λ1909 is collisionally quenced if $n_{\rm H} \gtrsim 10^{10}$ cm^{-3}. CIII]λ1909 is produced in conditions that are very different from the ones we found for the LIL-BLR. While the method can be applied to most quasars, the application seems to be especially straightforward to quasars whose spectrum is like SDSS J120144.36+011611.6 (if high metallicity is properly taken into account) or, at the other end, 3C390.3. In the first case we have dominance by the LIL-BLR, in the second case the LIL-BLR seems to be completely absent and physical conditions look radically different: high ionization and moderate density. An inspection of SDSS spectra covering both the 1900 Å blend and CIVλ1549 (up to $z \approx 3.5$) shows that SDSS J120144.36+011611.6 has many replicas at high redshift, accounting for at least a few percent of all quasars. These high-metallicity objects should be the first candidates to expand black hole mass computations to high redshift without relying on the $r_{\rm BLR}$ - L correlation.

To apply the photoionization method in the most effective way, determining $n_{\rm H}$ and U with the lowest uncertainty, spectral data should be of moderate resolution ($\lambda/\Delta\lambda \sim 1000$) as well as of high S/N. If the SiIIλ1814 line can be measured in an accurate way, it would be possible to derive independent estimates of U, $n_{\rm H}$, and $Z/Z_\odot$ in most quasars.

Especially the most extreme (in terms of AlIIIλ1860 strength) objects in bin A3 and A2 hold the promise to make possible an independent estimate of $n_{\rm H}$, U, and metallicity. Clearly, objects in bin A1 resembling their median spectrum are not well suited for an application of the method. Also, any source with CIII]λ1909/SiIII]λ1892$>$ 1 is subject to a large correction. In light of the many uncertainty, an average value of the product Un (obtained from the objects of the other spectral types) could be considered.

Pop. B objects should not avoided entirely, especially whenever SiIII]λ1892 $\gtrsim$ CIII]λ1909 after VBC removal.

The present exploratory analysis emphasized several sources of uncertainty. However, the parameter needed for $r_{\rm BLR}$ and $M_{\rm BH}$ computation, the product $Un_{\rm H}$, seems to be fairly stable and well-defined. Even with an error of a 0.3 in logarithm, the square root will be subject to a 0.15 uncertainty in logarithm, much lower than the uncertainty associated with the $r_{\rm BLR}$luminosity correlation. The large intrinsic spread of the correlation at low luminosity, its uncertain extrapolation at very high luminosity make preferable a one-by-one determination based on physical properties of an emitting region that remains similar to itself.

A. Negrete and D.Dultzin acknowledge support form grant IN111610-3 PAPIIT, DGAPA UNAM. Funding for the SDSS and SDSS-II has been provided by the Alfred P. Sloan Foundation, the Participating Institutions, the National Science Foundation, the U.S. Department of Energy, the National Aeronautics and Space Administration, the Japanese Monbukagakusho, the Max Planck

Society, and the Higher Education Funding Council for England. The SDSS Web Site is http://www.sdss.org. The SDSS is managed by the Astrophysical Research Consortium for the Participating Institutions listed at the SDSS Web Site.

REFERENCES

Aoki, K., Yoshida, M. 1999, ASPC, 162, 385
Appenzeller, I., et al. 1998, The Messenger, 94, 1
Bachev et al. 2004, ApJ, 617, 171
Baldwin, Ferland, Korista and Verner, 1995, ApJ, 455, L119
Baldwin J. A. et al. 1996, ApJ, 461, 682
Baskin, A. & Laor, A. 2005, MNRAS, 356, 1029
Bentz, M. C., et al. 2010, ApJ, 716, 993
Bevington, P. R. 1969, Data reduction and error analysis for the physical sciences, New York: McGraw-Hill, 1969
Boroson, T.A. & Green, R.F., 1992, ApJS, 80, 109
Botti, I., Lira, P., Netzer H., Kaspi, S. 2010, IAU Symposium, 267, 198
Bottorff M.C. & Gary J.F. 2000, MNRAS, 316, 103
Bruhweiler, F. & Verner, E., 2008, ApJ, 675, 83
Clavel, J., et al. 1991, ApJ, 366, 64
Clayton, D.D., 1983, Principles of Stellar Evolution & Nucleosynthesis, Chicago:University of Chicago Press, Ch. 7
Collin-Souffrin S. et al. 1988, MNRAS, 232, 539
Collin, S., et al. 2006, A&A, 456, 75
Constantin A. et al. 2002, ApJ, 565, 50
Davidson, K. & Netzer, H., 1979, Rev. Mod. Phys. 51, 715
Davidson, K. 2005, ASPC, 332, 101
Dumont, A. M. & Mathez, G., 1981, A&A, 102, 1
Dumont, A. M, & Collin-Souffrin, S., 1990 A&A 229, 292
Edlén & Swings, 1942, ApJ, 95, 532
Ekberg J.O. 1993, A&AS, 101, 1
Espey, B. R., Carswell, R. F., Bailey, J. A., Smith, M. G., & Ward, M. J. 1989, ApJ, 342, 666
Evans & Koratkar 2004, ApJS, 150, 73
Francis P.J. et al. 1991, ApJ, 373, 465
Feibelman, W.A., and Aller, L.H., 1987, ApJ, 319, 407
Feldman U. et al. 1992, ApJS, 81, 387
Ferland G. J. et al. 1998, PASP, 110, 761
Gaskell, C. M. 1982, ApJ, 263, 79
Gaskell, M. et al. 1999, ASPC, 175, 423
Graham, A. W. et al. 2011, MNRAS, 48
Hartig, G. F. & Baldwin, J. A. 1986, ApJ, 302, 64
Hu, C., et al. 2008, ApJ, 687, 78
Johansson S. et al. 2000, A&A, 361, 977
Joly, M., 1987, A&A, 184,33
Kaspi et al. 2000, ApJ, 533, 631
Kaspi et al. 2005, ApJ, 629, 61
Kriss G.A., 1994, ASPC, 61, 437
Korista K. et al. 1997, ApJS, 108, 401
Kuraszkiewicz, J. K. et al. 2002 ApJS, 143,257
Laor A. et al. 1994, ApJ, 420, 110
Laor A. et al. 1997a, ApJ, 477, 93
Laor A. et al. 1997b, ApJ, 489, 656
Leitherer, C., et al. 1999, ApJS, 123, 2
McLure & Jarvis 2002, MNRAS, 337, 109
Marziani, P., Sulentic, J. W., Dultzin-Hacyan, D., Calvani, M., & Moles, M. 1996, ApJS, 104, 37
Marziani P. et al. 2003, ApJS, 145, 199
Marziani P. et al. 2003b, MNRAS, 345, 1133
Marziani P. et al. 2008, RMAA serie de conferencias, 32, 69
Marziani P. et al. 2009, A&A, 495, 83
Marziani P. et al. 2010, MNRAS, arXiv:1007.3187v1
Matsuoka, Y., Kawara, K., & Oyabu, S. 2008, ApJ, 673, 62
Mathews & Ferland 1987, ApJ, 323, 456
Metzroth, K. G., Onken, C. A., Peterson B. M. 2006, ApJ, 647, 901
Negrete, C. A., Dultzin, D., Marziani, P., Sulentic J. W. 2010, ApJL, submitted
Netzer, H., & Trahktenbrot, B. 2007, ApJ, 654, 754
Netzer, H. 2009, ApJ, 695, 793
Netzer, H. & Marziani, P. 2010, ApJ, in press, arXiv:1006.3553v2
Onken, C. A., Peterson, B. M. 2002, ApJ, 572, 746
Onken, C. A., Ferrarese, L., Merritt, D., Peterson, B. M., Pogge, R. W., Vestergaard, M., & Wandel, A. 2004, ApJ, 615, 645
Osterbrock, D. E., & Ferland, G. J. 2006, Astrophysics of gaseous nebulae and active galactic nuclei, 2nd. ed. by D.E. Osterbrock and G.J. Ferland. Sausalito, CA: University Science Books, 2006,
Padovani, P., 1988, A&A, 192, 9
Padovani, P. & Rafanelli, P. 1988, A&A, 205, 53
Padovani, P., Burg, R.I., Edelson, R.A., 1990, ApJ, 353, 438
Peterson B. M. et al. 2004, ApJ, 613, 682.
Punsly, B. 2010, ApJ, 713, 232
Rees M.J. 1987, MNRAS, 228, 47
Richards, G. T., et al. 2010, arXiv preprint 2010arXiv1011.2282R
Richards, G. T., Vanden Berk, D. E., Reichard, T. A., Hall, P. B., Schneider, D. P., SubbaRao, M., Thakar, A. R., & York, D. G. 2002, AJ, 124, 1
Sigut T.A. et al. 2004, ApJ, 611, 81
Sulentic J. W. et al. 2000, ApJ, 536, L5
Sulentic J. W. et al. 2001, AIP Conference Proceedings, 599, 963
Sulentic J. W. et al. 2002, ApJ, 566, 71
Sulentic J. W. et al. 2006, RMxAA, 42, 23
Sulentic J. W. et al. 2006b, A&A, 456, 929
Sulentic J. W. et al. 2007, ApJ, 666, 757.
Trevese, D., Paris, D., Stirpe, G. M., Vagnetti, F., and Zitelli, V. 2007, A&A, 470, 491
Tytler, D., & Fan, X.-M. 1992, ApJS, 79, 1
Vanden Berk et al. 2001, AJ, 122, 549
Verner E. et al. 1999, ApJS, 120, 101
Verner E. et al. 2003, ApJ, 592, 59
Verner E. et al. 2004, ApJ, 611,780
Vestergaard M. and Peterson B.M. 2006, ApJ, 641, 689.
Vestergaard & Wilkes, 2001, ApJS, 134, 1
Wandel, A., Peterson, B. M., Malkan, M. 1999, ApJ, 526, 579
Wills, B. J., et al. 1999, ApJ, 515, L53
Woo, J.-H., et al. 2010, ApJ, 716, 269
Woosley, S. E., Weaver, T. A. 1995, ApJS, 101, 181
Zamfir, S., Sulentic, J. W., Marziani, P., & Dultzin, D. 2010, MNRAS, 403, 1759

4.12. Apéndice. Desarrollo de los cálculos para r_{BLR} y $M_{\rm BH}$.

De la definición del parámetro de ionización U (ec. 1.19), el tamaño de la región de líneas anchas es

$$r_{BLR} = \left[\frac{\int_{\nu_0}^{+\infty} \frac{L_\nu}{h\nu} d\nu}{4\pi U N_e c} \right]^{1/2}, \tag{4.1}$$

con $N_{\rm e}$ la densidad electrónica, c la velocidad de la luz, h la constante de Planck y la luminosidad específica, L_ν, está integrada sobre el límite de Lyman. Así, en términos de la longitud de onda, la luminosidad es $L_\lambda = 4\pi d_p^2 F_\lambda$ con $F_\lambda = \int_0^{\lambda_{Ly}} f_\lambda d\lambda$, el flujo integrado sobre todas las longitudes de onda y d_p la distancia propia al cuasar. De este modo, la r_{BLR} queda como

$$r_{BLR} = \frac{1}{h^{1/2} c} (U N_e)^{-1/2} \left(\int_0^{\lambda_{Ly}} f_\lambda \lambda d\lambda \right)^{1/2} d_p, \tag{4.2}$$

donde h es la constante de Planck. Considerando

$$f_\nu = f_{\nu_0} \left(\frac{\nu}{\nu_0} \right)^{-\alpha}, \tag{4.3}$$

entonces, con $\nu = c/\lambda$ y conociendo que $f_\lambda d\lambda = f_\nu d\nu$

$$\begin{aligned} f_\lambda &= f_\nu \left| \frac{d\nu}{d\lambda} \right| = f_{\nu_0} \left(\frac{\lambda}{\lambda_0} \right)^{\alpha} \left| \frac{d}{d\lambda} \frac{c}{\lambda} \right| = f_{\nu_0} \left(\frac{\lambda}{\lambda_0} \right)^{\alpha} c\lambda^{-2} \\ &= \underbrace{\frac{f_{\nu_0} c}{\lambda_0^2}}_{f_{\lambda_0}} \left(\frac{\lambda}{\lambda_0} \right)^{\alpha-2}. \end{aligned} \tag{4.4}$$

De este modo,

$$f_\lambda = f_{\lambda_0} \left(\frac{\lambda}{\lambda_0} \right)^{\alpha-2} \tag{4.5}$$

Planteamos un cambio de variable $\lambda \to \frac{\lambda}{\lambda_0}$,

$$f_{\left(\frac{\lambda}{\lambda_0}\right)} = f_{\lambda_0} \left(\frac{\lambda}{\lambda_0} \right)^{\alpha-2}. \tag{4.6}$$

Sin embargo probablemente no podamos medir el flujo del continuo a λ_0 debido a que nuestro límite va de $\lambda_{Ly} \rightarrow 0$, así que escalándolo a alguna λ podremos medirlo directamente del espectro. Usaremos $\lambda(1700\text{Å})$ porque en ese punto tenemos una ventana del continuo. De manera que ahora podemos escribir

$$f_{\lambda_0} = f_{\lambda,1700}\left(\frac{f_{\lambda_0}}{f_{\lambda,1700}}\right). \tag{4.7}$$

Así, si los límites de la integral de la ecuación 4.2 van de λ_i a λ_{i+1}, donde el límite superior es λ_{Ly}, entonces

$$\begin{aligned}
\int_0^{\lambda_{Ly}} f_\lambda \lambda d\lambda &= \sum_{i=1}^{N} \int_{\frac{\lambda_{0,i+1}}{\lambda_{0,i}}}^{1} f_{\left(\frac{\lambda}{\lambda_{0,i}}\right)} \lambda_{0,i} \left(\frac{\lambda}{\lambda_{0,i}}\right) \lambda_{0,i}\, d\left(\frac{\lambda}{\lambda_{0,i}}\right) \\
&= f_{\lambda,1700} \sum_{i=1}^{N} \lambda_{0,i}^2 \left(\frac{f_{\lambda_{0,i}}}{f_{\lambda,1700}}\right) \int_{\frac{\lambda_{0,i+1}}{\lambda_{0,i}}}^{1} \left(\frac{\lambda}{\lambda_{0,i}}\right)^{\alpha_i - 1} \frac{\lambda}{\lambda_{0,i}}\, d\left(\frac{\lambda}{\lambda_{0,i}}\right) \\
&= f_{\lambda,1700} \underbrace{\sum_{i=1}^{N} \lambda_{0,i}^2 \left(\frac{f_{\lambda_{0,i}}}{f_{\lambda,1700}}\right) \frac{1}{\alpha_i}\left[1 - \left(\frac{\lambda_{0,i+1}}{\lambda_{0,i}}\right)^{\alpha_i}\right]}_{I}
\end{aligned} \tag{4.8}$$

Usando la ecuación 4.4, encontramos el valor para $f_{\lambda_{0,i}}$:

$$f_{\lambda_{0,i}} = f_{\lambda,i+1}\left(\frac{\lambda_{0,i}}{\lambda_{0,i+1}}\right)^{\alpha_i - 2} \tag{4.9}$$

donde $\alpha_i = 1 - m_i$, con m_i la pendiente de la recta en el intervalo i.

De los continuos de Mathews & Ferland (1987) y Laor et al. (1997) (figura 20), tenemos que la pendiente

$$m = \frac{Log(f_\nu \cdot \nu)_2 - Log(f_\nu \cdot \nu)_1}{LogE_2 - LogE_1}. \tag{4.10}$$

Laor				Mathews & Ferland			
Log E	λ(Å)	Log ($f_\nu \cdot \nu$)	m	Log E	λ(Å)	Log ($f_\nu \cdot \nu$)	m
-8.000	$9.12X10^{10}$	10.517	0.796	-12.000	$9.12X10^{14}$	-30.00	4.103
-5.011	$9.35X10^{7}$	12.896	3.727	-6.000	$9.12X10^{8}$	-5.380	3.493
-2.034	$9.87X10^{4}$	23.988	0.000	-2.034	$9.87X10^{4}$	8.471	0.000
-0.687	4437	23.988	0.493	-0.687	4437	8.471	0.499
-0.296	1805	24.181	-0.002	0.237	528.3	8.933	0.001
-0.004	920.8	24.180	-0.598	0.611	223.7	8.933	-1.921
2.082	7.558	22.934	0.299	1.452	32.19	7.316	0.299
3.865	0.124	23.468	-0.669	3.865	0.124	8.038	-0.669
6.860	$1.26X10^{-4}$	21.463	-5.582	6.860	$1.26X10^{-4}$	6.035	-21.512
9.000	$9.12X10^{-7}$	9.517		9.000	$9.12X10^{-7}$	-40.00	

Donde podemos medir $f_{\lambda,1700}$ directamente del espectro. Para conocer el valor de $f_{\lambda,912}$ suponemos que α es constante entre estos valores. Por ejemplo, para los siguientes valores de Laor,

$$f_{\lambda,912.3} = f_{\lambda,1700}\left(\frac{912.3}{1700}\right)^{-1+0.002} \tag{4.11}$$

$$\begin{aligned} f_{\lambda,7.558} &= f_{\lambda,912.3}\left(\frac{7.558}{912.3}\right)^{-1+0.598} \\ &= f_{\lambda,1700}\left(\frac{912.3}{1700}\right)^{-1+0.002}\left(\frac{7.558}{912.3}\right)^{-1+0.598} \end{aligned} \tag{4.12}$$

y así sucesivamente. De este modo, el término

$$\frac{f_{\lambda_{0,i}}}{f_{\lambda,1700}} \tag{4.13}$$

en I (de la ecuación 4.8), es independiente de $f_{\lambda,1700}$ y depende solo de la pendiente del continuo (Laor o Mathews & Ferland), es decir, este cociente es el mismo para todos los objetos.

Para el continuo de Laor, tomamos en cuenta cuatro intervalos, para los cuales $\lambda_{0,i} = \lambda_{max}$ en cada intervalo. Para ser consistentes, las unidades de λ deben ser en cm.

$\lambda_{max}(10^{-8}cm)$	$\lambda_{min}(10^{-8}cm)$	m
912.3	7.558	-0.598
7.558	0.124	0.299
0.124	$1.26X10^{-4}$	-0.669
$1.26X10^{-4}$	$9.87X10^{-7}$	-5.582

$I_{Laor} = 9.703X10^{-11}(cm^2)$

Para el continuo de Mathews & Ferland, tomamos seis intervalos:

$\lambda_{max}(10^{-8}cm)$	$\lambda_{min}(10^{-8}cm)$	m
912.3	528.3	0.499
528.3	233.7	0.001
233.7	32.19	-1.921
32.19	0.124	0.299
0.124	$1.26X10^{-4}$	-0.669
$1.26X10^{-4}$	$9.12X10^{-7}$	-21.512

$I_{M\&F} = 2.120X10^{-10}(cm^2)$

Regresando a la ecuación 4.2,

$$r_{BLR} = \frac{1}{h^{(1/2)}c}(UN_e)^{(1/2)}\left(\int_0^{\lambda_{Ly}} f_\lambda \lambda d\lambda\right)^{(1/2)} d_p \tag{4.14}$$

donde

$$f_{\lambda_0} I = \int_0^{\lambda_{Ly}} f_\lambda \lambda d\lambda \tag{4.15}$$

y

$$d_P = \frac{c}{H_0}\zeta(z, \Omega_M, \Omega_\Lambda) \tag{4.16}$$

Entonces ahora podemos escribir

$$r_{BLR} = \frac{\zeta(z, \Omega_M, \Omega_\Lambda)}{H_0} \left(\frac{f_{\lambda_0} I}{hUN_e} \right)^{1/2}. \tag{4.17}$$

En donde suponemos un universo con

$$H_0 = 70 kms^{-1} Mpc^{-1} = 2.265X10^{-18} s^{-1} \tag{4.18}$$

y una densidad relativa de energía $\Omega_\Lambda = 0.7$ y $\Omega_M = 0.3$. Así

$$\zeta(z, \Omega_M, \Omega_\Lambda) = \left[1.500 \left(1 - e^{-\frac{z}{6.107}} \right) + 0.996 \left(1 - e^{-\frac{z}{1.266}} \right) \right]. \tag{4.19}$$

Finalmente, la masa del hoyo negro es

$$M = \frac{3}{4G} f_{0.75} r_{BLR} (FWHM)^2 \tag{4.20}$$

donde $G = 6.67X10^{-11} kg^{-1} m^3 s^{-2}$ es la constante gravitacional, y el término de la geometría es $f_{0.75} = 1.0$, como se explica en la sección 9.

Capítulo 5

Calibrando la relación empírica $r \propto L^{\alpha}$

El cálculo del tamaño de la región de líneas anchas, la r_{BLR}, es una herramienta poderosa que nos ayuda a entender más la estructura y las condiciones físicas al interior de los cuasares. La manera en la que la determinamos en el capítulo anterior, con base en el cálculo de las condiciones físicas en la BLR, es una forma más sólida de estimarla, en comparación con otros estudios en los que se maneja una correlación empírica de la r_{BLR} con la luminosidad del continuo, realizada con cuasares cercanos a $z < 1$ con mapeo de reverberación. En este capítulo hacemos una selección de los objetos con mapeo de reverberación que además tienen espectros en el UV, para calibrar la relación r_{BLR}–luminosidad con el método de fotoionización, explicado en la sección anterior. El resultado es que encontramos un buen acuerdo entre los valores de la r_{BLR} obtenidos con nuestro método y con el mapeo de reverberación.

En el apéndice 5.5, presento la selección completa de los cuasares usados en este estudio.

Trabajo enviado a *The Astrophysical Journal Letters* y en proceso de revisión.

To appear in The Astrophysical Jounal Letters
Preprint typeset using LaTeX style emulateapj v. 11/10/09

CALIBRATING THE $R \propto L^{\alpha}$ EMPIRICAL RELATIONSHIP WITH PHYSICAL CONDITIONS IN THE BLR OF QUASARS

C. Alenka Negrete[1] and Deborah Dultzin[1]
Instituto de Astonomía, Universidad Nacional Autónoma de México, Mexico

Paola Marziani[2]
INAF, Astronomical Observatory of Padova, Italy

Jack W. Sulentic[3]
Instituto de Astrofísica de Andalucía, Spain
To appear in The Astrophysical Jounal Letters

ABSTRACT

We compare estimates of the distance of the Broad Line Region $r_{\rm BLR}$ from the central continuum source in a sample of low redshift quasars (z <0.24). Estimates come from two independent methods: (1) reverberation mapping and (2) inferred physical conditions in the broad line region (BLR). The latter $r_{\rm BLR}$ values were computed from a photoionization method based on three diagnostic line flux ratios in the rest-frame range 1400-2000 Å (AlIIIλ1860/ SiIII]λ1892, CIVλ1549/AlIIIλ1860 and SiIIλ1814/ SiIII]λ1892). The method uses diagnostic diagrams constructed from `CLOUDY` simulations that allow us to compute the electron density $n_{\rm e}$ and ionization parameter U. The BLR distance $r_{\rm BLR}$ is then derived from the definition of the ionization parameter. The method permits us to establish a link between $r_{\rm BLR}$ and physical conditions in the BLR gas. We can then estimate the black hole mass $M_{\rm BH}$ using an appropriate virial estimator. We find good agreement between the values of $r_{\rm BLR}$ obtained from our method and from reverberation mapping.

Subject headings: galaxies: active — quasars: general — quasars: emission lines

1. INTRODUCTION

Quasars are intriguing objects whose intense activity arises in a small volume with fraction of parsec diameter which likely involves an accretion disk and central black hole. One of the main signatures of quasar activity is the presence of broad emission lines in the UV-optical-IR spectrum. Measuring the distance $r_{\rm BLR}$ of the Broad emission Line Region (BLR) from the central continuum source has been a big challenge due to the fact that it can not be resolved by imaging even in the nearest objects. The only direct way to measure $r_{\rm BLR}$ is through reverberation mapping. This technique measures the time delay τ in the response of the broad emission lines to changes in the ionizing continuum. The rest-frame distance is $r_{\rm BLR} = c \cdot \tau/(1+z)$. However, this technique requires an enormous amount of observational effort and has been applied to $\approx$ 40 nearby objects at $z < 0.4$ (Kaspi et al. 2000; Peterson et al. 2004; Denney et al. 2010). An indirect method for measuring $r_{\rm BLR}$ was proposed by Kaspi et al. (2000, 2005) who found a relationship between $r_{\rm BLR}$ and the optical continuum luminosity at 5100Å,

$$r_{BLR} \propto L^{\alpha} \tag{1}$$

with $\alpha \approx 0.69$. Recently Bentz et al 2009, were able to give a more accurate value of αsubtracting the luminosity of the host galaxy. The value given by these authors is α= 0.513, and this is the value used in this work.

This empirical relation does not have a solid physical basis although it is not surprising that the radius of the line emitting region might scale with source luminosity. We propose here an alternate approach for estimating $r_{\rm BLR}$ based on the simple assumption that gas emitting the UV resonance lines in a quasar spectrum is photoionized by the central continuum source.

We can link $r_{\rm BLR}$ with physical parameters such as electron density ($n_{\rm e}$) and ionization parameter (U) using the definition of the ionization parameter

$$U = \frac{\int_{\nu_0}^{+\infty} \frac{L_\nu}{h\nu} d\nu}{4\pi n_{\rm e} c r^2} \tag{2}$$

where L_ν is the specific luminosity per unit frequency ν, h is the Planck constant and c the speed of light. We can estimate $r_{\rm BLR}$ if we have a reasonable estimate of the product $n_{\rm e} \cdot U$ (Negrete et al. 2010, henceforth N10; see also Padovani et al. 1988 for an analogous approach based on the Hβ line).

An estimate of $r_{\rm BLR}$ enables us to estimate the black hole mass ($M_{\rm BH}$) assuming virial motions of the gas using:

$$M_{\rm BH} = f \frac{\Delta v^2 r_{\rm BLR}}{G} = \frac{3}{4G} f_{0.75} {\rm FWHM}^2 r_{\rm BLR} \tag{3}$$

where $f \approx 1.4$ is the geometry factor, corresponding to $f_{0.75} \approx 1.9$ (Onken et al. 2004; see also Woo et al. 2010), and G is the gravitational constant.

In §2 we describe our sample selection. We explain

[1] anegrete@astroscu.unam.mx, deborah@astroscu.unam.mx
[2] paola.marziani@oapd.inaf.it
[3] sulentic@iaa.es

the photoionization method and compare our estimates with reverberation values in §3. Our discussion and conclusions are given §4 and §5 respectively. Computations were made considering H_0 =70 km s^{-1}Mpc^{-1} and a relative energy density $\Omega_\Lambda = 0.7$ and $\Omega_M = 0.3$.

2. SAMPLE DEFINITION AND DATA REDUCTION.

We selected 14 of 35 quasars with reverberation data published by Peterson et al. (2004, henceforth P04) with S/N good enough in the rest-frame range 1400-2000 Å to allow an accurate line decomposition of CIII]λ1909, SiIII]λ1892, AlIIIλ1860, SiIIλ1814 and CIVλ1549. Our aim was to make a multi-component profile decomposition in order to extract the broad line component that is needed for our method. The redshift of this sample is $z <$ 0.24. We extracted UV spectra from the HST archive and carried out data reduction using standard IRAF tasks. Optical spectra of Hβ were taken from Marziani et al. (2003). Data were corrected by Galactic extinction. Table 1 presents our source sample with IDs given in Column 1 and other columns described below.

3. METHOD AND COMPARISON

N10 analyzed the flux ratios CIVλ1549/AlIIIλ1860 and SiIIλ1814/ SiIII]λ1892 that should enable us to constrain n_e and U making use of diagnostic maps derived from `CLOUDY` simulations. An array of simulations was computed by varying U and n_e in the range $-4.5 \leq \log U \leq 0$ and $7 \leq \log n_e \leq 14$ in steps of 0.25. The array computations assumed column density 10^{23} cm^{-2}. We repeated them assuming both metallicity equal to solar and to five time solar (see N10 for more details).

The first step of our method is to extract the broad component (BC) that is associated to the region predominantly emitting low ionization lines (LILs) like MgIIλ2800, FeII, part of the Balmer lines, SiIIλ1814, OIλ1304, and that is present in the overwhelming majority of Seyfert 1 and quasar spectra. To isolate this component we consider the Hβ line, and we use the Hβ BC to define the BC profile, shift and width in CIVλ1549 and in the other UV lines of interest. We take advantage of the fact that the BC is the sole or the dominant component in all LILs if FWHM(Hβ) $\lesssim$ 4000 km s^{-1} (Zamfir et al. 2010). For broader sources, the Hβ profile can be represented by the sum of the BC and a redshifted very broad component (VBC; FWHM$\sim$10000 km s^{-1}; present in the spectrum of NGC 7469 shown in Fig.1). The CIVλ1549 line is often dominated by blueshifted emission probably associated to a high-ionization outflow (Richards et al. 2002; Sulentic et al. 2007). To extract the BC from the CIVλ1549 line, we consider that the broad profile of CIVλ1549 can be described as the sum of the BC + a blueshifted component if FWHM(Hβ)$\lesssim$ 4000 km s^{-1}. Broader sources usually show additional CIVλ1549 VBC emission .

It is important to point out that the decompositions are not arbitrary. The sum of the three components (broad, blue-shifted, very-broad) reproduces the line profiles of the strongest lines of low-z quasars along the Eigenvector 1 sequence (Sulentic et al. 2000; Marziani et al. 2010). The relative intensity is different in the various lines but shifts and widths of the three components are consistent for all lines. More details are given

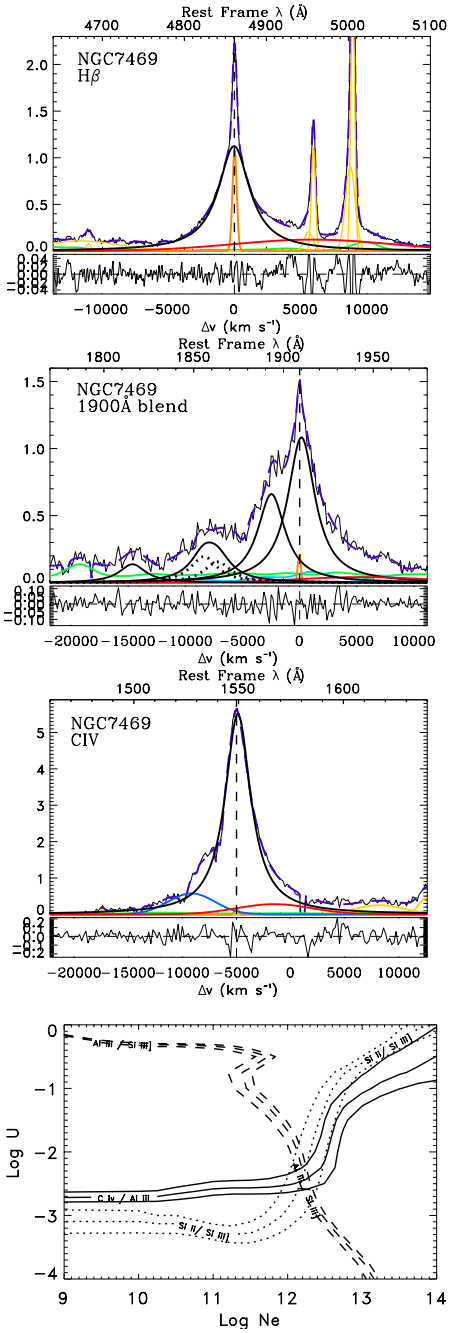

FIG. 1.— Fits for NGC 7469. In (a), (b), and (c) upper abscissa is rest frame wavelength in Å, lower abscissa is in radial velocity units, and ordinate is specific flux per unit wavelength in arbitrary units. Long dashed line is the restframe for (a) CIVλ1549, (b) CIII]λ1909 and (c) Hβ. Short dashed line is the fit to the whole spectrum. Panels under the fits are the residuals. In (d) abscissa is electron density in cm^{-3}, ordinate is the ionization parameter, both in logarithm scale. The point where the isocontours cross determine the values of log n_e and log U. The width of the isocontours are 1σ confidence.

by Marziani et al. (2010) where line component trends along the E1 sequence are shown.

Our multi-component model fits attempt to isolate the BC in CIVλ1549, SiIII]λ1892, AlIIIλ1860 and SiIIλ1814 by modeling and eliminating the blue-shifted and VB component. The BC of CIVλ1549, SiIII]λ1892, AlIIIλ1860 and SiIIλ1814 isolates emission that is believed to come from the same low-ionization region emitting the core of Hβ, and LILs like MgIIλ2800, FeII, SiIIλ1814. CIII]λ1909 is a semiforbidden line with a critical electron density $n_{\rm e} \sim 10^9$ cm^{-3} (Osterbrock & Ferland 2006). This density is usually lower than the one found from the diagnostic ratios based on the BC components of the UV lines (the only exception is 3C 390.3 that however seems to lack a BC proper). This means that either CIII]λ1909 is weak or that it is not produced in the same region. Perhaps it is produced farther or in regions of lower density inside the BLR (see N10 for references). Figure 1 shows the spectra of NGC 7469, an example of the fit used to get line intensities for (a) CIVλ1549 BC + narrow component (NC) + blue-shifted + VBC; (b) 1900Å blend that includes CIII]λ1909 BC + VBC, SiIII]λ1892 BC, AlIIIλ1860 BC and SiIIλ1814 BC; and (c) Hβ BC + NC + VBC. Narrow components are fitted whenever they are clearly visible, i.e. in Hβ, CIII]λ1909 and CIVλ1549. Fits to the lines of Mark 335 and Fairall 9 are shown by Marziani et al. (2010).

The core broad component of Hβ is produced in the LIL emitting part of BLR. As it does not present strong asymmetries, it is believed that the line broadening is due to Keplerian motions. It is regarded as "safe" to use FWHM(H$\beta_{\rm BC}$) as a BLR velocity dispersion indicator. This is not true for the blue-shifted component and for the VBC. The CIVλ1549 blue-shifted asymmetry found in many quasars is read as the signature of an outflowing wind. The large peak shift of the VBC similarly suggests that non-virial motions play a significant role.

Armed with line intensities of the BC, we are able to compute line ratios AlIIIλ1860/ SiIII]λ1892, CIVλ1549/AlIIIλ1860 and SiIIλ1814/ SiIII]λ1892. These values are input into `CLOUDY` (Ferland et al. 1998) allowing us to make contour plots in which we vary $n_{\rm e}$ and U. Panel (d) of Figure 1 shows the isocontour map based on line ratios for NGC 7469. The crossing points give us best estimates of $n_{\rm e}$ and U for the BC in that source. Col. 2 of Table 1 lists the estimated product $n_{\rm e}{\cdot}U$ for our sources, column 3 is the error at 2 sigma level confidence.

Now we can use Eq. 2 rewritten as

$$r_{BLR} = \left[\frac{\int_{\nu_0}^{+\infty} \frac{L_\nu}{h\nu} d\nu}{4\pi n_{\rm e} U c} \right]^{1/2} \quad (4)$$

The integral is carried out from the Lyman limit to the largest frequency on the rest frame specific flux f_ν. For the integral we will use an average of two Spectral Energy Distributions (SEDs) described by Mathews & Ferland (1987) and Laor et al. (1997). Finally we calculate $M_{\rm BH}$ using Eq. 3.

Col. 4 of Table 1 gives the estimated logarithms of the BLR radii in cm using the photoionization method. Col. 6 gives $r_{\rm BLR}$ computed using the Hβ time delay $\tau_{\rm cent}$ from Table 6 of P04. Cols. 7 and 9 give logarithm of black hole mass estimates in $M_\odot$ using the results of our method and the ones reported in Table 8 of P04, respectively. Columns 5 and 8 are the errors at 2 sigma level confidence.

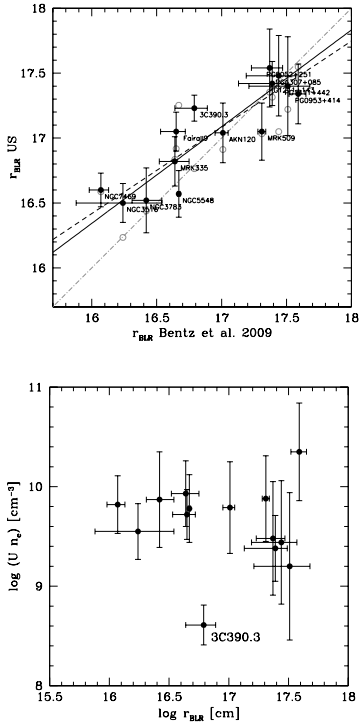

FIG. 2.— *upper panel:* $r_{\rm BLR}$ comparison. Abscissa is the logarithm of the $r_{\rm BLR}$ in cm using is the product $c \cdot \tau_{\rm cent}$ reported by Bentz et al. (2009); ordinate is log $r_{\rm BLR}$ using the method of the present paper. The dot-dashed line shows equality; the filled line shows the result of a weighted least square fit, the dashed line of an unweighted fit. Open circles indicete the expected values from the $r_{\rm BLR}$– L correlation derived by Bentz et al. (2009). *lower panel:* $U \cdot n_e$ product versus $r_{\rm BLR}$. We can consider that, except for the extreme object 3C390.3, the value of the product does not have significant changes.

Figure 3 presents the comparison of $r_{\rm BLR}$ and $M_{\rm BH}$. The agreement of our $r_{\rm BLR}$ with the Bentz et al. (2009) values better than the one obtained employing the $r_{\rm BLR}$– L correlation defined on the very same Bentz et al. (2009) data. We first consider the effect of continuum level uncertainties on line intensity. Errors on line intensity are quadratically propagated to compute errors for the diagnostic ratios and hence the for the product $U{\cdot}\, n_{\rm e}$. An important source of uncertainty is related to the dependence on the number of ionizing photons entering Eq. 2 on the SED; we consider the Mathews & Ferland (1987) and Laor et al. (1997) SEDs as extreme. Additional uncertainty in the FWHM measurements contributes to the $M_{\rm BH}$ errors.

4. DISCUSSION AND CONCLUSIONS

The Kaspi empirical relationship links the optical continuum luminosity to the radius of the BLR (see also Vestergaard & Peterson 2006, for an extension using the UV continuum luminosity). We derive $r_{\rm BLR}$ from es-

TABLE 1
Sample of Sources, Results and Comparison

Object name	n_e·U	Δ^a	Log(r_{BLR}) This work	Δ^a	Log($c\cdot\tau_{cent}$) P04[b]	Log(M_{BH}) This work	Δ^a	P04
(1)	(2)	(3)	(4)	(5)	(6)	(7)	(8)	(9)
3C 390.3	8.61	0.20	17.23	0.10	17.03	8.95	0.21	8.46
AKN 120	9.79	0.46	17.04	0.23	17.04	8.36	0.48	8.18
Fairall 9[b]	9.72	0.25	17.05	0.15	16.58	8.25	0.19	8.41
MRK 335[b]	9.93	0.33	16.82	0.19	16.45	7.27	0.26	7.15
MRK 509	9.88	0.43	17.05	0.22	17.31	7.99	0.43	8.16
NGC 3516	9.55	0.28	16.50	0.15	16.41	8.01	0.27	7.63
NGC 3783	9.87	0.48	16.52	0.25	16.42	7.30	0.48	7.47
NGC 5548	9.78	0.34	16.57	0.18	16.61	7.99	0.35	7.83
NGC 7469	9.82	0.29	16.60	0.13	16.08	7.41	0.26	7.09
PG 0052+251	9.48	0.57	17.54	0.30	17.46	8.91	0.58	8.57
PG 0953+414	10.35	0.49	17.34	0.23	17.59	8.27	0.45	8.44
PG 1211+143	9.38	0.33	17.42	0.17	17.43	7.92	0.35	8.16
PG 1307+085	9.44	0.62	17.48	0.31	17.55	8.85	0.61	8.64
PG 1411+442	9.20	0.74	17.40	0.38	17.45	8.11	0.80	8.65

[a] Errors are at a 2σ confidence level.
[b] Fits of strongest lines from Lyα to Hβ are shown by Marziani et al. (2010).

timated physical conditions in the BLR making careful efforts to derive these conditions only for the assumed virialized BC component of the lines. Figure 3 shows that both our r_{BLR} and M_{BH} estimates correlate well with those based upon reverberation mapping techniques. Good consistency between reverberation mapping and photoionization-based r_{BLR} was also obtained by Wandel et al. (1999) considering Hβ. Bentz et al. (2009) examined the $r_{BLR} \propto L^{\alpha}$ relationship for the 35 reverberated quasars and obtained an α index lower than the one found in previous work:

$$\log(r_{BLR,rev}) = -21.3 + 0.519(\lambda L_{\lambda}(5100\text{Å})) \quad (5)$$

The correlation between our photoionization radii and reverberation values can be expressed as:

$$\log(r_{BLR,n_eU}) = -3.367 + 1.192(r_{BLR,rev}). \quad (6)$$

This relation likely reflects the source-to-source stability of physical conditions in the emitting clouds and the validity of the $r_{BLR} \propto L^{\alpha}$ correlation. The low-ionization part of the BLR that should emit the BC we isolated is still prominent in high luminosity quasars (Marziani et al. 2009). The derived $n_e \cdot U$ values for the 8 high redshift quasars studied by N10 are consistent with those of low-z sources. Values of r_{BLR} for these sources are in agreement with the extrapolation of the Kaspi relationship at high luminosity.

In summary, we were able to estimate BLR distances from the central black hole using an independent photoionization method that yields results in agreement with reverberation values obtained by Bentz et al. (2009) for 14 sources that are in common. In a related paper (N10) we have shown that r_{BLR} values derived with our method for 8 high-z quasars also agree with the predictions based on the Kaspi relationship. An additional conclusion drawn from this work and N10 is the validity of the Kaspi relation for a wide range of luminosities (with the exception of low luminosity or dwarf AGN: Zhang et al. 2007) which might be explained on the basis of luminosity-independent physical conditions in the LIL emitting part of the BLR.

A. Negrete and D.Dultzin acknowledge support form grant IN111610-3 PAPIIT, DGAPA UNAM, and Yair

REFERENCES

Bentz, M. C., Peterson, B. M., Pogge, R. W., & Vestergaard, M. 2009, ApJL, 694, L166
Denney, K. D., et al. 2010, ArXiv e-prints, http://adsabs.harvard.edu/abs/2010arXiv1006.4160D
Ferland, G. J., Korista, K. T., Verner, D. A., Ferguson, J. W., Kingdon, J. B., & Verner, E. M. 1998, PASP, 110, 761
Kaspi, S., Maoz, D., Netzer, H., Peterson, B. M., Vestergaard, M., & Jannuzi, B. T. 2005, ApJ, 629, 61
Kaspi, S., Smith, P. S., Netzer, H., Maoz, D., Jannuzi, B. T., & Giveon, U. 2000, ApJ, 533, 631
Laor, A., Fiore, F., Elvis, M., Wilkes, B. J., & McDowell, J. C. 1997, ApJ, 477, 93
Marziani, P., Sulentic, J. W., Negrete, C. A., Dultzin, D., Zamfir, S., & Bachev, R. 2010, MNRAS, 409, 1033 http://adsabs.harvard.edu/abs/2010arXiv1007.3187M
Marziani, P., Sulentic, J. W., Stirpe, G. M., Zamfir, S., & Calvani, M. 2009, A&Ap, 495, 83
Marziani, P., Sulentic, J. W., Zamanov, R., Calvani, M., Dultzin-Hacyan, D., Bachev, R., & Zwitter, T. 2003, ApJS, 145, 199
Mathews, W. G., & Ferland, G. J. 1987, ApJ, 323, 456
Negrete, C. A., Dultzin, D., Marziani, P., & Sulentic, J. 2010, arXiv:1011.4248, ApJ submitted (N10)
Osterbrock, D. E., & Ferland, G. J. 2006, Astrophysics of gaseous nebulae and active galactic nuclei (University Science Books)
Padovani, P., & Rafanelli, P. 1988, A&A, 205, 53
Peterson, B. M., et al. 2004, ApJ, 613, 682 (P04)
Richards, G. T., Vanden Berk, D. E., Reichard, T. A., Hall, P. B., Schneider, D. P., SubbaRao, M., Thakar, A. R., & York, D. G. 2002, AJ, 124, 1
Sulentic, J. W., Bachev, R., Marziani, P., Negrete, C. A., & Dultzin, D. 2007, ApJ, 666, 757
Sulentic, J. W., Zwitter, T., Marziani, P., & Dultzin-Hacyan, D. 2000, ApJL, 536, L5
Vestergaard, M., & Peterson, B. M. 2006, ApJ, 641, 689
Wandel, A., Peterson, B. M., & Malkan, M. A. 1999, ApJ, 526, 579
Zamfir, S., Sulentic, J. W., Marziani, P., & Dultzin, D. 2010, MNRAS, 403, 1759
Zhang, X., Dultzin-Hacyan, D., & Wang, T. 2007, MNRAS, 374, 691

5.5. Apéndice. La muestra completa de cuasares.

Dado el espacio reducido de la Letter, no nos fue posible mostrar todos los ajustes de los espectros. A continuación presento los ajustes de la muestra completa con excepción de Fairall 9 y Mrk 0335 que los muestro en el capítulo 3 de la tesis. Para los primeros tres paneles, la abscisa superior es el marco de referencia en reposo de la línea, en Å, la abscisa inferior está en unidades de velocidad, la ordenada es el flujo específico en unidades arbitrarias. La línea vertical segmentada es el marco de referencia en reposo para CIVλ1549, CIII]λ1909 y Hβ. El recuadro inferior a cada ajuste son los residuos. En el primer panel está la línea CIVλ1549; en el segundo, el conjunto a 1900Å que incluye CIII]λ1909, SiIII]λ1892, el doblete de AlIIIλ1860 y SiIIλ1814; y en el tercer panel muestro a Hβ. Para estos tres paneles, la línea morada segmentada muestra el ajuste de todas las componentes; las líneas negras son las componentes centrales anchas; la línea azul en CIVλ1549 es la componente corrida al azul; la roja es la componente muy ancha, corrida al rojo; la naranja es la componente angosta; la verde es el pseudocontinuo que se forma con las múltiples componentes de FeII; la azul cielo en el conjunto a 1900Å es el pseudocontinuo de FeIII; y las amarillas son líneas adyacentes a CIVλ1549 y a Hβ. Al rededor de CIVλ1549, éstas líneas por lo general son débiles y en algunos casos están ausentes. Éstas son: NIV]λ1486, SiIIλ1533 y HeIIλ1640 compuesta por dos componentes, la central ancha y la corrida al azul. En la vecindad de Hβ tenemos a las líneas: HeIIλ4686 con dos componentes, la central y la angosta; el doblete de [OIII]$\lambda\lambda$4959,5007, en donde he considerado una componente semi–ancha para cada línea (Zamfir et al. 2010); y tres líneas muy débiles, no siempre presentes: [FeVII]λ5160, [FeVI]λ5178 y [NI]λ5199.

En el último panel mostramos los isocontornos de los cocientes AlIIIλ1860/SiIII]λ1892 en línea segmentada, SiIIλ1814/SiIIλ1814 en línea punteada y CIVλ1549/AlIIIλ1860 en línea continua, cada uno con sus respectivas bandas de error a 2σ.

En particular mencionaré a los objetos PG1211+143, PG1307+085 y PG1411+442, para los cuales en el conjunto de líneas a 1900Å (terceros paneles), las componentes AlIIIλ1860 y SiIIλ1814 son débiles y/o la S/N es baja, de modo que éstas líneas se confunden con el ruido. Como resultado, no encontramos una buena concordancia de los valores

de $N_{\rm H}$ y U. Para estos objetos, el valor del producto $N_{\rm H}{\cdot}U$ es el promedio de los cruces de Al III]λ1860/Si III]λ1892 con C IVλ1549/Al III]λ1860 y Al III]λ1860/Si III]λ1892.

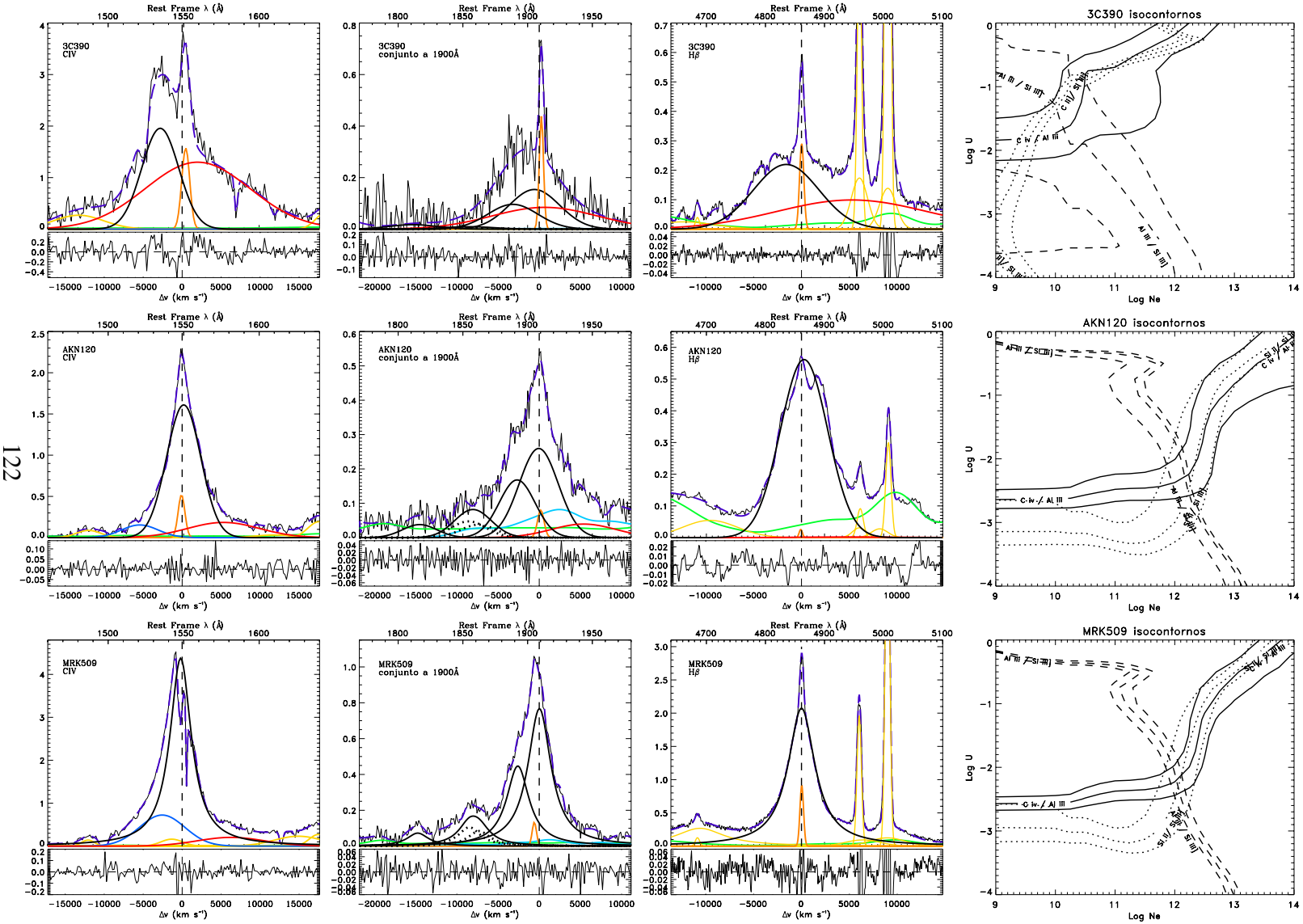
Rest Frame λ (Å)
3C390
CIV
3C390
conjunto a 1900Å
3C390
Hβ
3C390 isocontornos
AKN120
CIV
AKN120
conjunto a 1900Å
AKN120
Hβ
AKN120 isocontornos
MRK509
CIV
MRK509
conjunto a 1900Å
MRK509
Hβ
MRK509 isocontornos
Δv (km s⁻¹)
Log U
Log Ne

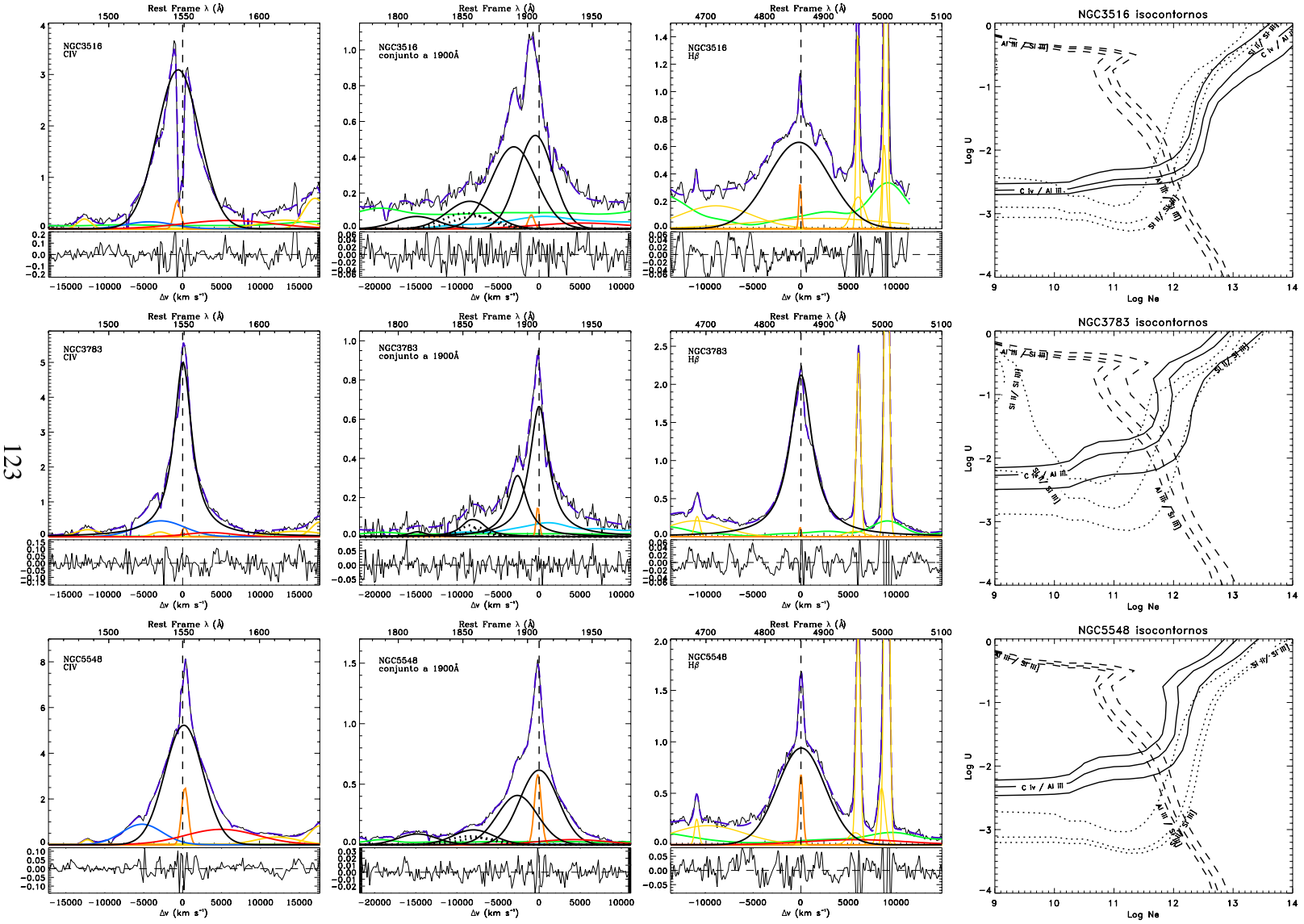
Rest Frame λ (Å)
NGC3516
CIV
NGC3516
conjunto a 1900Å
NGC3516
Hβ
NGC3516 isocontornos
NGC3783
CIV
NGC3783
conjunto a 1900Å
NGC3783
Hβ
NGC3783 isocontornos
NGC5548
CIV
NGC5548
conjunto a 1900Å
NGC5548
Hβ
NGC5548 isocontornos
Δv (km s⁻¹)
Log U
Log Ne
C IV / Al III
Si IV / Si III]
Al III / Si III]

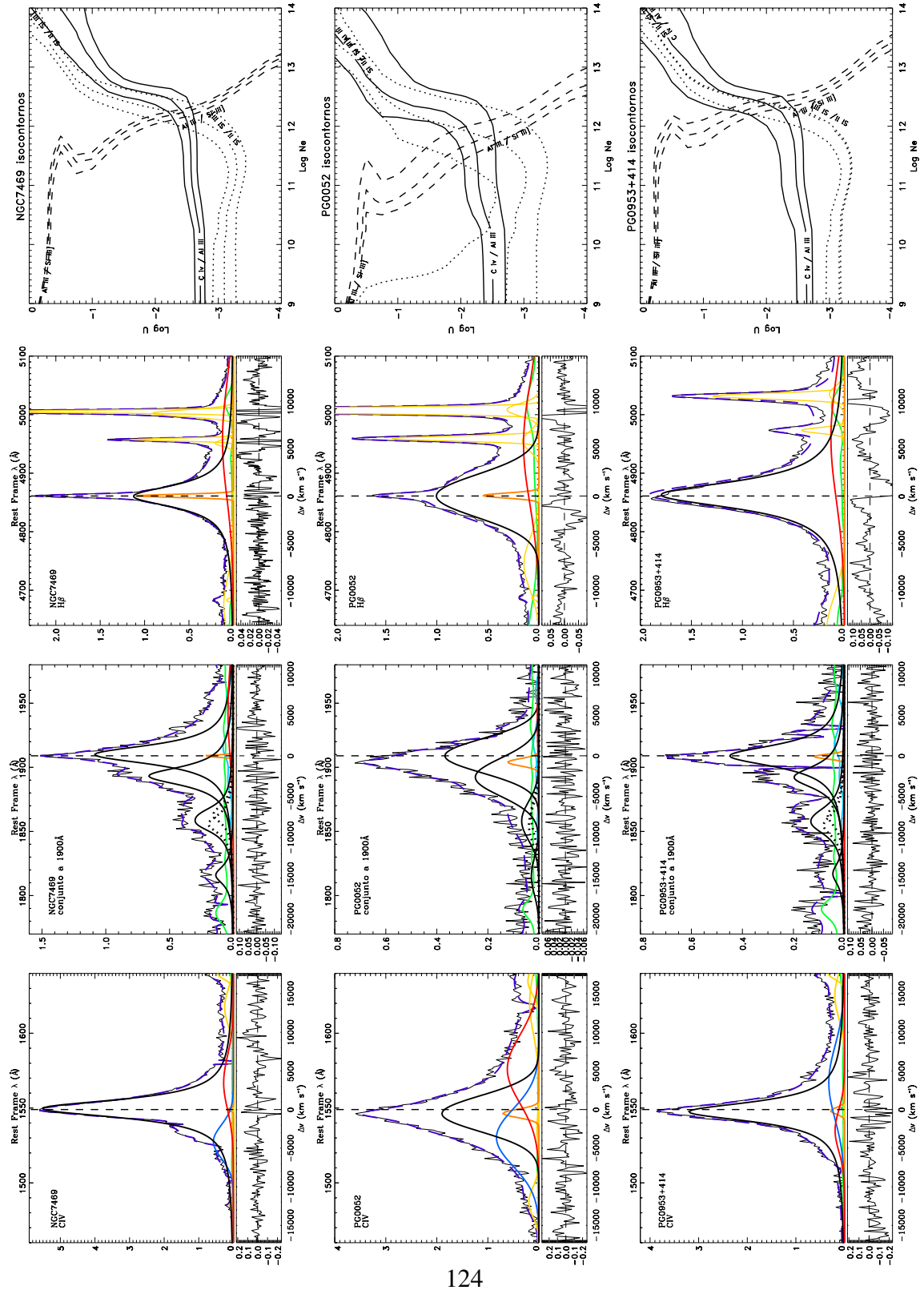
NGC7469 isocontornos
PG0052 isocontornos
PG0953+414 isocontornos
Log U
Log Ne
C IV / Al III
Si IV / O IV]
He II / Si II
Al III / Si II
NGC7469
CIV
NGC7469
conjunto a 1900Å
NGC7469
Hβ
PG0052
CIV
PG0052
conjunto a 1900Å
PG0052
Hβ
PG0953+414
CIV
PG0953+414
conjunto a 1900Å
PG0953+414
Hβ
Rest Frame λ (Å)
Δv (km s⁻¹)

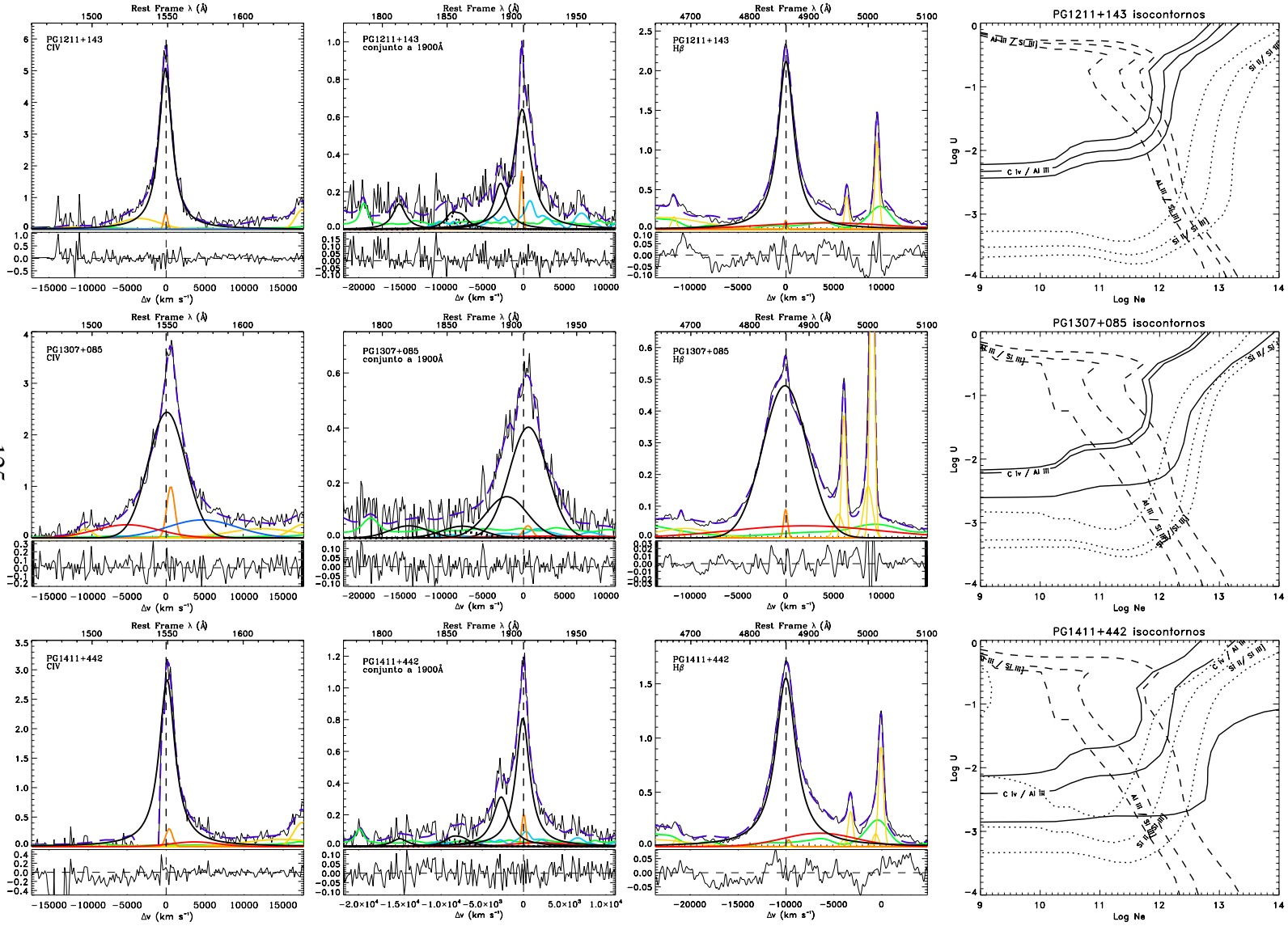
PG1211+143
CIV
PG1211+143
conjunto a 1900Å
PG1211+143
Hβ
PG1211+143 isocontornos
PG1307+085
CIV
PG1307+085
conjunto a 1900Å
PG1307+085
Hβ
PG1307+085 isocontornos
PG1411+442
CIV
PG1411+442
conjunto a 1900Å
PG1411+442
Hβ
PG1411+442 isocontornos
Rest Frame λ (Å)
Δv (km s⁻¹)
Log U
Log Ne
C IV / Al III
Si IV / Si III
Al III / Si III
Si IV / Si III

Capítulo 6

Conclusiones generales.

El estudio espectroscópico de los cuasares depende en gran medida de la capacidad resolutiva de los telescopios empleados. En la última década se han construido telescopios como el VLT que nos han permitido poder ver las características finas de los perfiles de líneas, que a su vez nos permite deconvolucionar entre tres o más componentes entremezcladas.

Usando observaciones del HST en el UV, cuantificamos el corrimiento y la asimetría al azul de la línea CIVλ1549 y con su introducción al espacio del eigenvector E1 obtuvimos un espacio de parametros de 4 dimensiones, lo cual facilita una interpretación física e incluso evolutiva. En este punto separamos únicamente la componente angosta del resto de la línea, midiendo el desplazamiento en términos del centroide medido a la mitad de la línea $c(1/2)$, sin separar la componente azul de la central, dando como resultado que las masas calculadas con esta línea resultaron ser sistemáticamente mayores a las calculadas con H$\beta_{\rm BC}$. En otras palabras, la suma de ambas componentes, la central más la azul, no es un buen estimador virial.

La separación de las componentes espectrales de las líneas anchas es un paso muy importante en el estudio de los cuasares. El segundo resultado es acerca de la deconvolución de las componentes de las líneas espectrales más prominentes a lo largo del rango óptico–

UV (Hβ, MgIIλ2800, SiIII]λ1892, AlIIIλ1860, CIVλ1549, HeIIλ1640 y Lyα). Encontramos tres componentes, la primera es la componente central ancha que emerge de la región de líneas anchas, la segunda es la componente corrida al azul que se cree es producida en un viento saliente y la tercera es la componente muy ancha que no está presente en todos los cuasares y cuya interpretación no es clara.

Desarrollamos un método efectivo que nos permite calcular la distancia de la fuente central de ionización a la región de emisión de las líneas anchas r_{BLR} de un modo independiente al mapeo de reverberación, a la correlación empírica r_{BLR}- Luminosidad y a la dinámica estelar. Nuestro método está basado en la medición de los parámetros físicos al interior de los cuasares y es aplicable para cuasares de alta z (al menos hasta $z \sim 3$). Derivamos las densidades del hidrógeno $N_{\rm H}$ y el parámetro de ionización U y con el producto de ambos calculamos la r_{BLR}. El valor promedio del producto $N_{\rm H}{\cdot}U$ es ~9.5. Encontramos una concordancia en los resultados de nuestro método con los del mapeo de reverberación, el cual nos proporciona una medición directa del r_{BLR}, pero sólo se ha podido aplicar a una treintena de cuasares brillantes.

Nuestro método es igualmente eficiente para cuasares a bajas z y es seguro al menos para z~3. Podemos suponer que se puede usar a z mayores debido a que se basa en parámetros físicos medibles en cada cuasar.

El cálculo de $M_{\rm BH}$ a distintas z, nos permite hablar de una evolución a nivel cosmológico pues a z mayores la $M_{\rm BH}$ también es mayor con una cota de $10^{10} M_{\odot}$. Sin embargo, todavía no podemos explicar el hecho de que a etapas más tempranas del universo, los hoyos negros de las galaxias son más masivos.

Capítulo 7

Trabajo a futuro.

A lo largo de esta tesis, hemos visto que el espacio de parámetros descrito por el Eigenvector 1 (E1) es una herramienta muy útil en el intento de unificación de la diversidad de cuasares de tipo 1. En su versión de tres dimensiones, es decir considerando los parámetros FWHM(Hβ), $R_{\rm FeII}$ = W(Fe II$_{\rm opt}$)/W(Hβ) y Γ_{soft} (el índice espectral en rayos–X suaves), proponemos dos estudios. Por un lado, hemos ampliado la muestra considerada en el capítulo 2 (Negrete et al. 2011 en preparación) y por otro, estamos haciendo una revisión del parametro Γ_{soft}, determinado ahora con datos modernos del telescopio espacial XMM-Newton, (X-ray Multi-Mirror Mission) para rayos–X suaves y duros (Anguiano et al. en preparación). En el trabajo de Sulentic et al. (2000), se trabajó con datos de ROSAT, que cubrían sólo rayos–X suaves.

Para ampliar la muestra, usamos los objetos del catálogo Hamburg/ESO (Wisotzki et al. 2000) que cubre las magnitudes ópticas en el intervalo $13 \leqslant B_J \leqslant 17.5$ y el corrimiento al rojo de entre $0 < z < 3.2$. Éste es un catálogo completo en el sentido de que no discriminan entre las fuentes extendidas a bajas z, a diferencia de otros catálogos que por lo general están sesgados porque presentan excesos de cuasares radio fuertes, o con emisión intensa en el infrarrojo, el UV, o los rayos–X. Otros catálogos de cuasares brillantes como el Palomar–Green (PG), usado para describir al E1 (Sulentic et al. 2000), se sabe que no representan muestras completas. Además discrimina los cuasares de bajo z de galaxias an-

fitrionas extendidas y la técnica de selección fotométrica presenta exceso en el UV. En el catálogo PG los cuasares son hasta $z < 2.2$.

Del catálogo Hamburg/ESO, ya hemos observado cerca de una centena de cuasares. Usamos el telescopio de 2.1 mts del Observatorio Astronómico Nacional de San Pedro Mártir. Seleccionamos objetos con bajo corrimiento al rojo, $z < 0.9$, debido a que a z más altas, la línea de Hβ sale del rango óptico. Además, tomamos objetos brillantes, con una magnitud mínima de 17. Magnitudes más débiles nos conducen a una acumulación del cielo que dificulta la extracción de las líneas de nuestro interés. Un aspecto importante de los espectros obtenidos es que se dieron tiempos de exposición largos (1.5 horas para la mayoría de los objetos), que da como resultado una señal a ruido muy alta, lo que permite ver a detalle los perfiles de las líneas, de donde podemos deducir las características físicas de las nubes que las emiten.

El propósito de este trabajo es no sólo ampliar la muestra del E1, sino que además, evitamos que tenga algún tipo de sesgo observacional. De este modo podremos estar más seguros de los resultados obtenidos en el espacio de parámetros E1. Usaremos además la técnica de separación de componentes propuesta en esta tesis, para trabajar sólo con la componente ancha central.

Bibliografía

Baldwin, J. A., Ferland, G. J., Korista, K. T., Carswell, R. F., Hamann, F., Phillips, M. M., Verner, D., Wilkes, B. J., & Williams, R. E. 1996, ApJ, 461, 664

Bentz, M. C., Peterson, B. M., Netzer, H., Pogge, R. W., & Vestergaard, M. 2009, ApJ, 697, 160

Bentz, M. C., Walsh, J. L., Barth, A. J., Yoshii, Y., Woo, J.-H., Wang, X., Treu, T., Thornton, C. E., Street, R. A., Steele, T. N., Silverman, J. M., Serduke, F. J. D., Sakata, Y., Minezaki, T., Malkan, M. A., Li, W., Lee, N., Hiner, K. D., Hidas, M. G., Greene, J. E., Gates, E. L., Ganeshalingam, M., Filippenko, A. V., Canalizo, G., Bennert, V. N., & Baliber, N. 2010, ApJ, 716, 993

Boroson, T. A. & Green, R. F. 1992, ApJS, 80, 109

Collin, S., Kawaguchi, T., Peterson, B. M., & Vestergaard, M. 2006, A&A, 456, 75

Dultzin-Hacyan, D. & Ruano, C. 1996, A&A, 305, 719

Dultzin-Hacyan, D., Taniguchi, Y., & Uranga, L. 1999, in Astronomical Society of the Pacific Conference Series, Vol. 175, Structure and Kinematics of Quasar Broad Line Regions, ed. C. M. Gaskell, W. N. Brandt, M. Dietrich, D. Dultzin-Hacyan, & M. Eracleous, 303–+

Ferland, G. J. 2000, Hazy, A Brief Introduction to Cloudy 94 (www.nublado.org: www.nublado.org)

Francis, P. J., Hewett, P. C., Foltz, C. B., Chaffee, F. H., Weymann, R. J., & Morris, S. L. 1991, ApJ, 373, 465

Ghez, A. M., Duchêne, G., Matthews, K., Hornstein, S. D., Tanner, A., Larkin, J., Morris, M., Becklin, E. E., Salim, S., Kremenek, T., Thompson, D., Soifer, B. T., Neugebauer, G., & McLean, I. 2003, ApJ, 586, L127

Ghez, A. M., Salim, S., Hornstein, S. D., Tanner, A., Lu, J. R., Morris, M., Becklin, E. E., & Duchêne, G. 2005, ApJ, 620, 744

Ghez, A. M., Salim, S., Weinberg, N. N., Lu, J. R., Do, T., Dunn, J. K., Matthews, K., Morris, M. R., Yelda, S., Becklin, E. E., Kremenek, T., Milosavljevic, M., & Naiman, J. 2008, ApJ, 689, 1044

Gültekin, K., Richstone, D. O., Gebhardt, K., Lauer, T. R., Tremaine, S., Aller, M. C., Bender, R., Dressler, A., Faber, S. M., Filippenko, A. V., Green, R., Ho, L. C., Kormendy, J., Magorrian, J., Pinkney, J., & Siopis, C. 2009, ApJ, 698, 198

Kaspi, S., Maoz, D., Netzer, H., Peterson, B. M., Vestergaard, M., & Jannuzi, B. T. 2005, ApJ, 629, 61

Kaspi, S., Smith, P. S., Netzer, H., Maoz, D., Jannuzi, B. T., & Giveon, U. 2000, ApJ, 533, 631

Kellermann, K. I., Sramek, R., Schmidt, M., Shaffer, D. B., & Green, R. 1989, AJ, 98, 1195

Khachikian, E. Y. & Weedman, D. W. 1974, ApJ, 192, 581

Komossa, S. 2008, in Revista Mexicana de Astronomia y Astrofisica Conference Series, Vol. 32, Revista Mexicana de Astronomia y Astrofisica Conference Series, 86–92

Laor, A., Fiore, F., Elvis, M., Wilkes, B. J., & McDowell, J. C. 1997, ApJ, 477, 93

Magorrian, J., Tremaine, S., Richstone, D., Bender, R., Bower, G., Dressler, A., Faber, S. M., Gebhardt, K., Green, R., Grillmair, C., Kormendy, J., & Lauer, T. 1998, AJ, 115, 2285

Marconi, A. & Hunt, L. K. 2003, ApJ, 589, L21

Marziani, P., Sulentic, J. W., Dultzin-Hacyan, D., Calvani, M., & Moles, M. 1996, ApJS, 104, 37

Marziani, P., Sulentic, J. W., Negrete, C. A., Dultzin, D., Zamfir, S., & Bachev, R. 2010, MNRAS, 409, 1033

Marziani, P., Sulentic, J. W., Zamanov, R., Calvani, M., Dultzin-Hacyan, D., Bachev, R., & Zwitter, T. 2003, ApJS, 145, 199

Marziani, P., Sulentic, J. W., Zwitter, T., Dultzin-Hacyan, D., & Calvani, M. 2001, ApJ, 558, 553

Mathews, W. G. & Ferland, G. J. 1987, ApJ, 323, 456

Matsuoka, Y., Kawara, K., & Oyabu, S. 2008, ApJ, 673, 62

Misner, C. W., Thorne, K. S., & Wheeler, J. A. 1973, Gravitation (San Francisco: W.H. Freeman and Co., 1973)

Miyoshi, M., Moran, J., Herrnstein, J., Greenhill, L., Nakai, N., Diamond, P., & Inoue, M. 1995, Nature, 373, 127

Osterbrock, D. E. & Ferland, G. J. 2006, Astrophysics of gaseous nebulae and active galactic nuclei (2nd. ed. by D.E. Osterbrock and G.J. Ferland. Sausalito, CA: University Science Books)

Peterson, B. M., Ferrarese, L., Gilbert, K. M., Kaspi, S., Malkan, M. A., Maoz, D., Merritt, D., Netzer, H., Onken, C. A., Pogge, R. W., Vestergaard, M., & Wandel, A. 2004, ApJ, 613, 682

Robson, I. 1996, Book Review: Active galactic nuclei, Wiley, Praxis

Rokaki, E., Lawrence, A., Economou, F., & Mastichiadis, A. 2003, MNRAS, 340, 1298

Salpeter, E. E. 1964, ApJ, 140, 796

Sambruna, R. M., Maraschi, L., & Urry, C. M. 1996, ApJ, 463, 444

Seyfert, C. K. 1943, ApJ, 97, 28

Shakura, N. I. & Sunyaev, R. A. 1973, A&A, 24, 337

Shapovalova, A. I., Popović, L. Č., Collin, S., Burenkov, A. N., Chavushyan, V. H., Bochkarev, N. G., Benítez, E., Dultzin, D., Kovačević, A., Borisov, N., Carrasco, L., León-Tavares, J., Mercado, A., Valdes, J. R., Vlasuyk, V. V., & Zhdanova, V. E. 2008, A&A, 486, 99

Sulentic, J. W., Bachev, R., Marziani, P., Negrete, C. A., & Dultzin, D. 2007, ApJ, 666, 757

Sulentic, J. W., Marziani, P., Zamanov, R., Bachev, R., Calvani, M., & Dultzin-Hacyan, D. 2002, ApJ, 566, L71

Sulentic, J. W., Repetto, P., Stirpe, G. M., Marziani, P., Dultzin-Hacyan, D., & Calvani, M. 2006, A&A, 456, 929

Sulentic, J. W., Zwitter, T., Marziani, P., & Dultzin-Hacyan, D. 2000, ApJ, 536, L5

Tremaine, S., Gebhardt, K., Bender, R., Bower, G., Dressler, A., Faber, S. M., Filippenko, A. V., Green, R., Grillmair, C., Ho, L. C., Kormendy, J., Lauer, T. R., Magorrian, J., Pinkney, J., & Richstone, D. 2002, ApJ, 574, 740

Ulrich, M., Maraschi, L., & Urry, C. M. 1997, ARA&A, 35, 445

Vestergaard, M. & Peterson, B. M. 2006, ApJ, 641, 689

Wang, T., Brinkmann, W., & Bergeron, J. 1996, A&A, 309, 81

Weedman, D. W. 1983, ApJ, 266, 479

Wills, B. J., Laor, A., Brotherton, M. S., Wills, D., Wilkes, B. J., Ferland, G. J., & Shang, Z. 1999, ApJ, 515, L53

Zamfir, S., Sulentic, J. W., Marziani, P., & Dultzin, D. 2010, MNRAS, 403, 1759

Zel'Dovich, Y. B. & Novikov, I. D. 1964, Soviet Physics Doklady, 9, 246